N73-24036

NASA CONTRACTOR REPORT

NASA CR-2244

NASA CR-2244

CASE FILE COPY

DESIGN AND EXPERIMENTAL RESULTS FOR A TURBINE WITH JET FLAP STATOR AND JET FLAP ROTOR

by James L. Bettner and Jerry O. Blessing

Prepared by
DETROIT DIESEL ALLISON DIVISION
GENERAL MOTORS CORPORATION
Indianapolis, Ind. 46206
for Lewis Research Center

NATIONAL AERONAUTICS AND SPACE ADMINISTRATION • WASHINGTON, D. C. • MAY 1973

1. Report No.	2. Government Accession No.	3. Recipient's Catalog No.
NASA CR-2244		

4. Title and Subtitle	5. Report Date
DESIGN AND EXPERIMENTAL RESULTS FOR A TURBINE WITH JET FLAP STATOR AND JET FLAP ROTOR	May 1973
	6. Performing Organization Code
7. Author(s)	8. Performing Organization Report No.
James L. Bettner and Jerry O. Blessing	EDR 7389
	10. Work Unit No.
9. Performing Organization Name and Address	
General Motors Corporation Indianapolis, Indiana 46206	11. Contract or Grant No. NAS 3-14303
	13. Type of Report and Period Covered
12. Sponsoring Agency Name and Address	Contractor Report
National Aeronautics and Space Administration Washington, D.C. 20546	14. Sponsoring Agency Code

15. Supplementary Notes

Project Manager, Stanley M. Nosek, Airbreathing Engines Division, NASA Lewis Research Center, Cleveland, Ohio

16. Abstract

The overall performance and detailed stator performance of a negative hub reaction turbine design featuring a moderately low solidity jet flap stator and a jet flap rotor were determined. Testing was conducted over a range of turbine expansion ratios at design speed. At each expansion ratio, the stator jet flow and rotor jet flow ranged up to about 7 and 8 percent, respectively, of the turbine inlet flow. The performance of the jet flap stator/jet flap rotor turbine was compared with that of a turbine which used the same jet flap rotor and a conventional, high solidity plain stator. The effect on performance of increased axial spacing between the jet stator and rotor was also investigated.

17. Key Words (Suggested by Author(s))	18. Distribution Statement
Turbine aerodynamics Jet flap airfoils Aerodynamic variable geometry Stator-rotor spacing	Unclassified - unlimited

19. Security Classif. (of this report)	20. Security Classif. (of this page)	21. No. of Pages	22. Price*
Unclassified	Unclassified	164	$3.00

* For sale by the National Technical Information Service, Springfield, Virginia 22151

Page Intentionally Left Blank

TABLE OF CONTENTS

LIST OF TABLES

LIST OF ILLUSTRATIONS

LIST OF ILLUSTRATIONS (cont)

LIST OF ILLUSTRATIONS (cont)

LIST OF ILLUSTRATIONS (cont)

LIST OF ILLUSTRATIONS (cont)

LIST OF ILLUSTRATIONS (cont)

Page Intentionally Left Blank

DESIGN AND EXPERIMENTAL RESULTS FOR A TURBINE WITH JET FLAP STATOR AND JET FLAP ROTOR

by

James L. Bettner and Jerry O. Blessing

Detroit Diesel Allison, Division of General Motors

SUMMARY

A jet flap stator was designed and tested to demonstrate increased blade loading and the capability to vary turbine flow rate aerodynamically. These stator vanes were tested both as a full annular cascade and with a previously tested jet flap rotor assembly. The effects of axial spacing between the stator and the rotor were also investigated.

The stator vanes were tested (with the rotor assembly removed) over various stator expansion ratios at stator cavity-to-inlet total pressure ratios of 0.75, 1.0 and 1.80 and also at the jet-off condition. As much as 33% primary flow reduction was achieved with 10% jet flow at 0.6 ideal exit Mach number. This flow reduction dropped to 22% as the exit ideal Mach number was increased to 1.0.

Turbine performance was evaluated on the basis of thermodynamic (plus pumping) efficiency. This thermodynamic expression of efficiency charges the turbine for the ideal power of the primary stator jet flow and rotor jet flow streams. It also gives the turbine credit for the pumping power required to pump the rotor jet flow from the turbine center line to the rotor blade.

At the design speed and expansion ratio, the maximum turbine thermodynamic (plus pumping) efficiency was 88.4%. This value was obtained with optimum values of rotor and stator cavity pressure ratios of $P_{T_{IR}}/P_{T_0}$ = 0.6 and $P_{T_{IS}}/P_{T_0}$ = 0.70. This measure of efficiency decreased to 85% when $P_{T_{IS}}/P_{T_0}$ was increased to 1.0. The maximum thermodynamic (plus pumping) efficiency of 91.2% occurred at the low expansion ratio of 1.4 with $P_{T_{IR}}/P_{T_0}$ = 0.8 and $P_{T_{IS}}/P_{T_0}$ = 0.70 - 0.75. There are several other ways to define turbine efficiency. For example, efficiency may be expressed as the actual power (τN) developed by the turbine divided by the ideal power ($\dot{m}_p \Delta H'_{0-3}$) of only the primary flow stream. This definition is called base efficiency. Another expression for efficiency is thermodynamic efficiency which considers the same terms as the thermodynamic (plus pumping) efficiency without the rotor jet flow pumping term. At

design speed and expansion ratio and with jet cavity pressure ratio values of $P_{T_{IS}}/P_{T_0} = 0.70$ and $P_{T_{IR}}/P_{T_0} = 0.6$, the base and thermodynamic efficiency values were 87.90 and 87.10%, respectively, for the jet flap stator/jet flap rotor turbine. These values compare with plain stator/jet flap rotor turbine base and thermodynamic efficiency values of 89.1 and 88%, respectively, when that turbine was operating under the same conditions. In general, operating the jet flap stator/rotor turbine with optimum values of $P_{T_{IR}}/P_{T_0}$ and $P_{T_{IS}}/P_{T_0}$ over a range of turbine expansion ratios showed that the jet flap stator turbine was about one point less efficient than a plain stator turbine which used the same jet flap rotor and operated over the same range of expansion ratios. The solidity of the jet flap stator was 22% less than that of the plain, solid stator.

Axial spacing between the stator and the rotor had little effect on the stage performance for the two positions tested.

INTRODUCTION

The NASA Lewis Research Center has sponsored a series of experimental investigations of several advanced concepts designed to increase blade loading while maintaining good turbine performance. One of these concepts — the jet flap blade—not only increased blade loading, but also demonstrated the capability to vary the turbine flow rate aerodynamically. The jet flap is a high velocity jet which emanates from the airfoil trailing edge pressure surface. The interaction of this jet with the mainstream flow deflects the mainstream flow in the tangential direction. This deflection produces an acceleration on the suction surface and a deceleration on the pressure surface in the aft region of the airfoil. The accelerated flow on the suction surface reduces the amount of diffusion and eliminates, or at least delays, flow separation. Flow rate control is accomplished by the tangential deflection of the mainstream which reduces the effective vane throat dimension.

The design and experimental results for the series of jet flap rotor turbines and impulse cascades are presented in References 1 through 5.* These studies were aimed at determining the increase in blade loading capacity by using the jet flap on a series of blade designs with a progressive decrease in blade solidity. As the solidity of an airfoil is reduced, the force or loading on the airfoil increases. The increased loading generally results in increased diffusion or flow deceleration on the blading suction surface. This increased diffusion is associated with flow separation from the surface and results in increased losses. The results discussed in References 1 through 5 showed that the jet flap did increase the loading capability of blades at moderately low levels of solidity. However, at very low levels of solidity, the jet flap could not prevent flow separation and the result was a decrease in turbine performance.

Experimental studies with high reaction first-stage stator jet flap vanes (References 6 and 7), not only supported the results presented in References 1 through 5 regarding blade loading capability, but also demonstrated the potential of the jet flap stator to be used as an aerodynamic flow control device.

In view of these results, a full annulus of high reaction, jet flap stators was designed and tested. The experimental program consisted of tests on both the jet flap stator operated by itself and also in conjunction with the jet flap rotor described in Reference 2. The turbine, discussed in

*Reference numbers correspond to the numbers given in the Reference section of this report.

Reference 2, featured a conventional, lightly loaded, solid stator used with the modified jet flap rotor. This rotor assembly is shown in Figure 1 prior to installation. Documentation of the plain stator design and performance is presented in References 8 and 9, respectively. The turbine rig was modified to accept an annulus of jet flap stators whose solidity was about 22% less than the stator described in Reference 8. Jet flow was supplied through the vane tips and the original 30-in. (76.20-cm) OD tip and 21-in. (53.34-cm) ID hub flowpath was maintained.

Experimentally, the objectives of the jet flap stator turbine program were to demonstrate:

- Aerodynamic turbine flow control
- Performance comparable to the plain stator/modified jet flap rotor turbine described in Reference 2

Design values of stator cavity-to-inlet total pressure and temperature ratios were $P_{T_{IS}}/P_{T_0} = T_{T_{IS}}/T_{T_0} = 1.0$. With a radially constant slot size of 0.030 in. (0.0762 cm), this corresponded to 2.375% jet flow.

The test program consisted of

Phase I—Turbine design point optimization test
Phase II—Variable area test
Phase III—Stator detailed performance test
Phase IV—Rotor/stator axial spacing test

Rotor and stator cavity-to-inlet pressure ratios ranged up to 1.2 and 2.0, respectively, while the turbine expansion ratio was varied from 1.4 to 2.4. All tests with the jet flap rotor were conducted at design equivalent speed. Detailed radial-circumferential surveys of the flow fields just downstream of the rotor were conducted at several operating points. Also, tip, mean, and hub vane section surface static pressure distributions were obtained at each operating point. Surveys of total and static pressure and gas angle were also made downstream of the stator in Phase III tests with a cone probe.

All testing was conducted while operating the test rig with inlet conditions of approximately 2.7 atm absolute pressure and 650°R (361°K) temperature.

SYMBOLS

C_j	Jet momentum coefficient, $C_j = \dot{m}_s U_j/(\dot{m}_p + \dot{m}_s)V_1$
C_p	Specific heat at constant pressure
C_V	Jet velocity coefficient ($C_V = 0.97$)
C_x	Axial chord in. (cm)
$\overline{e}$	Kinetic energy loss coefficient
F	Blade force per unit length, lb_f/in. (N/m)
g_c	Gravitational constant, 32.174 $lb_m ft/lb_f/sec^2$ (1 kg·m/N·s^2)
$\overline{hb}$	Jet slot size, in. (cm)
H	Compressible shape factor, $H = \delta^*/\theta^*$
H_i	Incompressible shape factor
ΔH	Specific work output, Btu/lb (J/kg)
i	Incidence, deg
L	Lift, blade force in tangential direction, lb_f/in. (N/cm)
$\dot{m}$	Mass flow rate, lb/sec (kg/s)
M	Mach number
N	Rotational speed, rpm (rad/s)
P	Pressure, lb/in.^{2} (N/m^2)
r	Radial location, in. (cm)
R	Gas constant, ft-lb_f/lb_m-°R (m·N/kg·°K)
r_{le}	Leading edge radius, in. (cm)
r_{te}	Trailing edge radius, in. (cm)
R_e	Stator expansion ratio (P_{T_0}/P_{st_1})
R_{eTS}	Total-to-static stator expansion ratio (P_{T_0}/P_{st_1})
R_{eTT}	Total-to-total stage expansion ratio (P_{T_0}/P_{T_3})
S_p	Blade spacing, in. (cm)
T	Temperature, °R (°K)
U	Blade tangential velocity, ft/sec (m/s)
U_j	Jet velocity, ft/sec (m/s)
U_t	Tip speed, ft/sec (m/s)
V	Absolute gas velocity, ft/sec (m/s)
W	Relative gas velocity, ft/sec (m/s)
x	Axial coordinate, in. (cm)
y	Tangential coordinate, in. (cm)
α	Absolute gas angle measured from tangential, deg
σ_j	Jet flow angle, deg
δ_0	Ratio of turbine inlet air total pressure to standard sea sea level conditions
ϵ	Function of γ defined as $\dfrac{\gamma^* \left(\frac{\gamma+1}{2}\right)^{\gamma/(\gamma-1)}}{\gamma\left(\frac{\gamma^*+1}{2}\right)^{\gamma^*/(\gamma^*-1)}}$
δ^*	Displacement thickness, in. (cm)
θ^*	Momentum thickness, in. (cm)

$\eta_{T_{base}}$	Adiabatic efficiency defined as the ratio of turbine work based on torque, primary weight flow, and speed measurements to the ideal work based on inlet total temperature and on inlet and outlet total pressure
η_t	Adiabatic efficiency defined as the ratio of turbine work based on measured inlet and exit total temperature to ideal work based on measured inlet total temperature and pressure and on measured exit total pressure
$\eta_{T_{thermo}}$	Thermodynamic efficiency defined as the ratio of actual turbine power to the sum of the ideal powers of the primary flow, stator flow, and rotor flow
$\eta_{T_{thermo + pump}}$	Thermodynamic efficiency with pumping power defined as the ratio of the sum of turbine power plus the rotor pumping power to the sum of the ideal powers of the primary flow, stator flow, and rotor flow
θ	Circumferential position, deg
θ_{cr}	Squared ratio of critical velocity at turbine inlet temperature to critical velocity at standard sea level temperature
ρ	Density, lb/ft^3 (kg/m^3)
σ_x	Blade axial chord solidity defined as C_x/S_p
τ	Jet efflux angle relative to pressure surface, deg; or torque lb_f-ft (N·m)
ψ_t	Compressible tangential lift coefficient
$\bar{\omega}$	Total pressure loss coefficient
ϕ	Stator exit gas angle (measured from tangential), deg

Subscripts

0	Station at stator inlet
1	Station at free-stream conditions between stator and rotor
2	Station at outlet of rotor immediately downstream of trailing edge
3	Station downstream of turbine
cr	Condition at Mach number of unity
ma	Mass averaged
m1	Hypothetical mixed station
IR	Jet flow inlet station (rotor cavity)
IS	Jet flow inlet station (stator cavity)
j	Jet flow
ℓ	Local
eq	Base on standard inlet conditions

p	Primary flow
R	Rotor jet
s	Stator jet
st	Static
T	Total
th	Theoretical or ideal
u	Tangential direction
x	Axial direction
w	Based on stator exit wall taps
wo/j	Without stator jet
w/j	With stator jet

Superscripts

'	Ideal or isentropic

VANE AERODYNAMIC DESIGN

VELOCITY DIAGRAM STUDY

The velocity diagram and vane profile design procedure for the jet flap stator involved an iterative solution for five aerodynamic and geometric parameters. These parameters are:

- Vane loss characteristics (profile and secondary)
- Inlet mass flow reduction capability
- Jet slot size
- Vane camber
- Vane solidity

The design objective was to define a low solidity jet flap stator vane which produced, when the jet was activated, the same aerodynamic flow field into the rotor as produced by the higher-solidity, plain stator discussed in Reference 2. The overall design requirements were:

Equivalent flow in rotor, $\dot{m}_p\sqrt{\theta}_{cr_0}\epsilon_0/\delta_0$	47.7 lb/sec (21.636 kg/s)
Equivalent work, $\Delta H/\theta_{cr_0}$	20.0 Btu/lb (46,519 J/kg)
Equivalent speed, $N/\sqrt{\theta}_{cr_0}$	4660 rpm (487.99 rad/s)
Equivalent tip speed, $U_t/\sqrt{\theta}_{cr_0}$	610 ft/sec (185.928 m/s)

The experimental performance results of the jet flap stator turbine are compared with the performance of the plain stator turbine described in Reference 2.

The iterative solution was accomplished by developing a design computer program based on the jet flap throat sizing procedures described in the appendix of Reference 4. This program incorporates experimental results from previous jet flap blade and vane tests and analytical performance predictions. Inlet mass flow reduction data and vane profile loss (modified for different blockage levels) were reported in Reference 6 and included in the computer program. Secondary end wall loss characteristics of the plain stator operating in a similar environment as the current jet flap stator were determined in Reference 9. These losses were added to the jet flap stator profile loss in the vane end regions to produce the complete stator exit loss profile. Figures 4, 30, and 31 of Reference 4 describe the jet slot flow data as functions of slot size and pressure ratio across the jet for both bench and rotating blade tests that were incorporated in the jet flap stator design computer program. Information regarding the performance of the jet flap as a function of vane camber was also included in the program from Reference 6.

The output of the program defined (1) the jet flap stator throat dimensions which were sized for the jet-off condition and (2) the velocity diagrams (both at the stator throat and downstream of the trailing edge for the jet-on and jet-off conditions).

A matrix study of the effects of stator cavity pressure, jet slot size, and number of stators on turbine performance was conducted with the design program. The number of vanes was selected to be 40—the same number as the plain stator discussed in Reference 2. This was done so as not to introduce any new dynamic pressure effects on the rotor which would be caused by a different number of vane wakes and possibly distort the performance comparison between the jet flap stator turbine and the plain stator turbine discussed in Reference 2. Both of these turbines used the modified jet flap rotor. The matrix study showed that a stator jet slot size, $\overline{hb}$, of 0.030 in. (0.0762 cm) and cavity pressure ratio, $P_{T_{IS}}/P_{T_0}$, of unity along with 40 vanes would set up the desired velocity diagrams. This combination of design variables required a small amount of jet flow rate, $\dot{m}_s/\dot{m}_p = 2.375\%$, and kept the trailing edge thickness dimension to a reasonably small value while requiring a vane cavity pressure level that would be typical of a cooled gas producer turbine engine.

The selected aerodynamic and geometric design point conditions are given in Table I.

Tip, mean, and hub section negative hub reaction velocity diagrams with and without the jet turned on are presented in Figures 2 and 3, respectively. The stator exit flow is transonic at the mean section, subsonic at the tip, and supersonic at the hub section. The gas exits from the turbine in a near-axial direction. The diagrams reflect the reduction in stator inlet flow rate as the jet is turned on.

SOLIDITY CONSIDERATIONS AND AIRFOIL DESIGN

The objective of this research program was to determine the performance level and inlet mass flow control capability of a jet flap stator whose solidity was less than that of a conventionally designed plain stator. Definition of the solidity level was made by:

- Initially assuming a radially constant 25% reduction in solidity from the plain stator solidity discussed in Reference 2
- Performing a vane design satisfying the velocity diagrams of Figures 2 and 3 to determine if flow separation from the vane surfaces could be prevented when the jet flap was activated (Whenever flow separation could not be prevented, the solidity was increased and a new vane design completed.)

Vane section profile shapes were determined by iterating with the section geometry without jet flow until satisfactory surface velocity distributions were obtained. The surface velocities were computed by the two-dimensional compressible-flow methods described in Reference 10. The airfoil geometry was varied to keep the velocity levels on the pressure surface as low as possible and high loading levels as far back on the vane as possible.

The effect of free-stream static pressure distribution on the behavior of the suction surface boundary layer was investigated by using the methods of McNally (Reference 11). Flow separation was assumed to occur when the incompressible shape factor, H_i attained a value between 1.8 and 2.2. The section profiles and solidity levels were iterated upon until acceptable surface velocity distributions around the airfoils were obtained and the flow was on the verge of separating from the suction surface when the jet was turned off. When the jet was turned on the inlet flow was reduced, flow separation was prevented, and the design stator exit velocity diagrams would be achieved.

The jet-on flow field calculation was accomplished by considering the jet stream to behave as a solid flow boundary. The general shape of the jet was determined by satisfying the condition that the change in momentum across the blade row in the tangential direction as computed by the velocity diagrams of Figure 2 was equal to the lift of the airfoil as computed by the sum of the static pressure force on the blade and the change in momentum of the jet in the tangential direction. This may be expressed in equation form as:

$$L = -\dot{m}_p W_{u_0} + (\dot{m}_p + \dot{m}_s) W_{u_1} = \int_0^{C_x} \Delta P_{st_u}\, d_x + C_V \rho_{st_j} U_j^2\, \overline{hb} \cos \alpha_j \qquad (1)$$

But $W_{u_0} = 0$

Thus,

$$\int_0^{C_x} \Delta P_{st_u}\, d_x = (\rho_{st} W_x W_u)_1 \frac{S_p}{g_c 144} - C_V \rho_{st_j} U_j^2\, \overline{hb} \cos \alpha_j \qquad (2)$$

The two terms on the right-hand side of the equation were computed for the tip, mean, and hub sections. The jet stream was assumed to be approximately parabolic in shape emanating at the jet flap slot. The downstream direction of the jet stream was set equal to the design jet on stator exit angle. The approximate parabolic jet shape was maintained, but the exact position of the jet streamline relative to the airfoils was iterated upon until the integral of the static pressure distribution around the airfoil was satisfied. This requirement fixed the jet shape and, hence, the surface velocity around the vane with the jet on.

The aforementioned solidity-surface velocity distribution iteration resulted in the tip, mean, and hub jet-on/jet-off velocity distributions shown in Figures 4 and 5. Figure 6 illustrates the corresponding vane sections. Vane section cartesian coordinates are presented in Table II. This design satisfied all of the imposed constraints and resulted in a solidity reduction of about 22% from the plain stator design. The vane was on the verge of imminent flow separation at the tip section. This condition was alleviated when the jet was turned on.

The vane design of Figure 6 resulted in about a 25% increase in the value of ψ_t, the tangential lift coefficient for the jet flap stator over the plain stator. ψ_t is defined as:

$$\psi_t = \frac{S_p}{C_x}\left[\frac{\rho_{st1}\, V_{x1}\, \Delta V_{u1}}{P_{T_0} - P_{st1}}\right] \tag{3}$$

and is a compressible form of Zweifel's (Reference 12) actual-to-ideal loading coefficient. Table III lists geometric and aerodynamic design information for the jet flap and plain stator designs. Figure 7 compares the suction and pressure surfaces of the plain and jet flap vanes. The similarity in velocity diagrams and increase in loading (lift coefficient) for the two stator designs is evident in Table III.

JET SLOT DESIGN

The jet slot was designed to efflux normal — $\tau = 90$ deg to the pressure surface at the mean section. Because of slight airfoil twist in the radial direction τ varied from 93 deg at the hub section to 87 deg at the tip section. The slot was positioned 0.055 in. (0.1397 cm) from the trailing edge surface and formed by the Elox cutting process to produce a radially constant 0.030-in. (0.0762-cm) width jet slot. The radially constant slot width was dictated by (1) manufacturing cost considerations and (2) lack of reliable experimental data for radially variable jet slot performance. These jet slot details are shown in Figure 6.

VANE CAVITY DESIGN

The stator vane cavity was determined by requiring a wall thickness of 0.050 in. (0.1270 cm) over most of the airfoil. This thickness tapered to about 0.030 in. (0.0762 cm) in the very aft trailing edge region. These wall dimensions are shown in Figure 6.

The jet flap blade cavity design discussed in Reference 2 did not incorporate any means to assist the jet flow in turning from radial to axial directions as it entered and left the blade. Experimental results of that program demonstrated an unsatisfactory distribution of jet flow along the radial span of the jet slot. The jet flow could not negotiate the abrupt radial-to-axial turn where it entered the blade; this condition resulted in a deficiency of jet flow in the hub region. To overcome this difficulty in the jet flap stator, a series of turning vanes was incorporated in the blade cavity. These vanes are shown in Figure 8. They not only turned the jet flow but also provided stiffening to the airfoil structure.

The stator was supplied with jet flow through the tip section. At design turbine expansion ratio, the Mach number at the tip section was estimated to be 0.116 for a cavity pressure ratio of 1.0, and 0.130 for a cavity pressure of 2.0.

MECHANICAL DESIGN

TEST RIG

The test vehicle used for this program was a modification of the rig described in Reference 8. The modification consisted of:

- New splitline located upstream of the stators
- Primary plenum chamber located over the vane tip section
- Secondary plenum chamber in the form of a torus which fed the primary plenum chamber
- Suitable hub and tip wall spacing rings which permitted a 1-in. axial variation in axial spacing between the rotor and stator
- Complete jet flap stator assembly

The use of the two plenum chambers ensured the delivery of a circumferentially uniform, low Mach number jet flow to the stators. Seven flexible lines were distributed around the periphery of the secondary plenum torus to supply that plenum with facility jet flow air. Another set of 20 lines (which were equally spaced around the torus) delivered jet flow air to the vane tip section primary plenum chamber. This arrangement is shown in Figures 9 and 10. The highest jet flow Mach number at turbine design flow conditions was estimated to occur at the vane tip section cavity; its value was 0.116.

Concentric hub and tip wall spacer rings were fabricated to permit axial variation of the stator-rotor spacing. The hub ring OD was 21 in. (53.34 cm), and the ID of the tip ring was 30 in. (76.20 cm). Both of these rings were 1 in. (2.54 cm) in axial length. Where the spacing between stator and rotor was a minimum value, the rings were placed upstream of the stator assembly. This is the configuration shown in Figure 9. The spacing was increased 1 in. (2.54 cm) between the stator and rotor by removing (in the following order) the rotor, stator assembly, and spacing rings; the stator and rotor were then reinstalled in the turbine with the spacing rings between the stator and rotor.

The stator assembly consisted of hollow, investment cast Inco 718 material stator vanes spot welded in inner and outer bands. Airfoil profile contours were Elox machined in the hub and tip bands, and the vanes were spot welded in place. The vane ends were then sealed in the bands with epoxy. The seal was formed on the side of the hub and tip bands that was not in the flow path. Figure 11 shows the complete stator assembly viewed from the tip section. A view of the stator vane annulus positioned in the front half of the primary plenum chamber (looking forward), is illustrated in Figure 10. The openings for the 20 jet flow supply lines are

evident. The three rectangular surfaces with 21 tube fittings are used for securing the tip, mean, and hub section vane surface static pressure tube lines where they protrude from the test rig.

DYNAMIC ANALYSIS

The design of the hollow jet flap stator blades incorporated internal secondary air guide vanes. These features are shown in Figure 8. The stators were fixed at both ends to provide increased load-carrying ability, increased stiffness, and very high natural frequencies. Additional stiffening of the airfoil was accomplished by the internal jet flow guide vanes. The higher natural frequencies are desirable to avoid coincidence of the lower modes with inherent low frequency excitation which might be generated by rotor unbalance forces.

The fundamental bending mode frequency was estimated from previous jet flap blade vibration bench test data. The first bending mode frequency was indicated to be 3900 Hz, which is far above the rotor-generated excitation frequency yet well below the blade passage excitation frequency throughout a speed range of 70-110% $N/\sqrt{\theta}$.

STRESS ANALYSIS

The design of the primary plenum required a 0.500-in. (1.27-cm) wall thickness, 40 clamp bolts, and 20 equally spaced gussets on each side. This design resulted in a calculated stress of 16,300 psi (112.385×10^6 N/m^2) in the plenum chamber wall. The material used in the plenum was forged-type AISI-410 steel with an ultimate strength of 130,000 psi (896.318×10^6 N/m^2) at 250°F (121.11°C).

A stress analysis was performed on the airfoil with the results indicating low operational stresses. The ballooning stresses were calculated—using a conservative assumption of 50 psi (0.3447×10^6 N/m^2) internal pressure and a zero external pressure—and were found to be acceptable.

Table IV shows the forces that the gas exerts on the vane when the turbine was operating at the design point. These data were used to analyze the airfoil in four sections with the maximum bending stress of 4860 psi (33.508×10^6 N/m^2) occurring in the section nearest the hub. Deflections in the airfoil ranged from 0.005 in. (0.0127 cm) near the hub to 0.002 (0.0051 cm) near the tip.

The bending stresses in the airfoil about the axis of minimum moment of inertia were 8429 psi (58.116×10^6 N/m^2). For the bending stress about the maximum moment of inertia axis, 6464 psi (44.567×10^6 N/m^2) was calculated.

APPARATUS AND INSTRUMENTATION

The test apparatus included a single-stage cold air turbine test rig, suitable housing to provide uniform inlet flow conditions, and a dynamometer to absorb and measure turbine output.

Air was supplied at approximately 2.7 atm (273.6 kN/m^2) pressure and a temperature of approximately 650°R (361°K). The inlet pressure was controlled by the separate air compressor supply and/or by a throttle valve in the inlet supply line. Turbine expansion ratio was controlled by a throttle valve in the exhaust system duct.

The turbine test rig instrumentation is also described in Reference 8. Airflow was measured using a Bailey adjustable orifice which is calibrated with an ASME flow nozzle. Turbine power output was absorbed by two Dynamatic dry gap eddy current brakes. The torque of each dynamometer is measured separately by a dual output strain gage load cell connected in tension to the dynamometer torque arm.

Measurements of total temperature and total pressure were made at stations 0 and 3. These measuring stations are described in Figure 12. Turbine inlet temperature (station 0) was measured with 20 iron-constantan thermocouples arranged five to a rake. The sensing elements were located on centers of equal annular areas, and the rakes were spaced 90 deg apart. Four Kiel-type total pressure probes, also located at the inlet, were used to establish the desired inlet total pressure. The turbine exit measuring station (station 3) was located 4.75 in. (12.065 cm) downstream from the rotor and was instrumented with five combination total pressure, total temperature, self-aligning flow angle probes. The sensing elements of the five combination probes were located at the center of five equal annular areas.

Static pressures were measured with four taps on both the inner and outer walls located around the annulus at stations 0, 2, and 3. The stator outlet static pressure (station 1), located 0.5 in. (1.27 cm) downstream from the stator trailing edge, consisted of six taps located on the hub and tip casing walls, verniered across one vane spacing.

Rotor exit surveys were performed approximately 0.125 in. (0.318 cm) axially downstream of the rotor blade trailing edge (station 2). Total pressure, total temperature, and flow angle were measured at seven radii from hub to tip for a circumferential arc of 22 deg (0.38 rad). The measurements were taken concurrently with a single combination probe.

A stator exit survey was performed axially 0.5 in. (1.27 cm) behind the trailing edge of the stator vane. The survey was performed with a 15-deg half-angle cone probe which recorded total pressure, static pressure, and gas angle while the probe traversed circumferentially approximately 22 deg at 12 radial positions. A cone probe was chosen for this survey based on the experience of using a cone probe in both two- and three-dimensional high subsonic, transonic, and supersonic flow fields. Also, this type of probe is simple, rugged, and presents a minimal disturbance to the flow field. A photograph of the probe is shown in Figure 13. Details of the probe design are shown in Figure 14. The probe was set at the mean section flow gas angle. Incidence of flow on the probe was measured relative to this fixed angle. To obtain data near the outer wall, the foot of the probe was tilted down at an angle of 94.56 deg so that the probe tip element could approach within 0.107 in. (0.272 cm) of either the hub or tip wall before the probe body contacted the walls.

The stator vanes were instrumented with static pressure taps located at the hub, mean, and tip sections. To remain clear of hub and casing endwall boundary layer growth effects on static pressure measurements, the hub and tip taps were located 0.5 in. (1.27 cm) from the end walls. Figure 15 shows the hub section pressure surface static taps after instrumentation. Eight taps on the pressure surface and 12 taps on the suction surface were used at each of the three radial positions. All pressure taps had a 0.020-in. (0.0508-cm) ID opening except for those located in the aft trailing edge region. The trailing edge region taps were formed from 0.020-in. (0.0508-cm) OD, 0.010-in. (0.0254-cm) ID tubing that was buried in the suction and pressure surface walls. Burying the tubing within the walls avoided blocking the jet flow near the slot. Figure 16 shows the axial position of the surface static taps. All other pressure tap tubing was routed to the front of the vane internal cavity to avoid blockage of the jet slot in the instrumented vanes.

CALCULATION PROCEDURE

OVERALL TURBINE PERFORMANCE

Turbine performance was rated on the basis of the ratio of inlet total pressure to rotor exit total pressure. Inlet total pressure at station 0 was calculated from continuity by using the average of the 20 measured total temperatures, the average of the hub and tip static pressures, the mass flow rate, and the inlet annulus area. The flow was assumed to be axial. Exit total pressure at station 3 was also calculated from continuity using the mass flow rate, the annulus area, the average of the hub and tip static pressures, the average flow angle, and the total temperature. The total temperature was calculated from the enthalpy drop which, in turn, was based on the measured airflow, torque, and speed.

Three efficiencies were defined: base efficiency, thermodynamic efficiency, and thermodynamic plus pumping power efficiency. The base efficiency was calculated as a ratio of the actual power determined from torque and rotor speed measurements to the ideal power determined from the primary mass flow rate, inlet total temperature, and associated calculated expansion ratio, i.e.,

$$\eta_{T_{base}} = \frac{\tau N}{\dot{m}_p H'_{P_{0-3}}} \tag{4}$$

The thermodynamic efficiency charged the turbine for the available power of the jet flow in both the rotor and the stator, i.e.,

$$\eta_{T_{thermo}} = \frac{\tau N}{\dot{m}_p \Delta H'_{P_{0-3}} + \dot{m}_s \Delta H'_{s_{1-3}} + \dot{m}_R \Delta H'_{R_{1-3}}} \tag{5}$$

The thermodynamic plus pumping power efficiency charged the turbine for the power of the jet streams but it gave the turbine credit for the power required to pump the rotor jet flow from the turbine centerline to the rotor jet flap blade:

$$\eta_{T_{thermo + pump}} = \frac{\tau N + \dot{m}_R U_m^2}{\dot{m}_p \Delta H'_{P_{0-3}} + \dot{m}_s \Delta H'_{s_{1-3}} + \dot{m}_R \Delta H'_{R_{1-3}}} \tag{6}$$

ROTOR EXIT SURVEY

The performance of the turbine determined by a rotor exit survey at the design point condition was based on measured expansion ratio, inlet temperature, and exit temperature. The measured expansion ratio was based on the average total pressure indicated by the four inlet Kiel probes and the exit total pressure measured by the survey probe. The inlet total temperature was the average temperature of the 20 inlet thermocouples; the exit total temperature was measured by the thermocouple on the survey probe. These thermocouples were corrected for Mach number based on a linear variation of hub and tip static pressure and the measured total pressure. The isentropic work of the turbine was based on the measured inlet temperature and measured total pressure ratio. The actual work was the difference of the enthalpies associated with the measured inlet and exit temperatures. The efficiency at each station in the survey was the ratio of the actual work to the isentropic work, i.e.,

$$\eta_t = \frac{T_{T_0} - T_{T_2}}{T_{T_0}\left[1 - \left(\frac{P_{T_2}}{P_{T_0}}\right)^{\frac{\gamma-1}{\gamma}}\right]} \tag{7}$$

STATOR EXIT SURVEY

Surveys of total pressure, static pressure, and gas angle were made 0.5 in. (1.270 cm) downstream from the stator trailing edge at 12 radial depths with a 15 deg half-angle cone probe. The surveys encompassed two vane passages. Vane loss coefficient and boundary layer parameter calculations were made to evaluate the detailed stator performance as a function of stator expansion ratio, $R_{e_{TS}}$, and jet cavity pressure ratio, $P_{T_{IS}}/P_{T_0}$.

Loss Coefficients

Local Values

Kinetic energy loss coefficient:

$$\bar{\zeta}_f = 1 - \frac{V_1^2(r,\theta)}{V_{1_{th}}^2(r,\theta)} \tag{8}$$

where $V_{th} = f(P_{T_0}, P_{st_1})$ and

$V_1 = g(P_{T_1}, P_{st_1})$

Total pressure loss coefficient:

$$\overline{\omega}_f = \frac{P_{T_0} - P_{T_1}(r,\theta)}{P_{T_0} - P_{st_1}(r,\theta)} \tag{9}$$

Circumferentially Integrated Kinetic Energy Loss Coefficient

Stator exit actual and ideal energy loss coefficient:

$$\overline{\sigma}(r) = 1 - \frac{1/2\int_{\theta_1}^{\theta_2}\left[\rho_{st_1}(r,\theta)V_1(r,\theta)\sin\phi_1(r,\theta)\right]V_1^2(r,\theta)r\,d\theta}{1/2\int_{\theta_1}^{\theta_2}\left[\rho_{st_1}(r,\theta)V_1(r,\theta)\sin\theta_1(r,\theta)\right]V_{1_{th}}^2(r,\theta)r\,d\theta} \tag{10}$$

Stator exit mixed station kinetic energy loss coefficient (simultaneous solution of the following equations of motion):

1. Conservation of axial momentum (between stations 1 and m1):

$$g_c\int_{\theta_1}^{\theta_2}\rho_{st_1}(r,\theta)r\,d\theta + \int_{\theta_1}^{\theta_2}\rho_{st_1}(r,\theta)V_1^2(r,\theta)\sin^2\phi_1(r,\theta)r\,d\theta = \tag{11}$$

$$\left[P_{st_{m1}}(r)g_c + \sin^2\phi_{m1}(r)\rho_{st_{m1}}(r)V_{m1}^2(r)\right]r(\theta_2 - \theta_1)$$

2. Conservation of tangential momentum, (1→m1):

$$\int_{\theta_1}^{\theta_2}V_1(r,\theta)\cos\phi_1(r,\theta)\sin\phi_1(r,\theta)\rho_{st_1}(r,\theta)r\,d\theta = \tag{12}$$

$$\sin\phi_{m1}(r)\cos\phi_{m1}(r)\rho_{st_{m1}}(r)V_{m1}^2(r)r(\theta_2 - \theta_1)$$

Momentum Thickness, $\theta^*(r)$

$$\int_0^{\theta^*} V_{th_1}(r,\theta)\, \rho_{st_{th_1}}(r,\theta) \sin \phi_1(r,\theta)\, dy = \tag{21}$$

$$\int_{\theta_1}^{\theta_2} V_1(r,\theta) \left[V_{th_1}(r,\theta) \rho_{st_1}(r,\theta) \sin \phi_1(r,\theta) - V_1(r,\theta) \rho_{st_1}(r,\theta) \sin \phi_1(r,\theta) \right] r\, d\theta$$

Solve for $\theta^*(r)$

Boundary Layer Shape Factor, H(r)

$$H(r) = \frac{\delta^*(r)}{\theta^*(r)} \tag{22}$$

EXPERIMENTAL RESULTS

PHASE I—TURBINE DESIGN POINT OPTIMIZATION TEST

The Phase I turbine test involved operating the jet flap stator with the modified jet flap rotor discussed in Reference 2. Testing was conducted over a wide range of stator and rotor cavity pressure ratios while the design stage expansion ratio and design equivalent speed were maintained.

Reaction

Figure 17 demonstrates how the stator total-to-static expansion ratio, $P_{T_0}/\bar{P}_{st_1}$, and the overall turbine total-to-static expansion ratio, $P_{T_0}/\bar{P}_{st_3}$, varied with both rotor and stator cavity total-to-inlet total pressure ratios. However, except for very low values of stator $P_{T_{IS}}/P_{T_0}$, the turbine overall $P_{T_0}/\bar{P}_{st_3}$ maintained a nearly constant value. With zero stator flow ($P_{T_{IS}}/P_{T_0}$ equals approximately 0.62), increasing the rotor jet produced a slight increase in exit whirl and Mach number with the corresponding drop in turbine exit static pressure. Increased stator jet cavity pressure produced a reduction in flow through the turbine which (when coupled with increased rotor cavity pressure) tended to produce a constant value of turbine static pressure and, hence, a nearly constant turbine total-to-static expansion ratio. Figure 17 also illustrates the effect of rotor and stator cavity pressure on stator expansion ratio (or stator reaction) at turbine design overall expansion ratio. As the rotor jet cavity pressure is increased the rotor becomes more reactive (i.e., there is a greater static pressure decrease across the rotor). The stator, therefore, becomes less reactive in order for the turbine total-to-static pressure ratio to remain nearly constant across the entire turbine. As a result of the constant turbine total-to-static pressure ratio, the stator expansion ratio decreased as the rotor jet cavity pressure ratio increased. The design stator expansion ratio, $P_{T_0}/\bar{P}_{st_1} = 1.976$, was nearly obtained (2.02) at a rotor cavity pressure ratio of about 0.6. As the stator cavity pressure was increased there was a slight increase in stator expansion ratio except with zero jet flow in the rotor which showed a more pronounced increase. The stator exit static pressure was determined by averaging the 12 stator exit hub and tip static pressure readings.

Flow Rate

Equivalent primary flow as a function of stator cavity pressure ratio is shown in Figure 18. The equivalent design primary flow for the stator jet off is 49.85 lb_m/sec (22.611 kg/s) compared with a maximum measured value of about 49.45 lb_m/sec (22.43 kg/s). The design value of

primary flow for a stator cavity pressure ratio of 1.0 was 46.59 lb_m/sec (21.133 kg/s) and was obtained experimentally when $P_{T_{IR}}/P_{T_0} = 0.6$. This design value is to be expected because, as shown on Figure 17, $P_{T_{IR}}/P_{T_0} = 0.6$ set up the correct reaction level at the stator exit. These data show that an increase in stator and/or rotor cavity pressure ratio resulted in a decrease in primary flow. Figure 19 presents the percent of primary flow reduction obtained while maintaining a 2.03 stage expansion ratio. As much as 18% primary flow reduction was observed at $P_{T_{IS}}/P_{T_0} = 2.0$ and $P_{T_{IR}}/P_{T_0} = 1.2$. The design value of flow reduction was 6.4% when $P_{T_{IS}}/P_{T_0} = 1.0$. Using a typical measured value of jet-off flow, 49 lb/sec (22.226 kg/s), an experimental value of 5.4% was obtained when $P_{T_{IR}}/P_{T_0} = 0.6$ and $P_{T_{IS}}/P_{T_0} = 1.0$. Thus, a value of $P_{T_{IS}}/P_{T_0}$ slightly greater than 1.0 was necessary to produce the 6.4% flow reduction when considering $P_{T_{IR}}/P_{T_0} = 0.6$ and referencing the jet-off flow to the typical measured value of 49 lb/sec (22.226 kg/s).

The flow entering the rotor corrected to rotor inlet conditions (assuming a constant 2% stator total pressure loss) is shown in Figure 20 for various stator cavity pressure ratios. Up to a 12% net flow reduction was observed while maintaining a 2.03 stage expansion ratio. Figure 21 displays equivalent total flow as a function of stator cavity pressure ratio for lines of rotor cavity pressure ratio. As in Figure 18 for a given rotor cavity pressure ratio, an increase in stator cavity pressure resulted in decreasing the total flow. However, increases in rotor cavity pressure resulted in actually increasing the total flow because the rotor jet flow increase was greater than the primary flow reduction.

Figure 22 shows the effect of stator and rotor cavity pressure on equivalent stator jet flow. As would be expected, increasing the stator supply pressure resulted in an increase in stator jet flow. For the lower stator cavity pressure ratios, an increase in the rotor cavity pressure resulted in a higher stator exit static pressure and, therefore, a reduction in stator jet flow. As the stator cavity pressure was increased, this rotor cavity pressure effect was less pronounced. Figure 23 shows the ratio of stator jet flow to primary flow for various stator cavity pressure ratios. At design $P_{T_{IS}}/P_{T_0} = 1.0$, an experimental value of $\dot{m}_s/\dot{m}_p = 2\%$ was obtained whereas the design value was 2.375%. The amount of stator jet flow was computed by assuming the jet expanded from the cavity total pressure to downstream static pressure. In reality, the jet expanded to the pressure surface static pressure that existed at the jet slot exit. Because of the presence of the jet which stagnated the primary flow in the neighborhood of the slot, the jet slot exit static pressure was larger than downstream static pressure. Thus, there was probably less than design expansion ratio across the jet slot and, hence, less than design jet flow rate was observed experimentally.

Figure 24 shows how equivalent rotor jet flow increases with an increase in rotor cavity pressure ratio. The stator cavity pressure ratio up to 1.2 had little effect on the rotor jet flow for a constant 2.03 stage expansion ratio.

Gas Angle

Figure 25 demonstrates that the rotor cavity pressure ratio had a strong effect on rotor exit absolute gas angle. These angle data represent the average reading of the five yaw probes located in measurement plane 3 of Figure 12. These data show that an increase in rotor cavity pressure ratio tends to increase the rotor turning and thus increases negative exit whirl. The effect produced by an increase in stator cavity pressure is to lower the rotor inlet flow which then lowers the relative rotor exit velocity. Because the wheel speed remained constant, this caused an increase in positive whirl and resulted in a decrease in absolute exit gas angle. Using $P_{T_{IR}}/P_{T_0}$ = 0.6 to set up the correct reaction level across the stator, an exit absolute gas angle of 92.2 deg was obtained experimentally at the jet-on design point. This corresponds to a design value of 91.74 deg. For the jet-off design condition, an angle of 94.3 deg was determined experimentally while the design value was 91.67 deg.

Equivalent Torque and Work

Figure 26 shows the variation of equivalent torque with stator and rotor cavity pressure ratio at the design stage expansion ratio. As the stator cavity pressure is increased, the flow across the rotor blade decreases and results in a drop in equivalent torque. Increasing the rotor cavity pressure produces more turning in the rotor blade which increases the equivalent torque.

Equivalent specific work versus stator cavity pressure ratio is presented in Figure 27. Equivalent work is based on primary flow only. These data show that increasing the stator cavity pressure ratio first causes a decrease and than an increase in specific work. This indicates that, in general, the rate of decrease of torque is less than that of the primary flow.

Efficiency

The effect of rotor cavity pressure ratio on turbine efficiency is presented in Figure 28. Also shown in Figure 28 are both base and thermodynamic expressions of efficiency. A maximum thermodynamic efficiency of 87.1% was achieved at a rotor cavity pressure ratio of 0.60 and a stator cavity pressure ratio of 0.70. The maximum thermodynamic efficiency

was 88% for the modified jet flap rotor blade (Reference 2) operated with a plain stator. However, associated with this drop of 0.9 point in thermodynamic efficiency were increases in the thickness of the vane, a 22% reduction in solidity, and an increase in trailing edge blockage from 0.0237 to 0.110. The thermodynamic efficiency of the jet flap stator turbine (with both the stator and rotor jet flow off) was 84.6%, which compares with 85.3% for the solid stator turbine with no jet flow to its jet flap rotor. As the stator cavity pressure ratio was increased above 0.70, the gains made by the jet flow are outweighed by the ideal jet flow power term, $\dot{m}_S \Delta H'_{s_{1-3'}}$ in the thermodynamic efficiency definition described in Equation (6). Comparing the stators for a stator cavity pressure ratio of 0.70 on terms of base efficiency, shows the jet flap stator to be about a point lower across a range of rotor cavity pressure ratios from 0.37 to 1.20.

Figure 29 shows the variation of thermodynamic efficiency (with pumping power) as a function of stator and rotor cavity pressure ratio. As in Figure 28, the maximum efficiency occurs at a stator cavity pressure of 0.70 and a rotor cavity pressure ratio of 0.6. For these flow conditions of $Re_{TT} = 2.034$, $P_{T_{IR}}/P_{T_0} = 0.6$, and $P_{T_{IS}}/P_{T_0} = 0.7$, the maximum thermodynamic efficiency with pumping considered was 88.4% as compared with 87.1% when pumping was not considered. Furthermore, the 87.1% thermodynamic efficiency for the jet flap stator/jet flap rotor turbine was about one point lower than the plain stator/jet flap rotor efficiency of 88%. At design $N/\sqrt{\theta}_{cr_0}$ and Re_{TT}, (with $P_{T_{IR}}/P_{T_0} = 0.6$ and design $P_{T_{IS}}/P_{T_0} = 1.0$), the thermodynamic plus pumping efficiency was 85%.

Figure 30 shows the effect stator cavity pressure has on base efficiency for various rotor cavity pressure ratios. Because the turbine is not charged for the use of the ideal power capacity of the jet flows, the base efficiency, in general, increases for increases in both stator and rotor cavity pressure ratios. Comparing efficiencies at $P_{T_{IS}}/P_{T_0} = 0.7$ and $P_{T_{IR}}/P_{T_0} = 0.6$, the base efficiency was 87.9% for the jet flap stator turbine and 89.1% for the plain stator turbine.

Vane Surface Velocity Distribution

Surface static pressure taps, located at radial positions of 11.0, 12.75 and 14.50 in. (27.940, 32.385, and 36.830 cm), were used to determine the surface velocity distribution around the airfoil at each operating point of the test program. The 11.0 in. (27.940 cm) and 14.5 in. (36.830 cm) radial sections are 0.5 in. (1.27 cm) from the end walls and were selected to avoid end wall boundary layer effects on the vane surface static pressure measurements. The following examples are a few of the more interesting surface velocity distributions. These examples are:

- Comparisons of tip, mean, and hub measured and predicted jet-on and jet-off velocity distributions
- Effects of stator expansion ratio, stator jet flow, existence of flow separation, and presence of normal shocks on surface velocity distributions

Comparison With Design

Measured and predicted jet flap vane surface velocity distributions are presented in Figure 31 for the tip, mean, and hub sections, respectively, with the turbine operating at design overall expansion ratio, design stator expansion ratio, and design corrected speed with the jet turned off. Similar measured and design comparisons for the jet-on ($P_{T_{IS}}/P_{T_0} = 1.0$) flow conditions are shown in Figure 32. In general, the agreement between measured and predicted values was good for the pressure surfaces and fair for the suction surface. Where the agreement between measured and predicted values was considered poor (e.g., jet off and hub section in Figure 31), analyses of the radial distribution of flow rate showed there was experimentally more flow in the hub region than the design value. This would account for the larger-than-design values of surface velocity that were observed in the hub region.

Effect of Stator Expansion Ratio

Figure 33 presents the surface critical velocity ratios for various stage expansion ratios while maintaining stator and rotor cavity pressure ratios of 1.0 and 0.6, respectively. Because the vanes are beginning to choke at $R_{eTT} = 2.03$, there is little change in velocity distribution above this value. At $R_{eTT} = 1.4$, the flow accelerates on the suction surface to about $V/V_{cr} = 0.8$ at about 40% of the axial chord, then continues at a subsonic and fairly constant velocity level to the end of the vane. The constant velocity suggests separation. As R_{eTT} is increased, the primary flow increases and the stator jet flow increases. The velocities on the suction surface are higher, and continue to increase over the rest of the vane. The higher jet flow apparently is now more effective in suppressing separation.

Effect of Stator Jet Flow

The effect of stator cavity pressure on surface velocity distribution is presented in Figure 34. As the amount of jet flow was increased, an acceleration of the flow was promoted in the trailing edge region on the suction surface while a deceleration was promoted on the pressure surface. The increase in stator cavity pressure results in a decrease in primary flow which produces a drop in velocity level on the forward section of the vane.

Suction Surface Separation

During the off-design operation of the stator, suction surface flow separation was observed (Figure 35). For the jet-off condition, separation occurred at 40% axial chord and failed to reattach farther down the vane surface. While maintaining the same stator expansion ratio, the jet was activated ($P_{T_{IS}}/P_{T_0} = 1.8$) and the flow reattached to the vane surface.

Flow separation was observed only at the low stator expansion ratio flow conditions. This is attributed to increased suction surface diffusion which was much larger at the low expansion ratio conditions than it was at the higher expansion ratio flow conditions.

Normal Shock

Figure 36 illustrates a set of flow conditions where normal shocks appeared just downstream of the throat location on the hub section suction surface. The average stator expansion ratio was 1.8, while locally at the hub section it was 2.2 to 2.3. As the stator expansion ratio was increased, the shock position moved downstream and eventually off the trailing edge. It will be shown later that the existence of a shock was discernable in the stator exit cone probe circumferential survey. Figure 36 shows that for a fixed stator expansion ratio, increasing the stator jet cavity pressure amplified the effect of the shock on the surface static pressure behavior.

PHASE II—VARIABLE AREA TEST

Phase II of the test involved operating the turbine over a matrix of rotor cavity pressure ratios, stator cavity pressure ratios, and stage expansion ratios. Three rotor cavity pressure ratios were chosen in the optimum thermodynamic efficiency range ($P_{T_{IR}}/P_{T_0} = 0.50$, 0.60, and 0.80). Stage expansion, $R_{e_{TT_{0-3}}}$, was varied over a wide range extending from 1.4 to 2.4. Three stator cavity pressure ratios were selected; they were 0.75, 1.0, and 1.8.

A stator cavity pressure ratio of 0.75 was selected as a result of the high efficiency demonstrated at that level. The natural limit of a stator cavity pressure is that of the compressor discharge. This defines a cavity pressure ratio of 1.0 for a first-stage stator. A third stator cavity pressure ratio value of 1.8 was selected as a reasonable level for a second-stage stator.

Turbine Flow Rate

Figure 37 shows the effect that stator cavity pressure has on primary flow for various levels of rotor cavity pressure ratio at various settings of turbine expansion ratio. These data show that as the stage expansion ratio is increased the stator jet has less effect on reducing primary flow. This is because the influence of the jet flap on flow control is primarily a momentum interaction between the jet and the primary flow streams. The less the jet momentum—relative to the primary stream momentum—the less control the jet can exercise on the primary stream. As the stator expansion ratio increases, the momentum of the primary stream increases relative to that of the jet; the jet effectiveness in controlling the flow decreases. Percent of primary mass flow reduction is presented in Figure 38 as a function of percent of stator jet flow for lines of constant stator exit ideal Mach number. As much as 33% flow reduction was observed at 0.6 exit Mach number with 10% stator jet flow. Flow reduction drops off rapidly with an increase in Mach number to about 22% at a Mach number of 1.0.

Figures 39 and 40 present the variation of stator and rotor jet flow with stator and rotor cavity pressure ratios. These data show that the stator cavity pressure ratio that results in zero stator jet flow tends to decrease with an increase in stage expansion. This effect is caused by the decrease in stator exit static pressure that accompanies an increase in stage expansion. At a stator cavity pressure of 1.8, the stator jet slot was choked for the range of stage expansion ratios tested. The equivalent choked jet flow for the stator was found to be 1.32 lb/sec (0.598 kg/s). Figure 40 shows that for a given rotor cavity pressure ratio, the rotor jet flow increases with an increase in stage expansion ratio. The rotor jet slot did not choke over this range of stage expansion ratio and rotor cavity pressure ratio.

Equivalent stator inlet flow as a function of stator expansion ratio is presented in Figure 41. This plot has various symbols representing different stator cavity pressure ratios and different shading to show rotor cavity pressure ratio. These results show that when the rotor is operating with a fixed rotor jet cavity pressure ratio, it is actually behaving as a conventional solid rotor blade with certain unique reaction characteristics, and the flow characteristics of the turbine are entirely determined by the jet flap stator as it operates at various jet cavity and stator expansion ratios.

Turbine Static Pressure

Axial Gradients

Figure 42 presents local static pressure distribution through the turbine for various turbine expansion ratios and stator cavity pressure ratios of 0.75 and 1.80. In general, the turbine operated with negative reaction in the rotor hub region over most of the expansion ratios and cavity pressures investigated. As the stage expansion ratio was increased the rotor hub reaction increased and became positive at 2.06 for $P_{T_{IS}}/P_{T_0} = 0.75$ and 2.34 for $P_{T_{IS}}/P_{T_0} = 1.80$. An increase in stator cavity pressure ratio produced a decrease in the stator exit pressure and a slight increase in rotor exit pressure. Thus, the effect of an increase in stator cavity pressure was to permit the rotor to operate at more negative values of hub reaction.

Circumferential Gradients

Figures 43 and 44 present the stator exit end wall static pressures as a function of circumferential position for stage expansion ratios of 1.4 and 2.4, respectively. These static wall taps were located 0.5 in. (1.270 cm) axially behind the trailing edge of the stator and verniered across one vane passage. Circumferential gradients were found to increase with an increase of stage expansion and were more severe at the hub than at the tip. In general, as the stator cavity pressure is increased, the curves are slightly displaced to the left because of the increase in turning brought about by the stator jet.

Turbine Efficiency

The effect of stator cavity pressure ratio, rotor cavity pressure ratio, and turbine expansion ratio on thermodynamic (plus pumping) efficiency is presented in Figure 45. In general, the level of efficiency decreases with increasing turbine expansion ratio. The maximum thermodynamic (plus pumping) efficiency observed in the test program occurred at $R_{e_{TT}} = 1.4$, $P_{T_{IS}}/P_{T_0} = 0.7 - 0.75$, and $P_{T_{IR}}/P_{T_0} = 0.8$. This maximum value was 91.2%.

Figures 46, 47, and 48 present composite maps of specific work for three values of $P_{T_{IS}}/P_{T_0}$ as a function of the product of rotor cavity pressure ratio and primary flow for various stage expansion ratios and rotor cavity pressure ratios. Also shown in these illustrations are contours of constant thermodynamic efficiency. The optimum thermodynamic efficiency occurred around $P_{T_{IR}}/P_{T_0} = 0.7$ and ranged from a maximum value of

88.75% down to 82% as $P_{T_{IS}}/P_{T_0}$ was increased from 0.75 to 1.8. The $P_{T_{IS}}/P_{T_0}$ = 0.75 map compares most favorably with the corresponding plain stator map of Figure 49. The stage expansion ratio that results in the maximum efficiency tends to increase with an increase in stator cavity pressure ratio.

Rotor Exit Surveys

Circumferential traverses (using a combination total pressure, temperature, and yaw angle probe) performed immediately downstream of the rotor trailing edge were completed to map the flow characteristics existing in the turbine rotor. These surveys yield circumferential variation of temperature drop, total pressure ratio, blade exit absolute angle, and local efficiency. Contour maps were constructed from these surveys and are presented in Figures 50 through 53, for both the stator jet-on ($P_{T_{IS}}/P_{T_0}$ = 1.0) and jet-off flow conditions. Figures 50 and 51 show that the stage total pressure ratio, P_{T_0}/P_{T_2}, was not uniform over the annulus for either of the two operating points. The presence of the stator wakes developed a circumferential variation of peaks and valleys in the total pressure distribution at the turbine exit.

Efficiency contours are presented in Figures 52 and 53. For both operating conditions, the efficiencies near the hub and tip end walls are similar in level and pattern. The hub efficiency is about ten points lower than that of the tip. As the midchannel is approached, the jet-off efficiency shows improvement over that of the jet-on efficiency and is about 4.0 points higher at the mean section.

PHASE III—STATOR DETAILED PERFORMANCE TEST

The Phase III turbine rig configuration consisted of removing the rotor assembly and replacing it with spacers to provide a smooth hub wall flow path at the stator exit. With this arrangement, the stator was tested over various stator expansion ratios while maintaining a stator cavity-to-inlet total pressure ratio, $P_{T_{IS}}/P_{T_0}$, of 0.75, 1.00, 1.80, and also zero jet flow.

Turbine Flow Rate

Figure 54 shows the variation of equivalent primary flow rate over a range of stator expansion ratios for various stator cavity pressure ratios. The shaded symbols are Phase III (rotor removed) data. Also plotted in the illustration are open symbols representing Phase II data (with the rotor in position rotating at design speed over a range of rotor cavity pressure ratios). These data show that the rotor had very little effect on the primary

flow regardless of rotor cavity pressure ratio. At the design stator expansion ratio, the design values of primary flow—46.59 lb_m/sec (21.133 kg/s) with the jet on ($P_{T_{IS}}/P_{T_0}$ = 1.0) and 49.85 lb_m/sec (22.611 kg/s) with the jet off—were both achieved experimentally.

The stator jet flow is presented in Figure 55 as a function of stator expansion at various stator cavity pressure ratios. As before, both Phase II and III data are shown on the same graph. These results show that stator cavity pressure ratio and stator expansion ratio are the only independent variables that have any effect on stator jet flow.

Jet Momentum Coefficient

One of the more useful data correlating parameters is the jet momentum coefficient, C_j, which is the ratio of jet momentum to stator exit momentum. C_j is defined as

$$C_j = \frac{\dot{m}_s U_j}{(\dot{m}_p + \dot{m}_s) V_1} = \frac{\dot{m}_s U_j}{\dot{m}_1 V_1}$$

The jet velocity, U_j, is computed by assuming a linear hub-to-tip distribution of stator exit static pressure along with cavity pressure, $P_{T_{IS}}$, to determine the expansion ratio across the jet slot and, therefore, the jet critical velocity ratio, $U_j/U_{j_{cr}}$. $U_{j_{cr}}$ is computed by using the jet cavity total temperature. The jet momentum was determined, using the jet velocity and jet flow rate which was assumed proportional to the design radial distribution of $\dot{m}_s/(\dot{m}_p + \dot{m}_s)$.

Stator exit total and per unit depth mass flow were calculated, using local total pressure, temperature, and angle measurements obtained from Station 3 yaw probes. Figures 56, 57, and 58 show, respectively, the near-hub, mean and near-tip section variation of C_j with local stator expansion ratio for various stator cavity conditions. These data show that an increase in cavity pressure causes an increase in C_j. An increase in stator expansion causes the primary momentum to increase at a faster rate than the jet momentum and, therefore, lowering the jet momentum coefficient. At the lower stator expansion ratios, the exit static pressure is too high for the 0.75 cavity pressure ratio to result in jet flow. At $P_{T_{IS}}/P_{T_0}$ = 1.80 as a result of the acute gas angle at the hub and the jet momentum deflection, the primary mass flow in the hub region is reduced. This causes a decrease in primary stream momentum and a sharp increase in the jet momentum coefficient.

Lift

Figures 59, 60, and 61 presents specific lift as a function of local stator expansion ratio for different cavity pressure ratios and radial positions. Vane lift was calculated by summing the change in tangential jet momentum and the surface pressure forces on the vane. As shown in these data an increase in cavity pressure ratio results in an increase in specific lift.

As the jet flow was increased, the jet momentum force was increased while the primary flow was reduced. Associated with this primary flow reduction was a decrease in the vane pressure force. Apparently the increase in jet momentum force and decrease in primary mass flow outweighed the decrease in pressure force. A condition of limiting loading developed in the vane passage with increasing stator expansion ratio. At the hub section the specific lift continued to increase until the local stator expansion ratio reached about 2.5. At this point the complete hub passage was choked with a normal shock, which was probably located just at the trailing edge. Further increases in expansion ratio could not promote changes in the flow conditions upstream of this shock and the primary and jet condition remained constant. Furthermore, at the mean and tip sections, the flow might have been choked at the throat, but the specific lift continued to increase with increasing local expansion ratio caused by increasing lift developing between the throat and the trailing edge plane. The mean and tip section probably would also reach a limiting condition at a local $R_e > 2.7$ when the normal shock at those radial stations finally moves to the trailing edge.

Figure 62 is a composite map at the mean section which shows specific lift as a function of jet momentum coefficient for lines of constant ideal exit Mach number and cavity pressure ratio. Specific lift increases with an increase in cavity pressure ratio, exit Mach number, and jet momentum coefficient.

Figure 63 shows at the mean section, the effect that cavity pressure ratio has on lift coefficient, ψ_t, for various expansion ratios. At the design stator expansion ratio the experimental lift coefficient value was 0.735 whereas the design value was 0.727. As the cavity pressure is increased the amount of primary flow around the airfoil decreases, resulting in a decrease in surface pressure difference across the vane. This trend is also observed in the composite map in Figure 64 which shows lift coefficient decreasing for an increase in jet momentum coefficient and cavity pressure ratio for a given ideal exit Mach number.

Stator Exit Survey

Circumferential traverses with a cone probe were made at 12 radial depths to map the flow characteristics at the stator trailing edge. Figure 65 shows the survey cone probe in recording position 1/2 in. axially downstream of the vane trailing edge. The cone probe recorded static pressure, total pressure, and vane exit absolute flow angle. Stator exit surveys were made at the following operating conditions:

- $R_{eTS_{0-1}} = 2.0$ $\quad P_{T_{IS}}/P_{T_0} = 1.0$
- $R_{eTS_{0-1}} = 2.0$ $\quad \dot{m}_s = 0.0$
- $R_{eTS_{0-1}} = 1.5$ $\quad P_{T_{IS}}/P_{T_0} = 1.8$
- $R_{eTS_{0-1}} = 2.4$ $\quad P_{T_{IS}}/P_{T_0} = 1.0$

The high stator expansion ratio survey ($R_{eTS_{0-1}} = 2.4$) resulted in the circumferential traces shown in Figure 66. As the probe traversed into region 1 of Figure 66, low values of total pressure and Mach number were observed as a result of the wake from the vane trailing edge. Region 2 shows the high velocity flow of the free-stream section of the flow field. A normal shock wave was encountered in region 3. The shock is not strong enough to produce a measurable drop in total pressure, but is observed as an increase in static pressure (therefore, a decrease in Mach number). Expansion takes place in region 4 followed by a wake once again in region 5.

The cone probe surveyed close to the hub end wall: r = 10.66 in. (27.076 cm) and close to the tip end wall: r = 14.87 in. (37.769 cm). Figure 67 shows very good agreement between the static end wall taps and the cone probe average static pressure indicated near the end wall.

Figure 68 displays local stator exit static pressure divided by inlet total pressure in the near-midspan region. As would be expected, the subsonic 1.5 expansion ratio traces show no discontinuities in static pressure since there are no shocks present in the flow field.

Circumferential traces of midspan section stator exit total pressure divided by inlet total pressure are shown in Figure 69. Comparing the traces with the jet on ($P_{T_{IS}}/P_{T_0} = 1.0$) and jet off at a stator expansion ratio of 2.0, shows that the total pressure depression with the jet on is greater and, therefore, the loss is larger than that with the jet off. As the stator expansion is increased from 2.0 to 2.4 while maintaining $P_{T_{IS}}/P_{T_0} = 1.0$, the pressure drop also increased. Examination of

Figure 69, where $R_{e_{TS_{0-1}}} = 2.4$, $P_{T_{IS}}/P_{T_0} = 1.0$, the levels in the range of 8.0 to 11.0 circumferential degrees shows a total pressure loss that is attributable to a shock standing in the vane passage. Local Mach number at the stator exit was computed from the local static and total pressure and are presented in Figure 70. The wide range in magnitude along the circumference is evident. Figure 71 presents circumferential traces of the absolute stator exit gas angle in the midspan region. Comparing the traces for the jet off and jet on at an expansion ratio of 2.0 shows that the jet deflects the primary stream in the tangential direction by approximately 2.0 deg. Figure 71 shows that as the expansion ratio increases (because the momentum of the primary stream increases relative to the jet momentum) the jet becomes less effective in deflecting the flow.

Aerodynamic Midspan Losses

Local values of kinetic energy loss coefficient were computed from the survey data, using Equation (8). Typical traces for the mean radius are shown in Figure 72. These traces indicate how the wake loss level increases with increasing expansion ratio. Also Figure 72 shows the presence of a normal shock in the midspan survey plane at the high expansion ratio operating point. Figure 72 also shows that at the design $R_{e_{TS}}$ the loss level increases when the jet is strongly activated. This increase in loss is manifested from the jet orientation relative to the mainstream flow. The jet has a flow component directed upstream (i.e., opposed to the mainstream flow direction). This upstream component stagnates a portion of the main flow and results in a loss of total pressure.

Contour Maps

Contour maps of kinetic energy loss coefficient computed from Equation (8) are presented in Figures 73 through 76 for the four surveyed operating points. Uniform free-stream losses are exhibited radially for the subsonic operating condition (stator expansion ratio of 1.5). As the stator expansion ratio was increased, the hub free-stream losses increased because of shock losses in that region. Comparing the contours for the jet-off and $P_{T_{IS}}/P_{T_0} = 1.0$ conditions at a stator expansion of 2.0, shows the jet-on condition has higher losses in the free stream and in the stator wake regions. Figures 77 through 80 present stator pressure loss coefficient ($\overline{\omega}$) contour maps for the four surveyed operating points. The local values of total pressure loss were computed using Equation (9). These maps show the same trends as the kinetic energy coefficient maps.

Circumferentially Averaged Losses

By integrating circumferentially the actual and ideal kinetic energy—using Equation (10)—at the stator exit, the radial distribution of kinetic energy loss coefficient was computed. These results are shown in Figure 81. As in the contour maps at a stator expansion of 2.0, the loss with the jet on ($P_{T_{IS}}/P_{T_0} = 1.0$) is larger than with the jet off. While maintaining $P_{T_{IS}}/P_{T_0} = 1.0$, the loss decreases as the stator expansion is increased from 2.0 to 2.4. This effect may be caused by lower suction surface diffusion associated with the 2.4 expansion ratio. Using the relationship between actual and ideal kinetic energy of Figure 81 and assuming a linear hub-to-tip variation in exit static pressure as determined by the wall taps, an exit total pressure can be calculated, and a compatible pressure loss coefficient may thus be defined. The results of this calculation are presented in Figure 82 and demonstrates the same characteristics as that of Figure 81.

Mixed Station Calculation

A hypothetical mixed station (M1) was calculated from the survey data at the stator exit (Station 1). By definition, properties at this mixed station are uniform in the circumferential direction, but are allowed to vary in the radial direction. The expressions used in making the computations are described in the Calculation Procedure section.

Figures 83 through 86 present the radial variation of kinetic energy loss coefficient, measured and design values of pressure loss coefficient, and thermodynamic kinetic energy loss coefficient for the four surveyed operating conditions. Also shown in these illustrations are the losses measured at Station 3. Station 3 is far enough downstream of the vane trailing edge that most of the circumferential gradients should be dissipated. These data show that Station 3 losses were higher than those of the mixed station but that they showed the same general trends. Station 3 losses are higher in the end wall regions than in the midspan because of the boundary layer build up along the case between Stations 1 and 3.

Figures 83 and 84 show the level to which M1 losses increased above the stator exit (Station 1) loss levels. Typically, the M1 loss was about 10% larger than the trailing edge loss level.

Mixed station kinetic energy, total pressure loss, and thermodynamic kinetic energy loss coefficient values are presented in Figures 83 through 86, respectively, for the four surveyed operating points.

The jet-on ($P_{T_{IS}}/P_{T_0} = 1.0$) and jet-off total pressure loss, $\bar{\omega}$, at the design stator expansion ratio along with the design values are presented in Figures 83 and 84. These results show that in the midspan region the losses roughly doubled when the jet was activated to its design blowing rate. Furthermore, these results show that the design radial distribution of losses was fairly well achieved both with the jet on and with the jet off. All of these results illustrate that the vane performance improved in going from the hub to the tip region. This is to be expected since the exit Mach number decreased in moving radially from the hub section to the tip. Figure 86 presents loss data for the 1.5 stator expansion ratio off-design operating condition. Because of the low primary stream momentum at the hub region, the jet deflection resulted in a very acute gas exit angle. This produced a sharp increase in the effective flow length between Stations 1 and 3, and the end wall effects for this operating point overpower the vane losses in the hub region.

Complete Passage Loss Calculations

Complete passage mixed (Station M1) kinetic energy and measured (Station 3) thermodynamic kinetic energy loss coefficients were computed for the four surveyed operating points from Equations (18) and (19), respectively. These expressions are described in the Calculation Procedure Section and allow all of the survey information for a set of operating conditions to be represented by one number. The values of the two expressions of loss coefficients for the four surveyed points are:

Surveyed operating conditions	Equation (18): Complete passage mixed kinetic energy loss coefficient, $\bar{e}_{M1}$	Equation (19): Complete passage measured thermodynamic kinetic energy loss coefficient, $\bar{e}_{3_{thermo}}$
$\dot{m}_s = 0$		
$Re_{TS_{0-1}} = 2.0$	0.0458	0.1767
$P_{T_{IS}}/P_{T_0} = 1.0$		
$Re_{TS_{0-1}} = 2.0$	0.0671	0.2079
$P_{T_{IS}}/P_{T_0} = 1.8$		
$Re_{TS_{0-1}} = 1.5$	0.0522	0.3179
$P_{T_{IS}}/P_{T_0} = 1.0$		
$Re_{TS_{0-1}} = 2.4$	0.0632	0.1567

The complete passage mixed station loss values, $\bar{e}_{M1}$, exhibit the same trends as the radial variation of kinetic energy loss coefficient of Figure 81. That is, the design $R_{e_{TS}}$ jet-off flow conditions had the lowest loss and the design $R_{e_{TS}}$ jet-on flow conditions had the highest loss. Increasing the jet cavity pressure from the level corresponding to zero jet flow up to $P_{T_{IS}}/P_{T_0} = 1.0$ increased the mixed station complete passage kinetic energy loss from 0.0458 to 0.0671, an increase of 46.5%.

The complete passage measured thermodynamic loss coefficient, $\bar{e}_{3_{thermo}}$, demonstrated both different trends and much higher levels of loss than $\bar{e}_{M1}$. This is mainly caused by the very acute gas angle near the hub and attendant high hub section loss levels. Because of these Station 3 high hub section loss levels, $\bar{e}_{3_{thermo}}$ is not considered to be a representative stator loss level parameter.

Gas Angle Contour Plots

Stator exit gas angle contour maps are presented in Figures 87 through 90. Superimposed on these maps are the location of the stator wakes (defined by the maximum pressure loss). As the stator expansion was increased while maintaining a stator cavity pressure ratio of unity, the flow angle increased with the increase in primary flow momentum. If the stator expansion is held constant and the jet flow is increased from zero to a cavity pressure ratio of unity, the flow angle in the wake from the mean to the hub remains about the same. Other regions of the annulus show an increase in angle with a decrease in stator jet flow. Because of this angle distribution change, the location of the wake line shifts to the right in the region from the mean to the tip when the jet is turned on. As the stator expansion is reduced to 1.5, as shown in Figure 88, the decreased primary stream momentum allows the jet to be more effective in turning the flow and displays lower gas angles.

Circumferential Average Angle

A radial distribution of stator exit angle was determined by the ratio of axial and tangential momentum as measured by the survey cone probe at Station 1.

Figure 91 shows the radial variation of stator exit angle for a stator expansion ratio of 2.0 at a $P_{T_{IS}}/P_{T_0} = 1.0$ and also with the jet off. In general, the design angle for the jet off was achieved. Agreement with the design angle is also shown from the mean to the tip for the jet-on condition. About 1.5 deg of underturning was observed from the mean to hub sections for the jet on conditions.

Boundary Layer Parameters

Boundary layer momentum and displacement thicknesses were calculated for the four survey operating conditions. The respective computations are described in the Calculation Procedure Section. The ratio of these boundary layer parameters (shape factor) is shown in Figure 92 for the suction surface. The total and pressure surface shape factors were found to exhibit nearly the same magnitudes and radial distributions as the suction surface shape factor. These data show that for a stator expansion ratio of 2.0, the shape factor for the jet on ($P_{T_{IS}}/P_{T_0}$ = 1.0) is larger than that of the jet-off condition. This effect may be caused by an effective increase in trailing edge blockage which is a result of the jet. The 1.5 stator expansion ratio condition displays the lowest value of shape factor even though this condition has the least acceleration across the vanes. This can be explained by noting that the large value of cavity pressure ratio ($P_{T_{IS}}/P_{T_0}$ = 1.8) alters the vane surface velocity distribution such that the suction surface velocity was continuously increasing.

PHASE IV—ROTOR/STATOR AXIAL SPACING TEST

The recent data of Reference 13 has shown that axial spacing between the stator and rotor may have a beneficial effect on stage performance for blades with secondary flow. Phases I and II were tested with an axial spacing of 1.4 in. (3.556 cm). The axial spacing dimensions are described in Figure 93. For Phase IV, the axial spacing was increased to 2.4 in. (6.096 cm) and performance data were recorded for a range of stage expansion ratios for rotor and stator cavity pressure ratios of 0.6 and 1.0, respectively.

Figures 94 and 95 show that rotor/stator spacing has very little effect on equivalent primary flow or on the stator jet flow. Equivalent torque is shown in Figure 96 for Phase II and IV. These data show that torque is very slightly lower for Phase IV than that of Phase II. Figures 97 and 98 show that the increased spacing had essentially no effect on exit angle and equivalent rotor flow. Thermodynamic efficiency (with pumping) is shown in Figure 99 for Phases II and IV as a function of stage expansion ratio. The efficiency for the 2.4-in. (6.096-cm) axial spacing was about 1.5 points lower than for the 1.4-in. (3.556-cm) spacing at the low stage expansions. At design $R_{eTT_{0-3}}$ the efficiency for the two axial spacings was about the same; above the design $R_{eTT_{0-3}}$, the efficiency for the increased axial spacing appeared to be very slightly higher than the efficiency for the smaller axial clearance.

Two rotor exit surveys were made at the design expansion ratio for the stator jet on ($P_{T_{IS}}/P_{T_0}$ = 1.0), and off while maintaining a rotor cavity pressure ratio of 0.6. The resulting local stage expansion ratio contour maps are shown in Figures 100 and 101.

Comparing these two illustrations with the corresponding 1.4-in. (3.556-cm) axial spacing, Figures 50 and 51 show that the stator wakes became less well defined as the clearance was increased. When the turbine was operating with the small stator-rotor axial spacing, gas particles left the stator passage at their respective angles, moved through the required axial and circumferential distances to the rotor leading edge. When this axial spacing was increased, the required circumferential displacement also increased. Comparison of Phase IV results show how the stator wakes are still evident through the rotor, but are displaced circumferentially relative to the Phase II small axial spacing results.

Figures 102 and 103 present the efficiency contours at 2.4-in. (6.096-cm) axial clearance, and Figures 63 and 64 show this data for the 1.4-in. (3.556-cm) clearance. The increased clearance appears to dissipate the stator wakes for both the jet-on and jet-off operating conditions; however, the overall efficiency levels for the two tests appear to be about the same.

SUMMARY OF RESULTS

The performance of a single-stage turbine with a jet flap stator and jet flap rotor has been determined over a range of stator and rotor jet cavity pressure levels and turbine expansion ratios. The mean section solidity was 0.722 which corresponded to a value of tangential lift coefficient of 0.727. The results were compared with the performance of a turbine using the same jet flap rotor and a conventional stator of 0.923 mean section solidity and 0.581 tangential lift coefficient. Both turbines were designed to satisfy similar sets of negative hub reaction velocity diagrams. All testing was performed at design equivalent speed, $N/\sqrt{\theta}$ = 4660 rpm (487.99 rad/s), and with stator and rotor cavity total temperature equal to turbine inlet total temperature. The following observations were made:

The design stator total-to-static expansion ratio was 1.976. This value was very nearly achieved (2.02) when the turbine was operating at $P_{T_{IS}}/P_{T_0}$ = 1.0, $P_{T_{IS}}/P_{T_0}$ = 0.6, and R_{eTT} = 2.03.

With design total-to-total expansion ratio (R_{eTT} = 2.034) across the stator and $P_{T_{IS}}/P_{T_0}$ = 1.0, the design value of equivalent stator inlet flows was 46.59 lb/sec (21.133 kg/s). With these design values of expansion ratio and $P_{T_{IS}}/P_{T_0}$, the design stator inlet flow rate was experimentally obtained when $P_{T_{IR}}/P_{T_0}$ = 0.6.

When the jet was turned off the stator inlet flow increased to a maximum of 49.45 lb/sec (22.43 kg/s) as compared with the design flow (with no jet) of 49.85 lb/sec (22.611 kg/s) with the turbine operating at design speed ($N/\sqrt{\theta}$ = 4660 rpm (487.99 rad/s) and expansion ratio (R_{eTT} = 2.034).

At design turbine operating conditions the stator passed 2.0% jet flow instead of the 2.375% design value.

At design speed and expansion ratio, the maximum thermodynamic plus pumping efficiency occurred with $P_{T_{IR}}/P_{T_0}$ = 0.6, $P_{T_{IS}}/P_{T_0}$ = 0.7. For these conditions, the maximum thermodynamic with pumping considered was 88.4% as compared with a maximum value of 87.1% when pumping was not considered.

At design speed and expansion ratio, $P_{T_{IR}}/P_{T_0}$ = 0.6, and design, $P_{T_{IS}}/P_{T_0}$ = 1.0, the thermodynamic (plus pumping) efficiency was 85%.

The 87.1% maximum thermodynamic efficiency for the jet flap stator/jet flap rotor turbine was about one point lower than the plain stator/jet flap rotor maximum thermodynamic efficiency of 88%. This 0.9% point drop in thermodynamic efficiency was caused by increases in vane thickness, a 22% reduction in vane solidity, and an increase in trailing edge blockage.

In general, the level of efficiency increased with decreasing turbine expansion ratio. That maximum thermodynamic (plus pumping) efficiency that was observed in the complete test program occurred at $R_{eTT} = 1.4$, $P_{T_{IS}}/P_{T_0} = 0.7 - 0.75$, and $P_{T_{IR}}/P_{T_0} = 0.8$. This maximum value was 91.2%.

When using the base definition of efficiency, the turbine is not charged for the use of the ideal power capacity of the jet flow; the base efficiency, therefore, increases for any increase in both stator and rotor cavity pressure ratios. Comparing efficiencies at $P_{T_{IS}}/P_{T_0} = 0.7$, $P_{T_{IR}}/P_{T_0} = 0.6$, the base efficiency was 87.9% for the jet flap stator turbine and 89.1% for the plain stator turbine.

The effect that the rotor jet flow had on flow reduction was actually to lower the stator expansion ratio and thereby make the stator more effective in controlling turbine flow rate.

Primary flow reduction for a given percent stator jet flow increased as the stator exit Mach number was decreased. As much as 33% primary flow reduction was achieved with 10% jet flow at 0.6 ideal Mach number. This flow reduction drops to 22% as the exit ideal Mach number is increased to 1.0.

Whether or not the rotor was present in the turbine had essentially no effect on stator inlet or stator jet flow rates.

The design value of airfoil lift coefficient was 0.727. A value of 0.735 was determined experimentally.

Stator exit cone probe surveys showed the presence of shock waves in the free stream.

These surveys also showed that the vane loss increased with increased jet flow. For example, at the design stator expansion ratio, R_{eTS}, the mean section kinetic energy loss coefficient, $\bar{e}$, approximately doubled when the jet cavity pressure was increased from that of zero jet flow to 1.0.

The agreement between computed losses at a hypothetical fully mixed station and design values was fairly good both with the jet-on and jet-off flow conditions.

The complete passage mixed kinetic energy loss coefficient increased from 0.0458 to 0.0671, an increase of 46.5%, when the stator jet pressure ratio was increased from zero jet flow to the design value of unity.

Tests where the axial spacing between the rotor and stator was increased from 1.4 in. (3.556 cm) to 2.4 in. (6.096 cm) showed that this increased axial spacing had essentially no effect on turbine performance.

REFERENCES

1. Lueders, H. G. Experimental Investigation of Advanced Concepts to Increase Turbine Blade Loading. (Vol V, Performance Evaluation of Jet Flap Rotor Blade.) NASA CR-1580, May 1970.

2. Lueders, H. G. Experimental Investigation of Advanced Concepts to Increase Turbine Blade Loading. (Vol VII, Performance Evaluation of Modified Jet Flap Blade.) NASA CR-1759, March 1971.

3. Bettner, J. L. Experimental Investigation in an Annular Cascade Sector of Highly Loaded Turbine Stator Blading. (Vol IV, Performance of Jet Flapped Blade.) NASA CR-1423, September 1969.

4. Bettner, J. L. Design and Experimental Results of a Highly Loaded, Low Solidity, Jet Flap Rotor.. NASA CR-1968, March 1972.

5. Nosek, S. M. and Kline, J. F. Two-Dimensional Cascade Test of a Jet Flap Turbine Rotor Blade. NASA TMX-2183, 1971.

6. Gaedy, T. F. and Bettner, J. L. Experimental Investigation of Aerodynamic Flow Control by Jet Flap in a Two-Dimensional Cascade. Detroit Diesel Allison EDR 6709, May 1970.

7. Stabe, R. G. Design and Two-Dimensional Cascade Test of a Jet Flap Turbine Stator Blade with Ratio of Axial Chord to Spacing of 0.5. NASA TMX-2426, December 1971.

8. Lueders, H. G. Experimental Investigation of Advanced Concepts to Increase Turbine Blade Loading. (Vol I, Analysis and Design.) NASA CR-735, June 1967.

9. Lueders, H. G. Experimental Investigation of Advanced Concepts to Increase Turbine Blade Loading. (Vol II, Performance Evaluation of Plain Rotor Blade.) NASA CR-1172, August 1968.

10. Katsanis, T. FORTRAN Program for Calculating Transonic Velocities on a Blade-to-Blade Stream Surface of a Turbomachine. NASA TN-D-5427, 1969.

11. McNally, W. D. FORTRAN Program for Calculating Compressible Laminar and Turbulent Boundary Layers in Arbitrary Pressure Gradients. NASA TN-D-5681, May 1970.

12. Zweifel, O. "The Spacing of Turbomachine Blading, Especially With Large Angular Deflection." Brown Boveri Review, Vol 32, December 1945, pp 436-444.

13. H. J. Schum, E. M. Szanca, and F. P. Behning. Effect of Stator-Rotor Axial Clearance on Cold-Air Performance of a Turbine with Transpiration-Cooled Stator Blading. NASA TM X-67914.

APPENDIX

Table I.

Jet flap turbine design point conditions.

Equivalent work, $\Delta H/\theta_{cr_0}$	20 Btu/lb (46,519 J/kg)
Equivalent speed, $N/\sqrt{\theta}_{cr_0}$	4660 rpm (487.99 rad/s)
Equivalent tip speed, $U_t/\sqrt{\theta}_{cr_0}$	610 ft/sec (185.928 m/s)
Design turbine expansion ratio, P_{T_0}/P_{T_3}	2.034
Design stator (jet on) expansion ratio, P_{T_0}/P_{st_1}	1.976
Equivalent inlet flow (jet off), $\left(\frac{\dot{m}_p\sqrt{\theta}_{cr_0}\epsilon_0}{\delta_0}\right)_{wo/j}$	49.85 lb/sec (22.611 kg/s)
Equivalent inlet flow (jet on), $\left(\frac{\dot{m}_p\sqrt{\theta}_{cr_0}\epsilon_0}{\delta_0}\right)_{w/j}$	46.59 lb/sec (21.133 kg/s)
Inlet mass flow reduction, $1 - \frac{\left(\dot{m}_p\frac{\sqrt{\theta}\,cr_0\epsilon_0}{\delta_0}\right)_{w/j}}{\left(\dot{m}_p\frac{\sqrt{\theta}cr_0\epsilon_0}{\delta_0}\right)_{wo/j}}$	6.4%
Design stator cavity pressure ratio, $P_{T_{IS}}/P_{T_0}$	1.00
Stator jet flow, $\dot{m}_S/\dot{m}_p$	2.375%
Design rotor cavity pressure ratio, $P_{T_{IR}}/P_{T_0}$	1.00
Rotor jet flow, $\dot{m}_R/\dot{m}_p$	6.65%
Stator jet slot size, $\overline{hb}_S$	0.030 in. (0.0762 cm)

Table II.

Jet flap stator vane section coordinates.

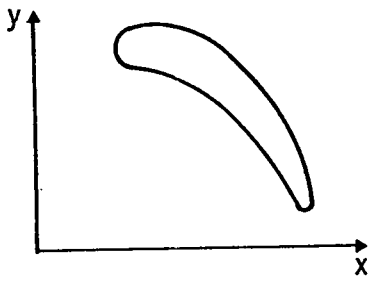

7389-102

Tip section

Suction				Pressure			
X		Y		X		Y	
(in.)	(cm)	(in.)	(cm)	(in.)	(cm)	(in.)	(cm)
1.3581	3.4495	4.8508	12.3210	3.0500	7.7470	3.0000	7.6200
1.4488	3.6799	4.9504	12.5740	2.9610	7.5209	2.9687	7.5404
1.4568	3.7002	4.9511	12.5757	2.9082	7.3868	3.0410	7.7241
1.4953	3.7980	4.9531	12.5808	2.8470	7.2313	3.1247	7.9367
1.5339	3.8961	4.9533	12.5813	2.7705	7.0370	3.2293	8.2024
1.5726	3.9944	4.9508	12.5750	2.6939	6.8425	3.3362	8.4739
1.6112	4.0924	4.9457	12.5620	2.6173	6.6479	3.4396	8.7365
1.6498	4.1904	4.9367	12.5892	2.5407	6.4533	3.5437	9.0009
1.6886	4.2890	4.9252	12.5100	2.4640	6.2585	3.6476	9.2649
1.7277	4.3883	4.9096	12.4703	2.3872	6.0634	3.7506	9.5265
1.7661	4.4858	4.8913	12.4239	2.3104	5.8684	3.8517	9.7833
1.8048	4.5841	4.8703	12.3705	2.2334	5.6728	3.9532	10.0411
1.8436	4.6827	4.8462	12.3093	2.1564	5.4772	4.0527	10.2938
1.8825	4.7815	4.8193	12.2410	2.0793	5.2814	4.1475	10.5346
1.9212	4.8798	4.7900	12.1666	2.0020	5.0850	4.2377	10.7637
1.9600	4.9784	4.7577	12.0845	1.9633	4.9867	4.2813	10.8745
1.9988	5.0769	4.7231	11.9966	1.9247	4.8887	4.3239	10.9827
2.0764	5.2740	4.6446	11.7972	1.8861	4.7906	4.3649	11.0868
2.1539	5.4709	4.5558	11.5717	1.8474	4.6923	4.4037	11.1853
2.2313	5.6675	4.4589	11.3256	1.8087	4.5940	4.4417	11.2819
2.3086	5.8638	4.3519	11.0538	1.7699	4.4955	4.4779	11.3738
2.3859	6.0601	4.2355	10.7581	1.7314	4.3977	4.5124	11.4614
2.4639	6.2583	4.1150	10.4521	1.6924	4.2986	4.5467	11.5486
2.5400	6.4516	3.9887	10.1312	1.6536	4.2001	4.5791	11.6309
2.6169	6.6469	3.8583	9.8000	1.6149	4.1018	4.6107	11.7111
2.6936	6.8417	3.7248	9.4604	1.5762	4.0035	4.6411	11.7883
2.7703	7.0365	3.5857	9.1076	1.5373	3.9047	4.6707	11.8635
2.8469	7.2311	3.4429	8.7449	1.4984	3.8059	4.6999	11.9377
3.0000	7.6200	3.1225	7.9311	1.4596	3.7073	4.7284	12.0101
3.0451	7.7345	3.0216	7.6748	1.3992	3.5539	4.7701	12.1161

Table II (Cont.)

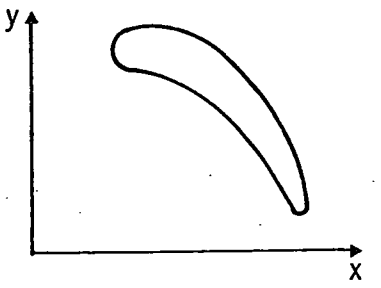

7389-102

Mean section

Suction				Pressure			
X		Y		X		Y	
(in.)	(cm)	(in.)	(cm)	(in.)	(cm)	(in.)	(cm)
1.5921	4.0439	4.7828	12.1483	3.0500	7.7470	3.0600	7.7724
1.6764	4.2580	4.8815	12.3990	2.9590	7.5158	3.0314	7.6997
1.6906	4.2941	4.8834	12.4038	2.9223	7.4226	3.0876	7.8425
1.7233	4.3771	4.8862	12.4109	2.8705	7.2910	3.1676	8.0457
1.7560	4.4602	4.8875	12.4142	2.8058	7.1267	3.2677	8.2999
1.7887	4.5432	4.8871	12.4132	2.7409	6.9618	3.3670	8.5521
1.8215	4.6266	4.8855	12.4091	2.6760	6.7970	3.4661	8.8038
1.8543	4.7099	4.8819	12.4000	2.6111	6.6321	3.5648	9.0545
1.8871	4.7932	4.8755	12.3837	2.5462	6.4673	3.6604	9.2974
1.9196	4.8757	4.8677	12.3639	2.4811	6.3019	3.7547	9.5369
1.9528	4.9601	4.8565	12.3355	2.4159	6.1363	3.8510	9.7815
1.9857	5.0436	4.8427	12.3004	2.3507	5.9707	3.9451	10.0205
2.0186	5.1272	4.8263	12.2588	2.2854	5.8049	4.0345	10.2476
2.0515	5.2108	4.8067	12.2090	2.2199	5.6385	4.1204	10.4658
2.0844	5.2943	4.7845	12.1526	2.1545	5.4724	4.2031	10.6758
2.1174	5.3781	4.7595	12.0891	2.1216	5.3888	4.2430	10.7772
2.1503	5.4617	4.7324	12.0202	2.0888	5.3055	4.2819	10.8760
2.2162	5.6291	4.6674	11.8551	2.0559	5.2219	4.3202	10.9733
2.2822	5.7967	4.5863	11.6492	2.0232	5.1389	4.3572	11.0672
2.3479	5.9636	4.4970	11.4223	1.9893	5.0528	4.3933	11.1589
2.4136	6.1305	4.4012	11.1790	1.9574	4.9717	4.4265	11.2433
2.4792	6.2971	4.2977	10.9161	1.9242	4.8874	4.4601	11.3286
2.5448	6.4637	4.1867	10.6342	1.8915	4.8044	4.4918	11.4091
2.6101	6.6296	4.0685	10.3339	1.8586	4.7208	4.5225	11.4871
2.6753	6.7952	3.9455	10.0215	1.8257	4.6372	4.5520	11.4858
2.7405	6.9608	3.8133	9.6857	1.7927	4.5534	4.5806	11.6347
2.8055	7.1259	3.6715	9.3256	1.7598	4.4698	4.6077	11.7035
2.8704	7.2908	3.5267	8.9578	1.7268	4.3860	4.6336	11.7693
3.0000	7.6200	3.2029	8.1353	1.6938	4.3022	4.6588	11.8333
3.0450	7.7343	3.0818	7.8277	1.6331	4.1480	4.7020	11.9430

Table II (Cont.)

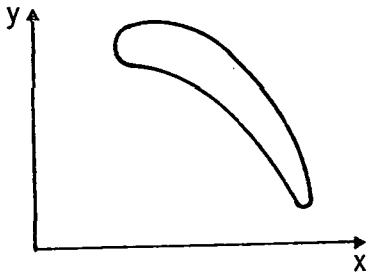

7389-102

Hub section

Suction				Pressure			
X		Y		X		Y	
(in.)	(cm)	(in.)	(cm)	(in.)	(cm)	(in.)	(cm)
1.8254	4.6365	4.7209	11.9910	3.0500	7.7470	3.1200	7.9248
1.9201	4.8770	4.8207	12.2445	2.9571	7.5110	3.0943	7.8595
1.9236	4.8859	4.8218	12.2473	2.9360	7.4574	3.1312	7.9532
1.9505	4.9542	4.8245	12.2542	2.8940	7.3507	3.2039	8.1379
1.9774	5.0225	4.8246	12.2544	2.8409	7.2158	3.2926	8.3632
2.0043	5.0909	4.8226	12.2494	2.7879	7.0812	3.3808	8.5872
2.0313	5.1595	4.8183	12.2384	2.7347	6.9461	3.4701	8.8140
2.0583	5.2280	4.8110	12.2199	2.6815	6.8110	3.5570	9.0347
2.0854	5.2969	4.8016	12.1960	2.6283	6.6758	3.6442	9.2562
2.1225	5.3911	4.7834	12.1498	2.5749	6.5402	3.7321	9.4795
2.1396	5.4345	4.7741	12.1262	2.5215	6.4046	3.8185	9.6989
2.1667	5.5034	4.7562	12.0807	2.4680	6.2687	3.9030	9.9136
2.1938	5.5722	4.7361	12.0296	2.4143	6.1323	3.9860	10.1244
2.2210	5.6413	4.7127	11.9702	2.3606	5.9959	4.0674	10.3311
2.2482	5.7104	4.6862	11.9029	2.3068	5.8592	4.1480	10.5359
2.2754	5.7795	4.6565	11.8275	2.2798	5.7906	4.1865	10.6337
2.3025	5.8483	4.6247	11.7467	2.2528	5.7221	4.2243	10.7297
2.3568	5.9862	4.5538	11.5666	2.2258	5.6535	4.2614	10.8239
2.4111	6.1241	4.4740	11.3639	2.1987	5.5846	4.2984	10.9179
2.4652	6.2616	4.3878	11.1450	2.1716	5.5158	4.3341	11.0086
2.5192	6.3987	4.2997	10.9212	2.1446	5.4472	4.3691	11.0975
2.5731	6.5356	4.2090	10.6908	2.1280	5.4051	4.3894	11.1490
2.6268	6.6720	4.1122	10.4449	2.0903	5.3093	4.4345	11.2636
2.6805	6.8084	4.0112	10.1884	2.0632	5.2405	4.4648	11.3405
2.7340	6.9443	3.9056	9.9202	2.0360	5.1714	4.4945	11.4160
2.7874	7.0799	3.7952	9.6398	2.0089	5.1026	4.5226	11.4874
2.8407	7.2153	3.6766	9.3385	1.9817	5.0335	4.5492	11.5549
2.8938	7.3502	3.5512	9.0200	1.9546	4.9646	4.5737	11.6171
3.0000	7.6200	3.2728	8.3129	1.9274	4.8955	4.5968	11.6758
3.0472	7.7398	3.1365	7.9667	1.8704	4.7508	4.6373	11.7787

Table III.

Comparison of solid stator and jet flap stator geometric characteristics.

	Tip		Mean		Hub	
	Solid stator	Jet flap stator	Solid stator	Jet flap stator	Solid stator	Jet flap stator
Radius—r, in. (cm)	15.00 (38.10)	15.00 (38.10)	12.75 (32.38)	12.75 (32.38)	10.50 (26.67)	10.50 (26.67)
Axial chord—C_x, in. (cm)	2.100 (5.334)	1.680 (4.267)	1.848 (4.693)	1.445 (3.670)	1.630 (4.140)	1.210 (3.073)
Spacing—S_p, in. (cm)	2.356 (5.984)	2.356 (5.984)	2.003 (5.087)	2.003 (5.087)	1.649 (4.188)	1.649 (4.188)
Solidity, σ_x	0.891	0.714	0.923	0.722	0.988	0.735
Tangential lift coef, ψ_t	0.616	0.827	0.581	0.727	0.394	0.472
Turning downstream of throat, deg	6	17.9	6	16.5	6	14.0
Incidence—i, deg	0	15.3	0	14.3	0	10.0
Leading edge radius—r_{le}, in. (cm)	0.063 (0.160)	0.100 (0.254)	0.055 (0.139)	0.100 (0.254)	0.049 (0.124)	0.100 (0.254)
Trailing edge radius—r_{te}, in. (cm)	0.0125 (0.0317)	0.050 (0.127)	0.0125 (0.0317)	0.050 (0.127)	0.0125 (0.0317)	0.050 (0.127)
$V/V_{cr})_0$ with jet		0.254		0.244		0.234
$V/V_{cr})_0$ without jet	0.255	0.264	0.250	0.262	0.245	0.260
$V/V_{cr})_1$ with jet		0.828		1.016		1.090
$V/V_{cr})_1$ without jet	0.809	0.832	1.017	1.026	1.106	1.104

Table IV.

Jet flap radial distribution of equivalent forces.

Radius (r)		Force per unit length in the axial direction $(F_x/\delta_0 \ell)$		Force per unit length in the tangential direction $(F_y/\delta_0 \ell)$	
in.	cm	lb_f/in.	N/m	lb_f/in.	N/m
10.5775	26.8668	13.3628	2340.17	6.2890	1101.36
10.7985	27.4281	13.1013	2294.37	6.9571	1218.36
11.1475	28.3146	13.0343	2282.64	7.2814	1266.40
11.7402	29.8201	12.9275	2263.94	7.4087	1297.45
12.4387	31.5942	13.1217	2297.95	6.8490	1199.43
13.3202	33.8333	12.4097	2173.26	8.3963	1470.41
14.1774	36.0105	12.5815	2203.34	8.2699	1448.27
14.6002	37.0845	12.0506	2110.37	8.3158	1456.31
14.8242	37.6534	12.0444	2109.28	8.2076	1437.36
14.9562	37.9887	11.8036	2067.11	7.9293	1388.62

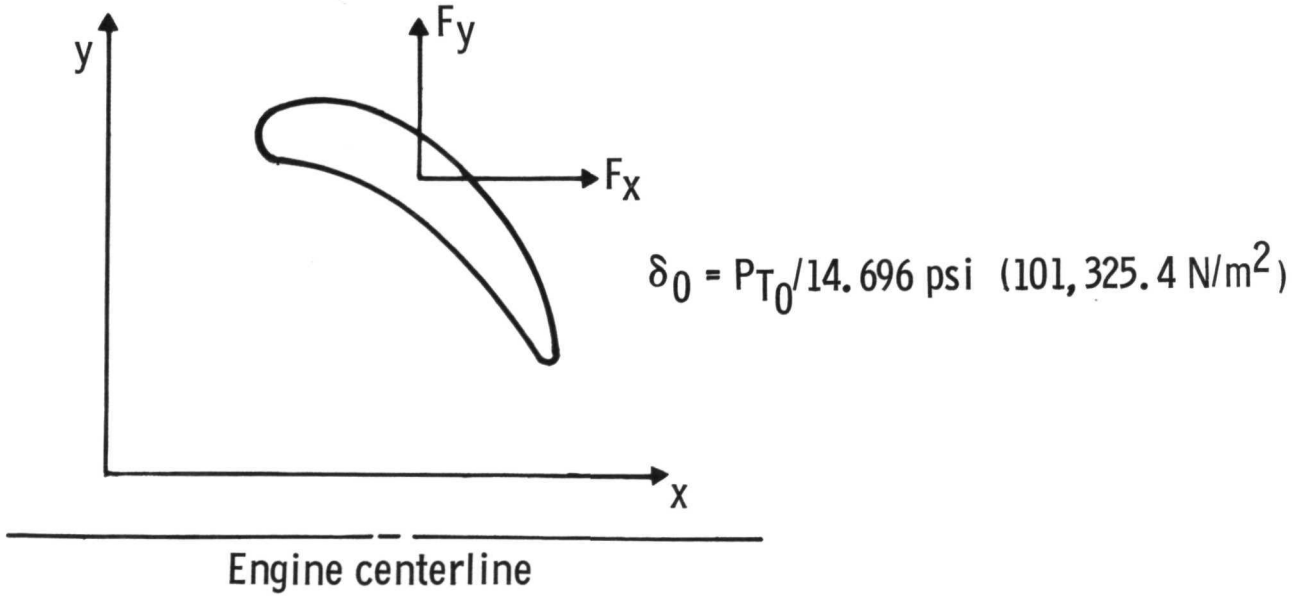

$\delta_0 = P_{T_0}/14.696$ psi (101,325.4 N/m^2)

7389-103

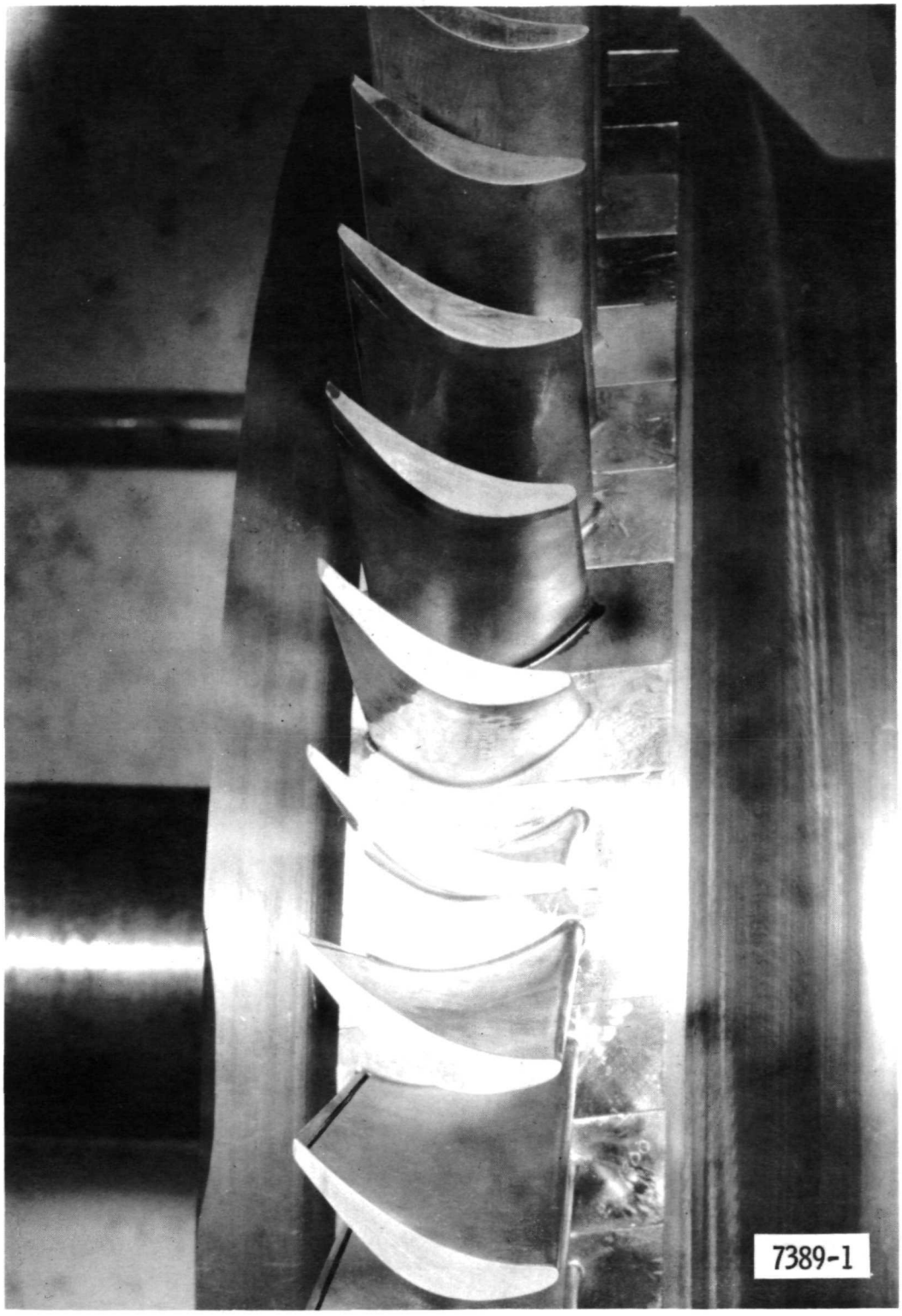

Figure 1. Modified jet flap rotor assembly.

Equivalent specific work—$\Delta H/\theta_{cr}$,	20.0 Btu/lb (46,519 J/kg)
Equivalent weight flow into stator—$\dot{m}_p\sqrt{\theta}_{cr}/\varepsilon_0$	46.59 lb/sec (21.133 kg/s)
Equivalent weight flow into rotor—$\dot{m}_p\sqrt{\theta}_{cr}/\delta_0$	47.70 lb/sec (21.636 kg/s)
Secondary-to-primary flow rate ratio—$\dot{m}_s/\dot{m}_p$	2.375%
Equivalent rotor speed—$N/\sqrt{\theta}_{cr}$,	4660 rpm (487.99 rad/s)
Equivalent tip speed—$U_t/\sqrt{\theta}_{cr}$	610 ft/sec (185.928 m/s)
Pressure ratio—$R_{e_{T-T}}$	2.034
Jet slot size—$\overline{hb}$	0.030 in. (0.0762 cm)
Jet cavity-to-inlet total pressure ratio —$P_{T_{IS}}/P_{T_0}$	1.00

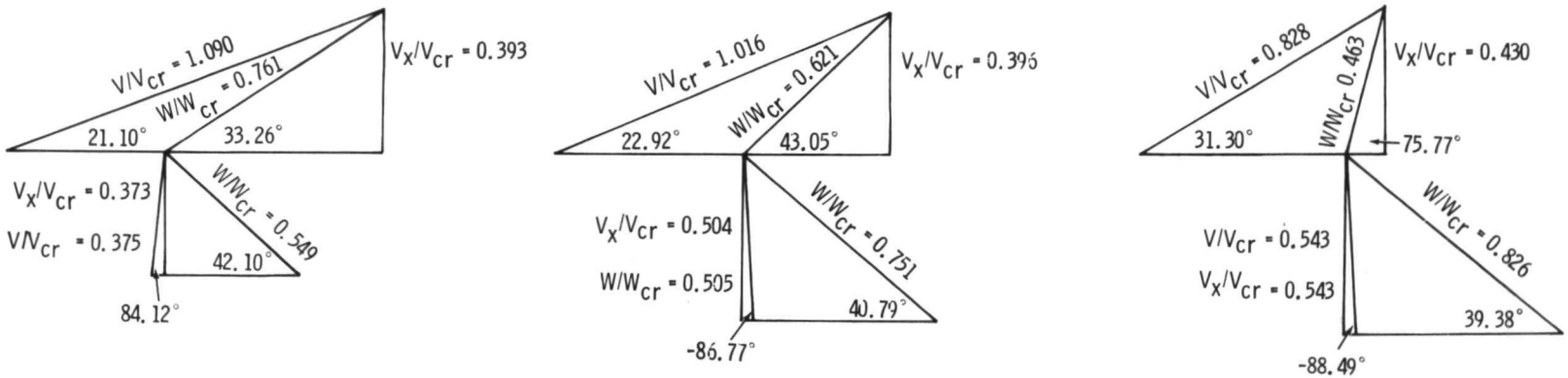

Figure 2. Stage velocity diagrams with stator jet flap.

Equivalent weight flow into stator—$\dot{m}_p \sqrt{\theta}_{cr}/\delta_0$,	49.85 lb/sec (22.611 kg/s)
Equivalent weight flow into rotor—$\dot{m}_1 \sqrt{\theta}_{cr}/\delta_0$,	49.85 lb/sec (22.611 kg/s)
Equivalent rotor speed—$N/\sqrt{\theta}_{cr}$	4660 rpm (487.99 rad/s)
Equivalent tip speed—$U_t/\sqrt{\theta}_{cr}$,	610 ft/sec (185.928 m/s)
Total pressure ratio—$R_{e_{T-T}}$	2.031

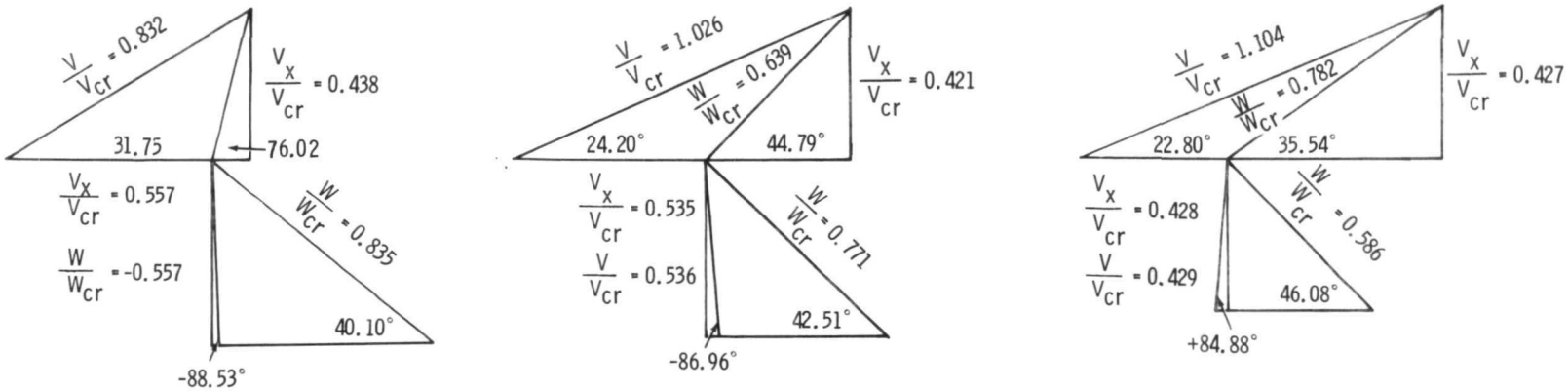

Figure 3. Stage velocity diagrams without stator jet flap on.

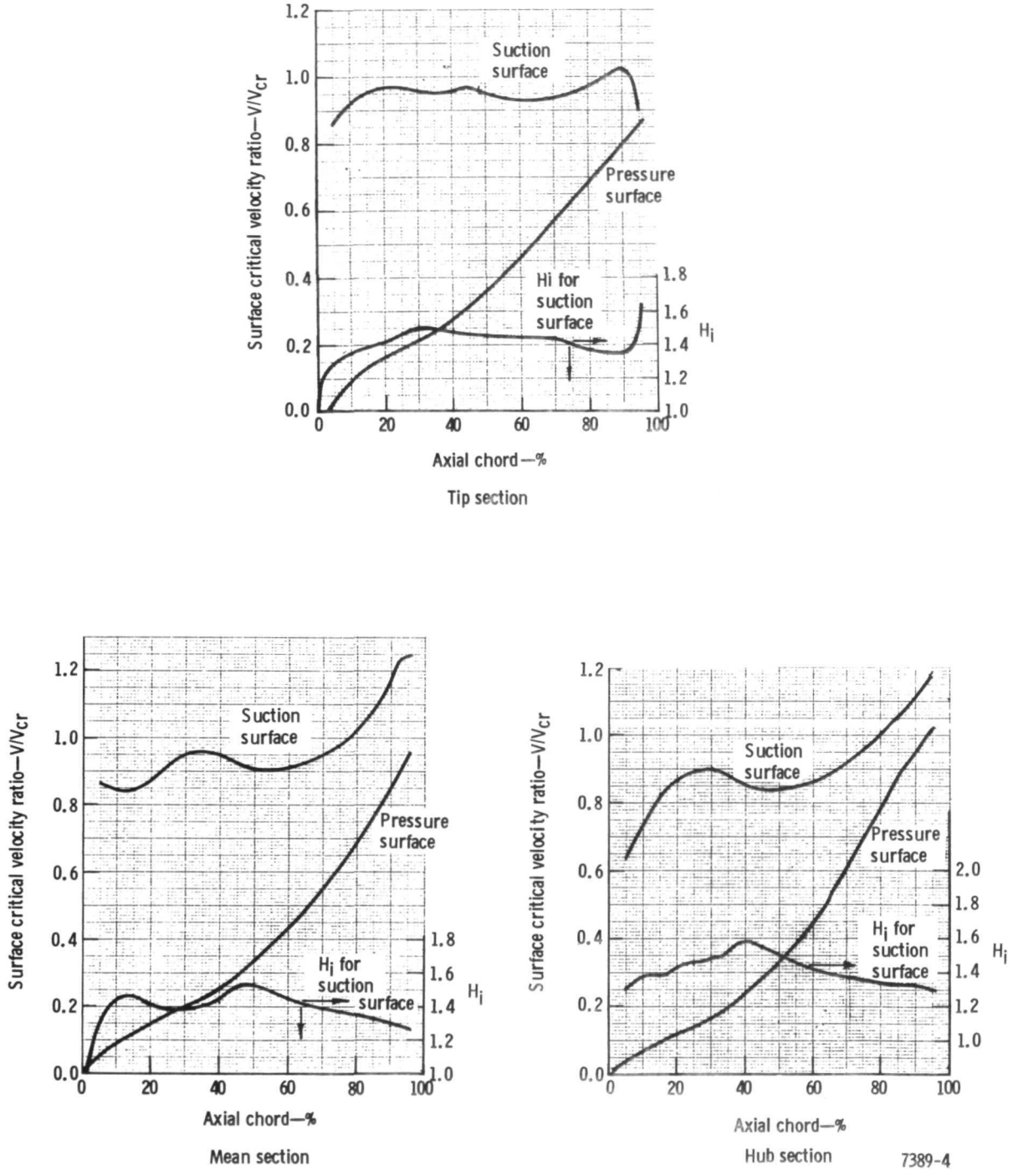

Figure 4. Jet flap stator velocity and boundary layer shape factor distribution with jet flap off.

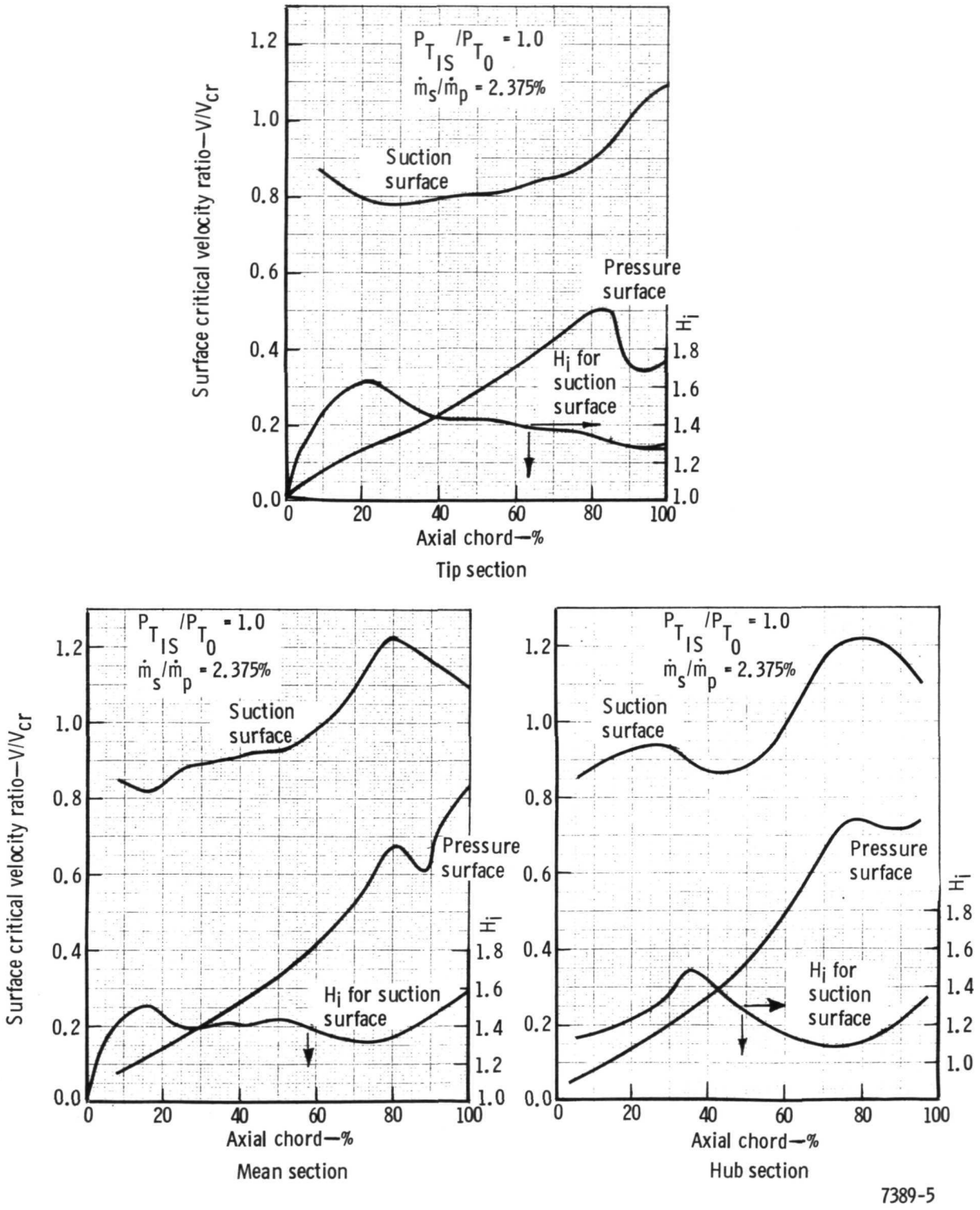

Figure 5. Jet flap stator velocity and boundary layer shape factor distribution with jet flap on.

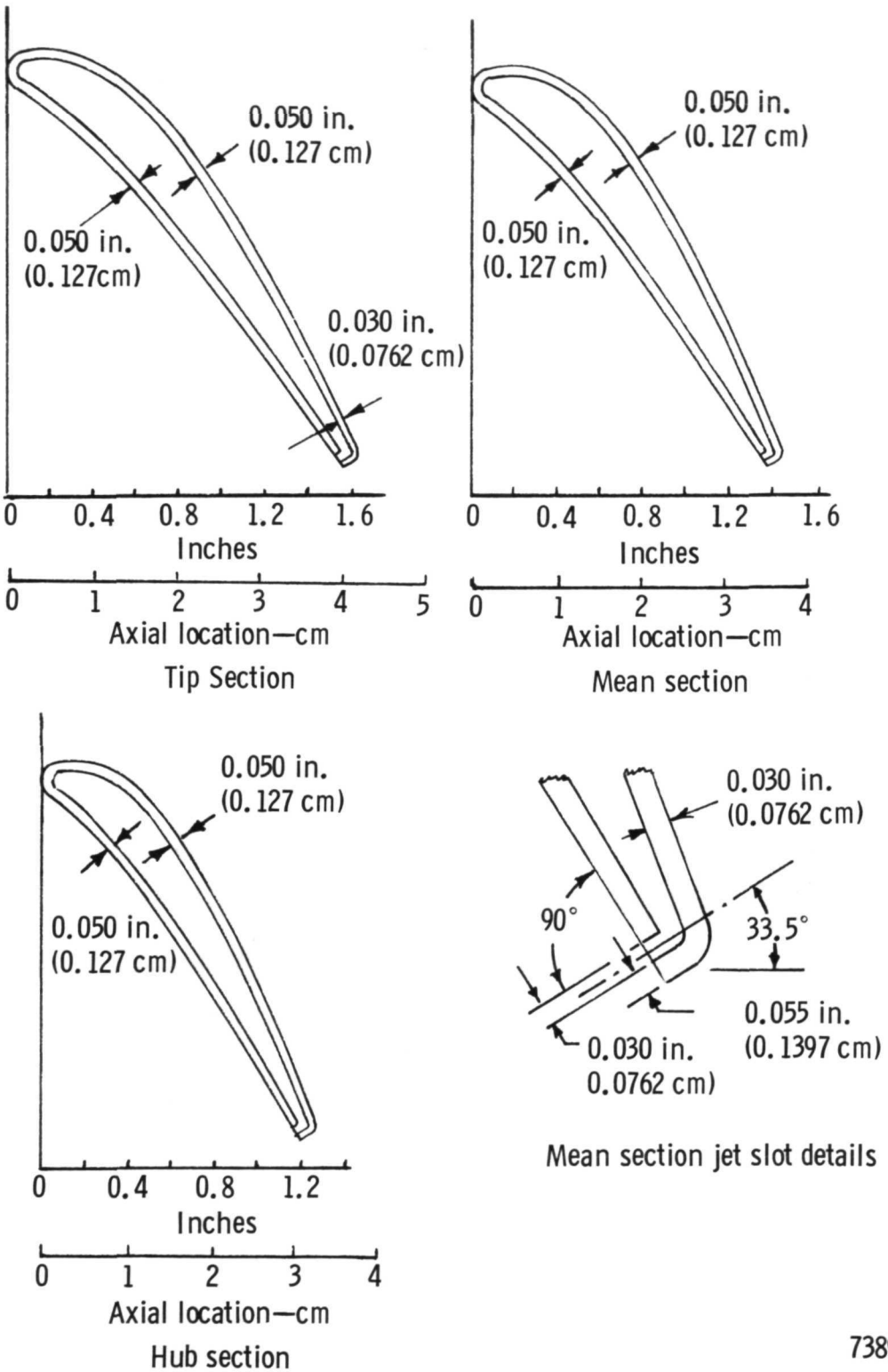

Figure 6. Tip, mean, and hub section and jet slot details.

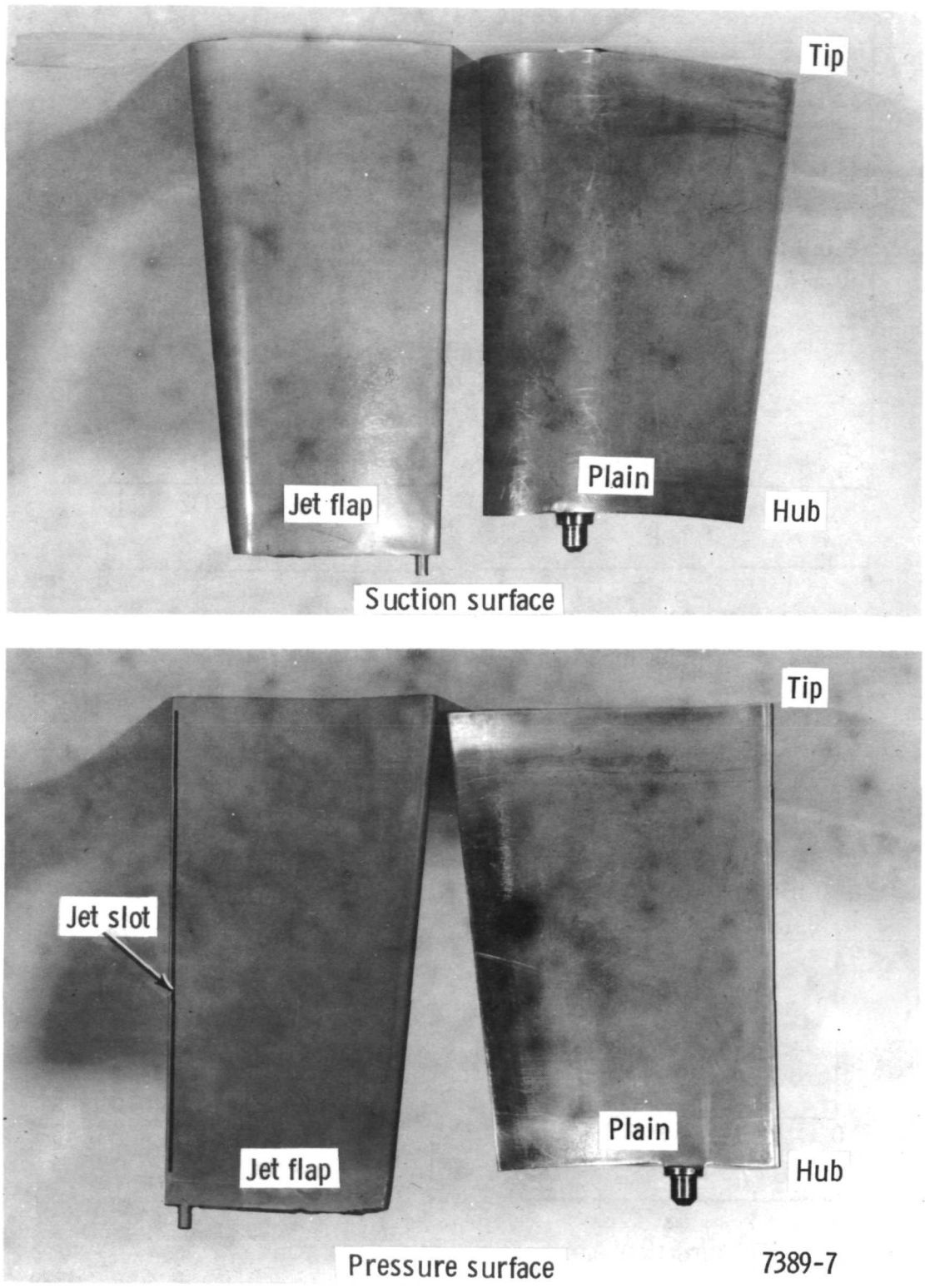

Figure 7. Suction and pressure surfaces of the plain and jet flap stator vanes.

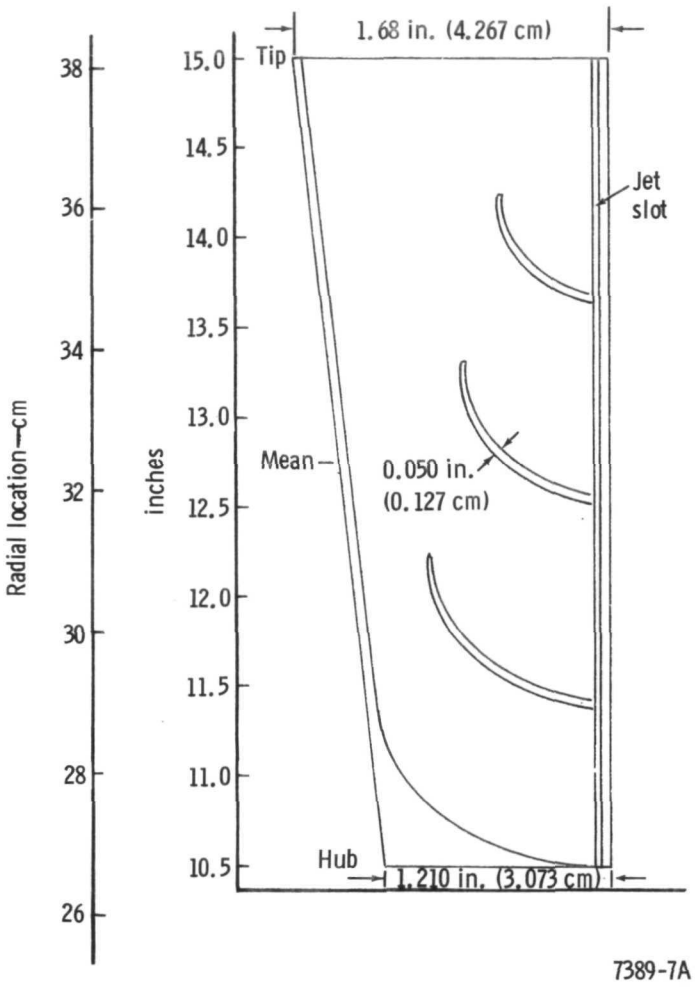

Figure 8. Jet flap stator internal guide vane assembly.

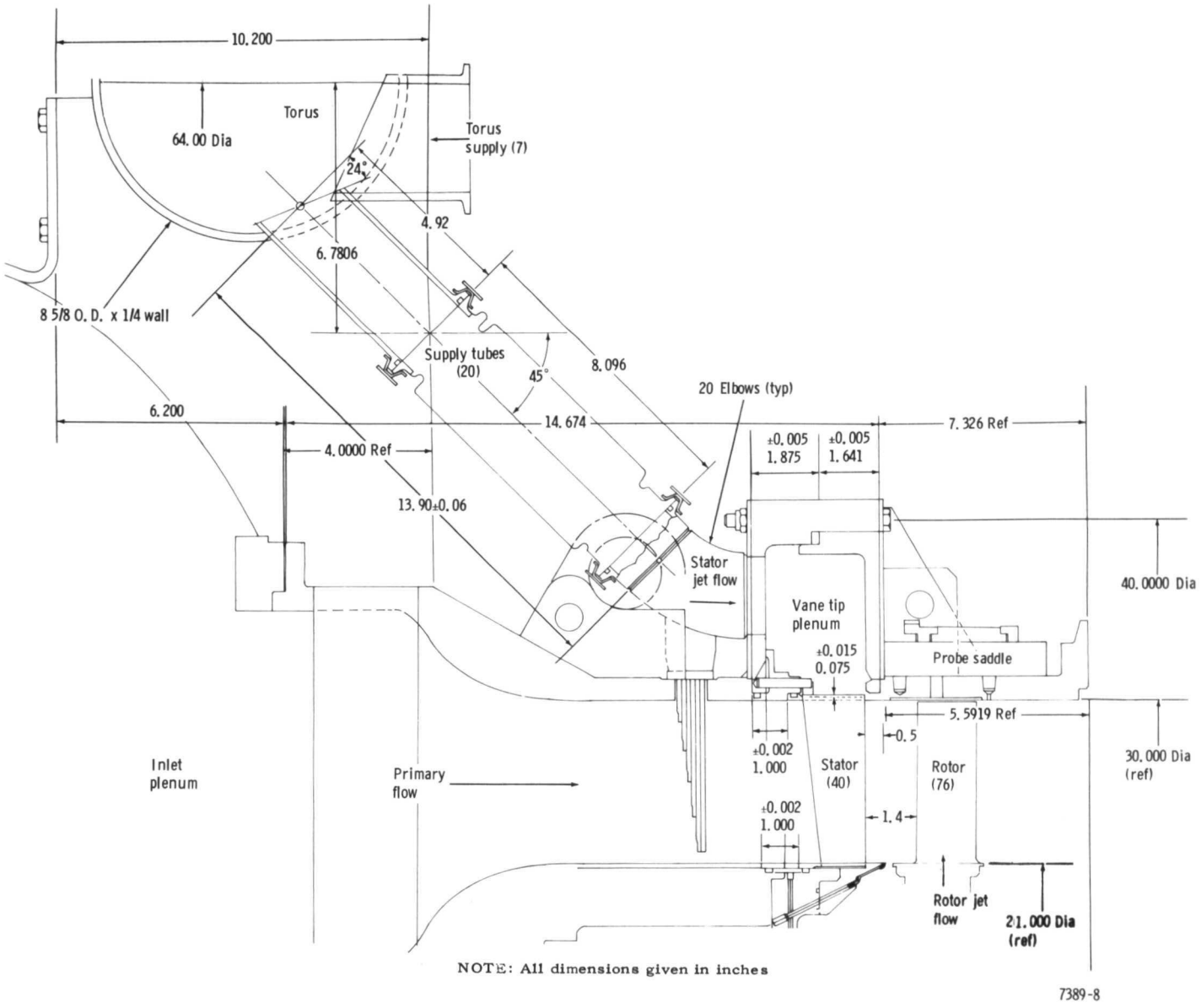

Figure 9. Rework of forward rig case.

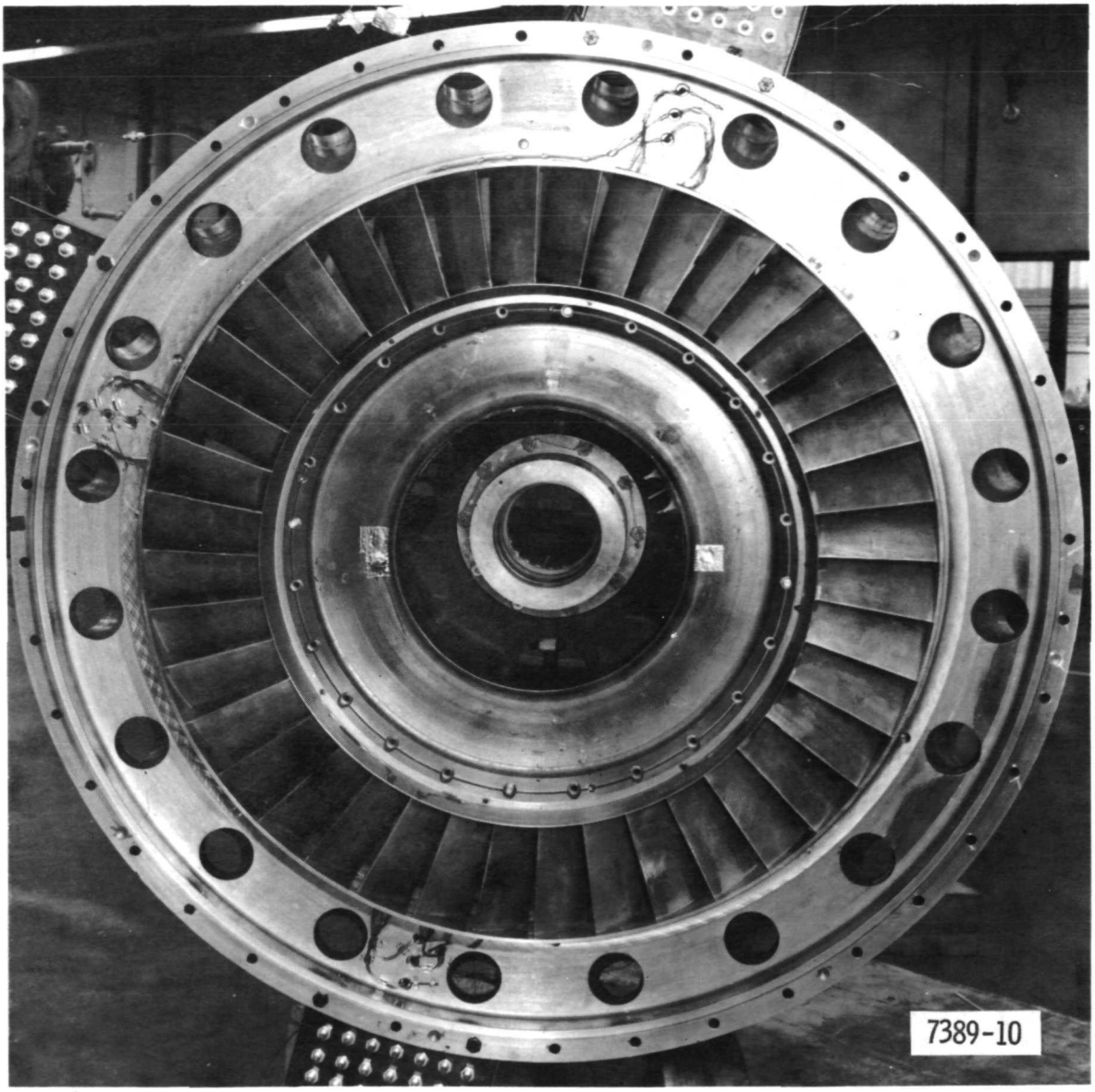

Figure 10. Jet flap stator assembly (aft looking forward).

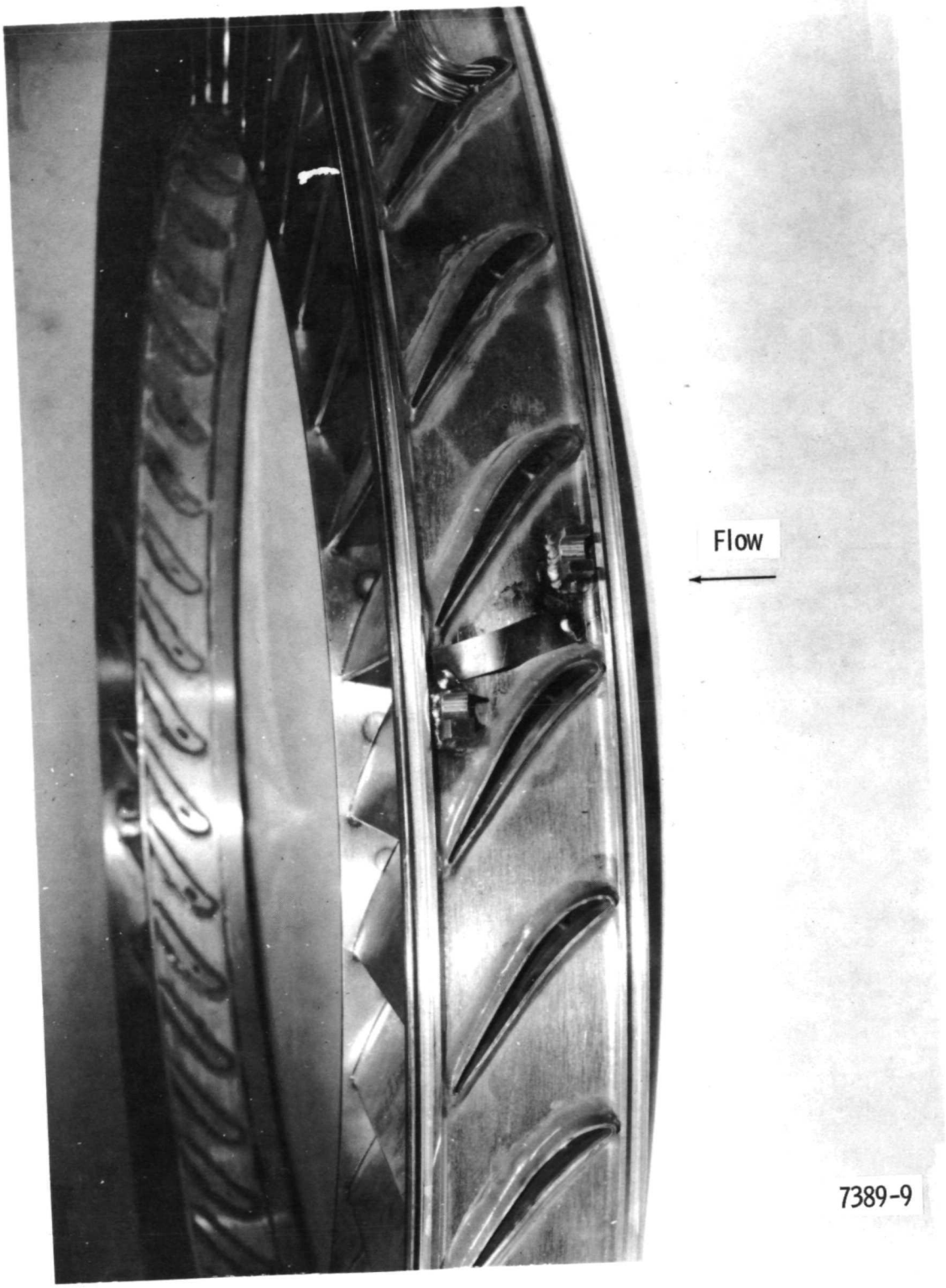

Figure 11. Jet flap stator assembly.

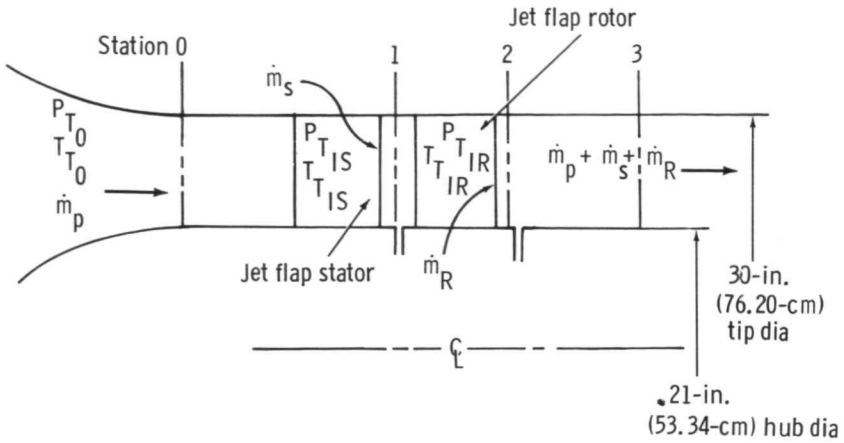

Design Point Conditions

Equvialent work, $\Delta H/\theta_{cr_0}$	20 Btu/lb (46,519 J/kg)
Equivalent speed, $N/\sqrt{\theta}_{cr_0}$	4660 rpm (487.99 rad/s)
Design expansion ratio, P_{T_0}/P_{T_3}	2.034
Equivalent inlet flow (jet on), $\left(\frac{\dot{m}_p \sqrt{\theta}_{cr_0}}{\delta_0}\right)_{w/j}$	46.59 lb/sec (21.33 kg/s)
Design stator cavity pressure ratio, $P_{T_{IS}}/P_{T_0}$	1.00
Percent stator jet flow, $\dot{m}_s/\dot{m}_p$	2.375%
Design rotor cavity pressure ratio, $P_{T_{IR}}/P_{T_0}$	1.00
Percent rotor jet flow, $\dot{m}_R/\dot{m}_p$	6.65%
Percent inlet mass flow reduction, $1 - \frac{\left(\dot{m}_p \frac{\sqrt{\theta}_{cr_0}}{\delta_0}\right)_{w/j}}{\left(\dot{m}_p \frac{\sqrt{\theta}_{cr_0}}{\delta_0}\right)_{wo/j}}$	6.4%
Equivalent inlet flow (jet off), $\left(\frac{\dot{m}_p \sqrt{\theta}_{cr_0}}{\delta_0}\right)_{wo/j}$	49.85 lb/sec (22.611 kg/s)

7389-11

Figure 12. Jet flap turbine flowpath schematic and design point conditions.

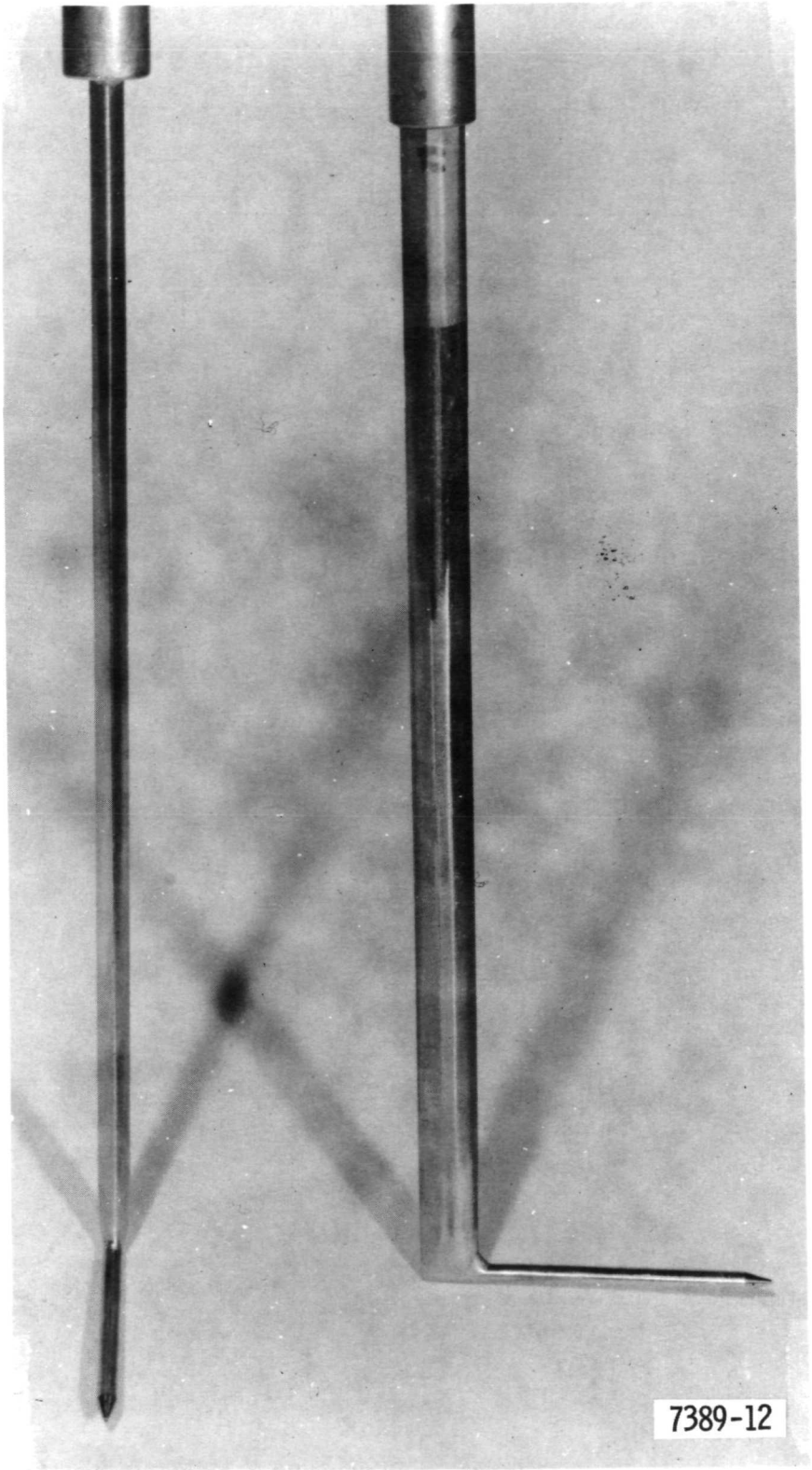

Figure 13. Stator exit survey cone probe.

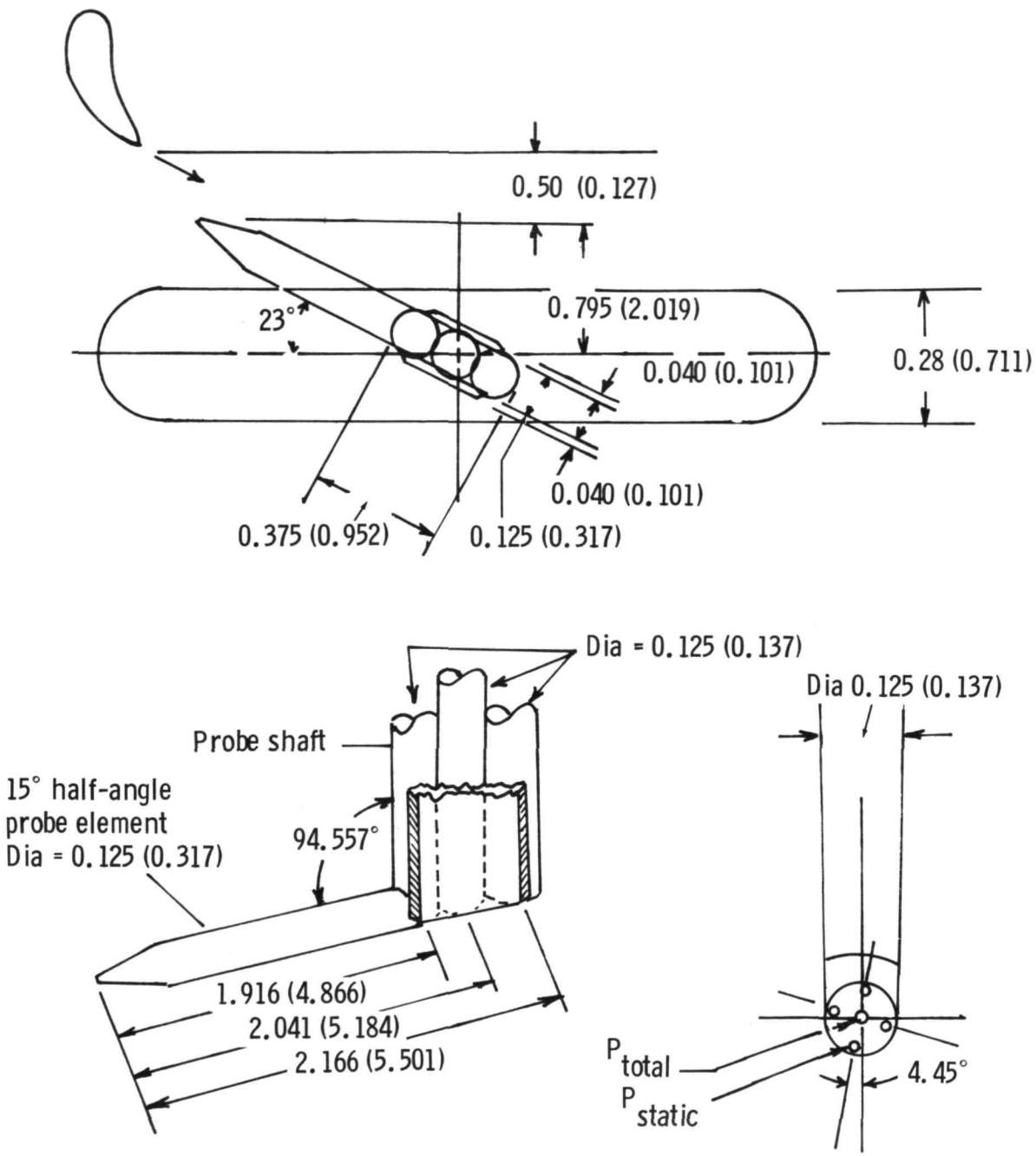

Note: All dimensions are in inches (centimeters)

7389-13

Figure 14. Stator exit survey cone probe geometry.

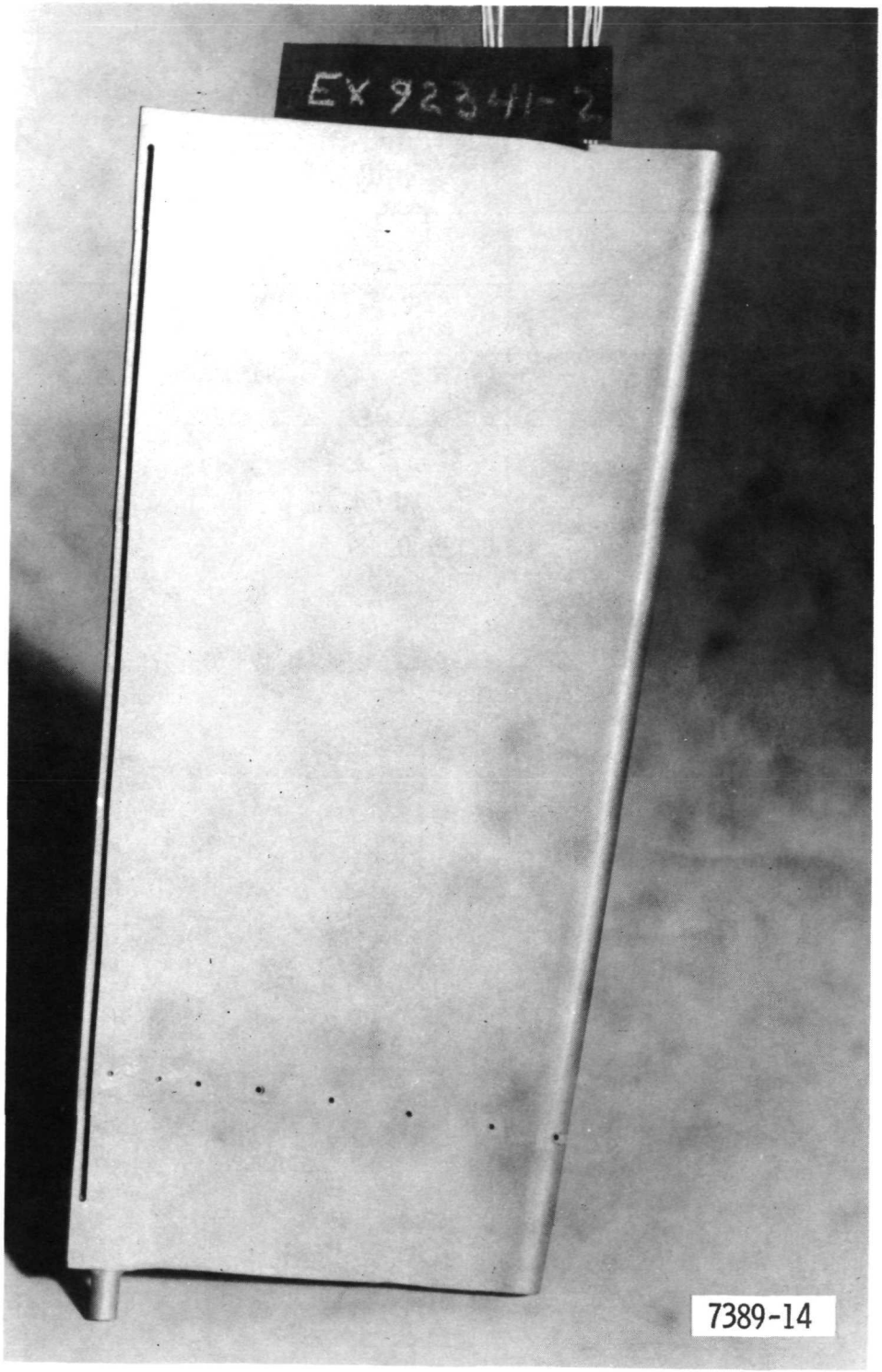

Figure 15. Jet flap stator hub pressure surface static taps.

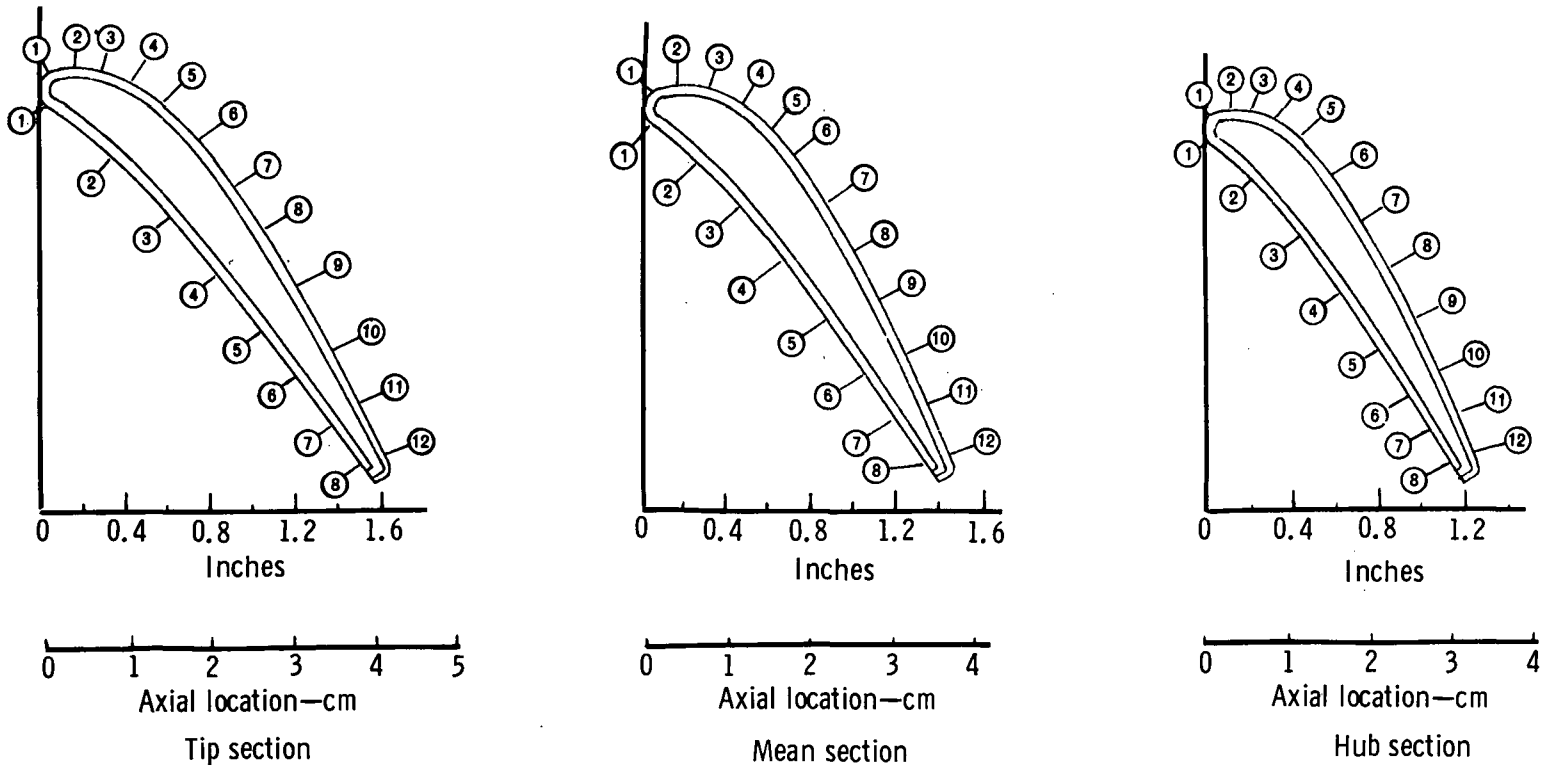

Figure 16. Static pressure tap location.

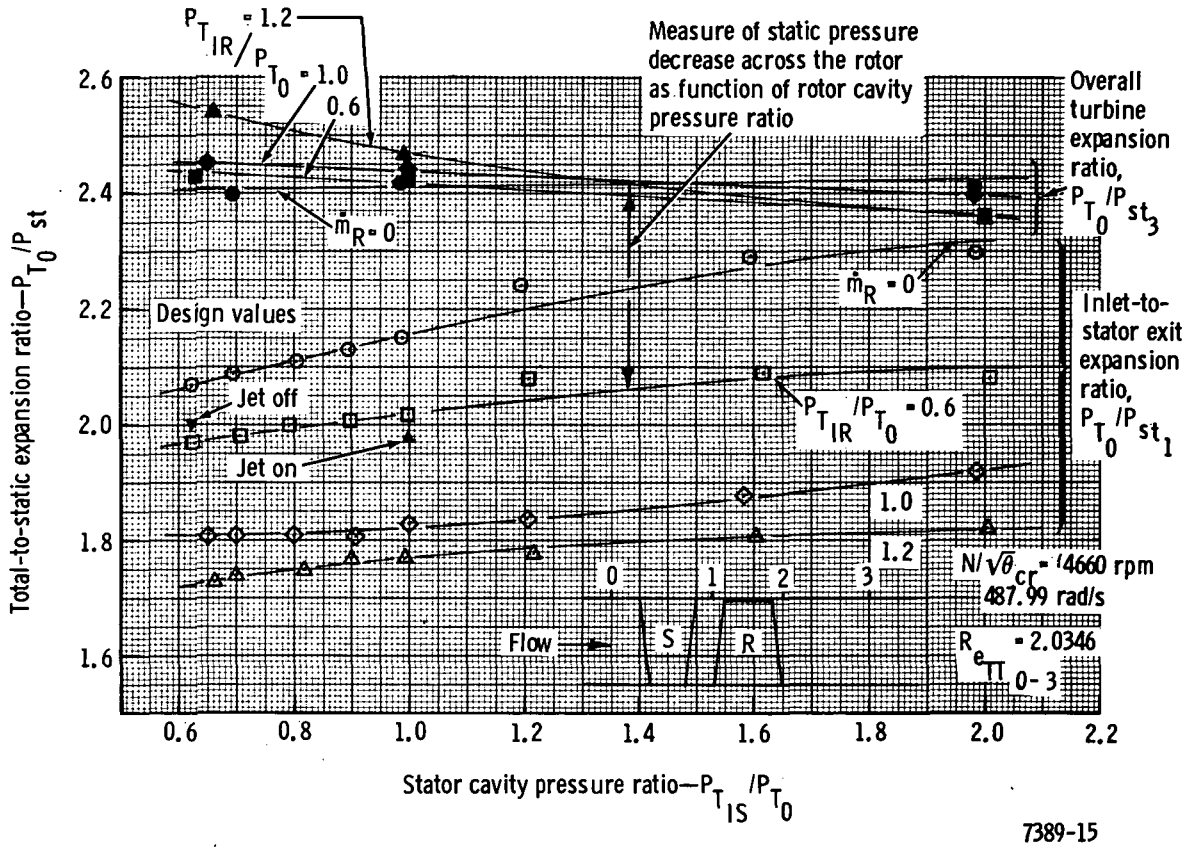

Figure 17. Effect of rotor and stator cavity pressure on stator and overall turbine total-to-static expansion ratios.

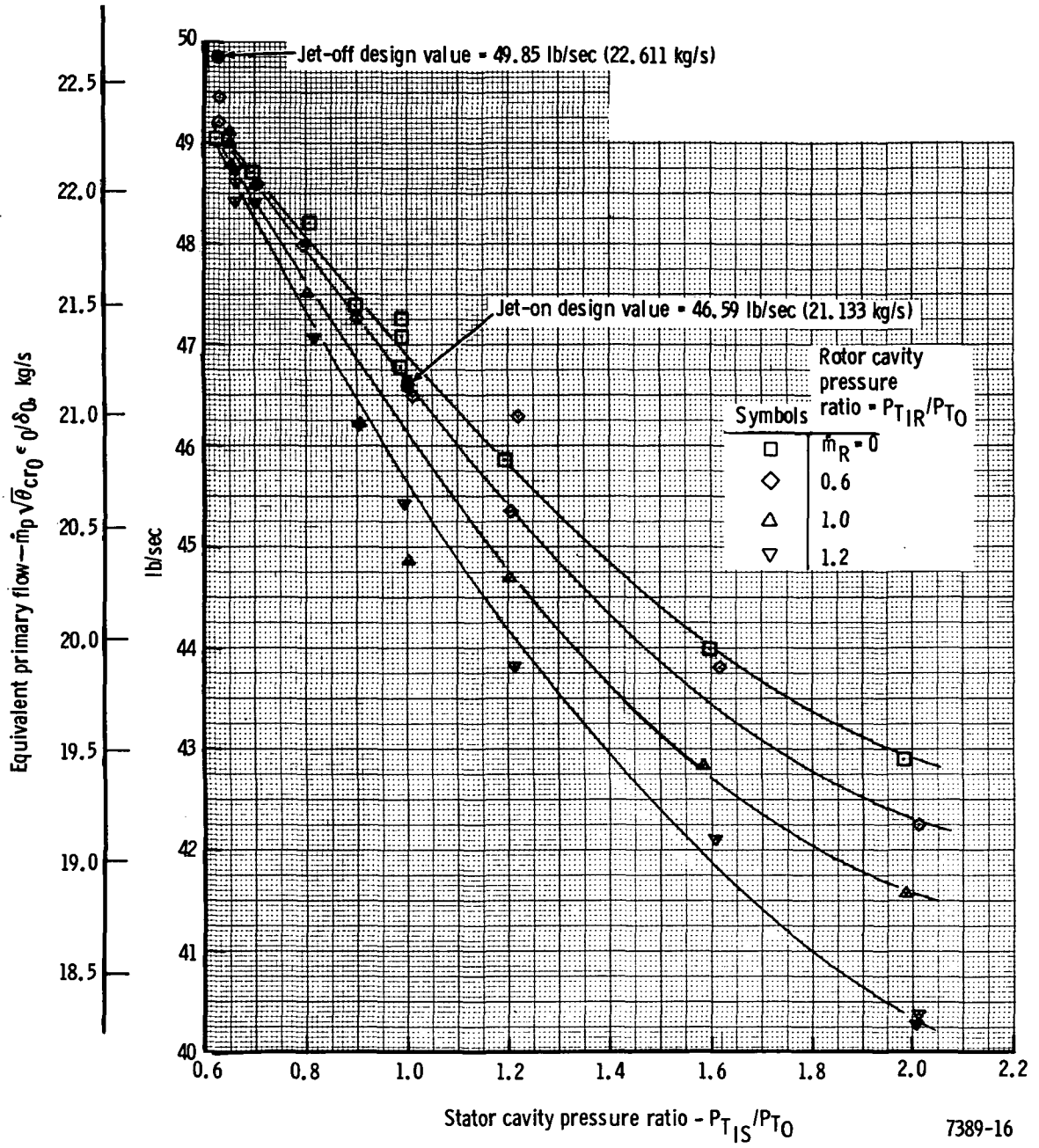

Figure 18. Equivalent primary flow variation with stator and rotor cavity pressure ratio at design speed and expansion ratio.

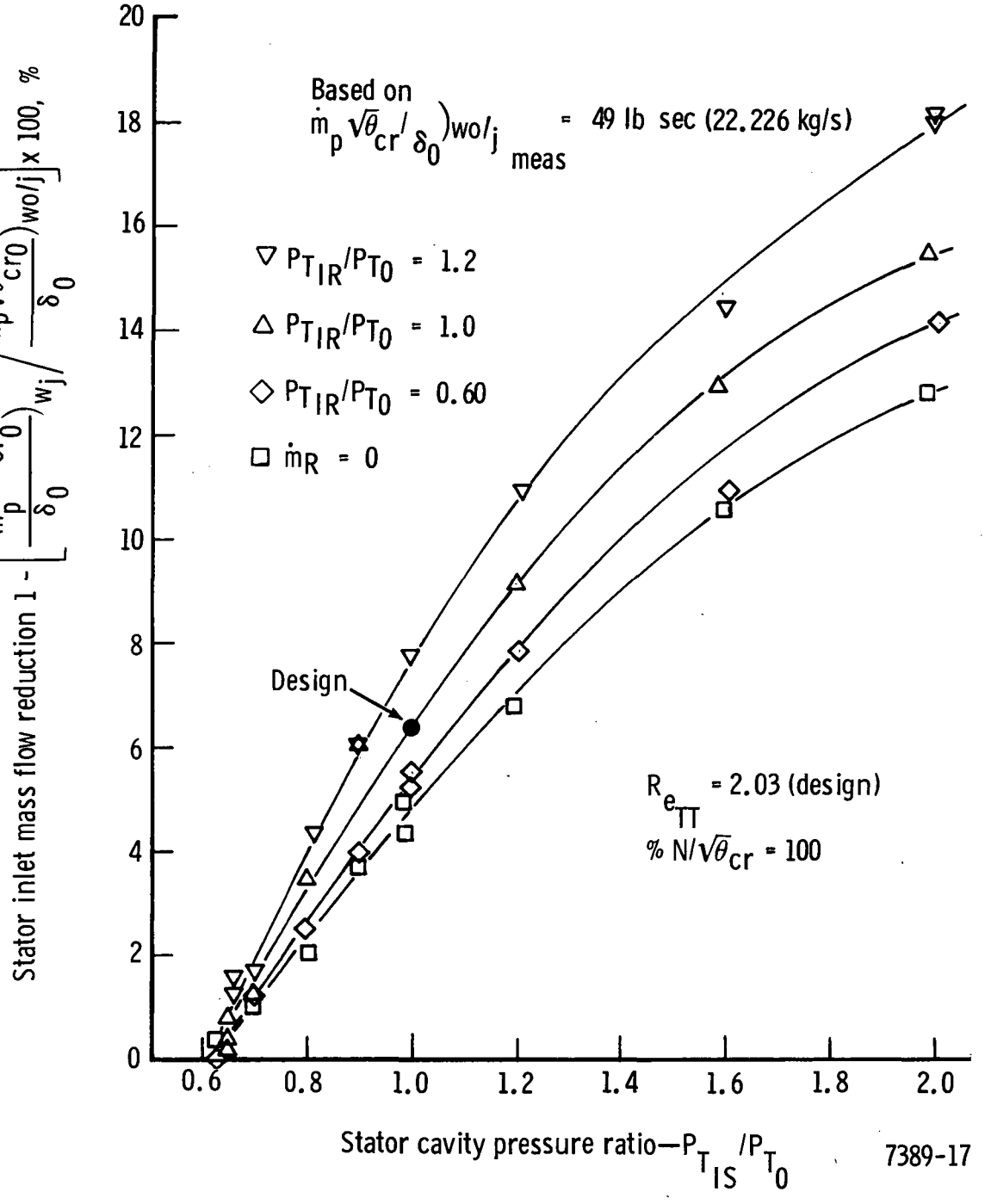

Figure 19. Effect of stator and rotor cavity pressure ratio on stator inlet flow reduction at design speed and expansion ratio.

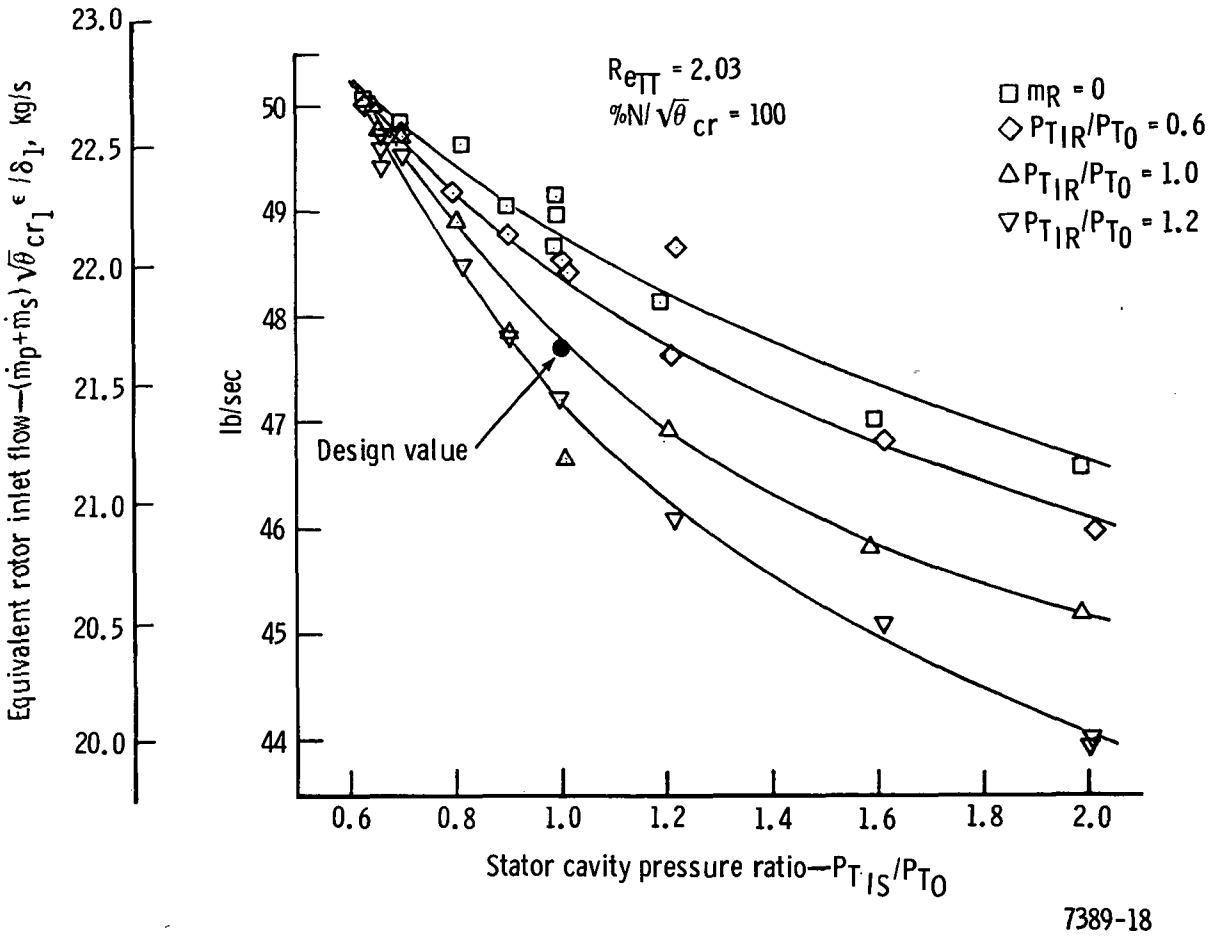

Figure 20. Variation of rotor inlet flow with stator and rotor cavity pressure ratio.

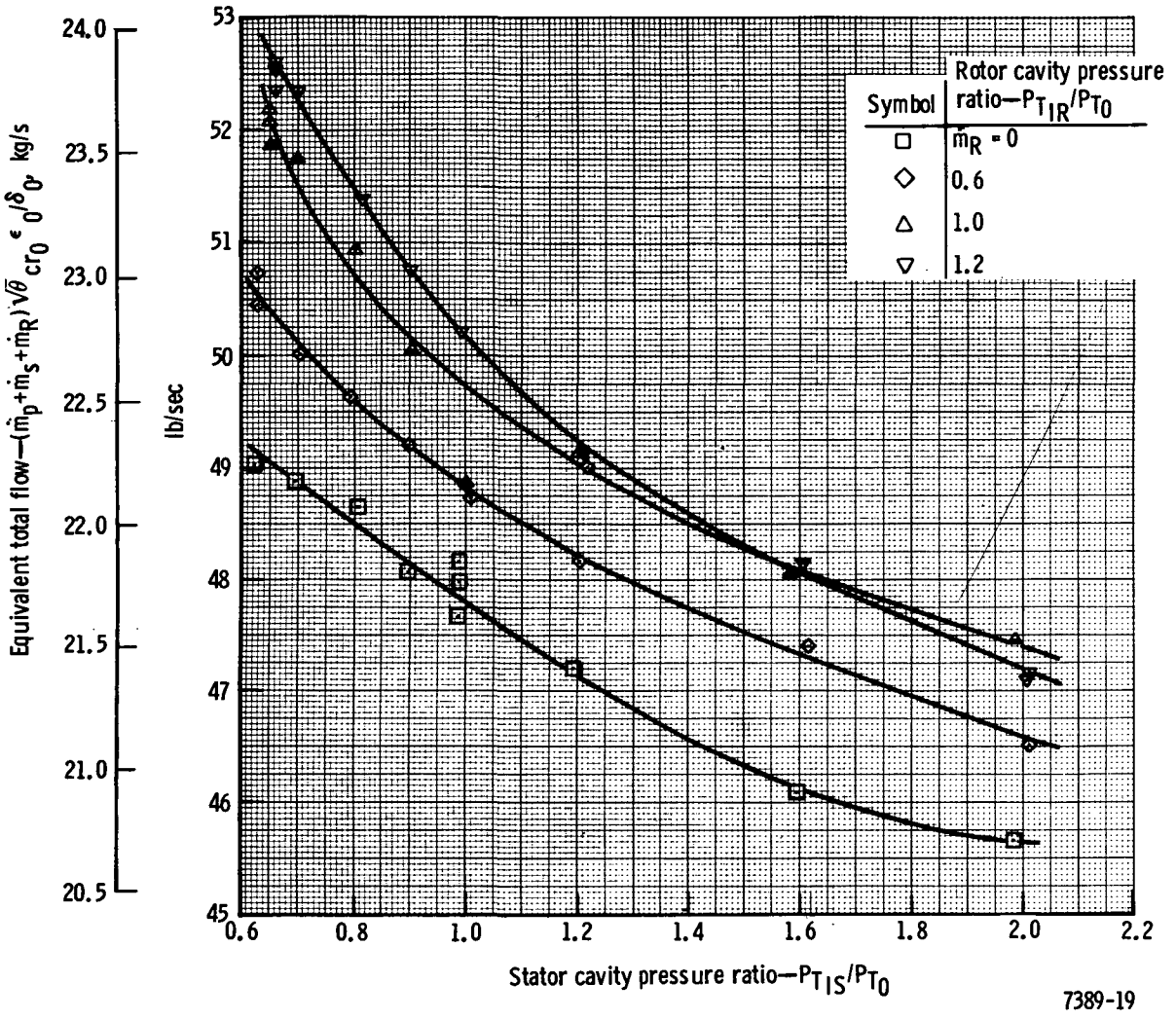

Figure 21. Variation of total flow with stator and rotor cavity pressure at design speed and expansion ratio.

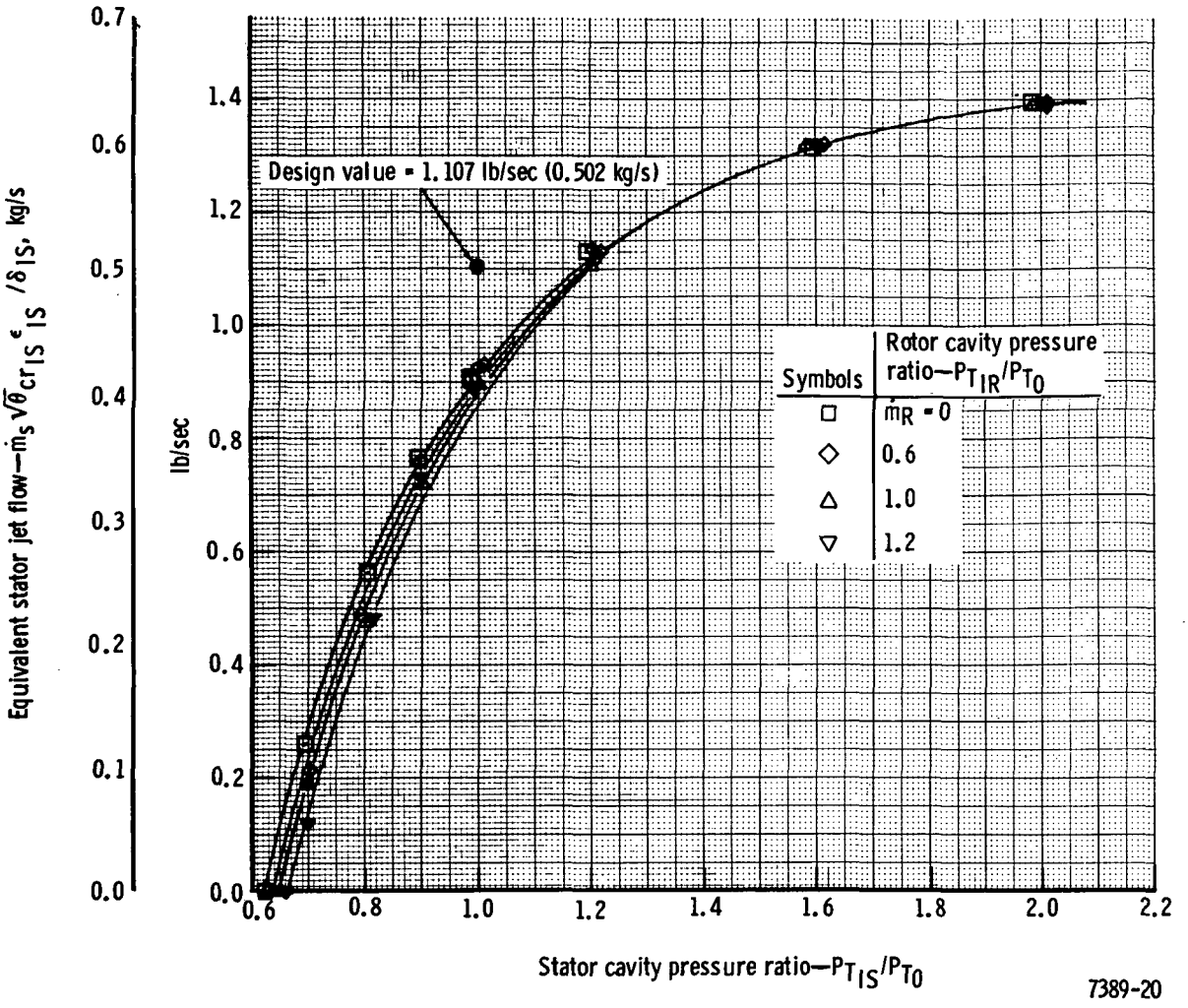

Figure 22. Variation in equivalent stator jet flow for various stator and rotor cavity pressure ratios of design speed and expansion ratio.

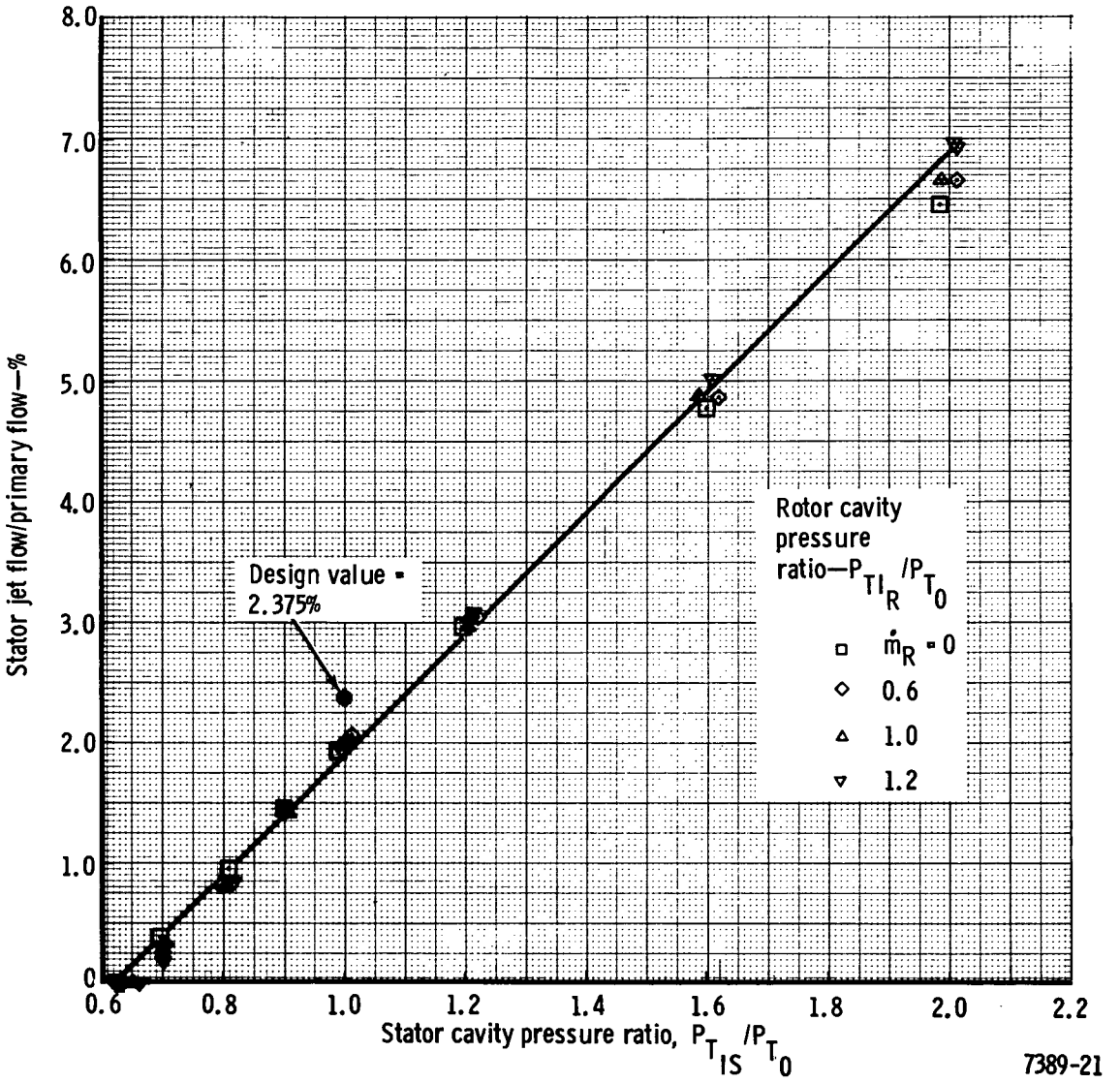

Figure 23. Variation of stator jet-to-primary flow ratio with stator and rotor cavity pressure ratios at design speed and expansion ratio.

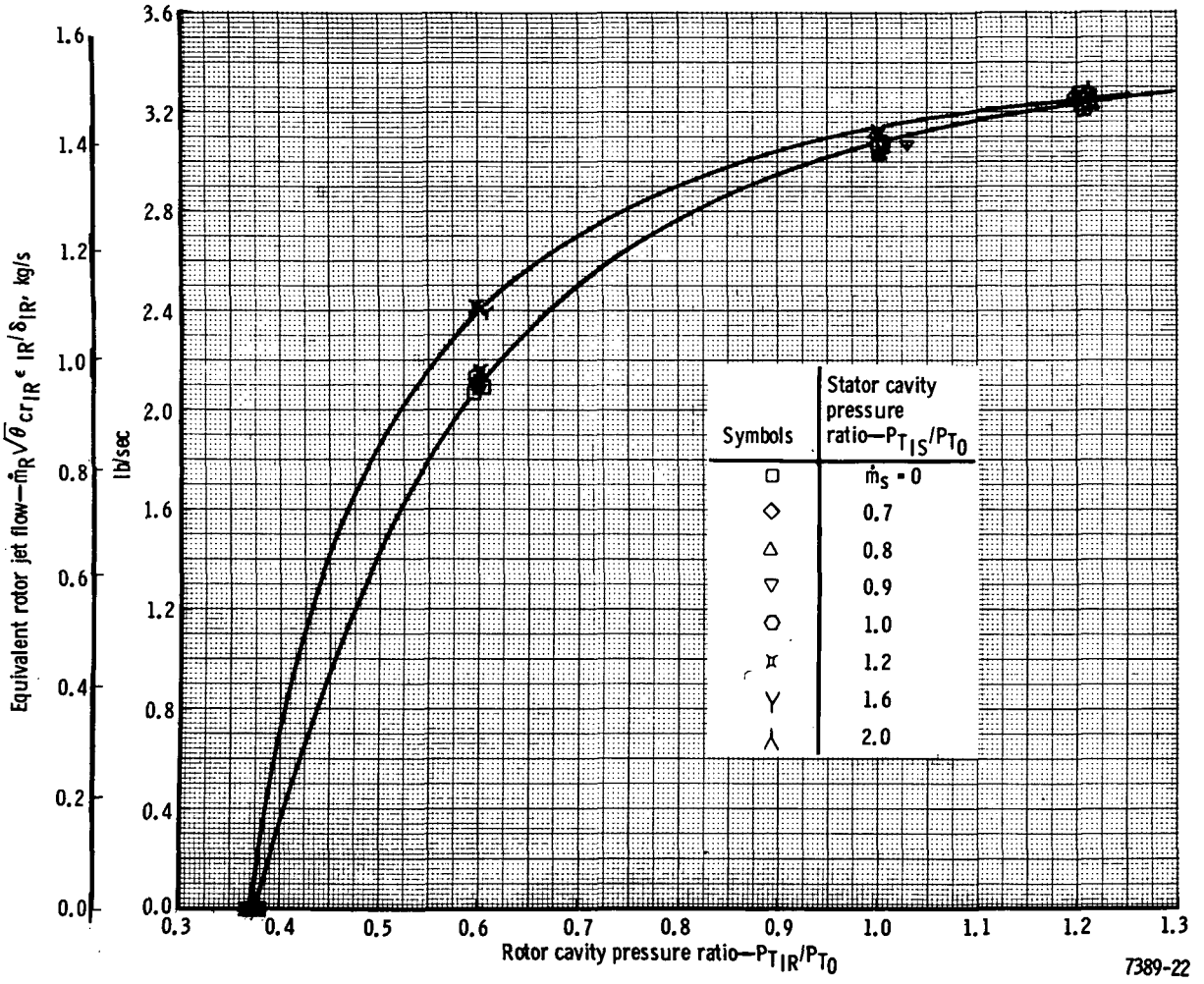

Figure 24. Equivalent rotor jet flow variation for various rotor and stator cavity conditions at design speed and expansion ratio.

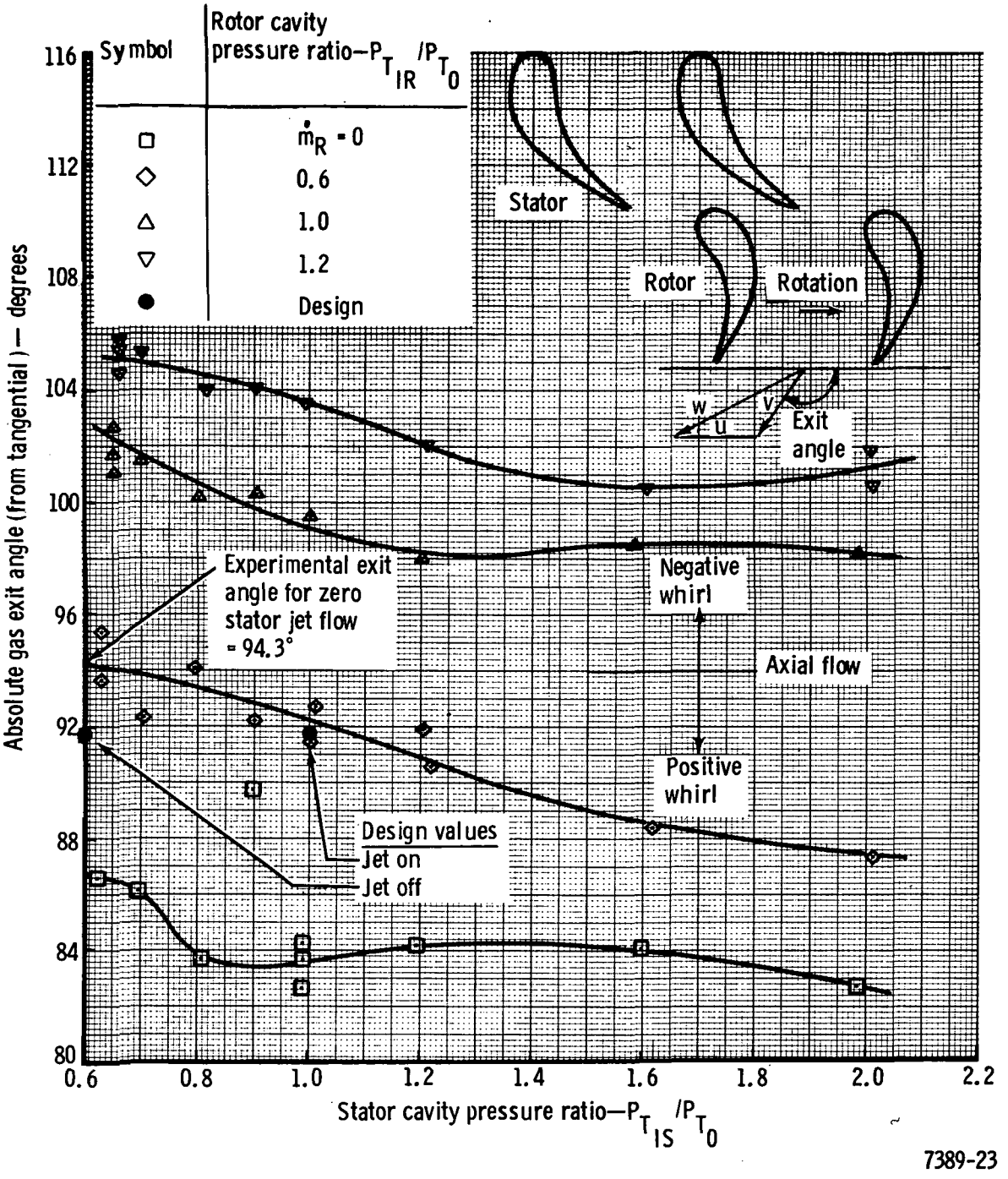

Figure 25. Variation in rotor exit absolute gas angle with stator and rotor cavity pressure ratios at design speed and expansion ratio.

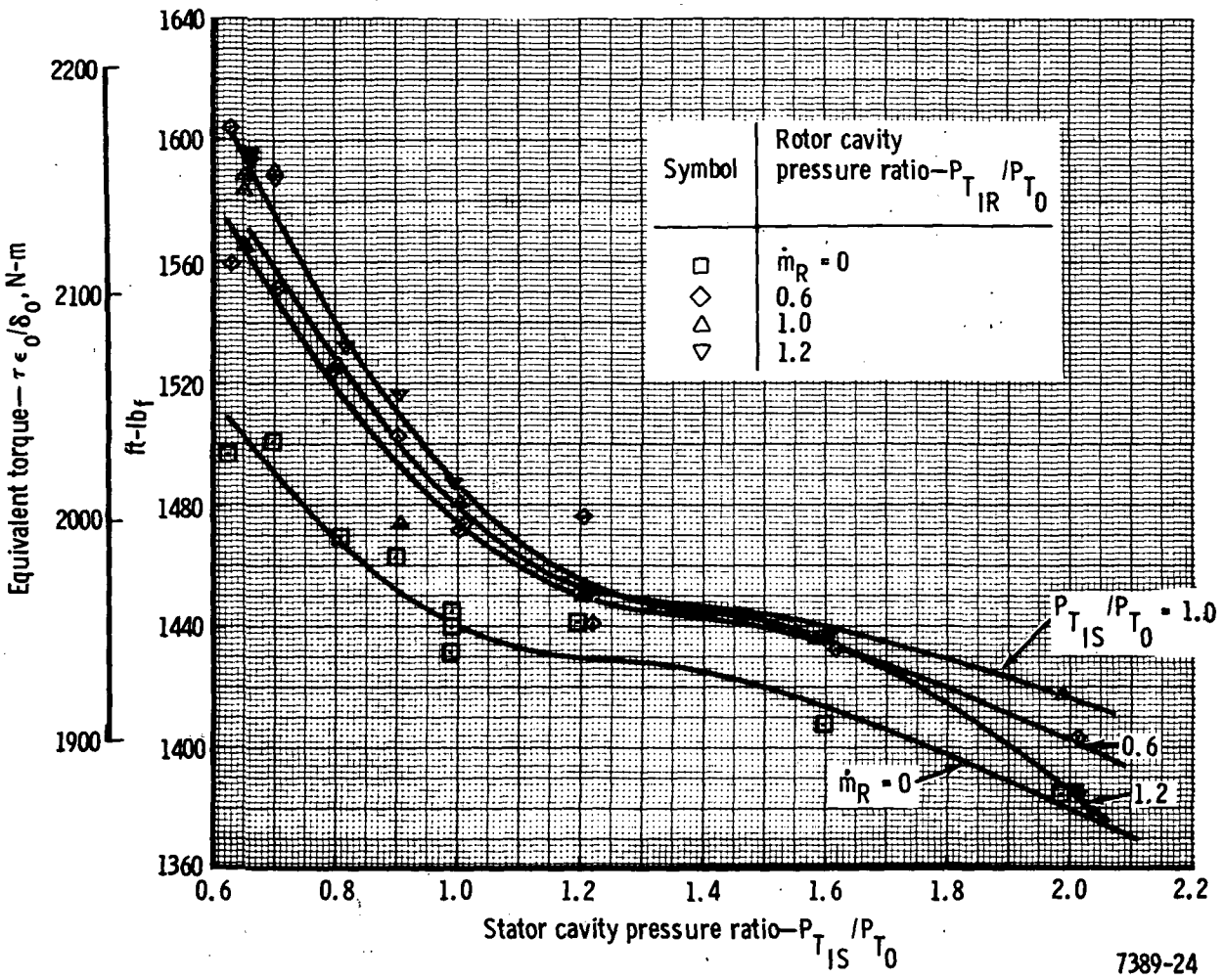

Figure 26. Variation in equivalent torque with stator and rotor cavity pressure ratios at design speed and expansion ratio.

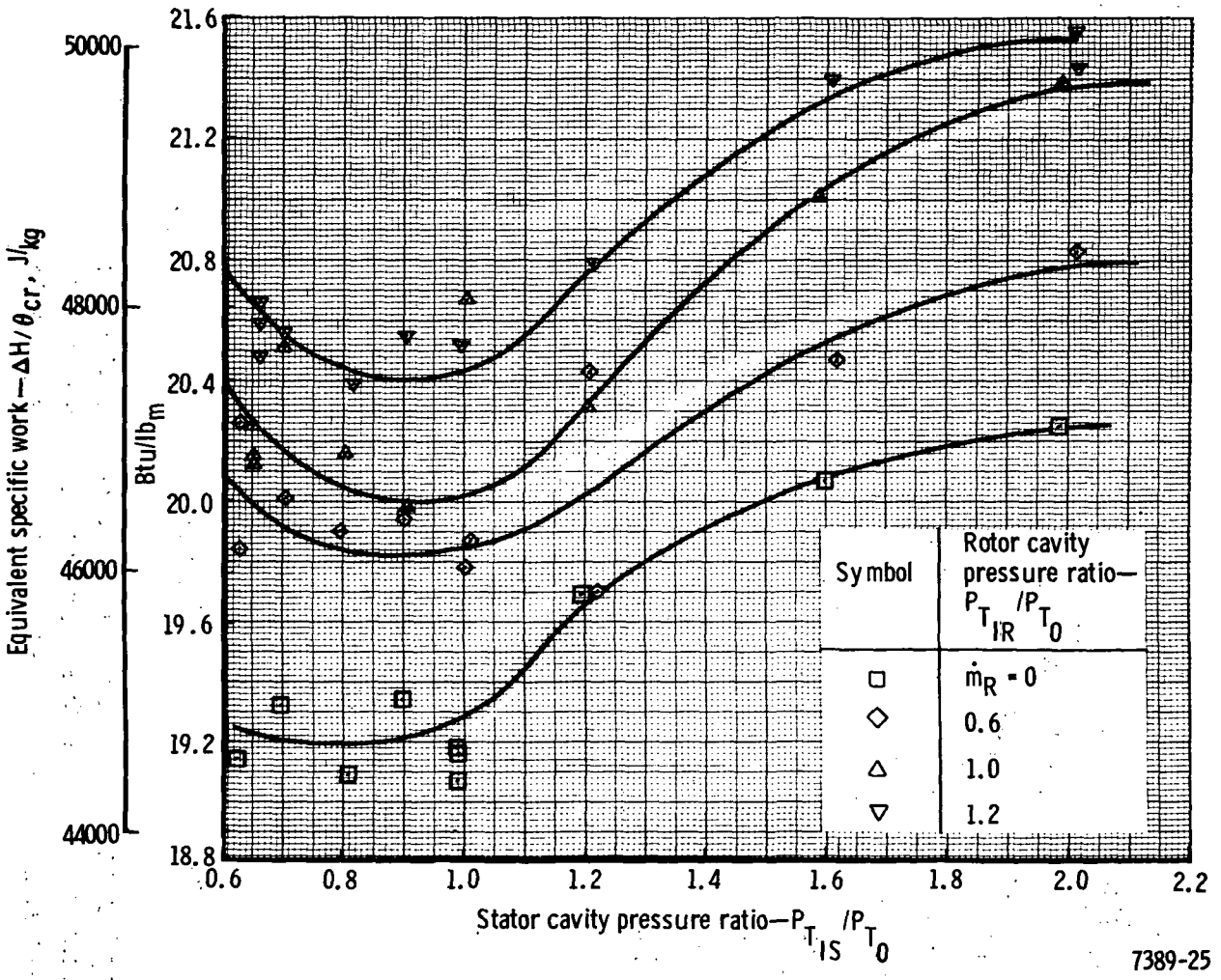

Figure 27. Variation in equivalent work with stator and rotor cavity pressure ratios at design speed and expansion ratio.

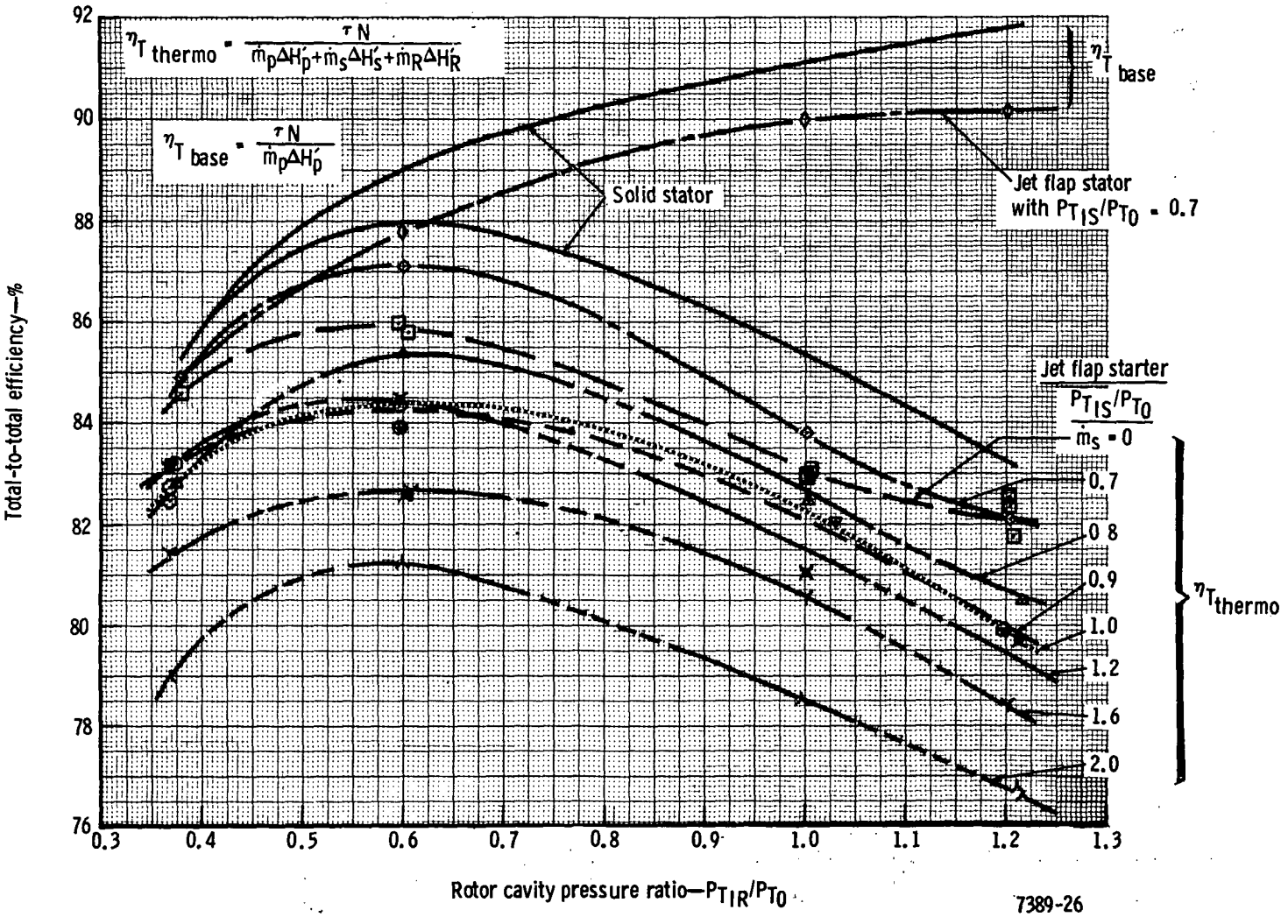

Figure 28. Jet flap turbine thermodynamic and base total-to-total efficiency variation with stator and rotor jet cavity pressure ratios at design speed and expansion ratio.

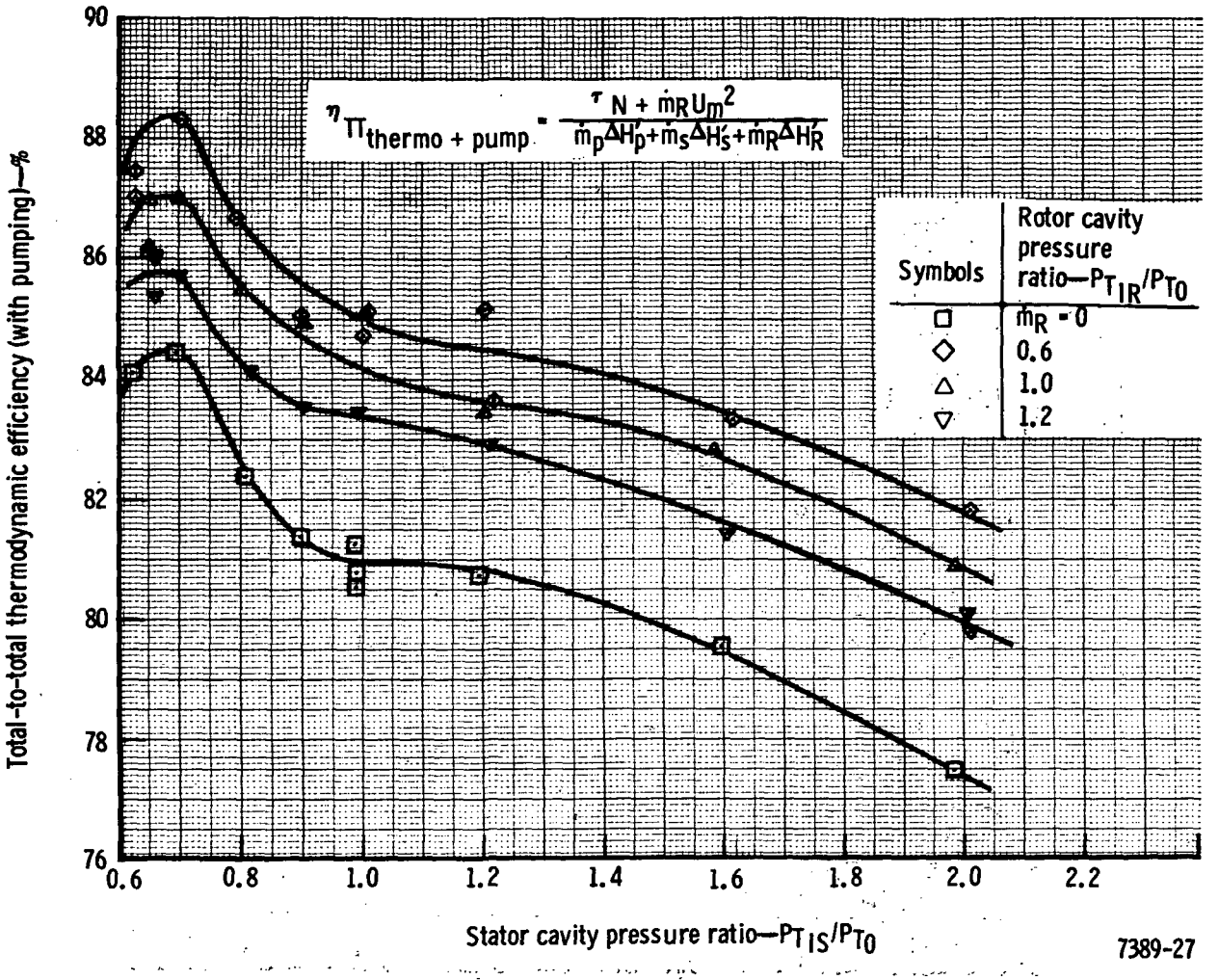

Figure 29. Variation in thermodynamic efficiency (with pumping) with stator and rotor cavity pressure ratio at design speed and expansion ratio.

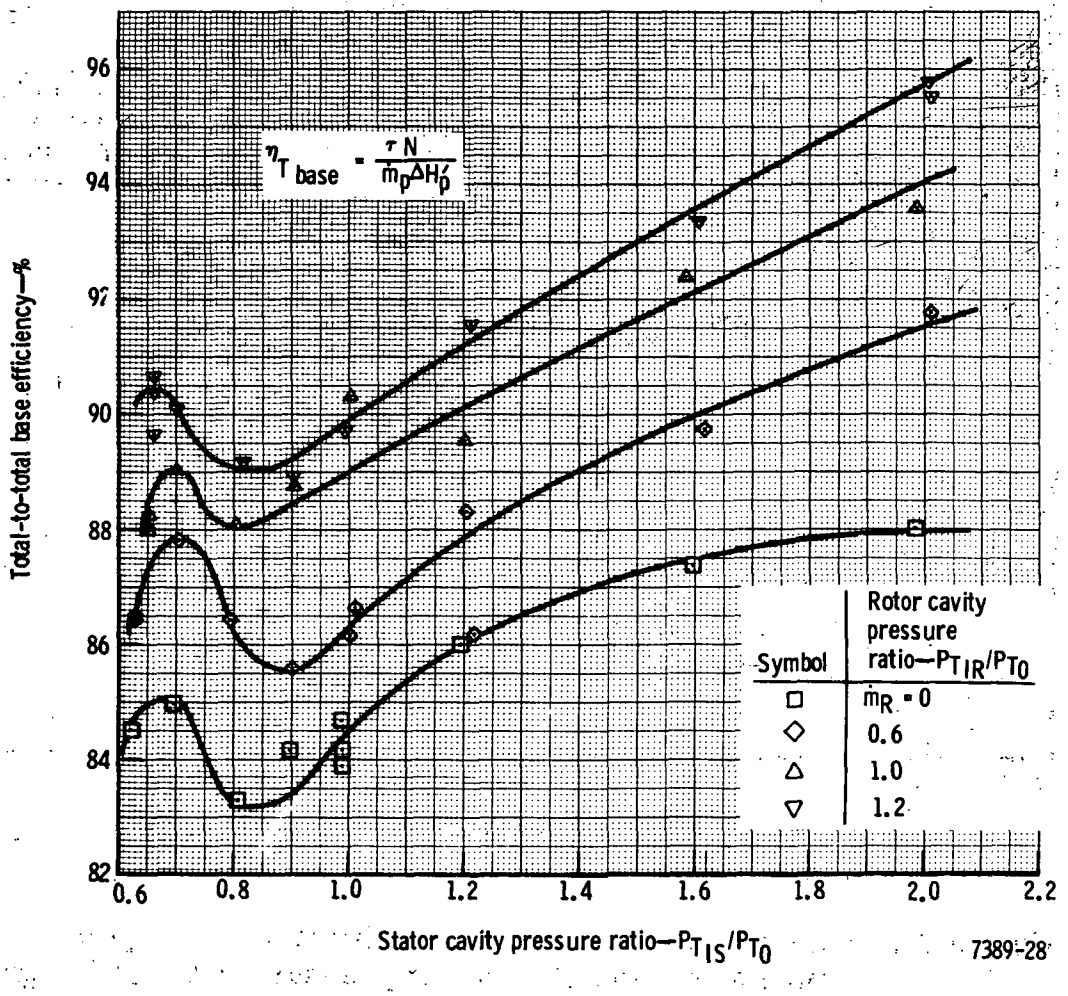

Figure 30. Variation of base efficiency with stator and rotor cavity pressure ratios at design speed and expansion ratio.

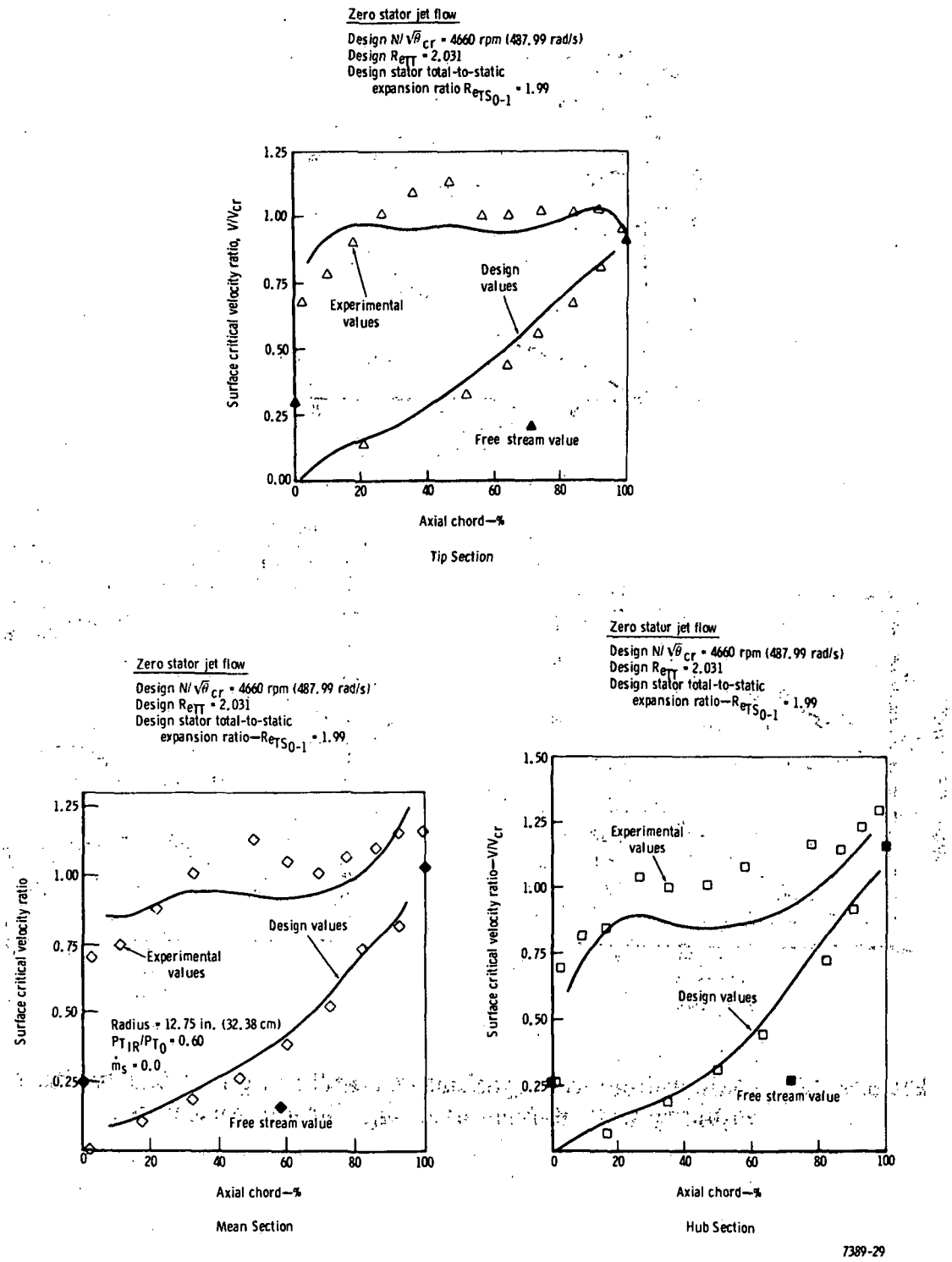

Figure 31. Comparison of experimental and design surface velocity distribution at design jet-off flow conditions.

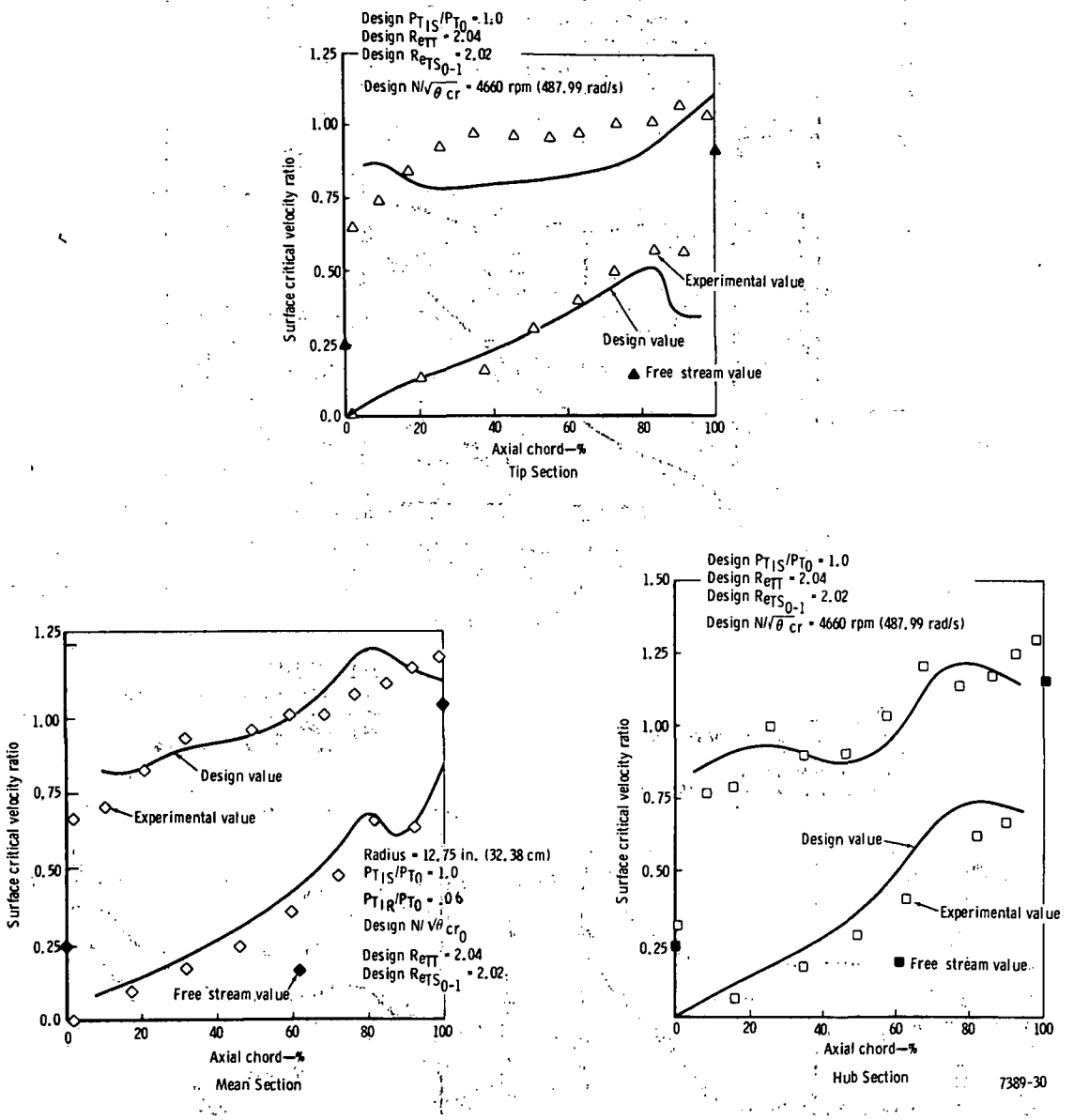

Figure 32. Comparison of experimental and design stator surface velocity distribution at design jet-on conditons.

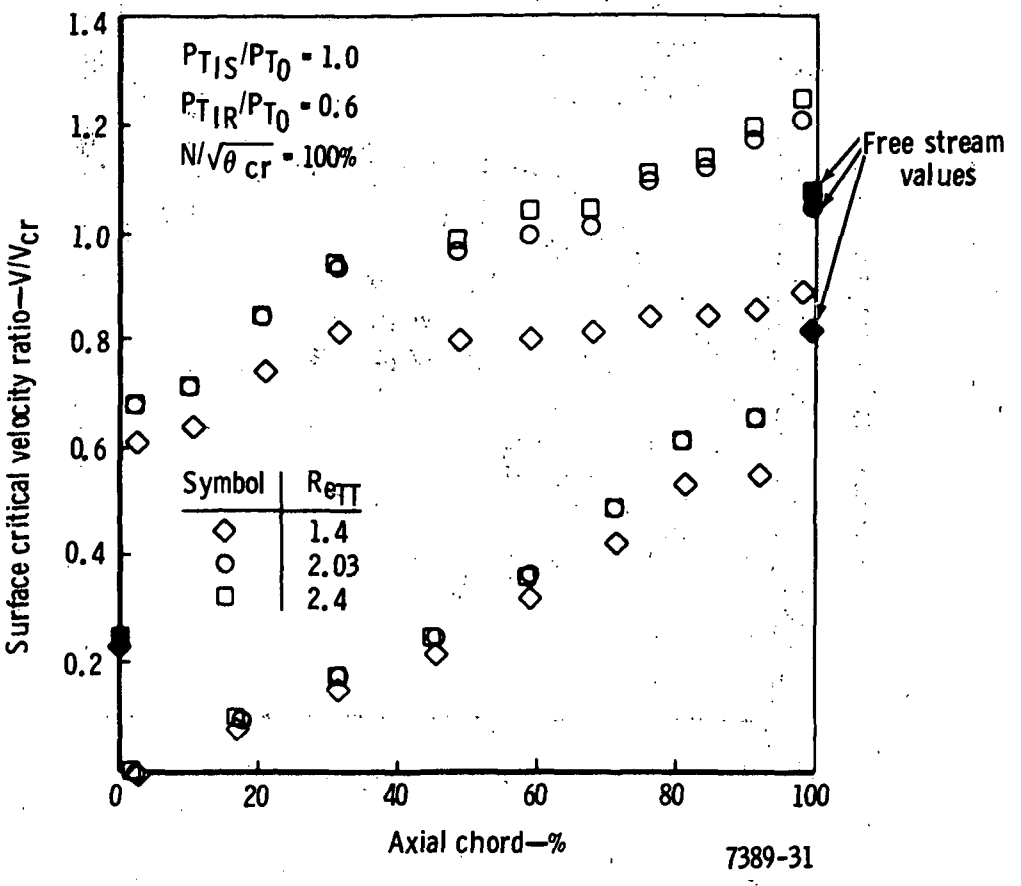

Figure 33. Variation of stator mean section critical velocity ratio distribution with turbine expansion ratio at design speed.

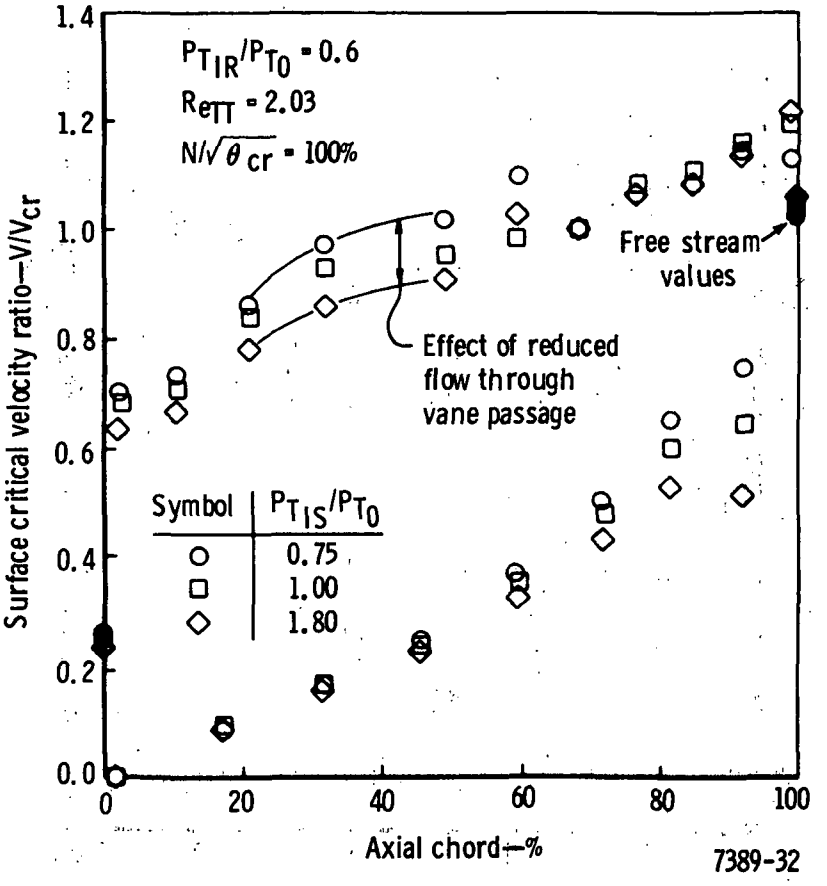

Figure 34. Variation of stator mean section critical velocity ratio distribution with stator cavity pressure ratio at design speed and expansion ratio.

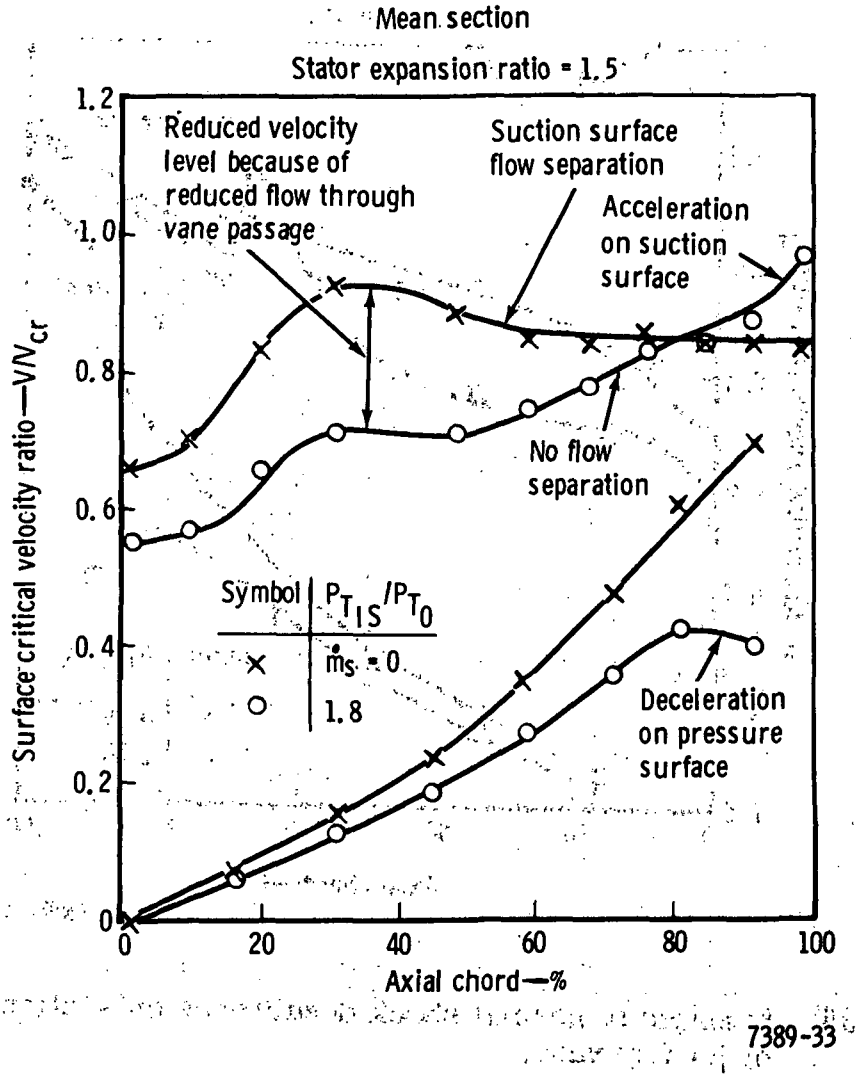

Figure 35. Example of surface flow reattachment by use of jet flap.

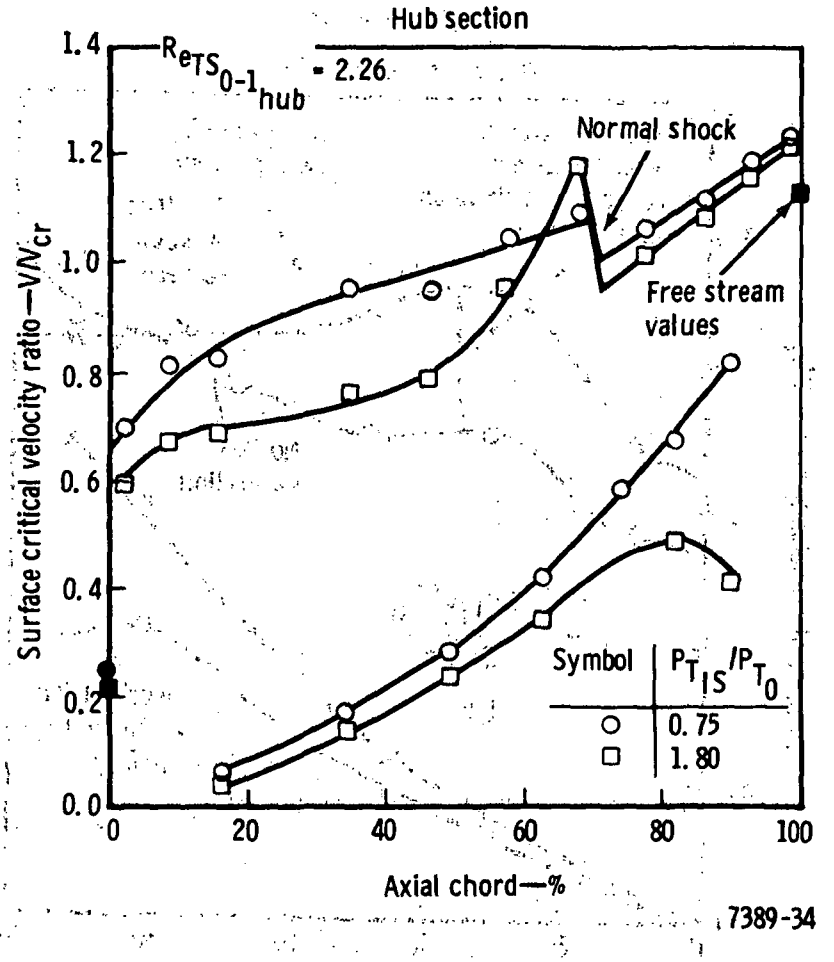

Figure 36. Example of normal shock occurrence on suction surface of jet flap vane.

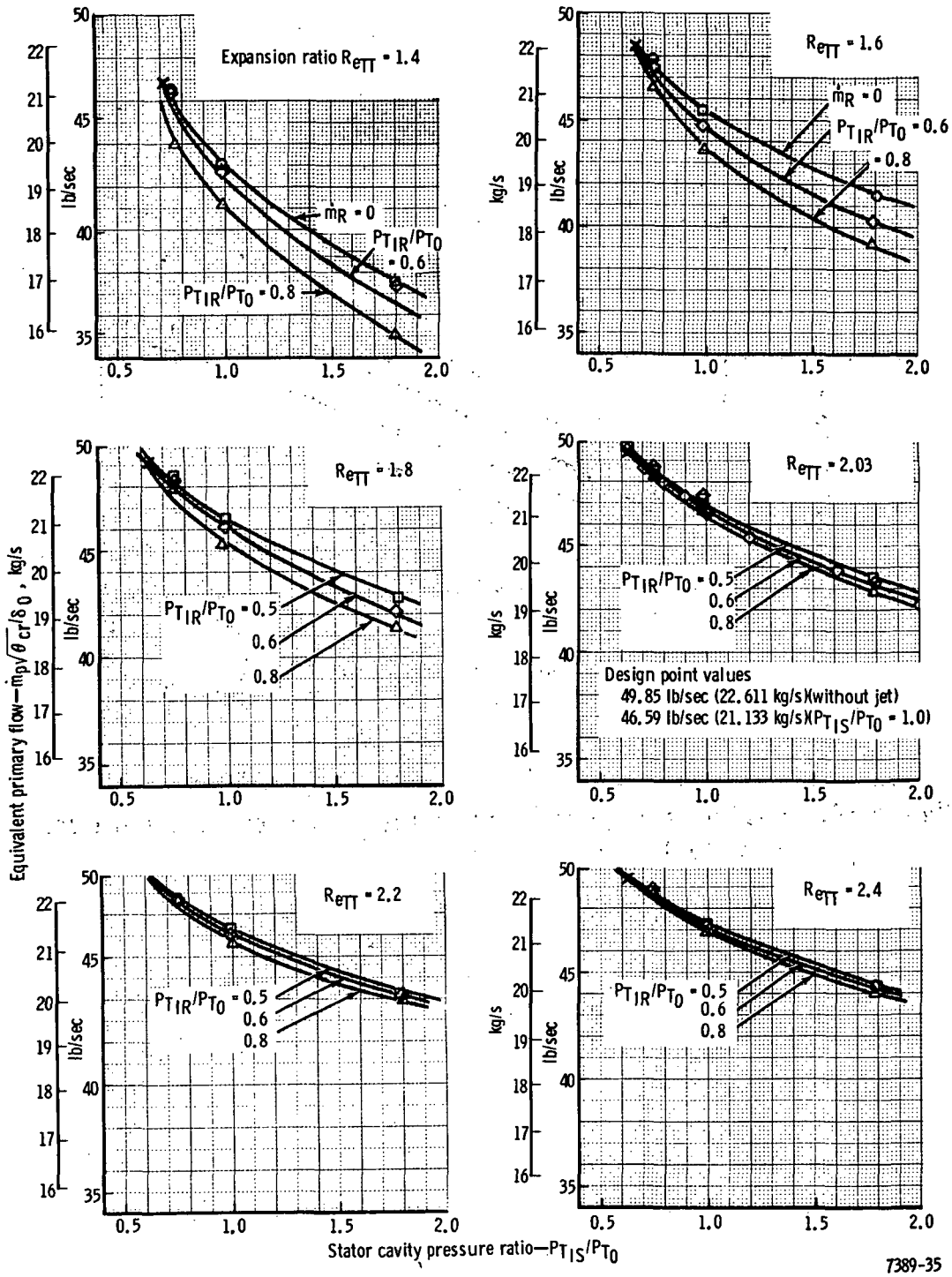

Figure 37. Variation of stator inlet flow with both stator and rotor cavity pressure ratios over a range of turbine expansion ratios with turbine at design speed.

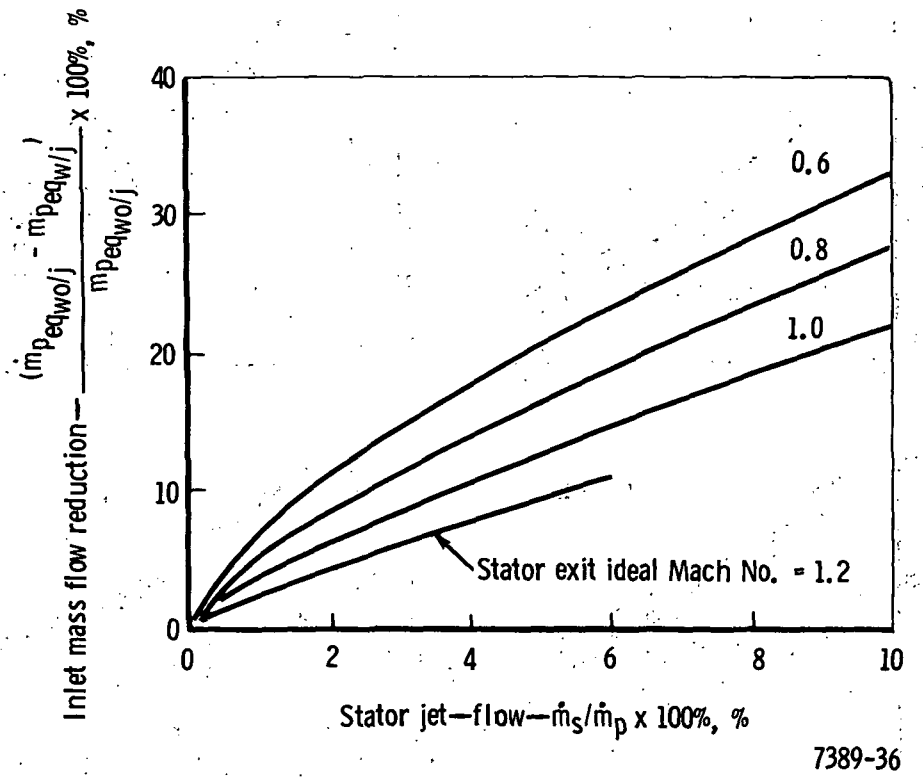

Figure 38. Variation in percent primary flow reduction with percent stator jet flow.

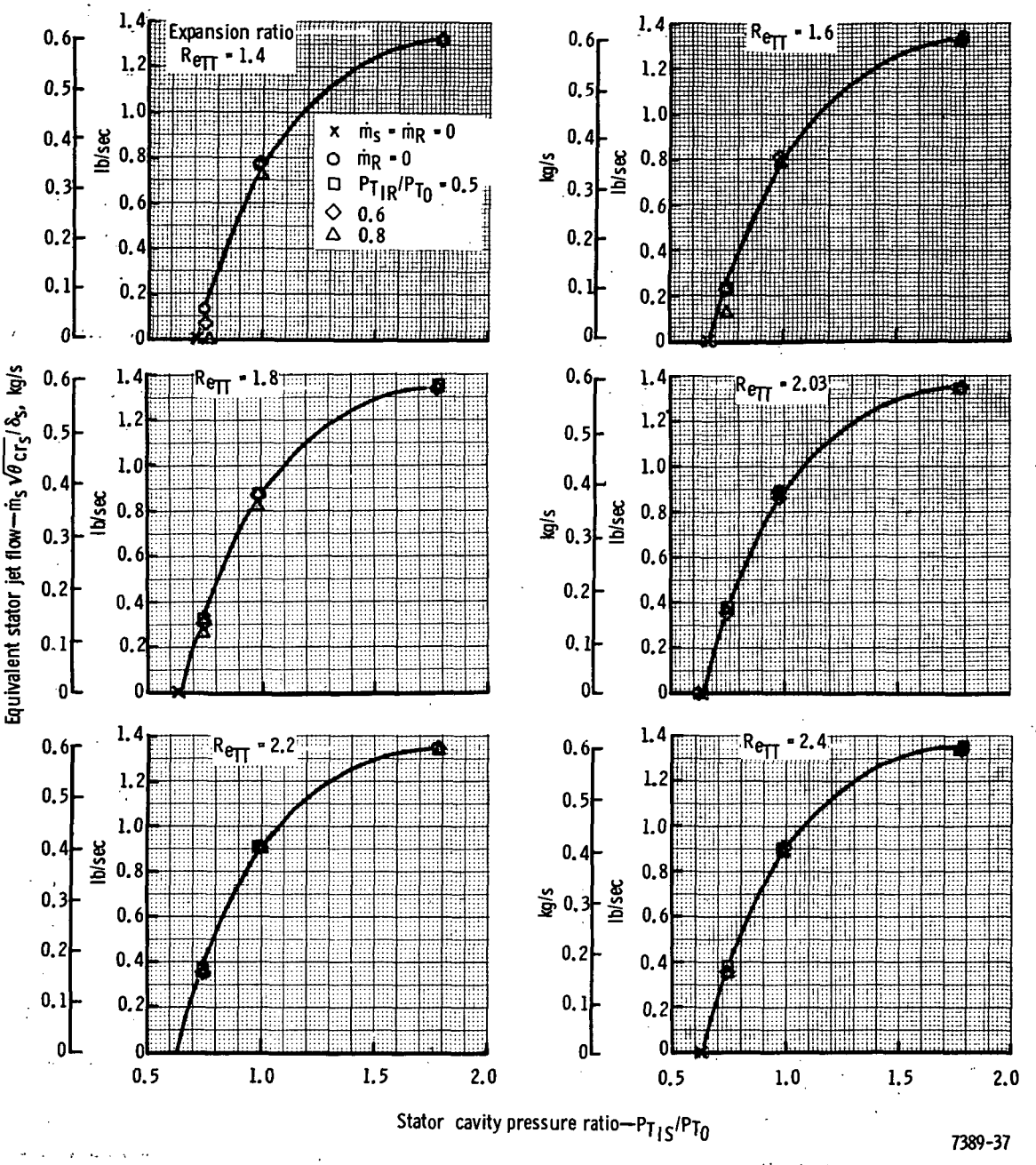

Figure 39. Variation of stator jet flow with both stator and rotor cavity pressure ratios over a range of turbine expansion ratios.

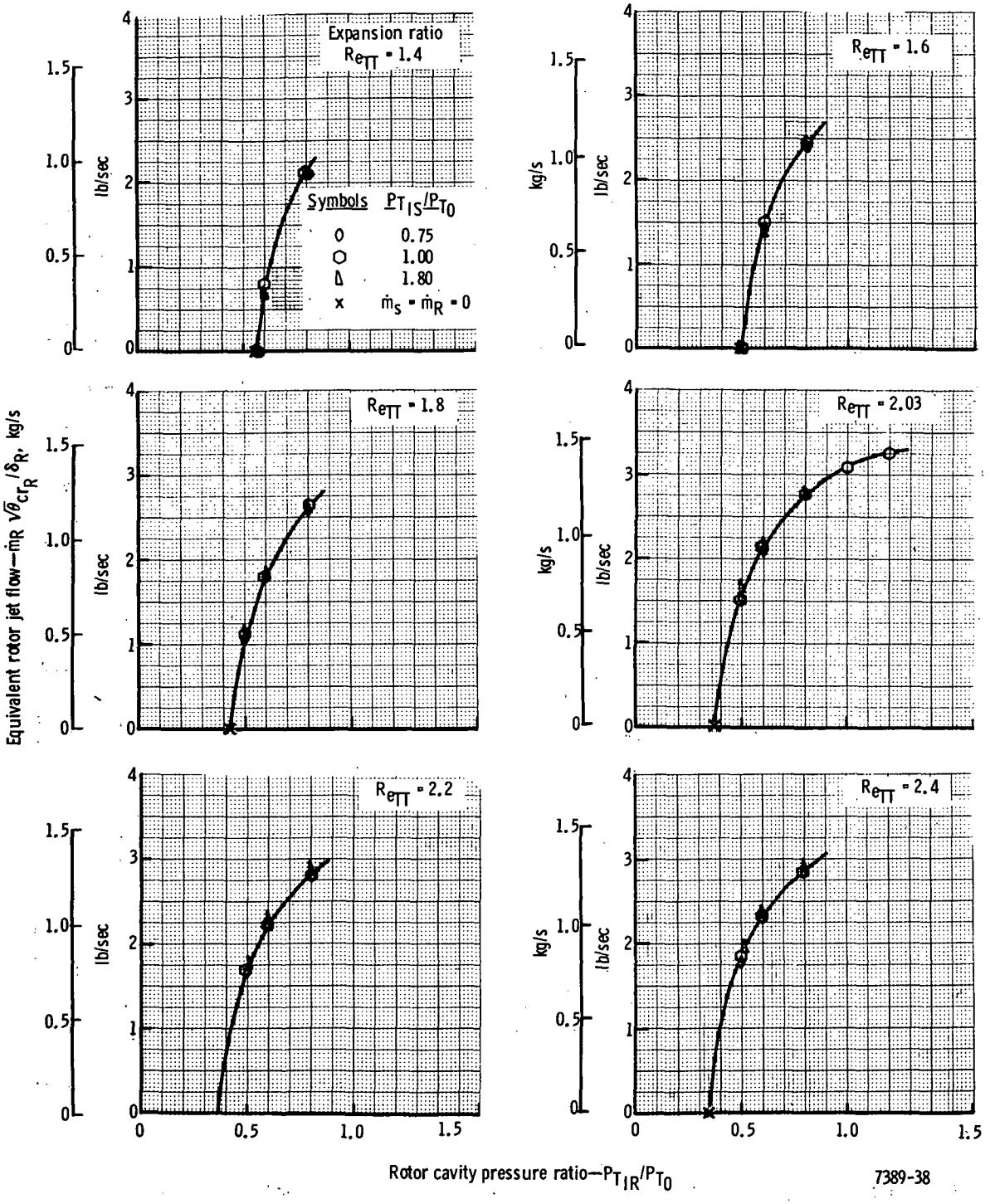

Figure 40. Variation of rotor jet flow with both stator and rotor cavity pressure ratios over a range of turbine expansion ratios.

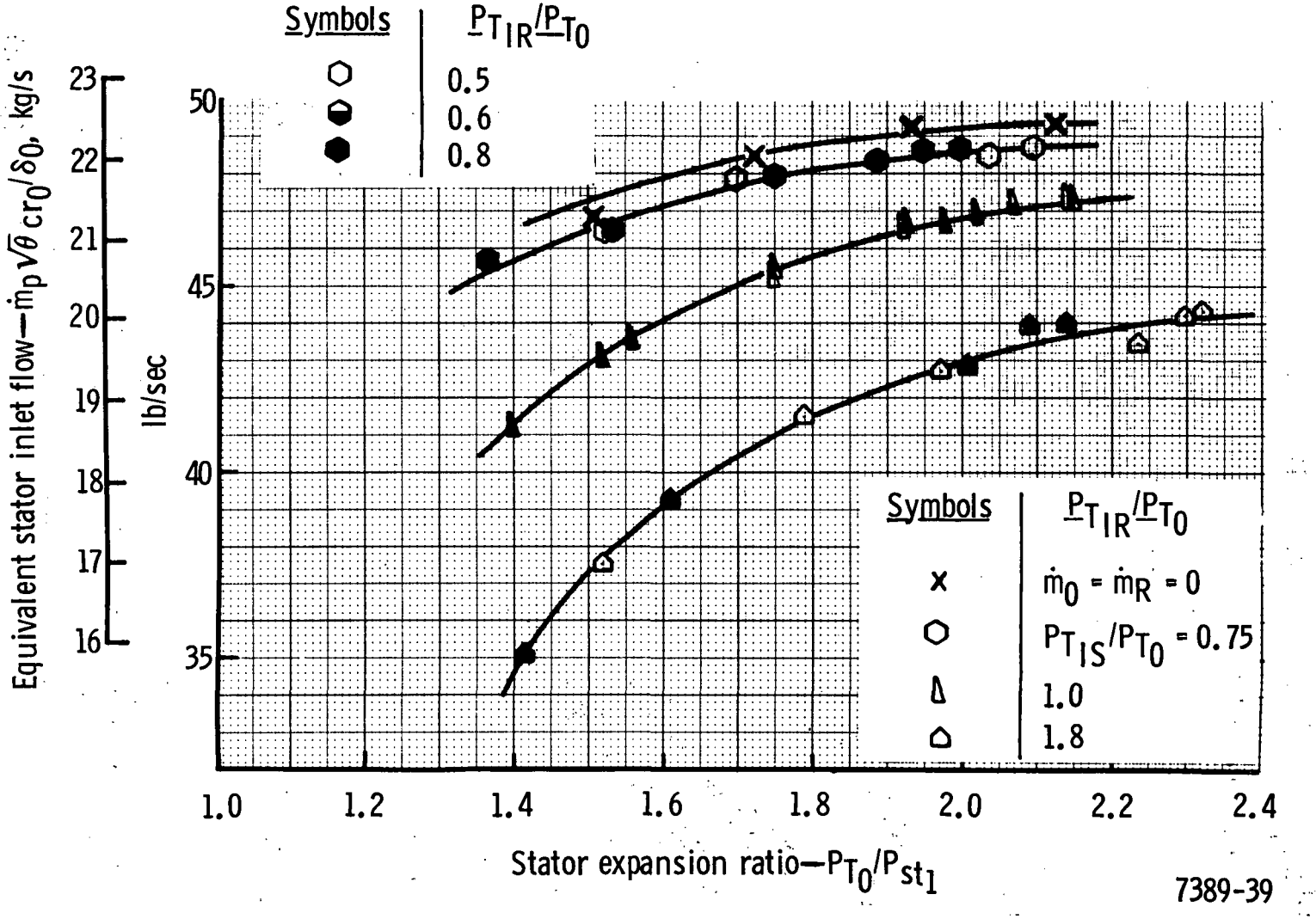

Figure 41. Effect of rotor and stator cavity pressure ratio on the variation of stator inlet flow with average stator expansion ratio.

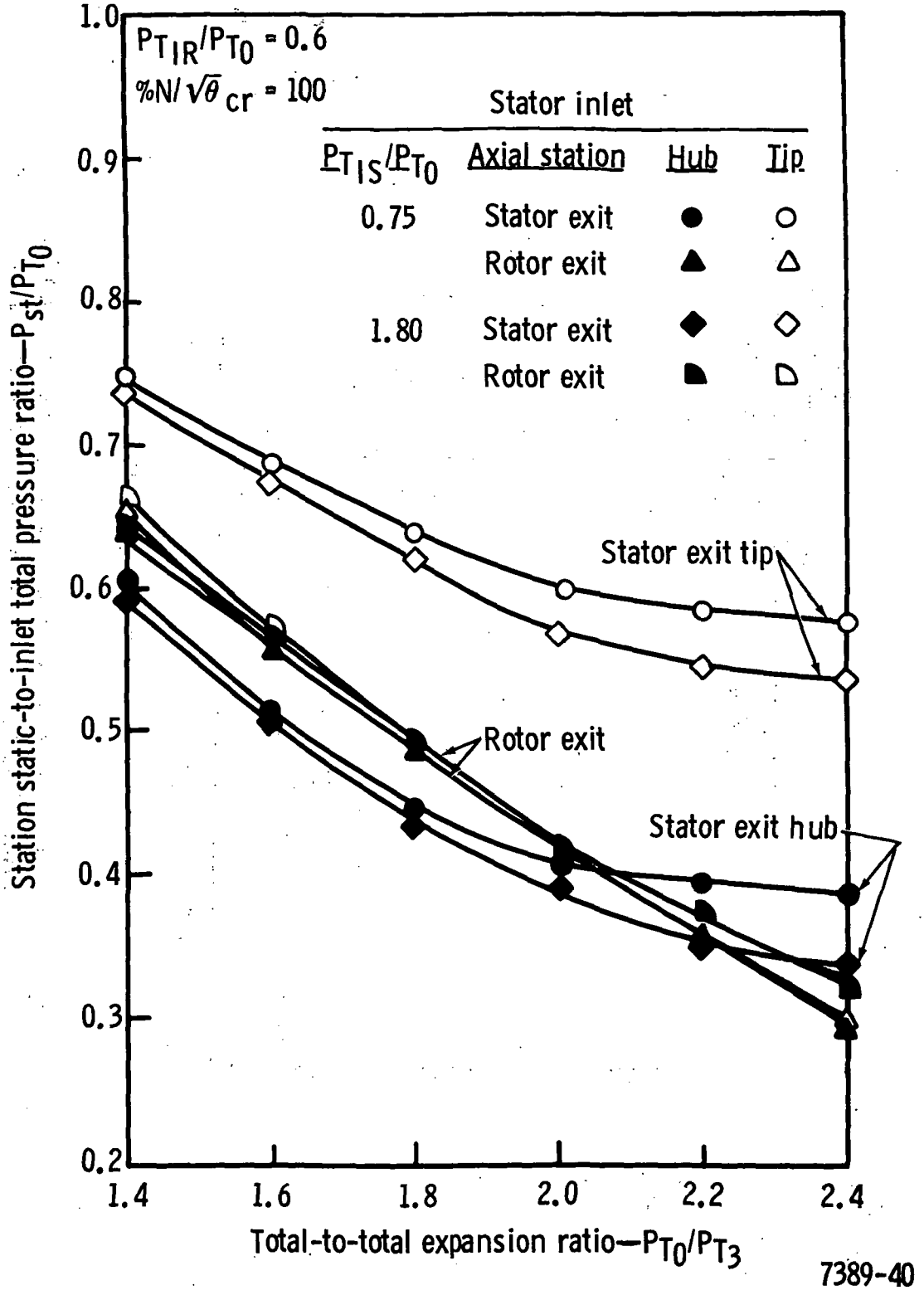

Figure 42. Variation of static pressure through turbine with jet cavity and turbine expansion ratio.

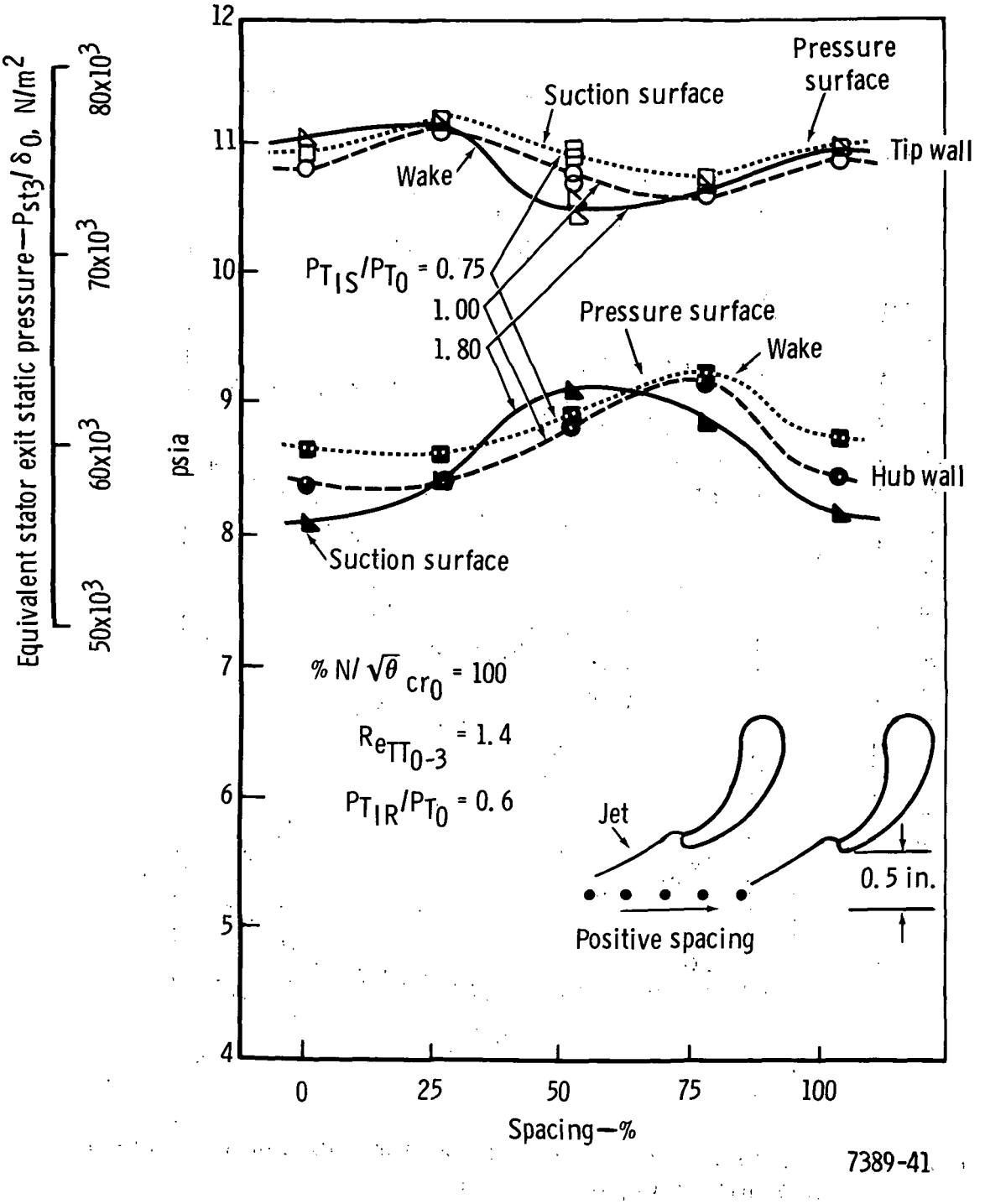

Figure 43. Circumferential variation of stator exit static pressure—1.4 turbine expansion ratio.

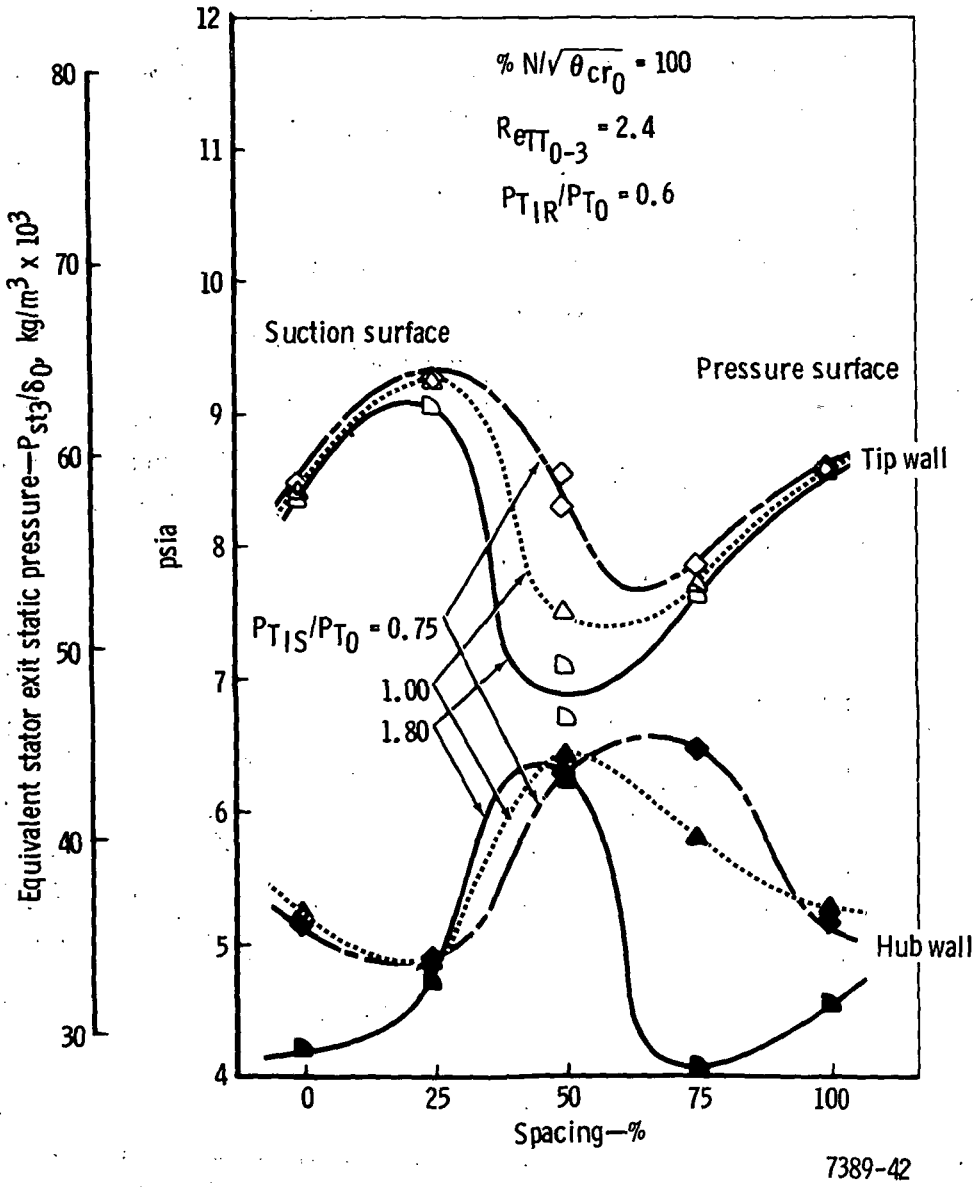

Figure 44. Circumferential variation of stator exit static pressure—2.4 turbine expansion ratio.

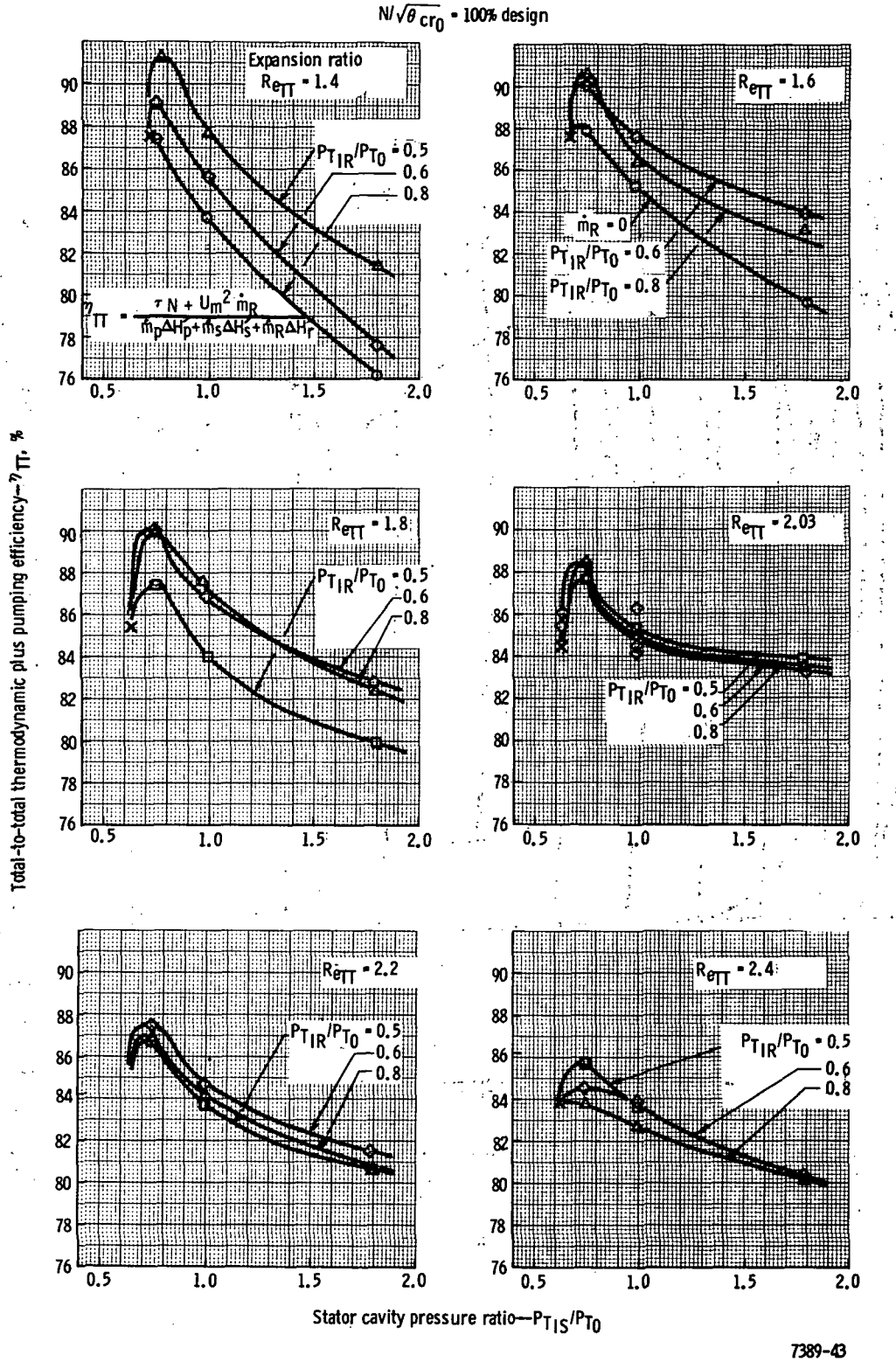

Figure 45. Variation of turbine efficiency with both stator and rotor cavity pressure over a range of turbine expansion ratios.

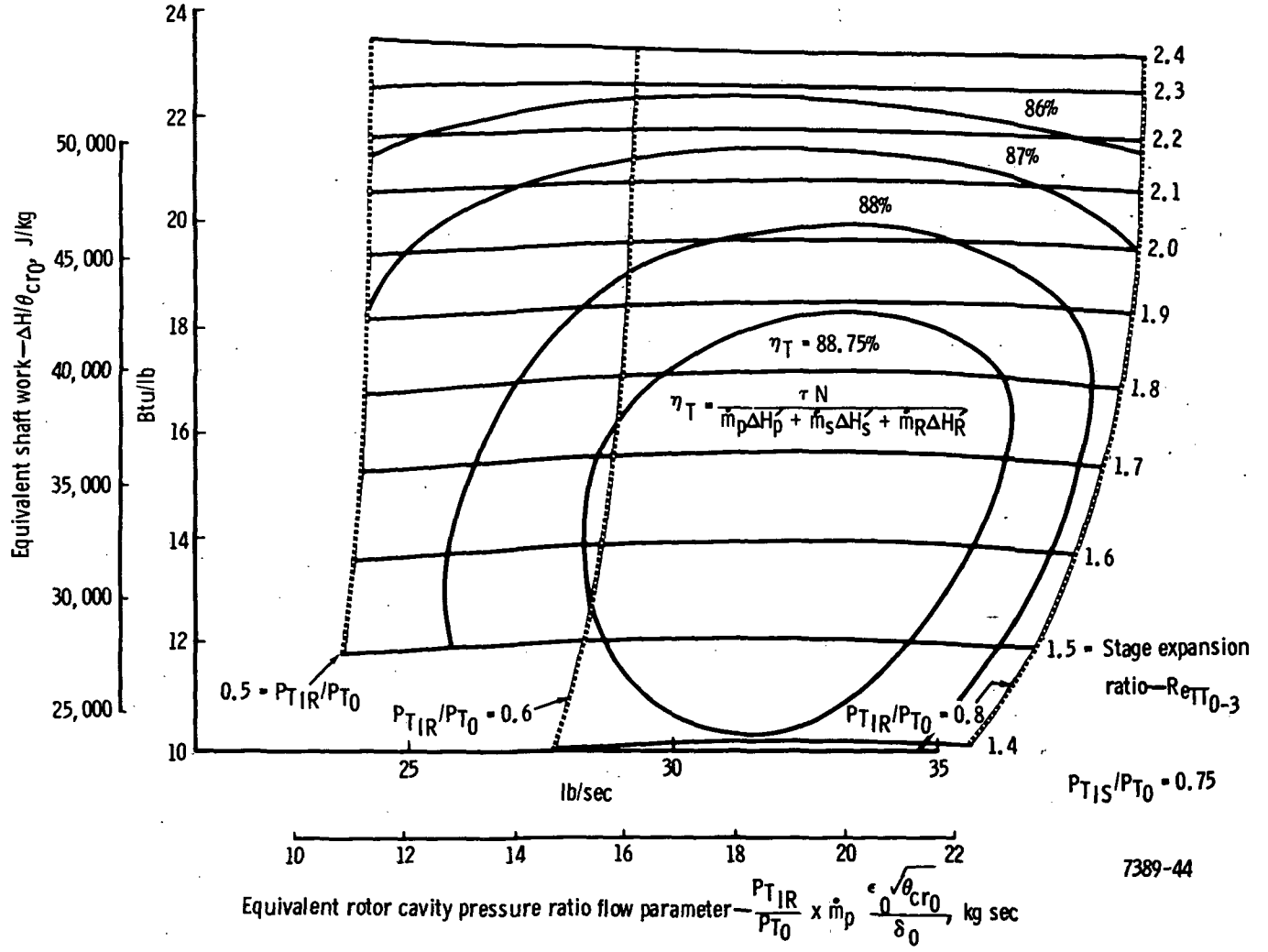

Figure 46. Overall performance variation at design equivalent speed with rotor cavity-to-inlet pressure ratio and stage expansion ratio for a 0.75 stator cavity pressure ratio.

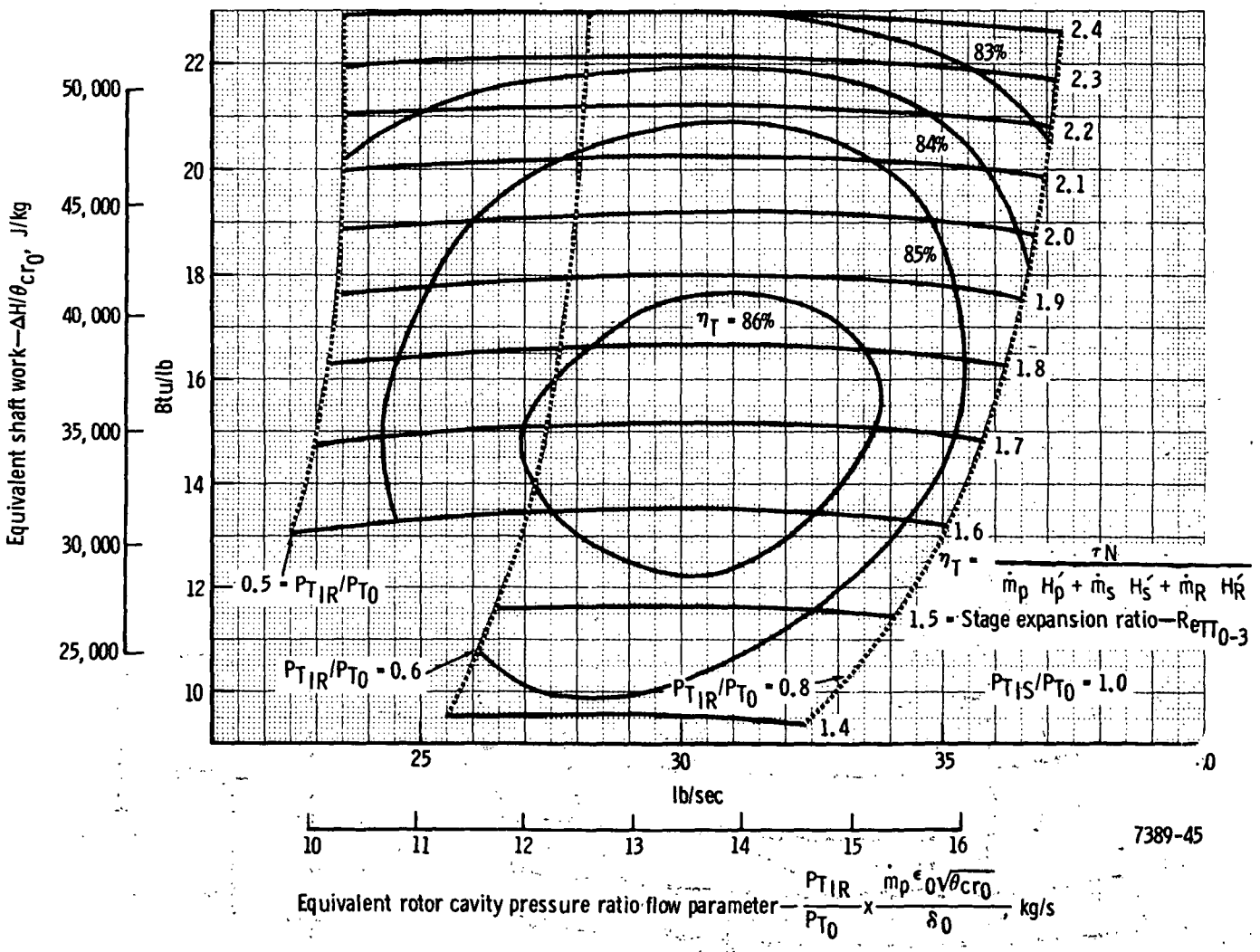

Figure 47. Overall performance variation at design equivalent speed with rotor cavity-to-inlet pressure ratio and stage expansion ratio for 1.0 stator cavity pressure ratio.

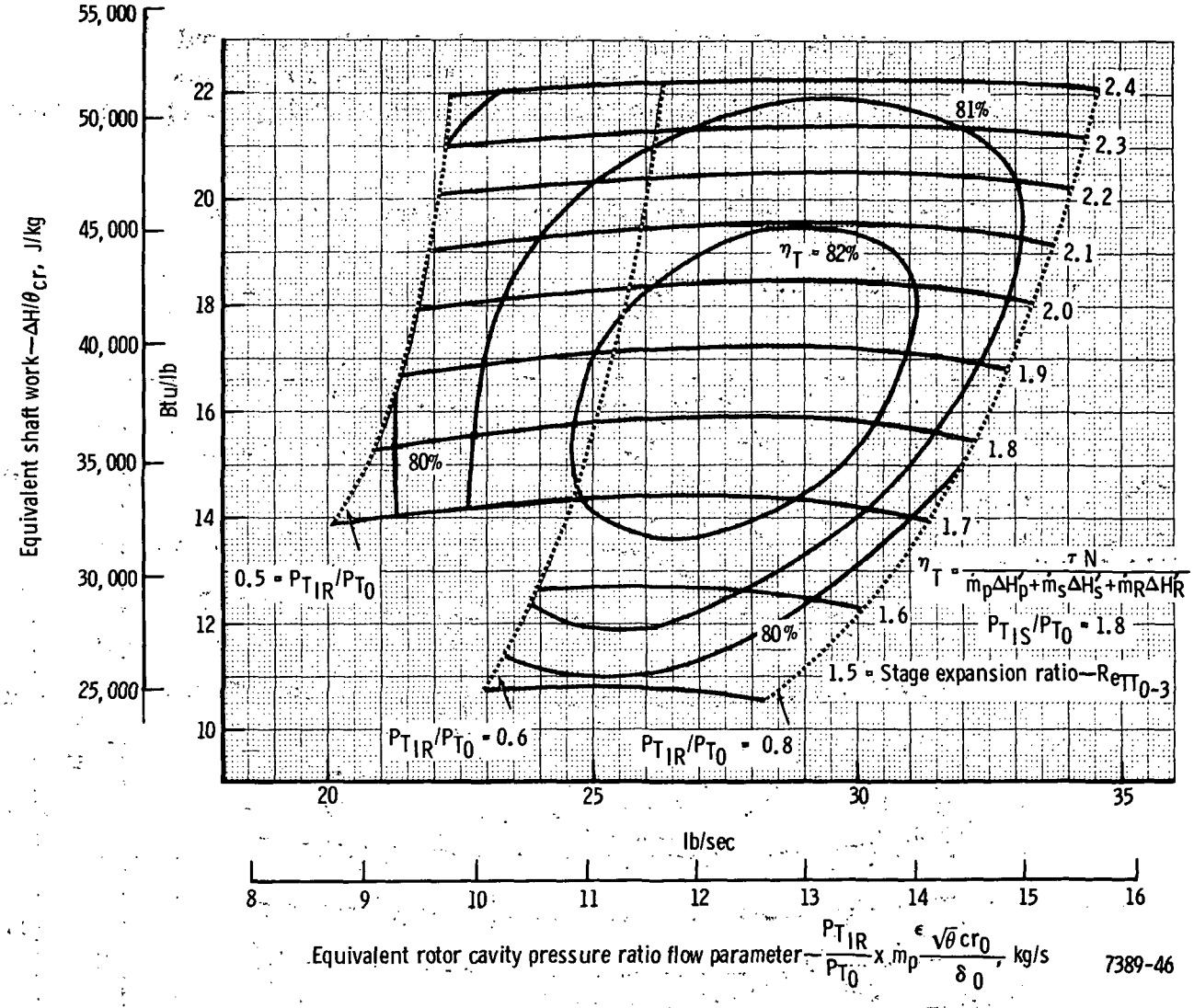

Figure 48. Overall performance variation at design equivalent speed with rotor cavity-to-inlet pressure ratio and stage expansion ratio for a 1.8 stator cavity pressure ratio.

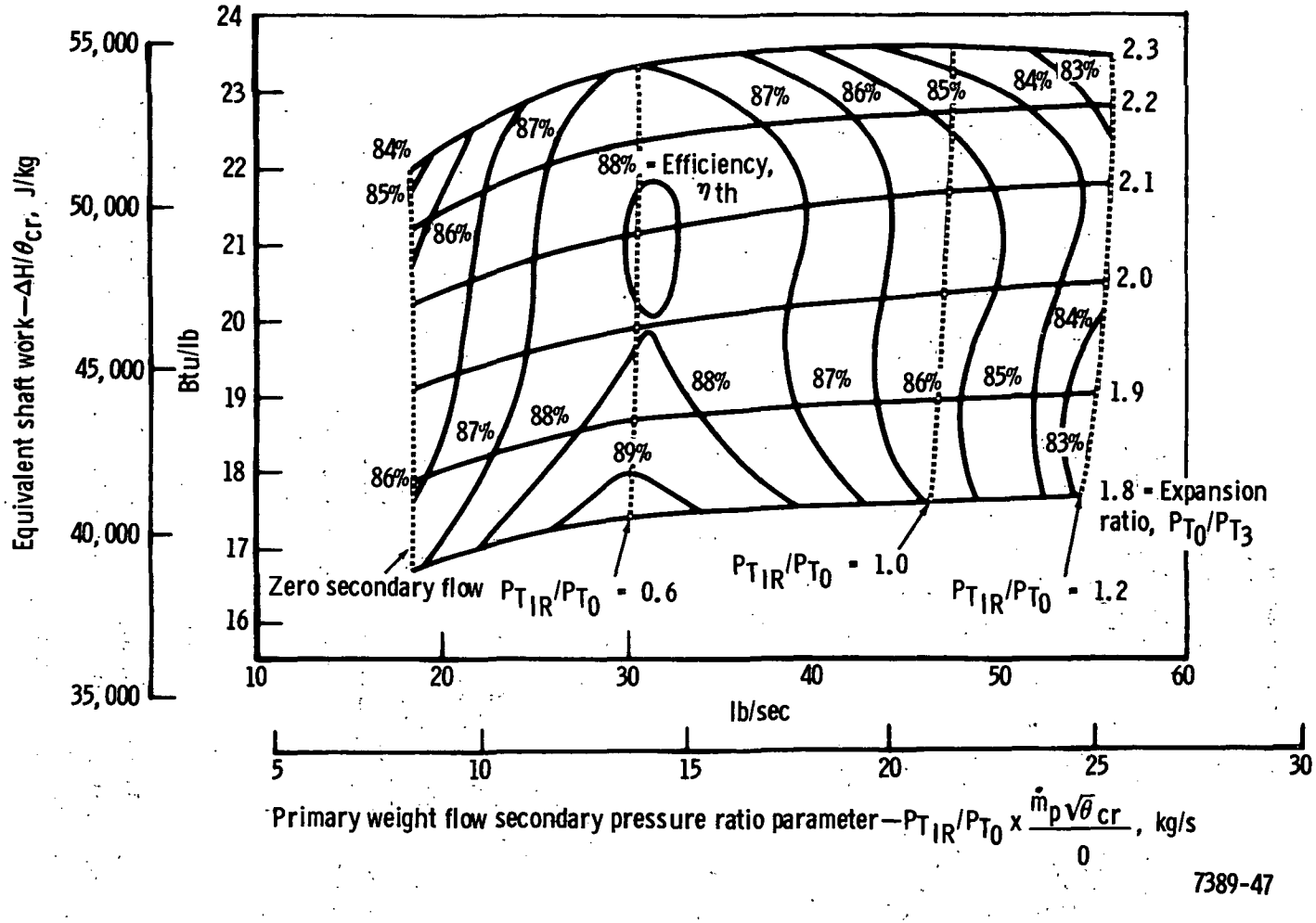

Figure 49. Overall performance variation of modified jet-flap rotor blade turbine at design equivalent speed with secondary-to-primary pressure ratio and turbine expansion ratio (performance based on thermodynamic efficiency).

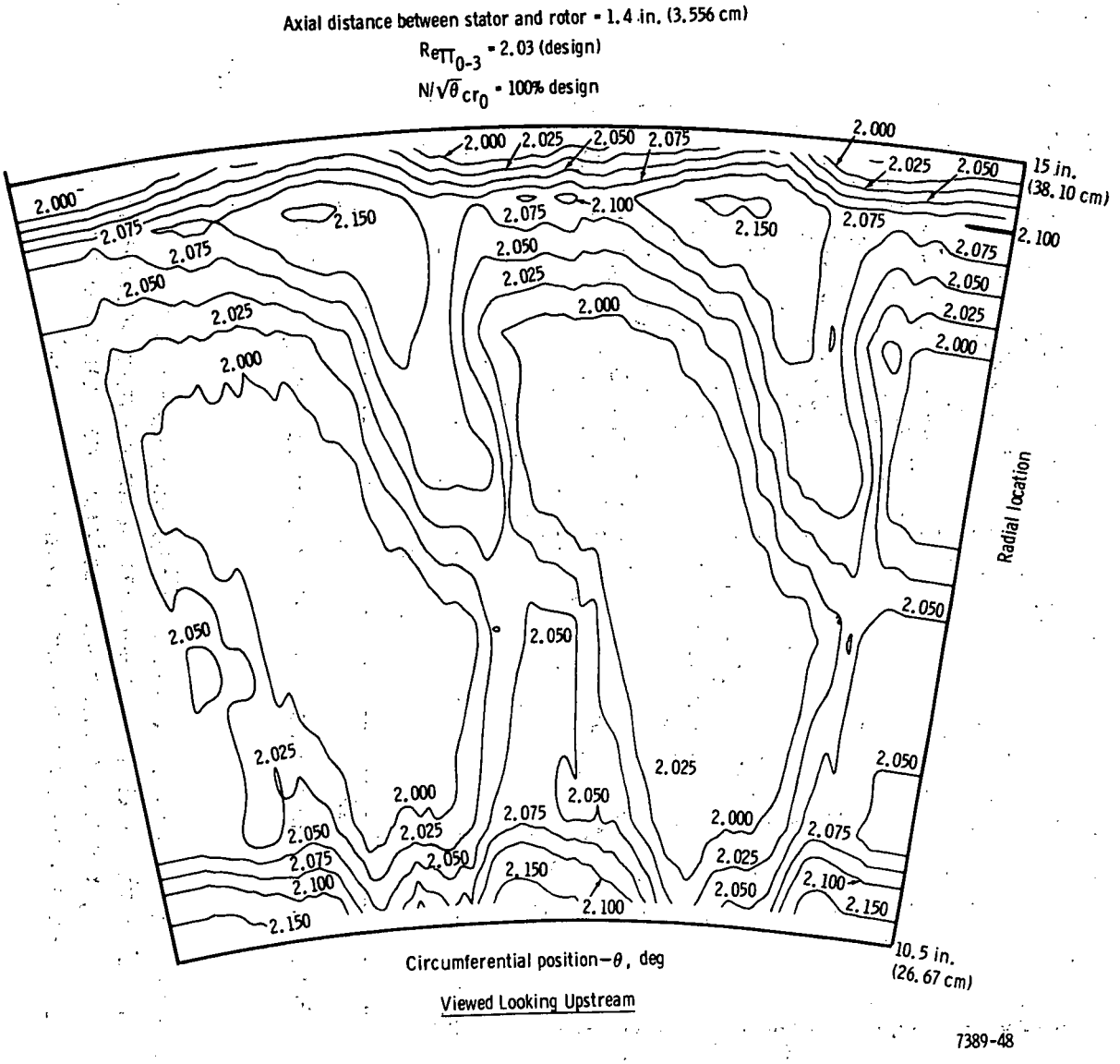

Figure 50. Phase II local stage total-to-total expansion ratio contour map for the stator jet off and a rotor cavity pressure ratio of 0.6.

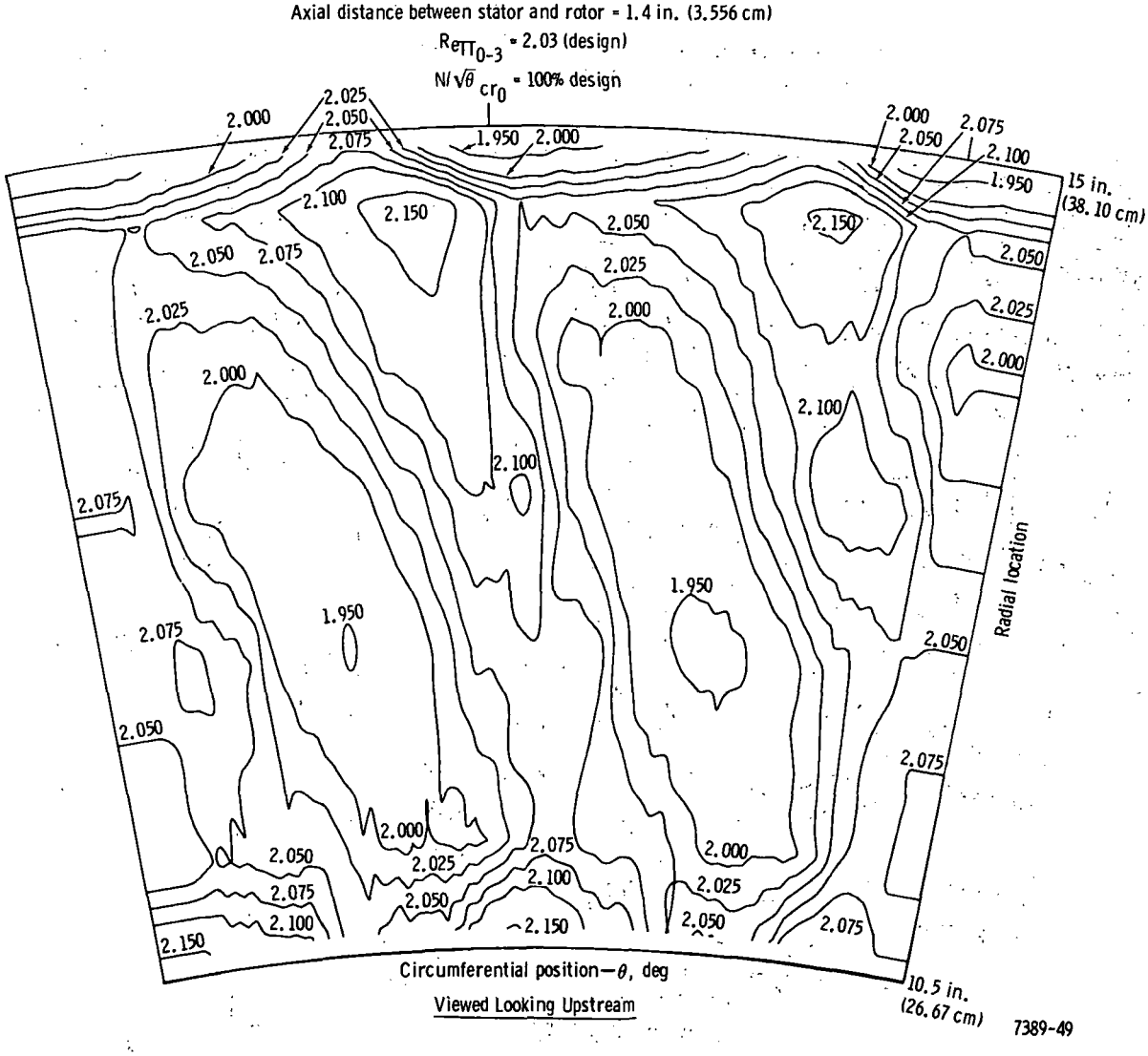

Figure 51. Phase II local stage total-to-total expansion ratio contour map for the jet-on condition (stator $P_{T_{IS}}/P_{T_0}$ = 1.0, rotor $P_{T_{IR}}/P_{T_0}$ = 0.6).

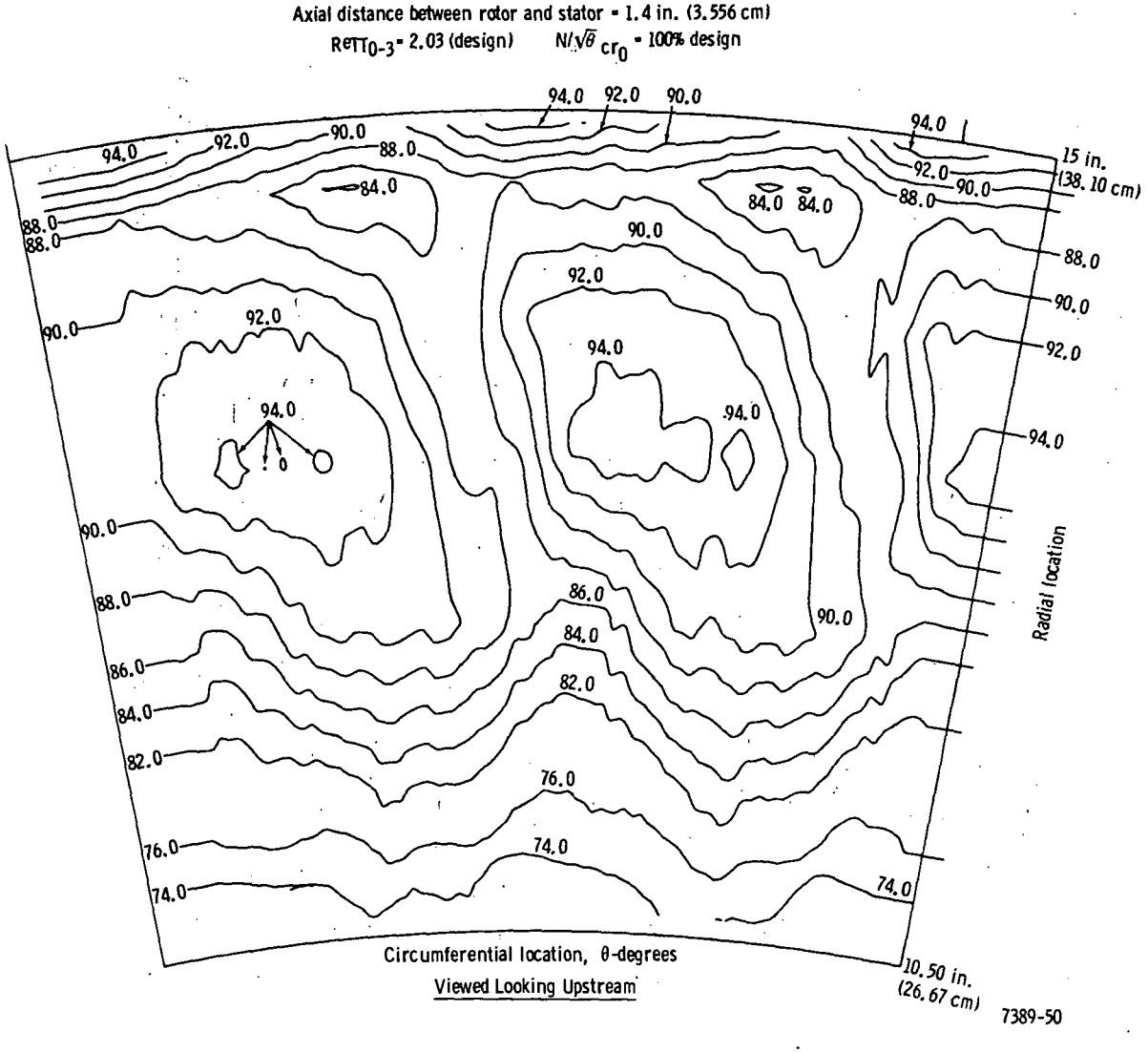

Figure 52. Phase II efficiency contours at rotor exit for stator jet-off condition ($\dot{m}_s = 0$ and $P_{T_{IR}}/P_{T_0} = 0.6$).

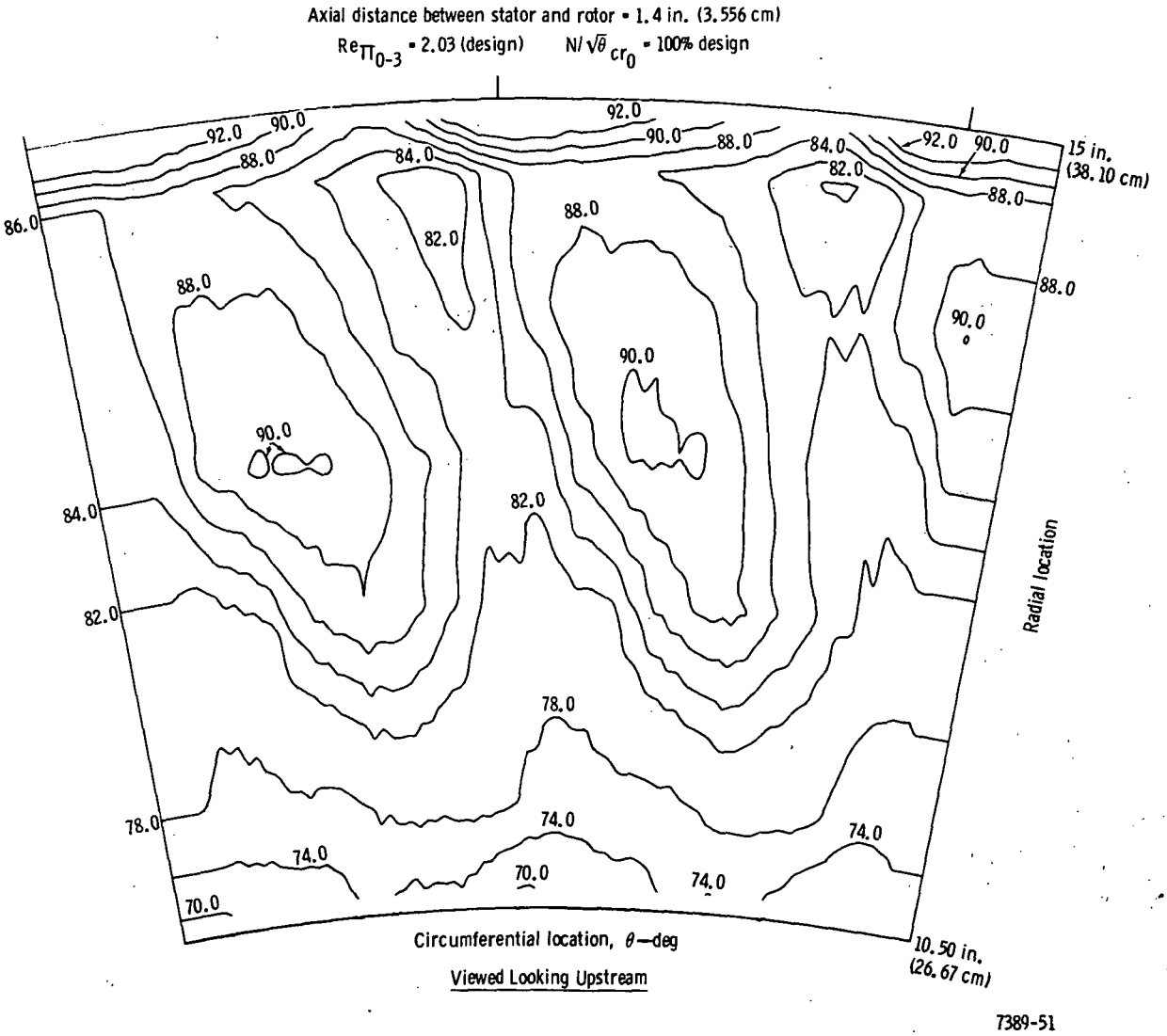

Figure 53. Phase II efficiency contours at rotor exit for jet-on condition ($P_{T_{IS}}/P_{T_0}$ = 1.0 and $P_{T_{IR}}/P_{T_0}$ = 0.6).

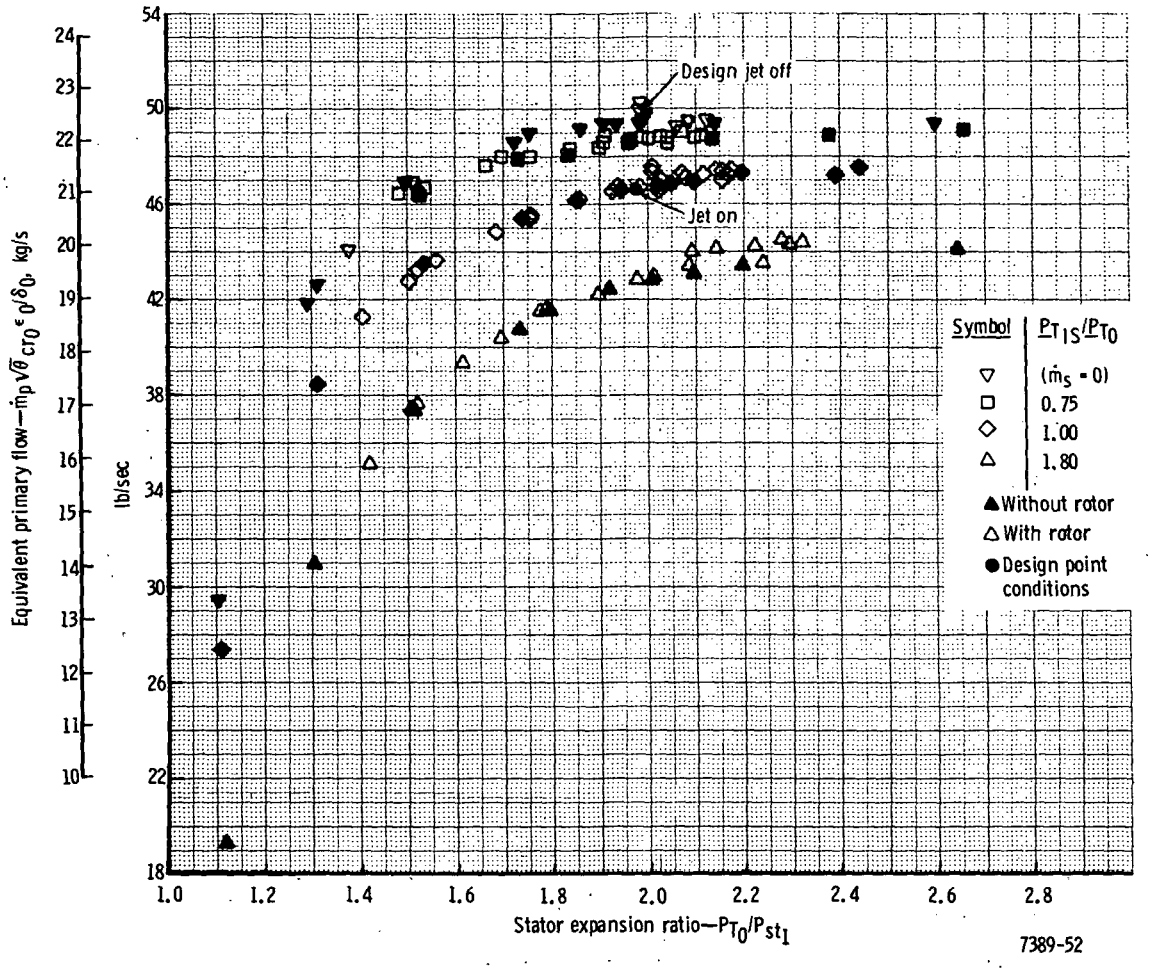

Figure 54. Effect of rotor presence on equivalent primary flow rate for various stator and rotor cavity pressure ratios.

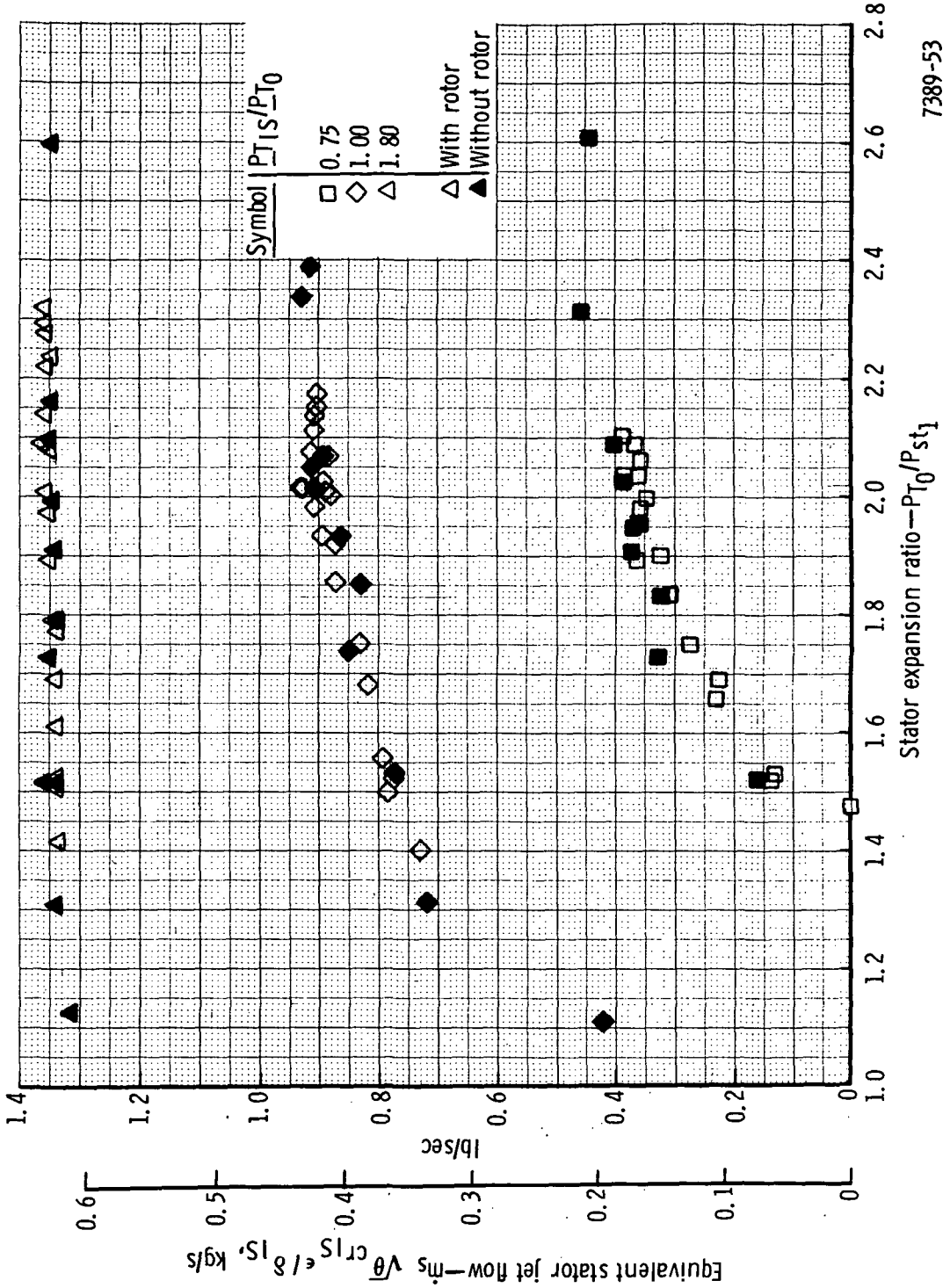

Figure 55. Equivalent stator flow rate for Phase II and III for various stator and rotor cavity pressure ratios.

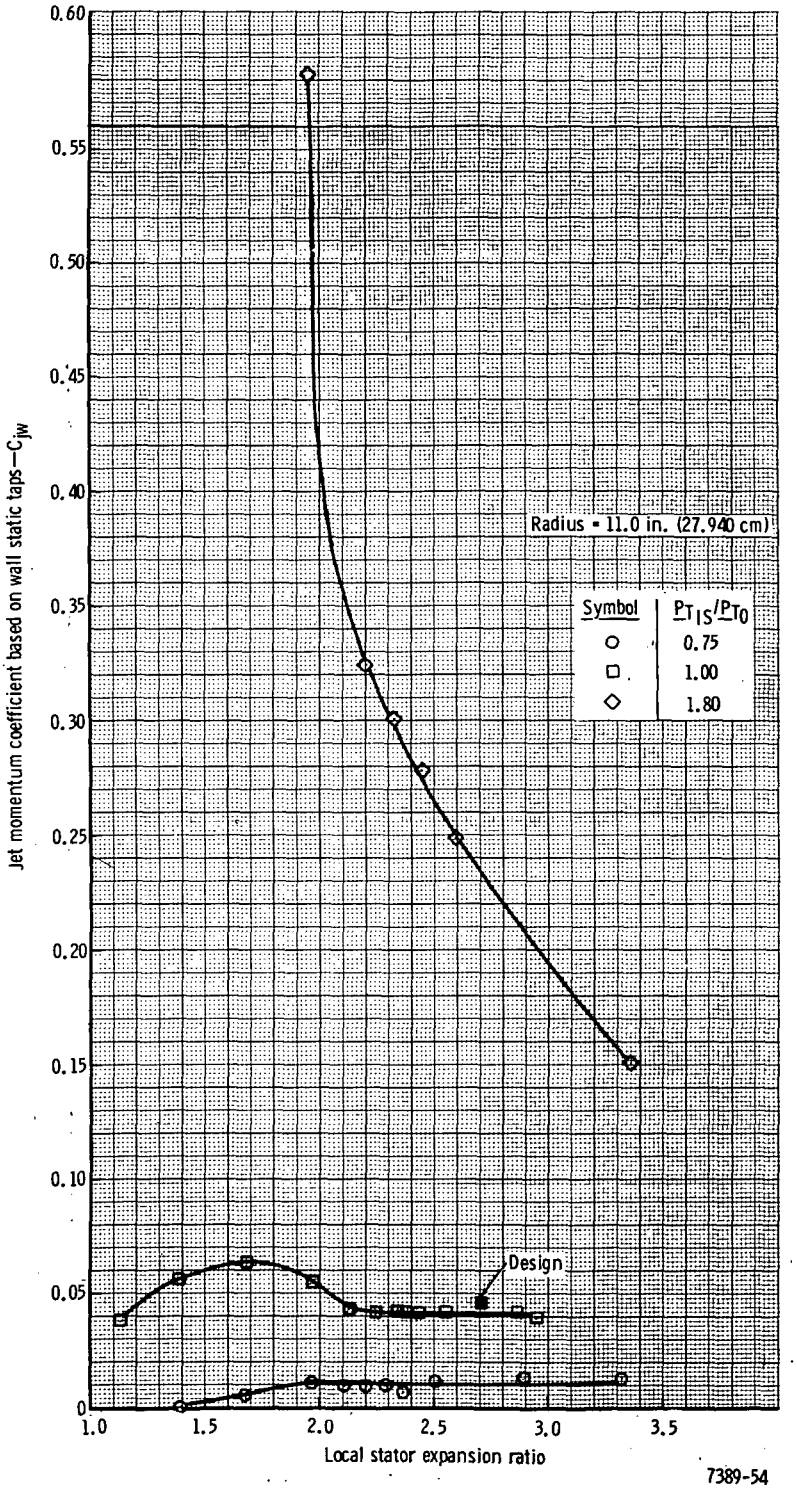

Figure 56. Jet momentum coefficient variation with stator expansion ratio at near-hub section.

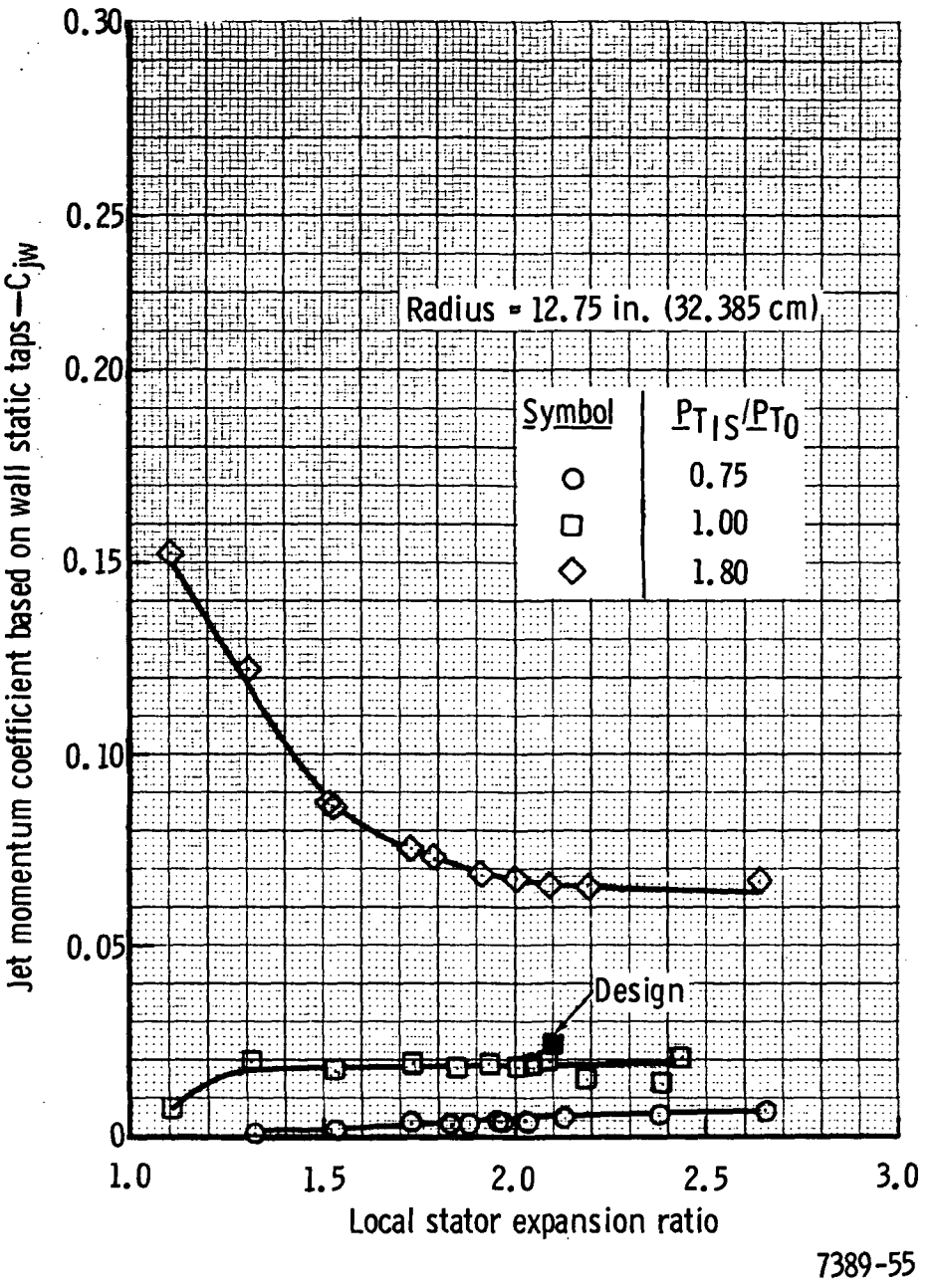

Figure 57. Jet momentum coefficient variation with stator expansion ratio at mean section.

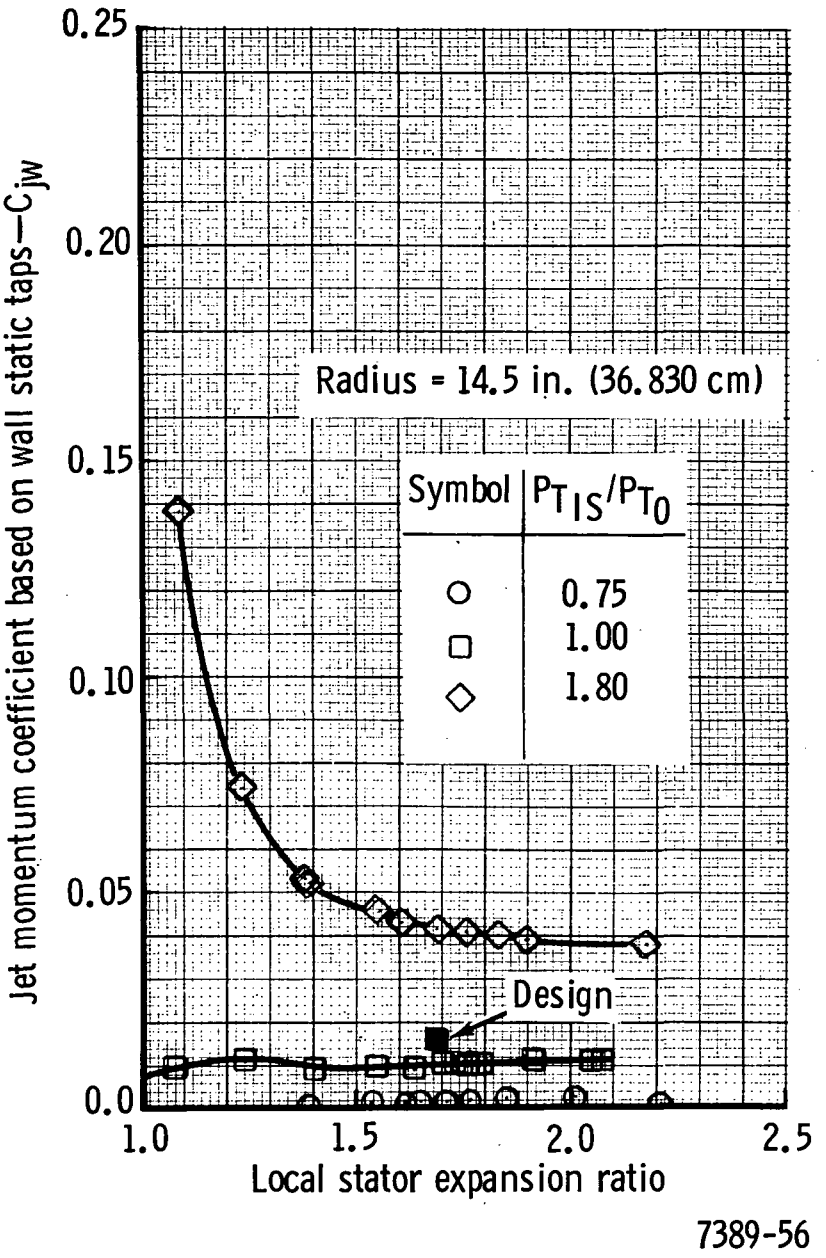

Figure 58. Jet momentum coefficient variation with stator expansion ratio at near-tip section.

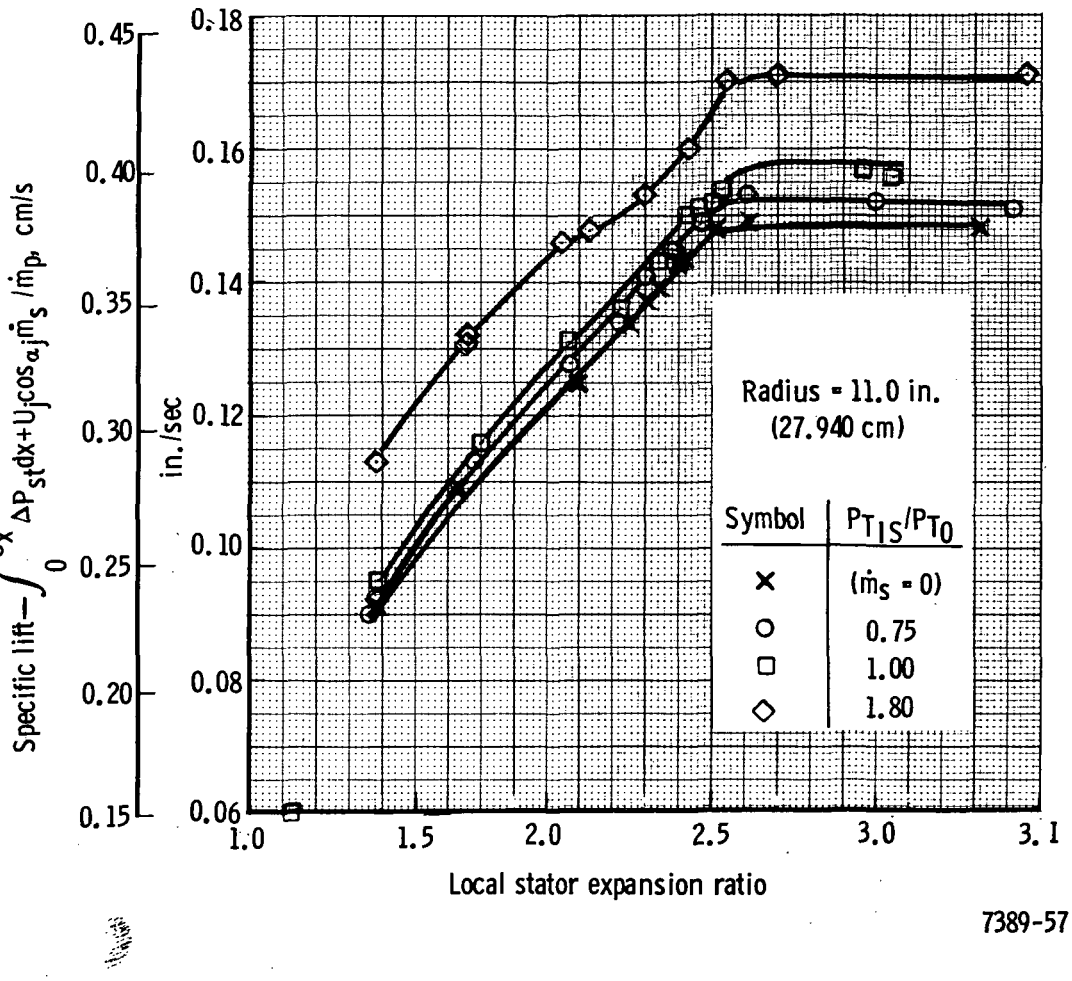

Figure 59. Specific lift at hub section.

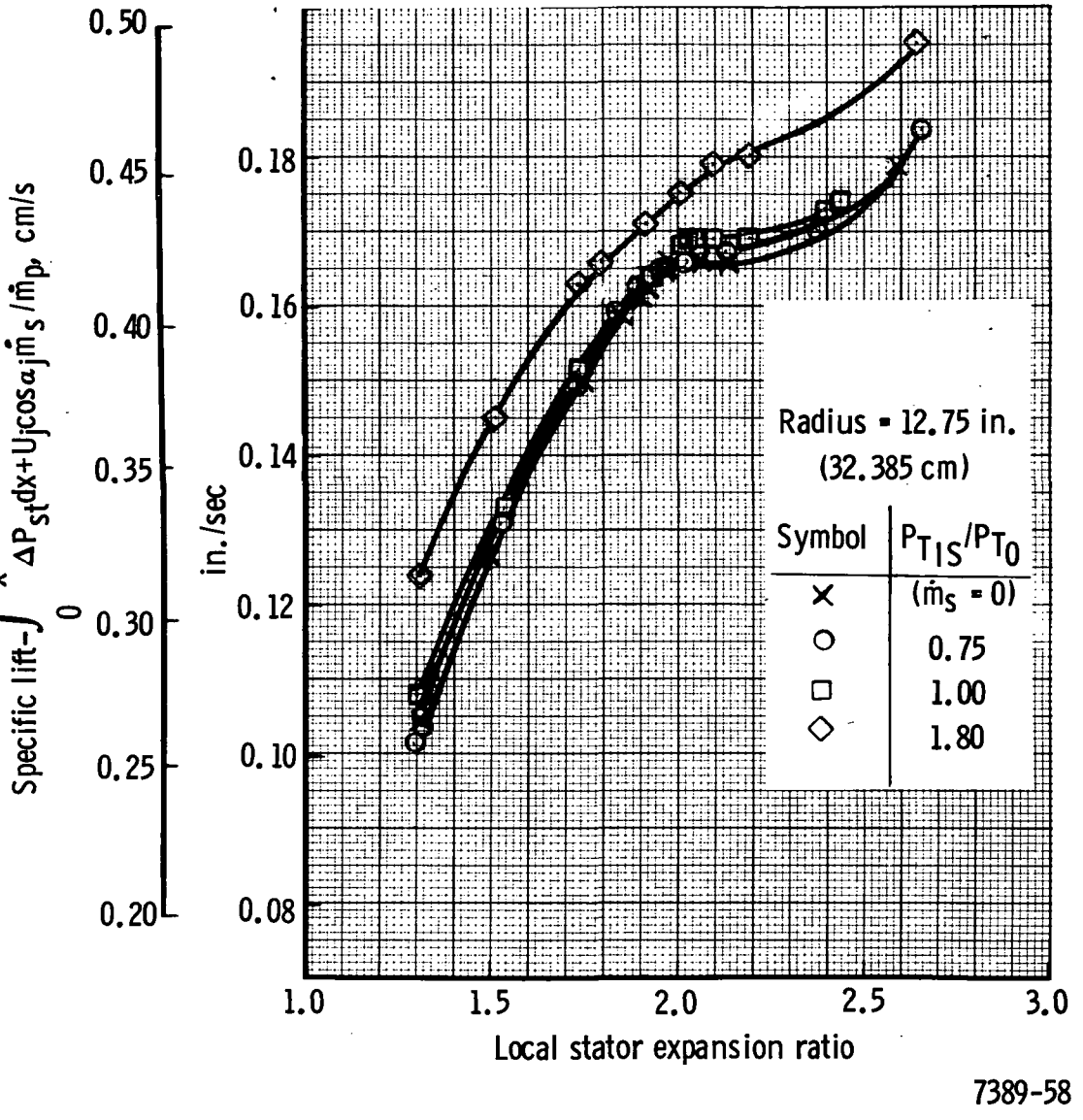

Figure 60. Specific lift at mean section.

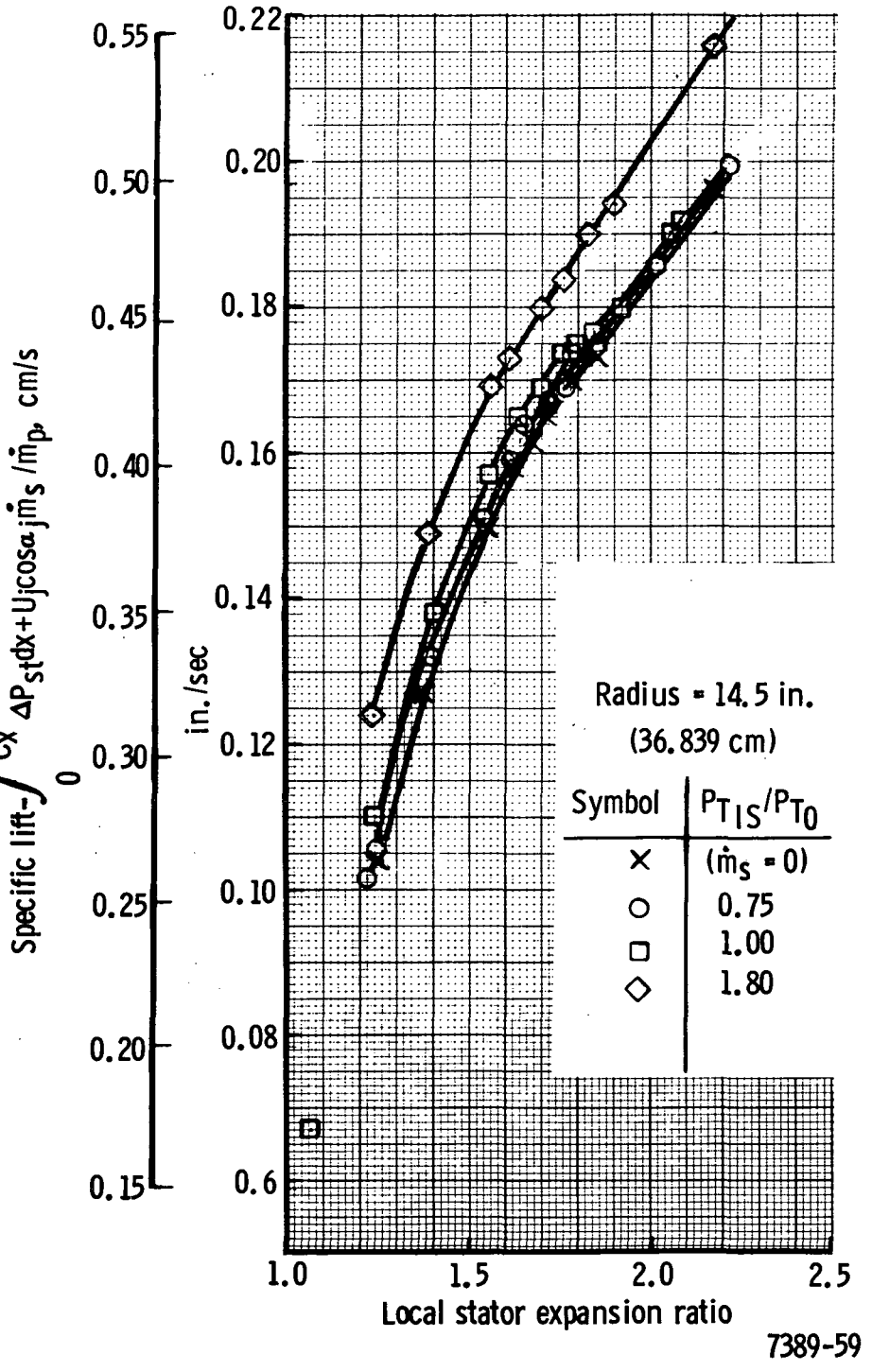

Figure 61. Specific lift at tip section.

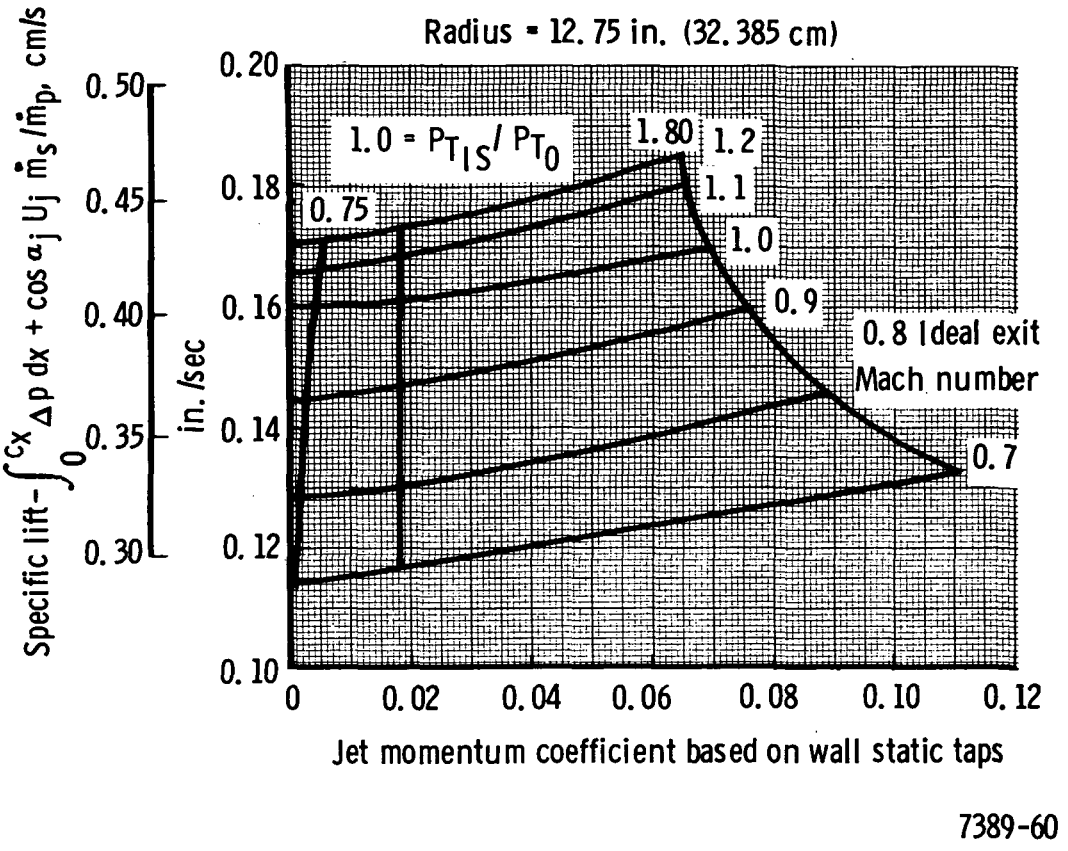

Figure 62. Mean section specific lift variation with jet momentum coefficient.

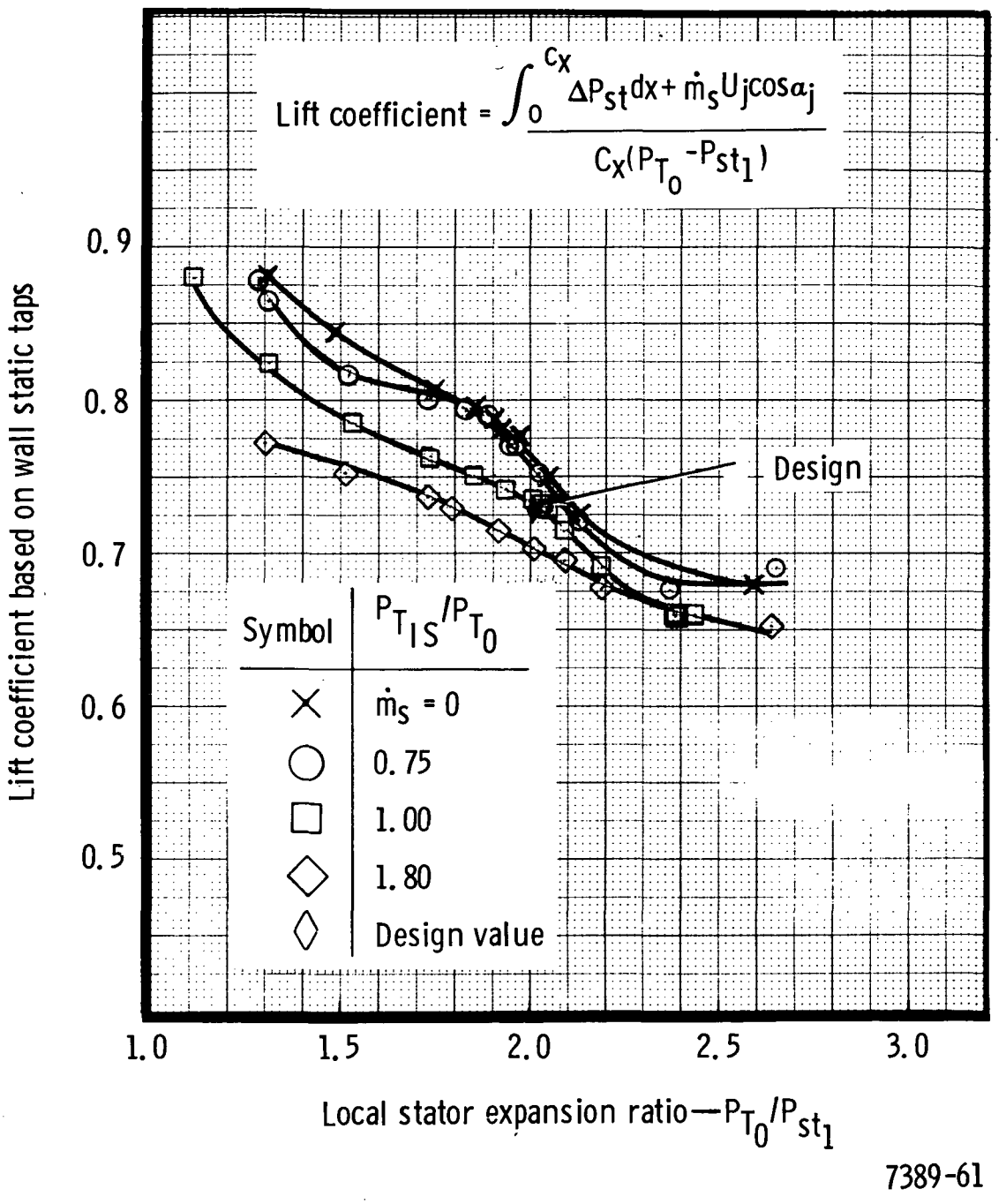

Figure 63. Mean section lift coefficient variation with expansion ratio.

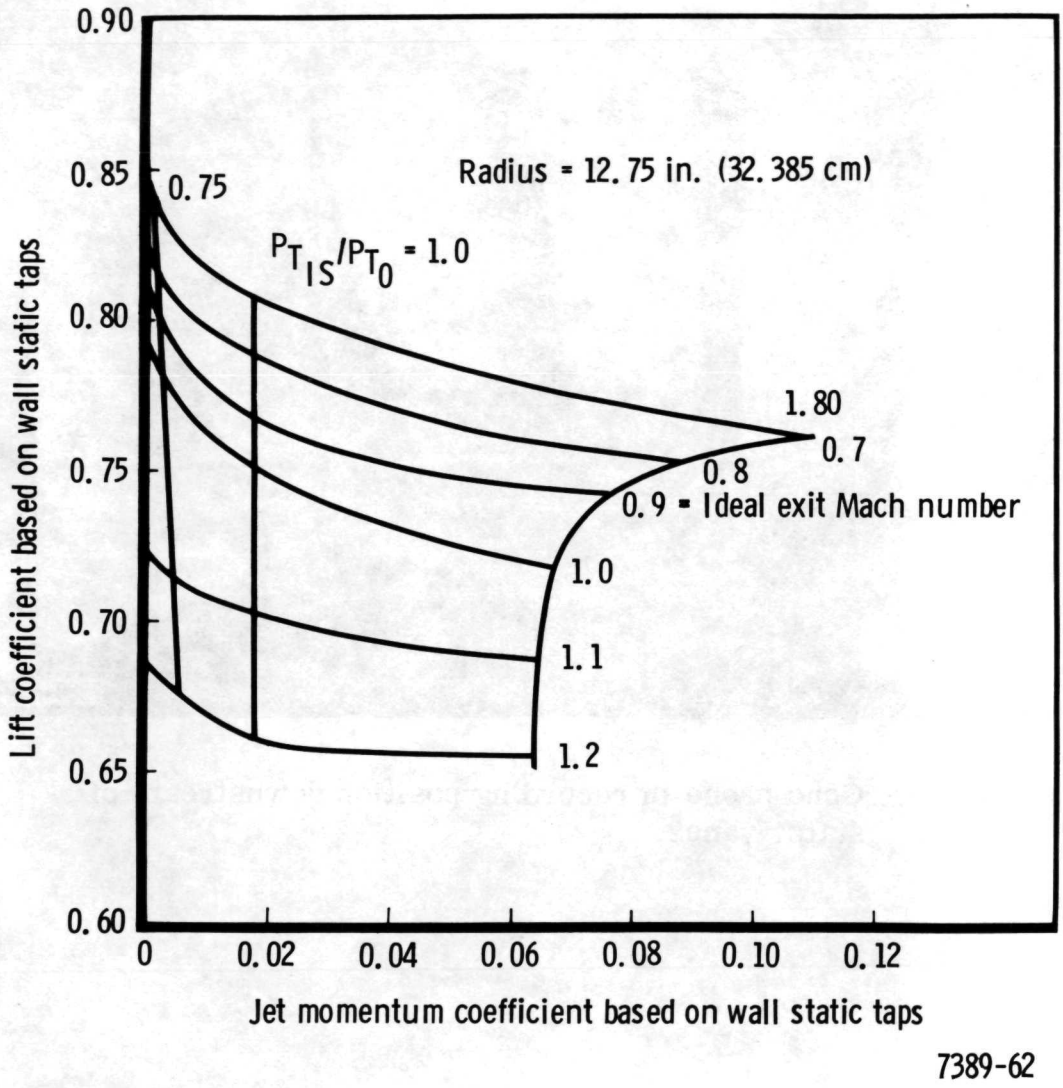

Figure 64. Mean section lift coefficient variation with jet momentum coefficient.

Figure 65. Cone probe in recording position downstream of stator vanes.

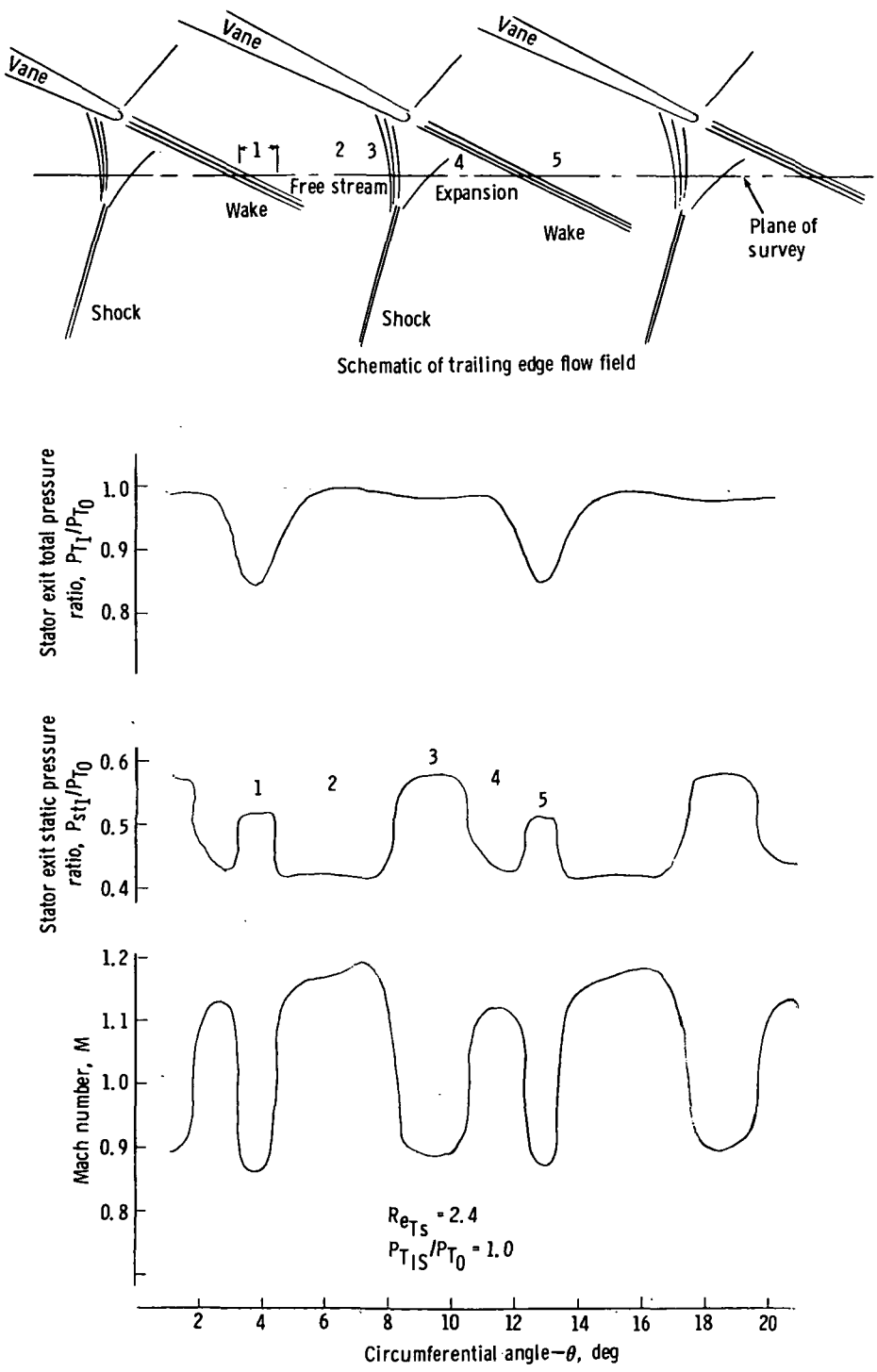

Figure 66. Schematic and cone probe measurements of jet flap vane trailing edge flow field.

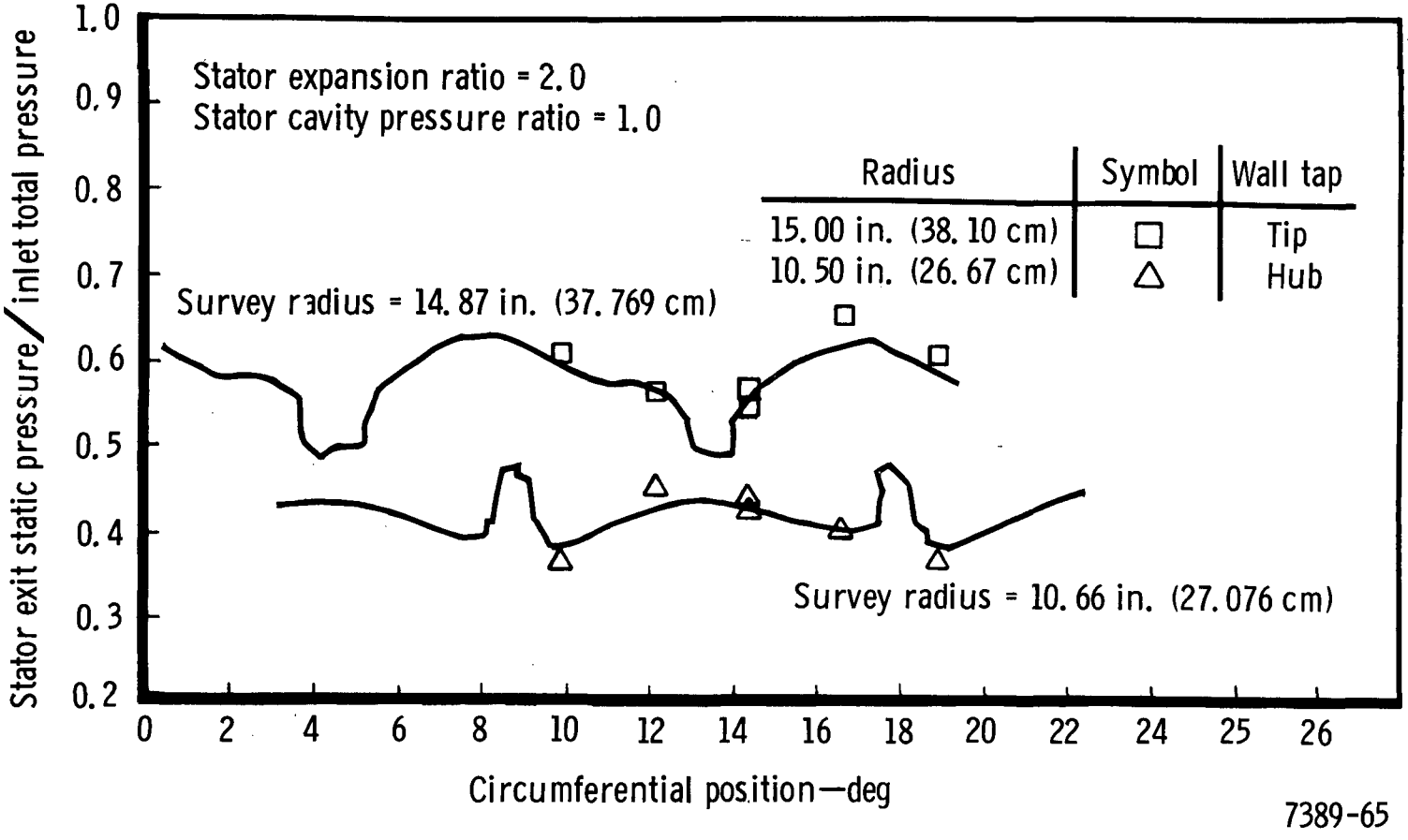

Figure 67. Comparison of exit wall tap pressure and survey pressure near walls.

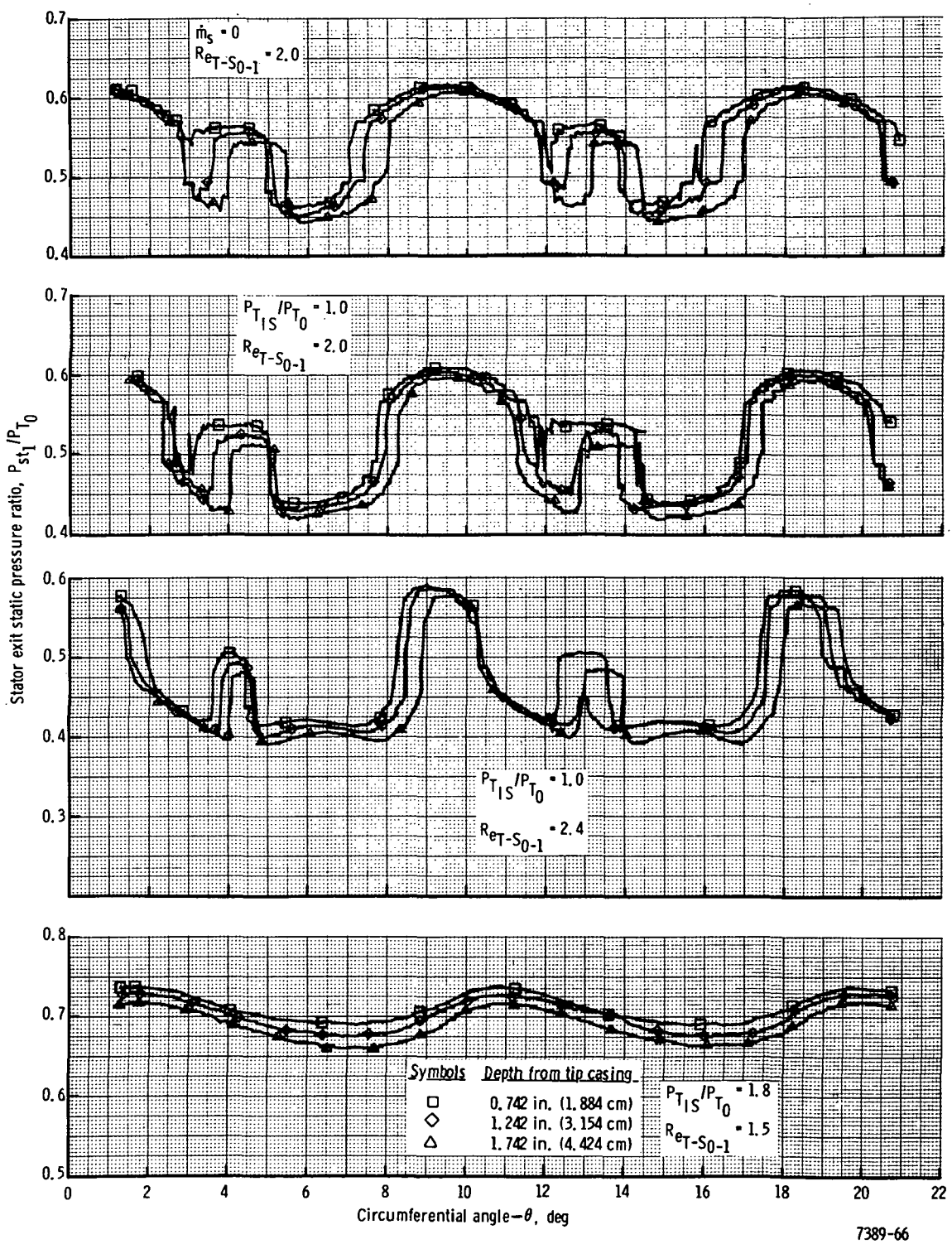

Figure 68. Typical midspan region survey of stator exit static pressure ratio.

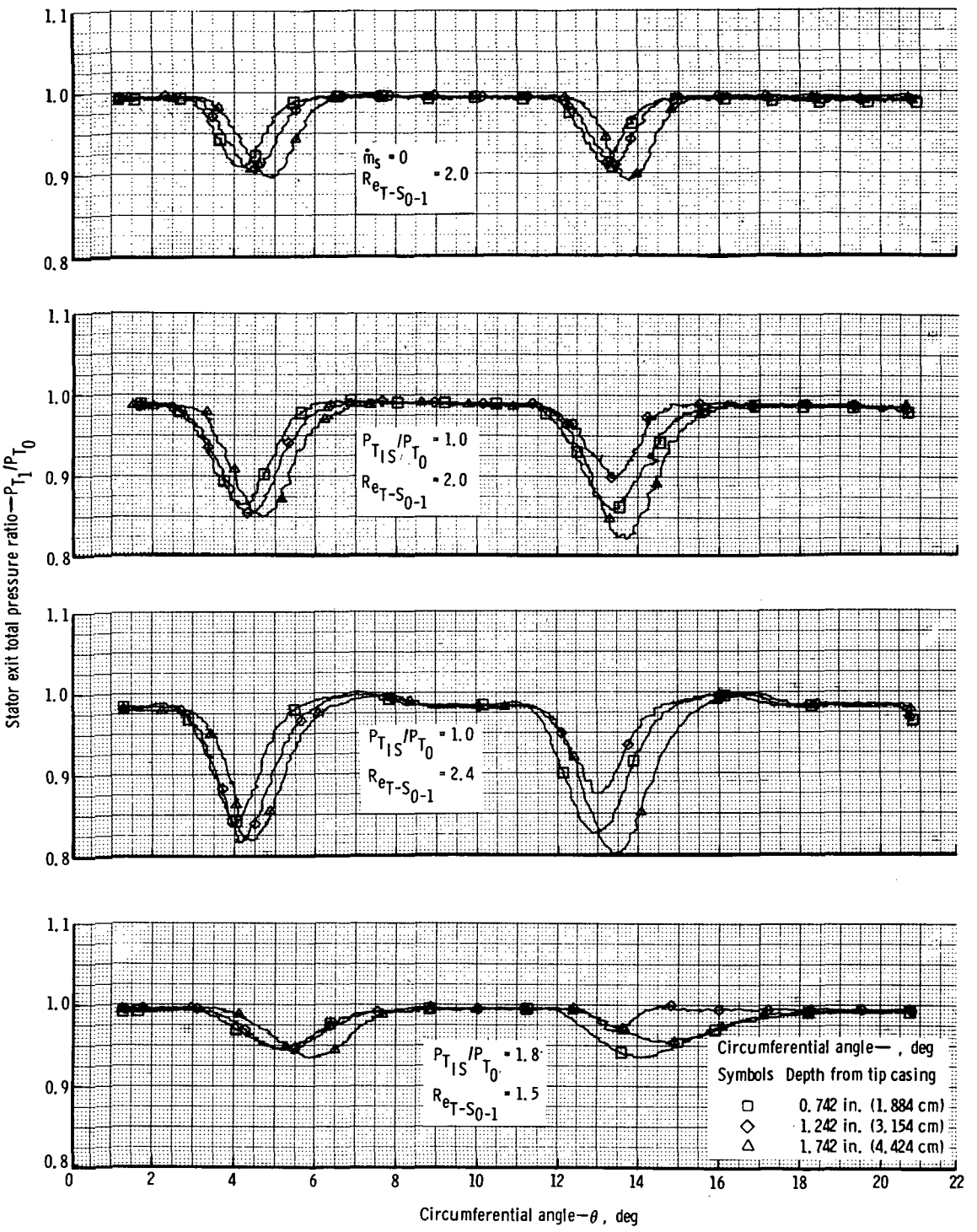

Figure 69. Typical midspan region survey of stator exit total pressure ratio.

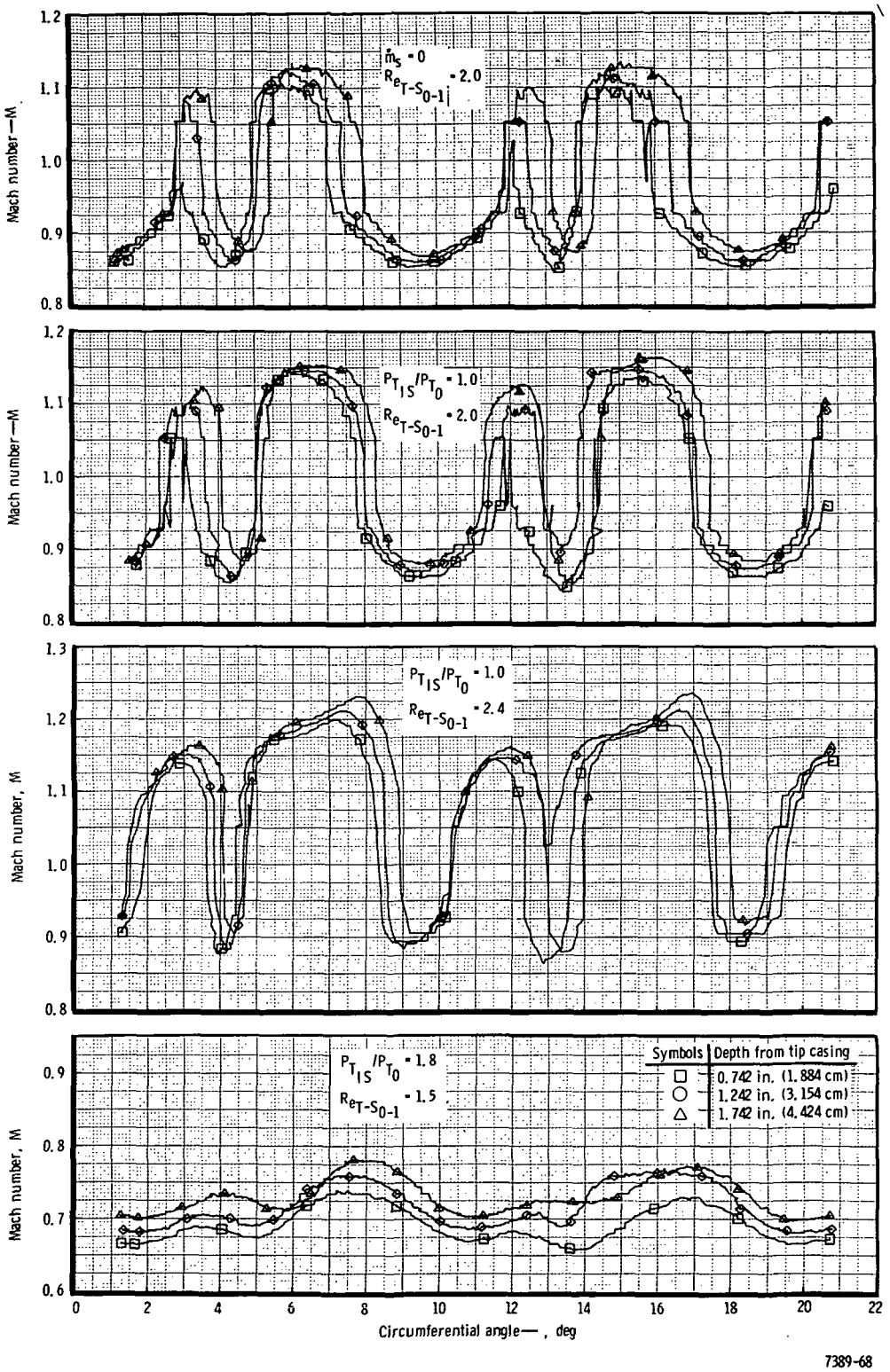

Figure 70. Typical midspan region survey of stator exit Mach number.

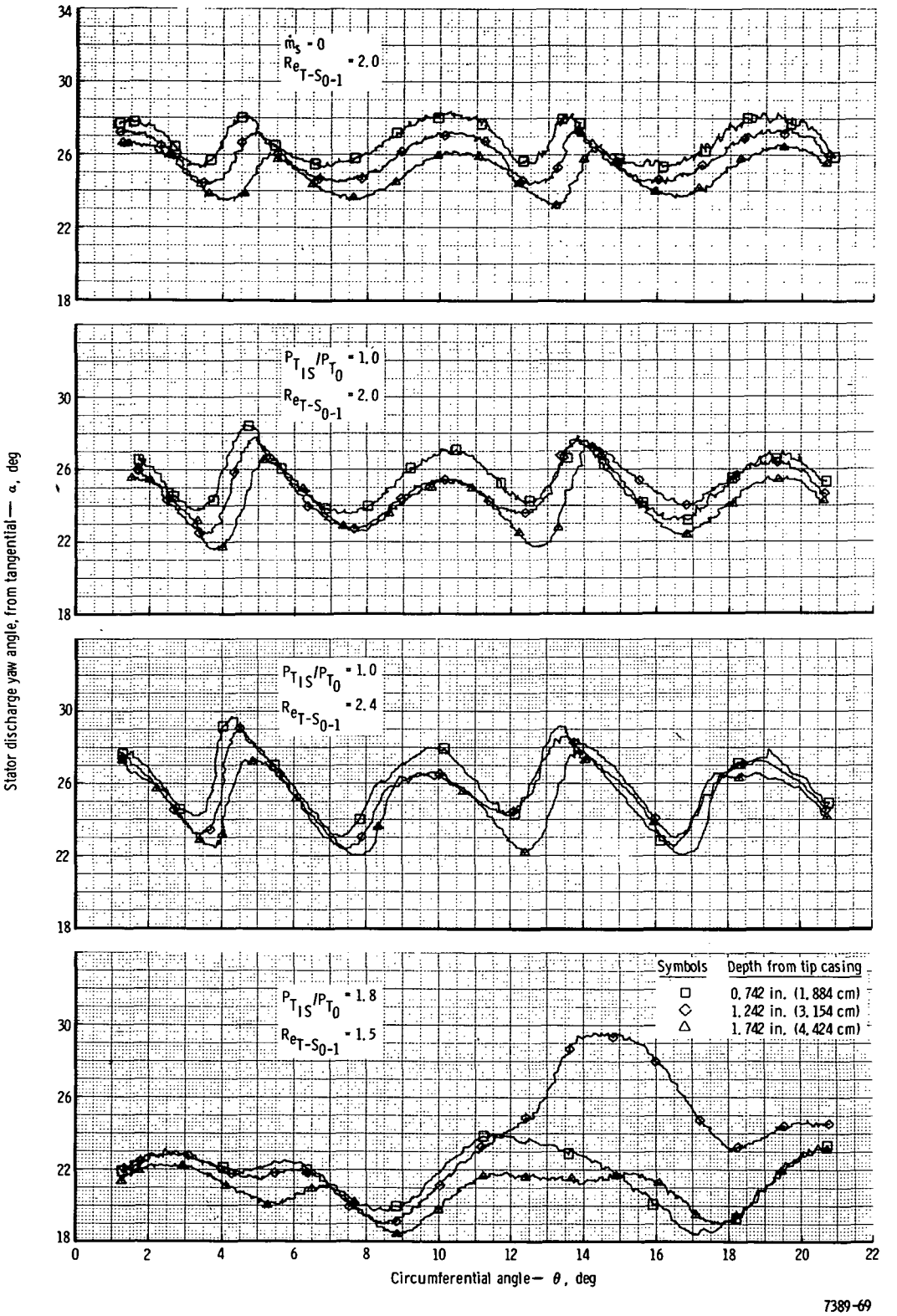

Figure 71. Typical midspan region survey of stator exit gas angles.

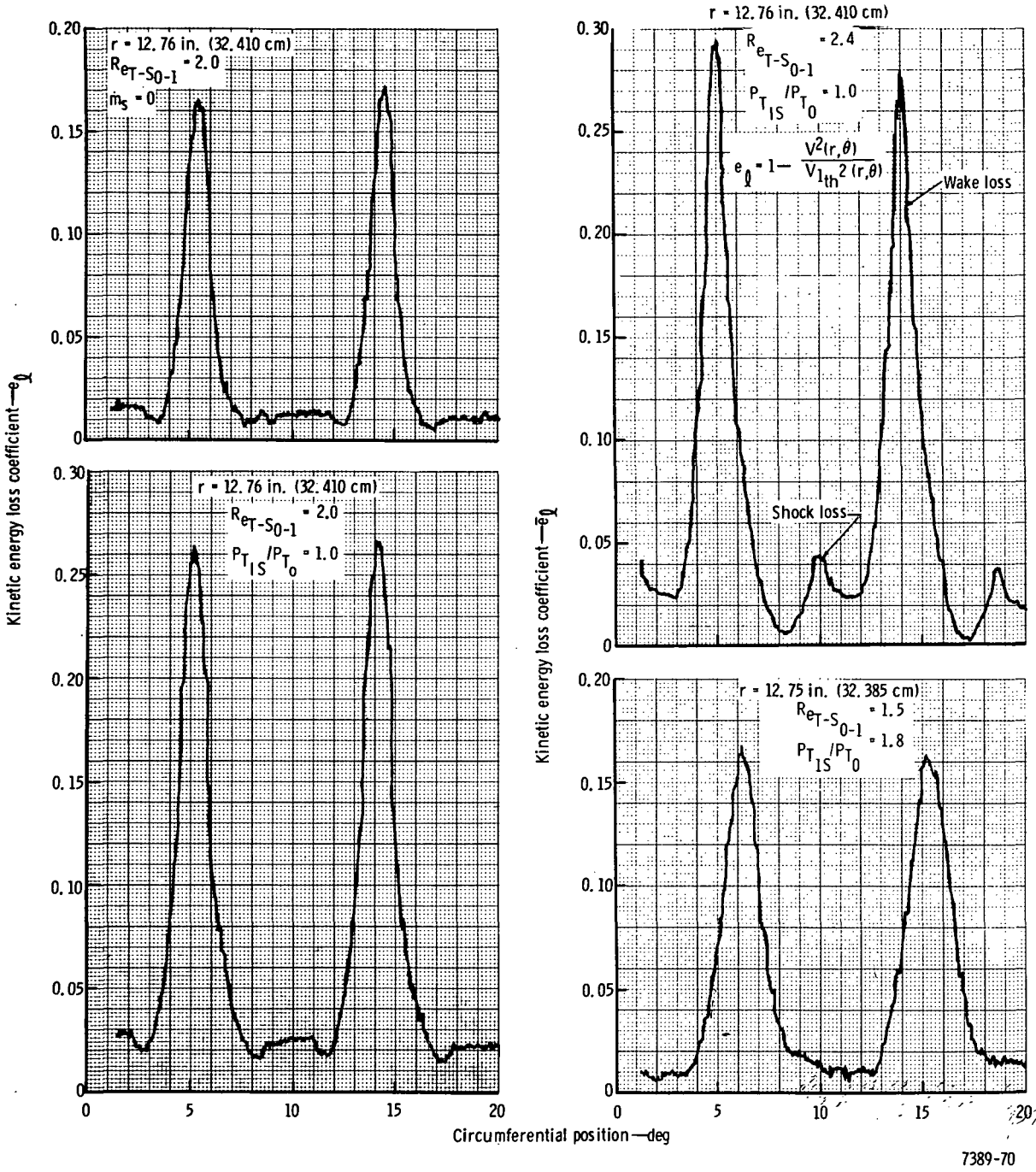

Figure 72. Typical energy loss coefficient trace.

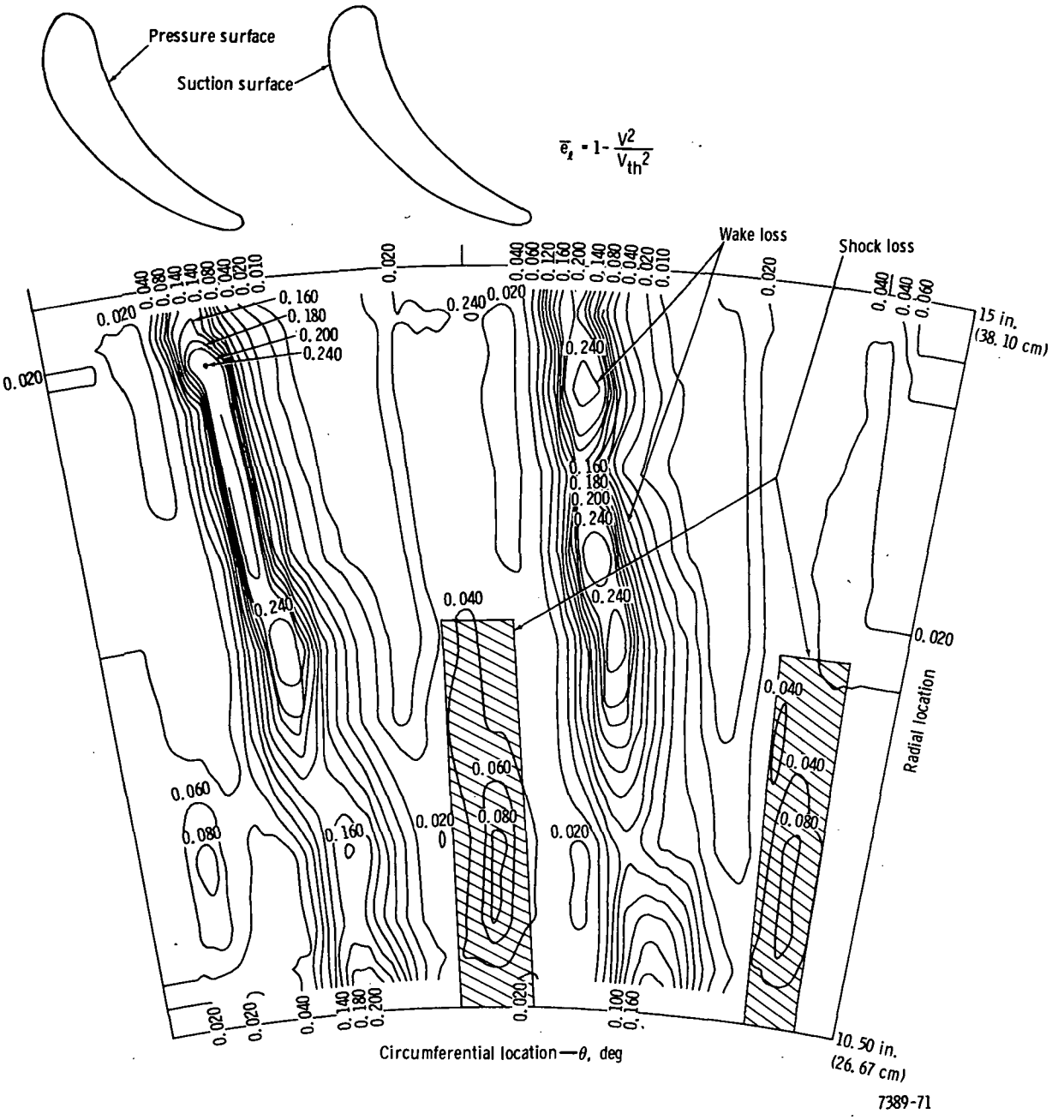

Figure 73. Kinetic energy loss coefficient at stator exit for stator expansion ratio $R_{e_{T-S_{0-1}}} = 2.4$ and $P_{T_{IS}}/P_{T_0} = 1.0$.

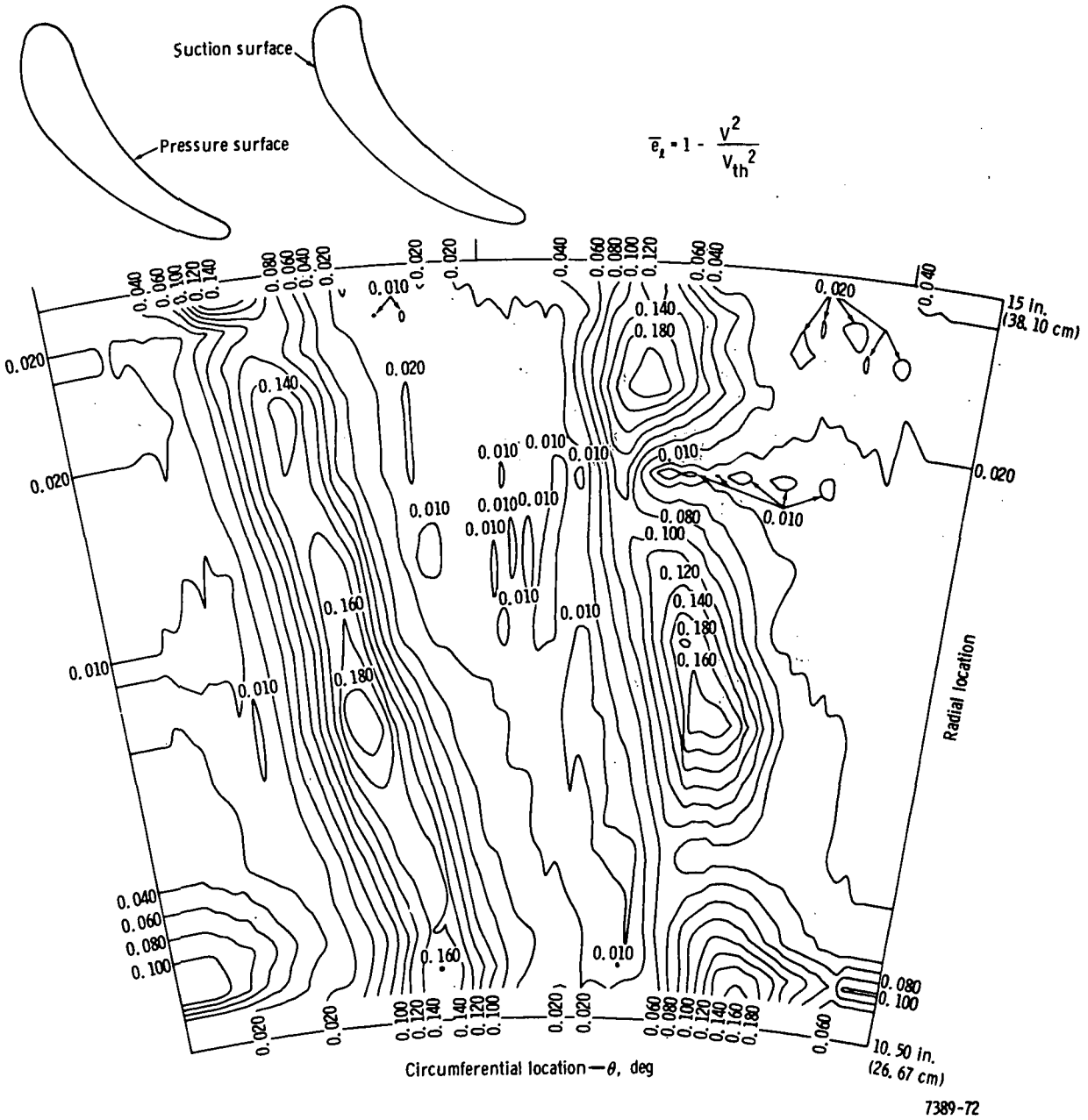

Figure 74. Kinetic energy loss coefficient at stator exit for stator expansion ratio $R_{e_{T\text{-}S_{0\text{-}1}}} = 1.5$ and $P_{T_{IS}}/P_{T_0} = 1.8$.

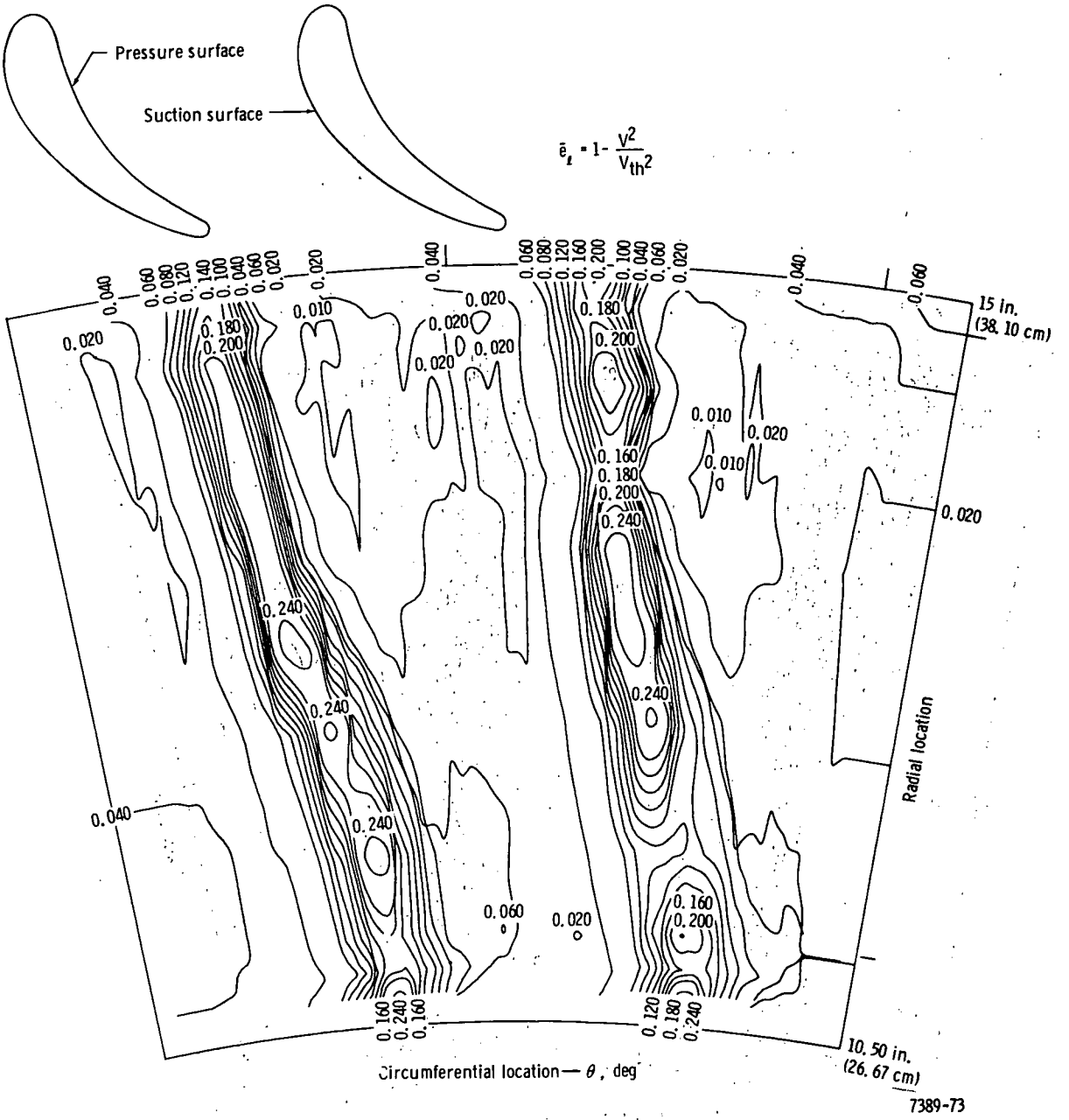

Figure 75. Kinetic energy loss coefficient at stator exit for stator expansion ratio $R_{e_{T-S_{0-1}}} = 2.0$ and $P_{T_{IS}}/P_{T_0} = 1.0$.

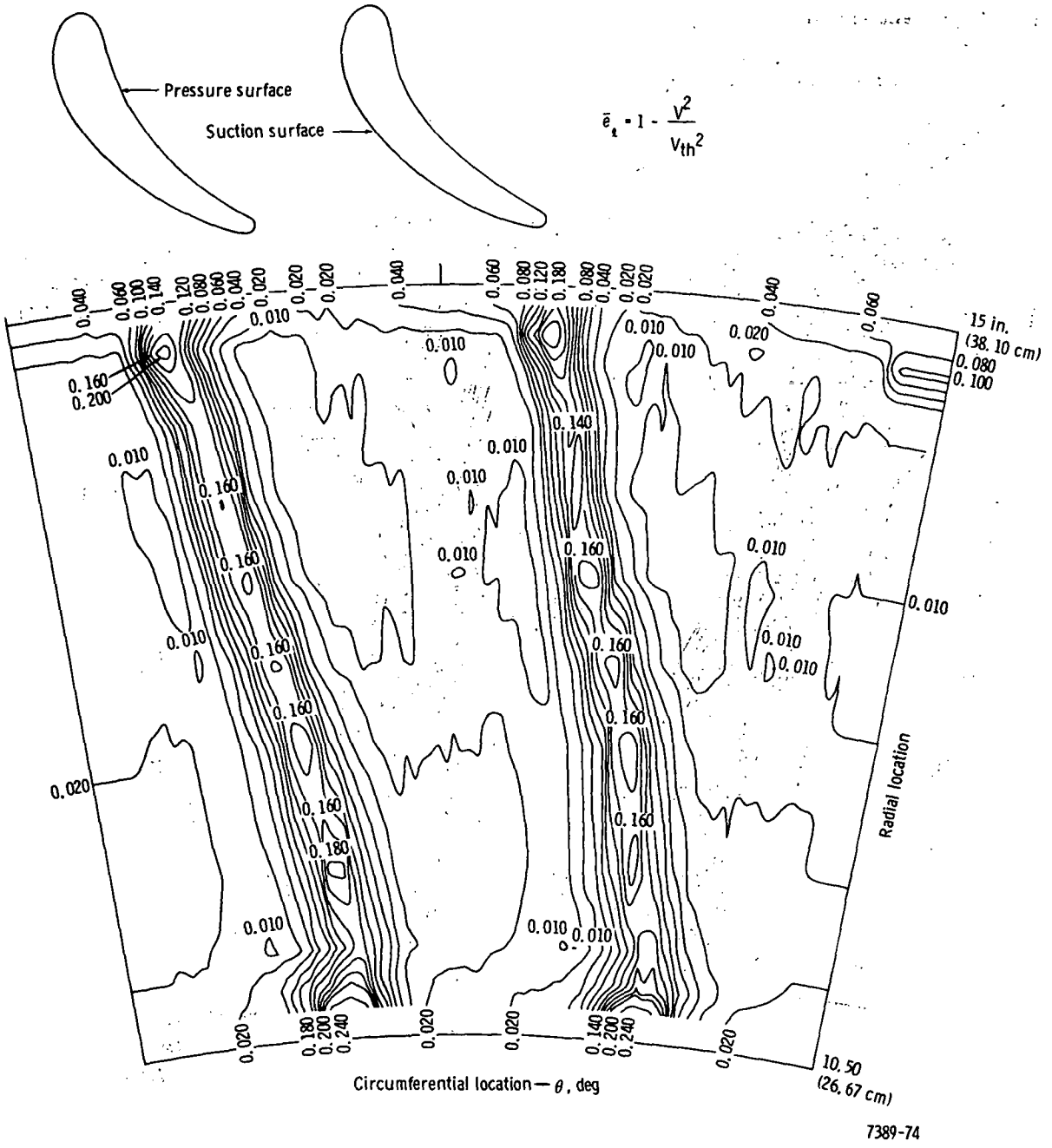

Figure 76. Kinetic energy loss coefficient at stator exit for stator expansion ratio $R_{e_{T-S_{0-1}}} = 2.0$ and zero jet flow.

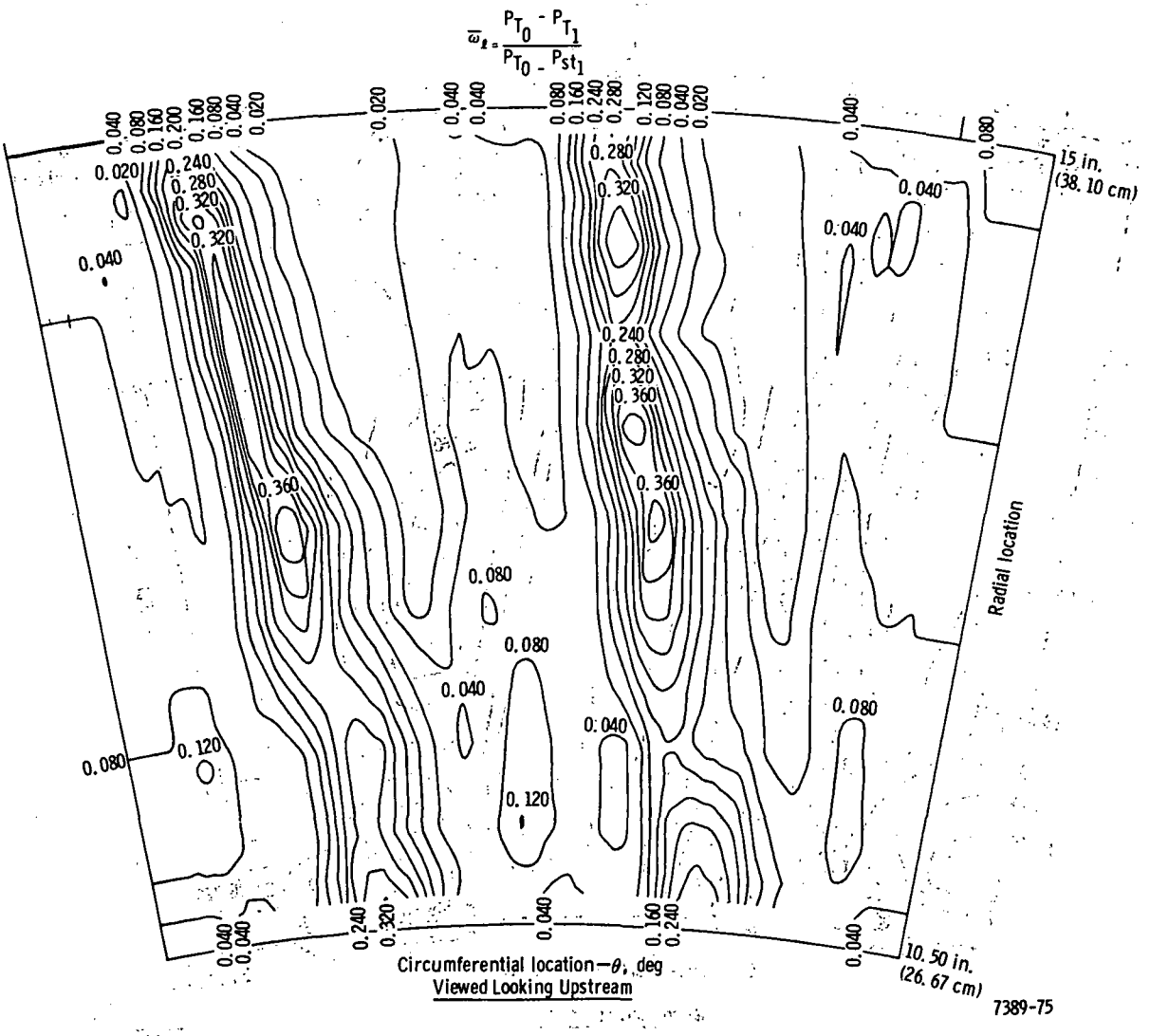

Figure 77. Stator exit pressure loss coefficient, $\overline{\omega}_\ell$, contour map for jet on ($P_{T_{IS}}/P_{T_0}$ = 1.0) and stator expansion $Re_{T\text{-}S_{0\text{-}1}}$ = 2.4.

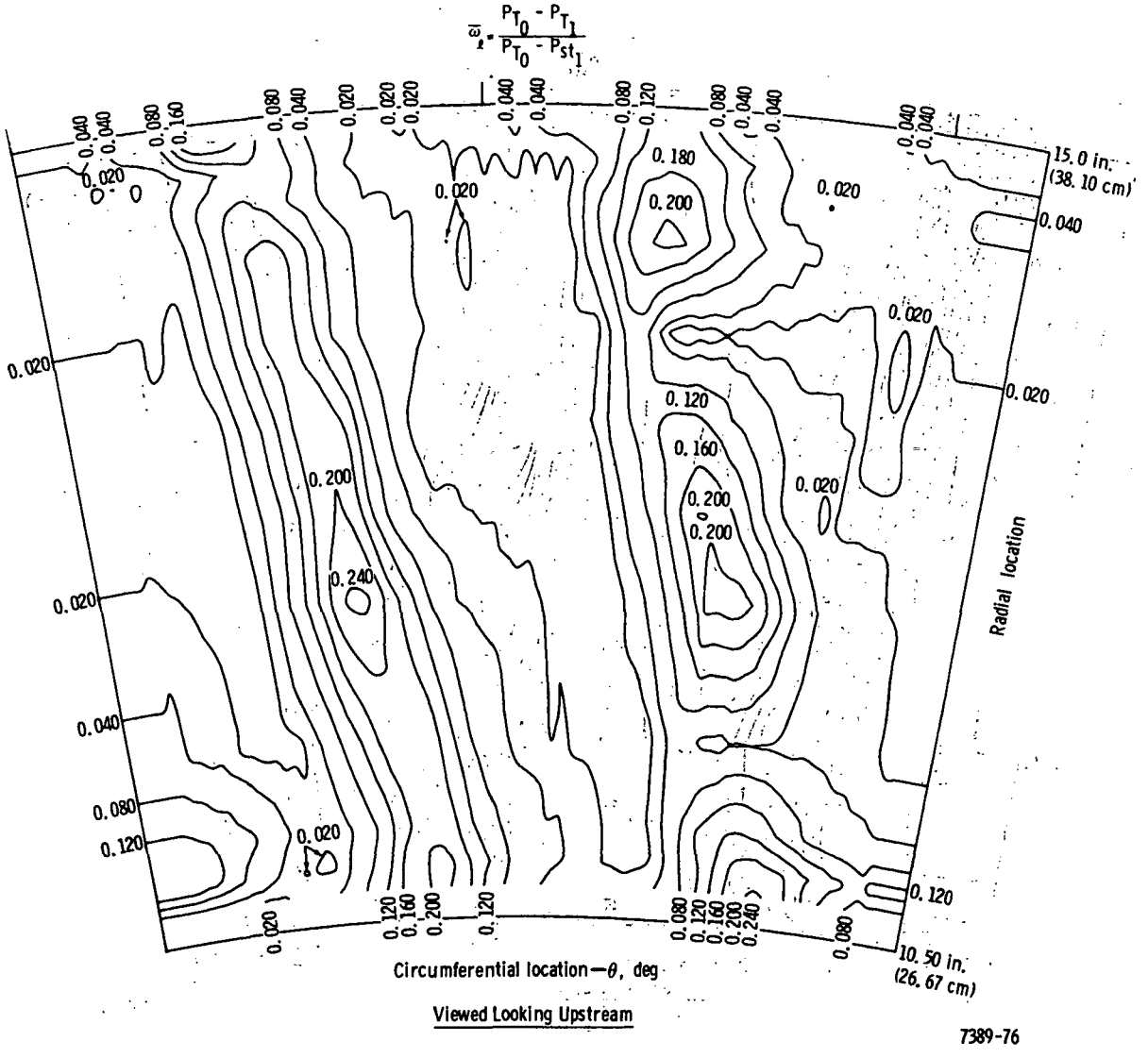

Figure 78. Stator exit pressure loss coefficient, $\bar{\omega}_\ell$, contour map for jet on ($P_{T_{IS}}/P_{T_0}$ = 1.8) and stator expansion ratio $R_{e_{T\text{-}S_{0\text{-}1}}}$ = 1.5.

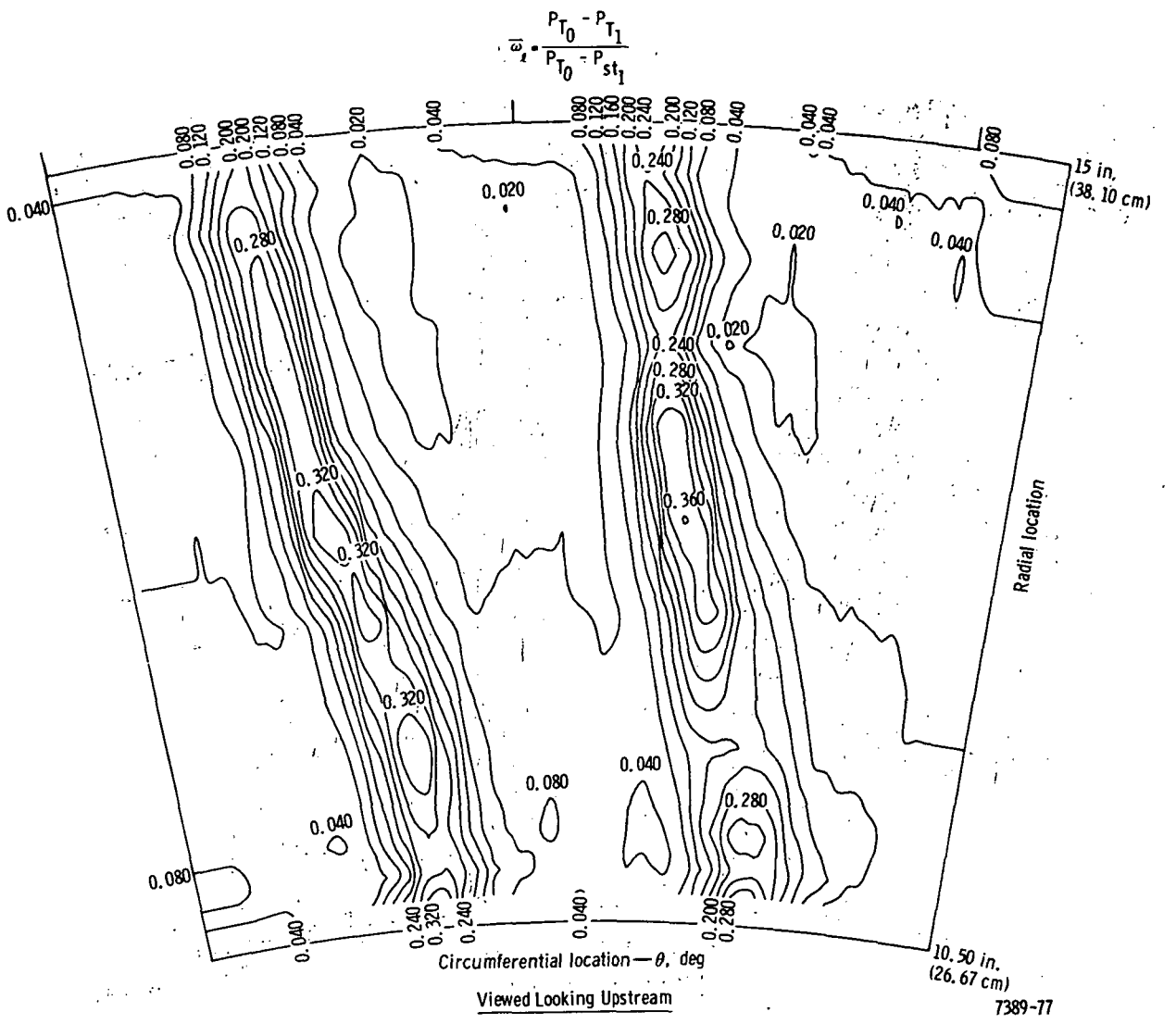

Figure 79. Stator exit pressure loss coefficient, $\bar{\omega}_\ell$, contour map for jet on ($P_{T_{IS}}/P_{T_0}$ = 1.0) and stator expansion ratio $R_{e_{T-S_{0-1}}}$ = 2.0.

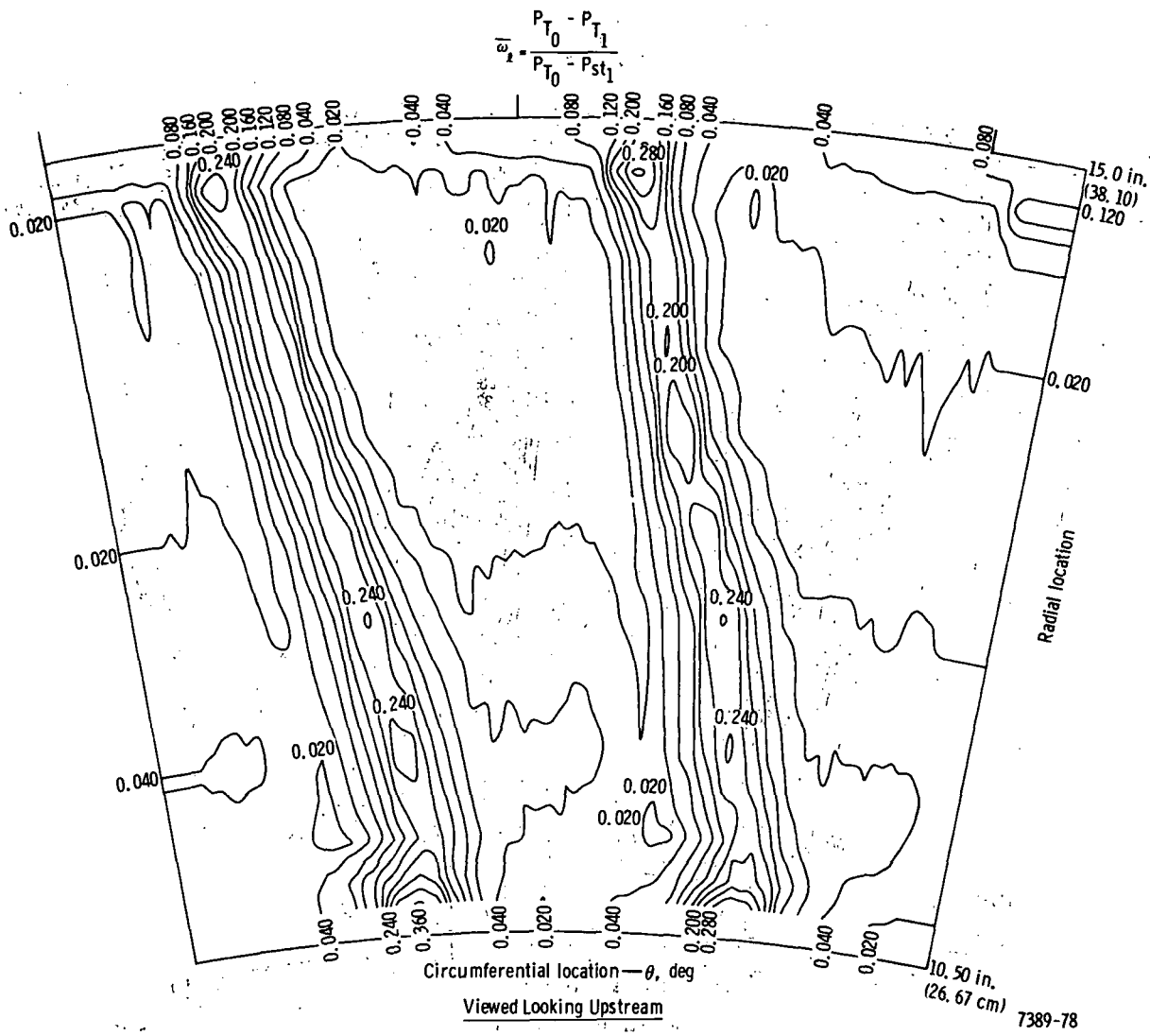

Figure 80. Stator exit pressure loss coefficient, $\bar{\omega}_\ell$, contour map for jet off and stator expansion $R_{e_{T\text{-}S_{0\text{-}1}}} = 2.0$.

$$e_1(r) = 1 - \frac{\text{Actual kinetic energy}}{\text{Ideal kinetic energy}} = 1 - \frac{1/2\int_{\theta_1}^{\theta_4} (\rho_{st_1} V_1 \sin\alpha) V_1^2 r d\theta}{1/2\int_{\theta_1}^{\theta_4} (\rho_{st_1} V_1 \sin\alpha) V_{th}^2 r d\theta}$$

Stator expansion ratio	P_{T_1}/P_{T_0}	Symbol
1.5	1.8	◇
2.0	$\dot{m}_s = 0$	○
2.0	1.0	□
2.4	1.0	△

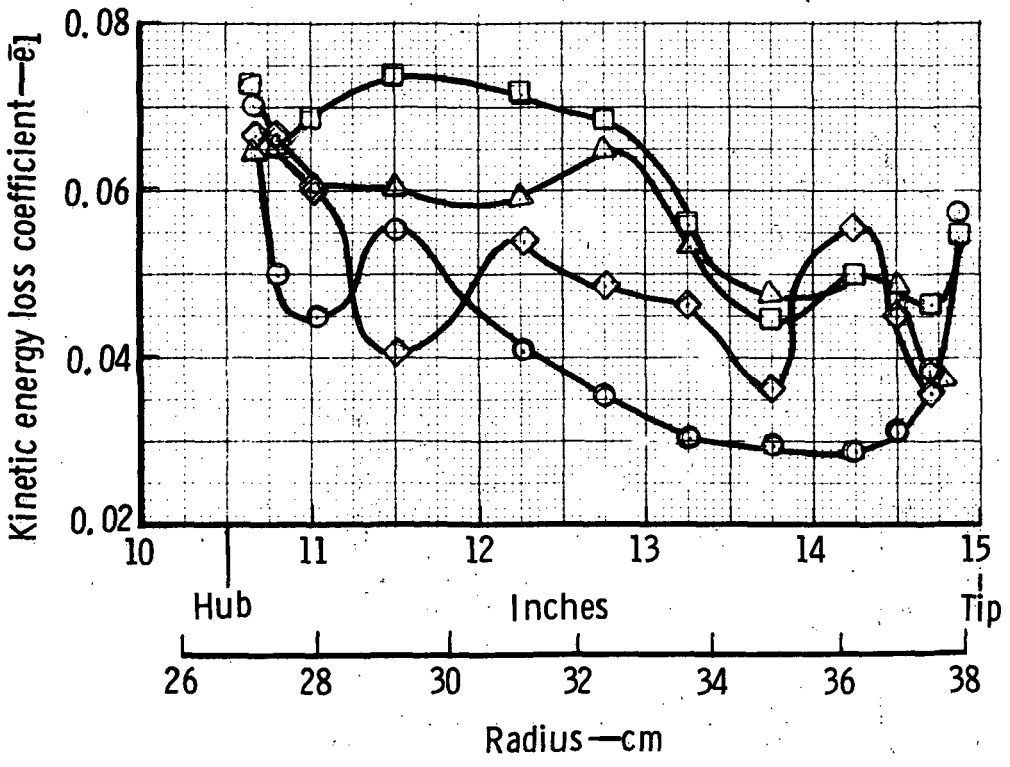

7389-79

Figure 81. Variation of kinetic energy loss coefficient with radius at several operating conditions.

$$\bar{e}_1(r) = 1 - \frac{1/2\int_{\theta_1}^{\theta_2} \left(\rho_{st_1} V_1 \sin\alpha_1\right) V_1^2 \, r\,d\theta}{1/2\int_{\theta_1}^{\theta_2} \left(\rho_{st_1} V_1 \sin\alpha_1\right) V_{th}^2 \, r\,d\theta} \qquad \text{(Solve for } \bar{e}_1 \text{ (r))}$$

$$1-\bar{e}_1(r) = \frac{1-\left(P_{st_1}/P_{T_1}\right)^{\left(\frac{\gamma-1}{\gamma}\right)}}{1-\left(P_{st_1}/P_{T_0}\right)^{\left(\frac{\gamma-1}{\gamma}\right)}} \qquad \text{(Solve for } P_{T_1} \text{ for assumed linear variation of } P_{st_1}\text{)}$$

$$\bar{\omega}(r) = \left(P_{T_0} - P_{T_1}\right)/\left(P_{T_0} - P_{st_1}\right)$$

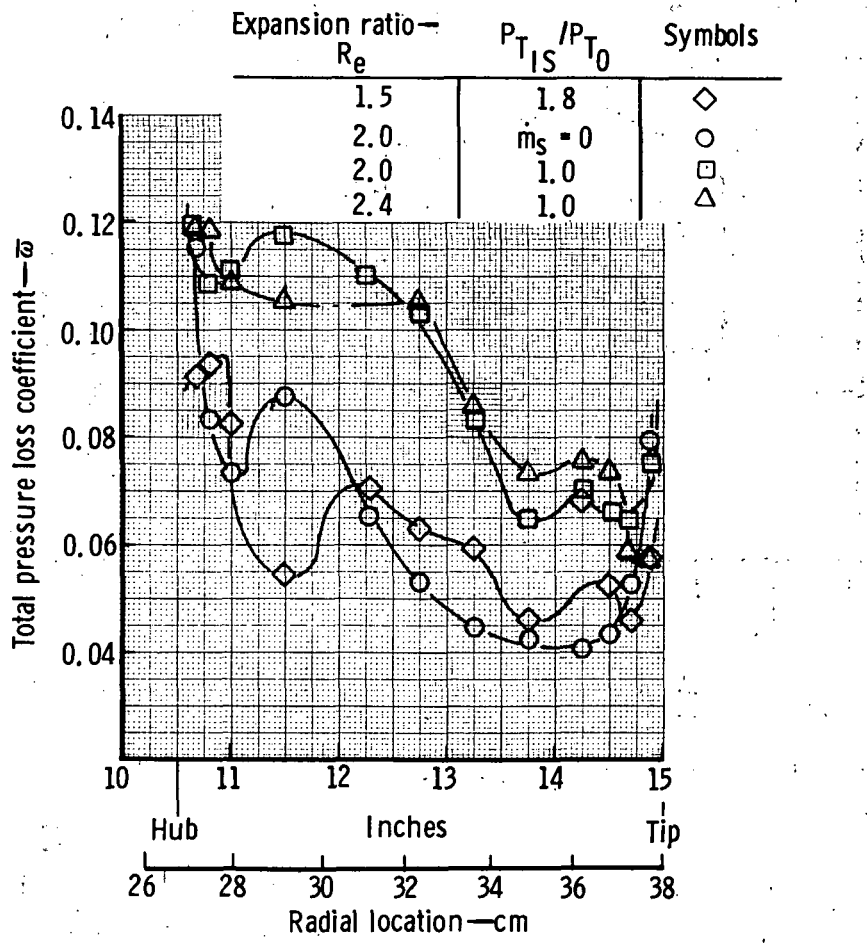

Figure 82. Variation of total pressure loss coefficient with radius at several stator operating conditions.

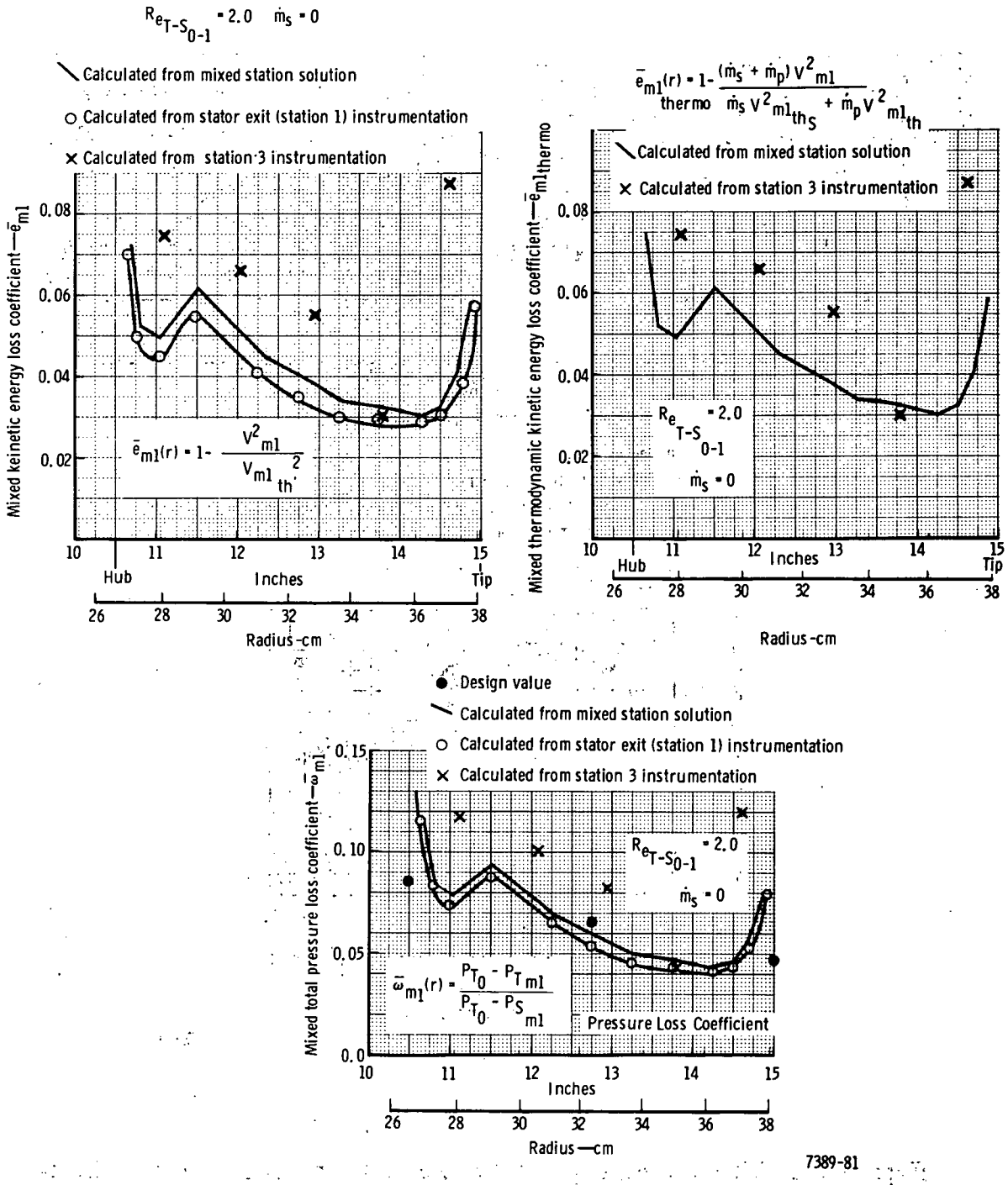

Figure 83. Kinetic energy, pressure, and thermodynamic kinetic energy loss coefficients at mixed station for $R_{e_{T-S_{0-1}}} = 2.0$ and the jet-off condition.

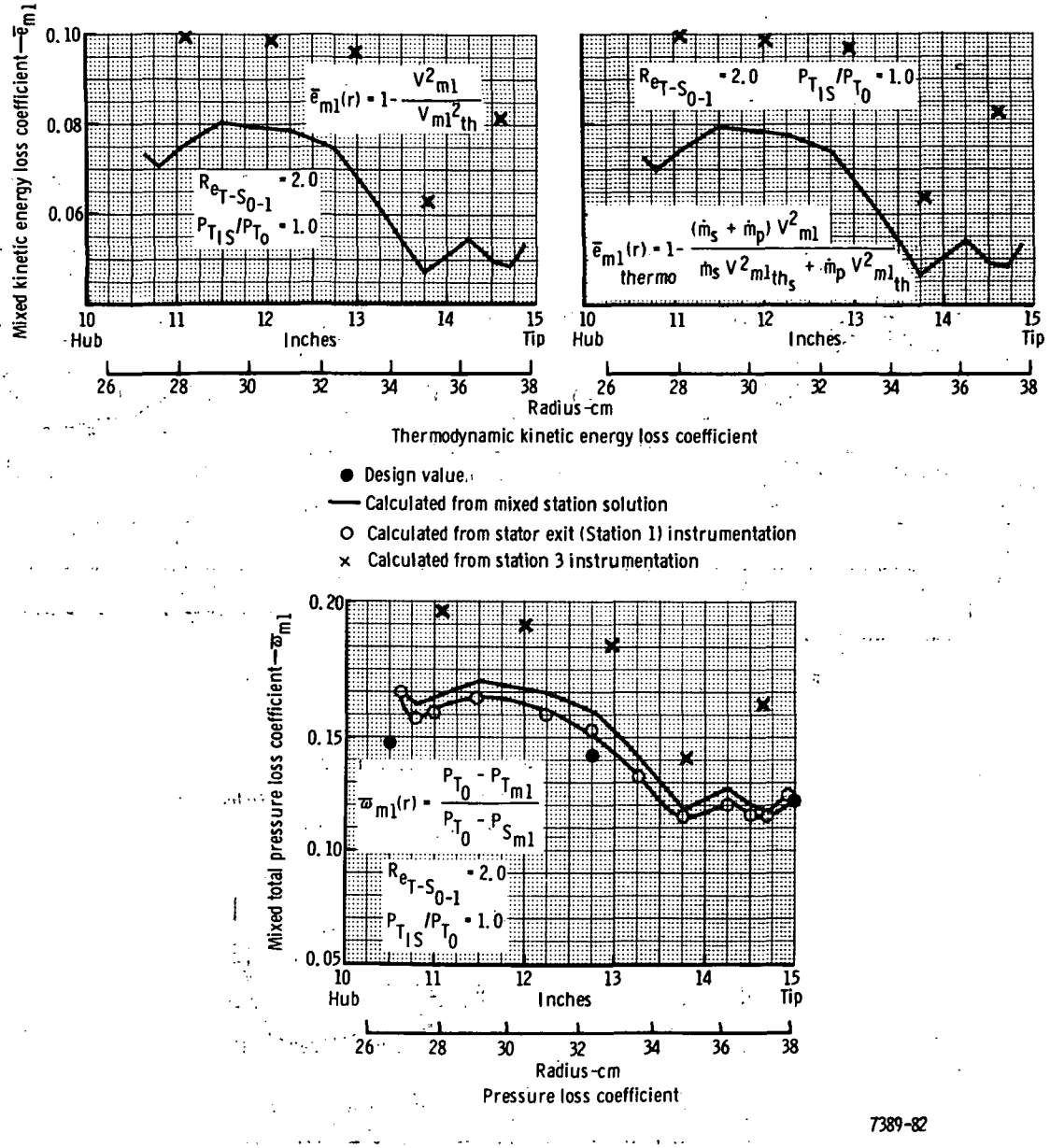

Figure 84. Kinetic energy, pressure, and thermodynamic kinetic energy loss coefficients at mixed station for $Re_{T-S_{0-1}} = 2.0$ and $P_{T_{IS}}/P_{T_0} = 1.0$.

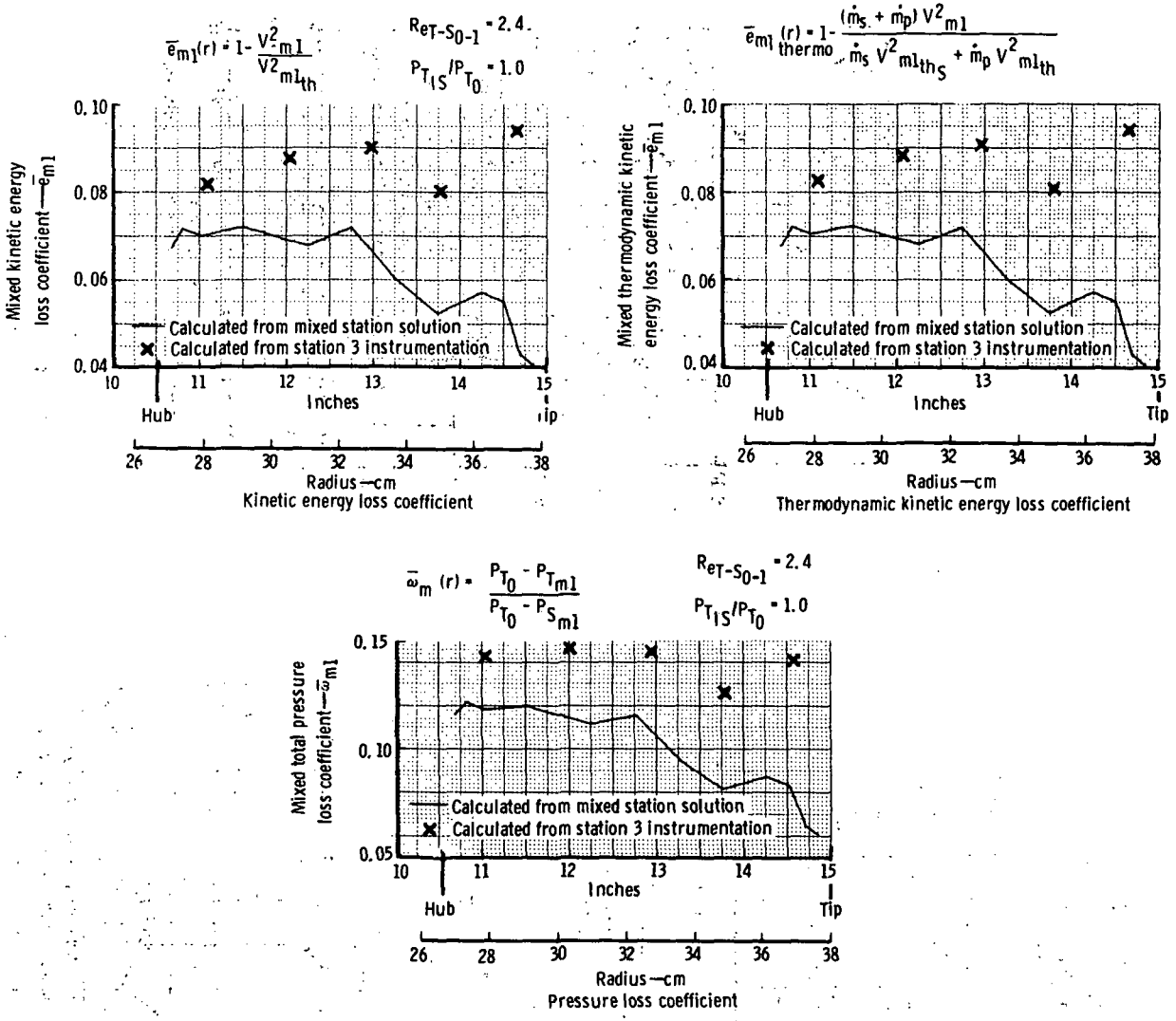

Figure 85. Kinetic energy, pressure, and thermodynamic kinetic energy loss coefficients at mixed station for $Re_{T-S_{0-1}} = 2.4$ and $P_{T_{IS}}/P_{T_0} = 1.0$.

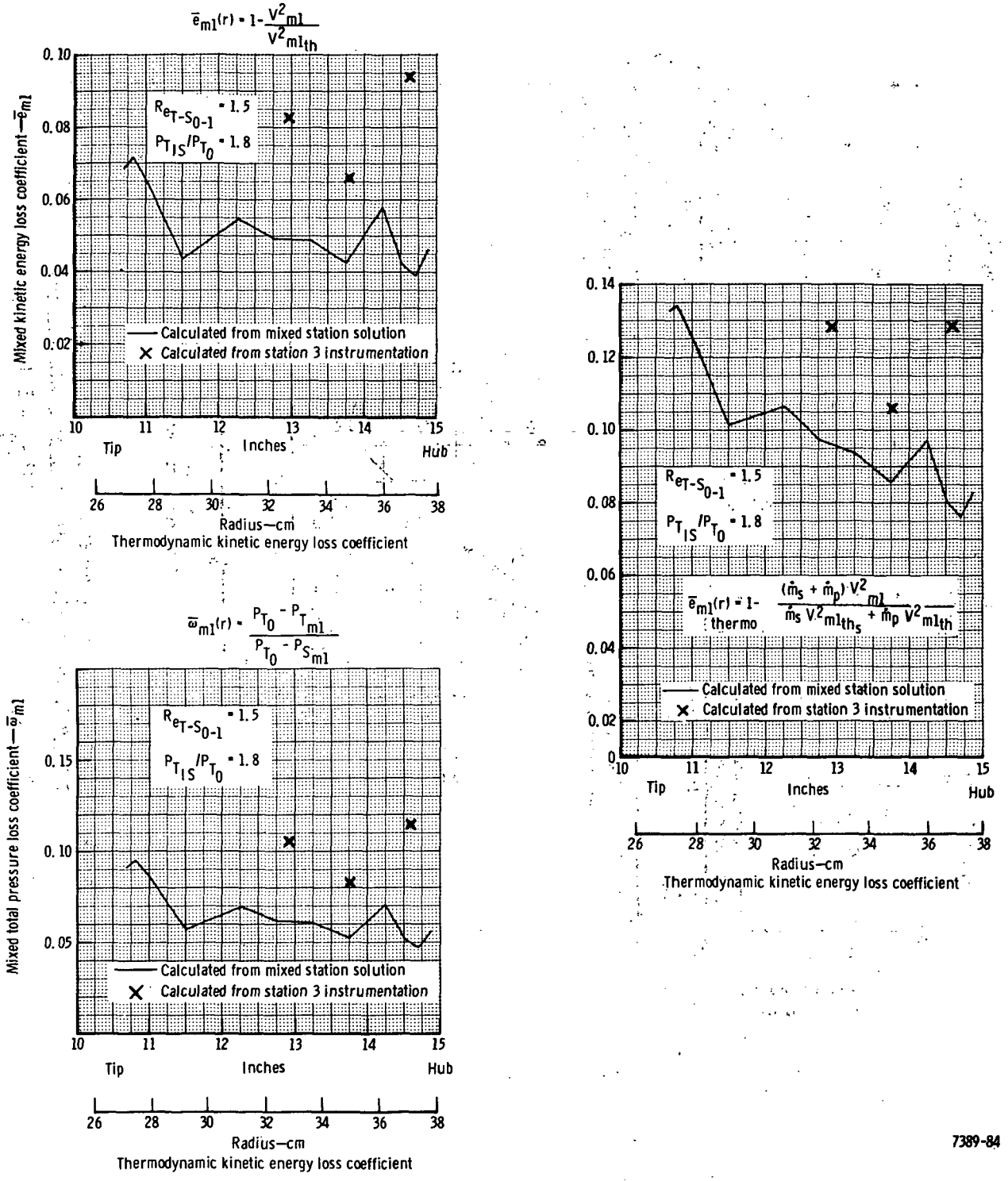

Figure 86. Kinetic energy, pressure, and thermodynamic kinetic energy loss coefficients at mixed station for $R_{e_{T-S_{0-1}}} = 1.5$ and $P_{T_{IS}}/P_{T_0} = 1.8$.

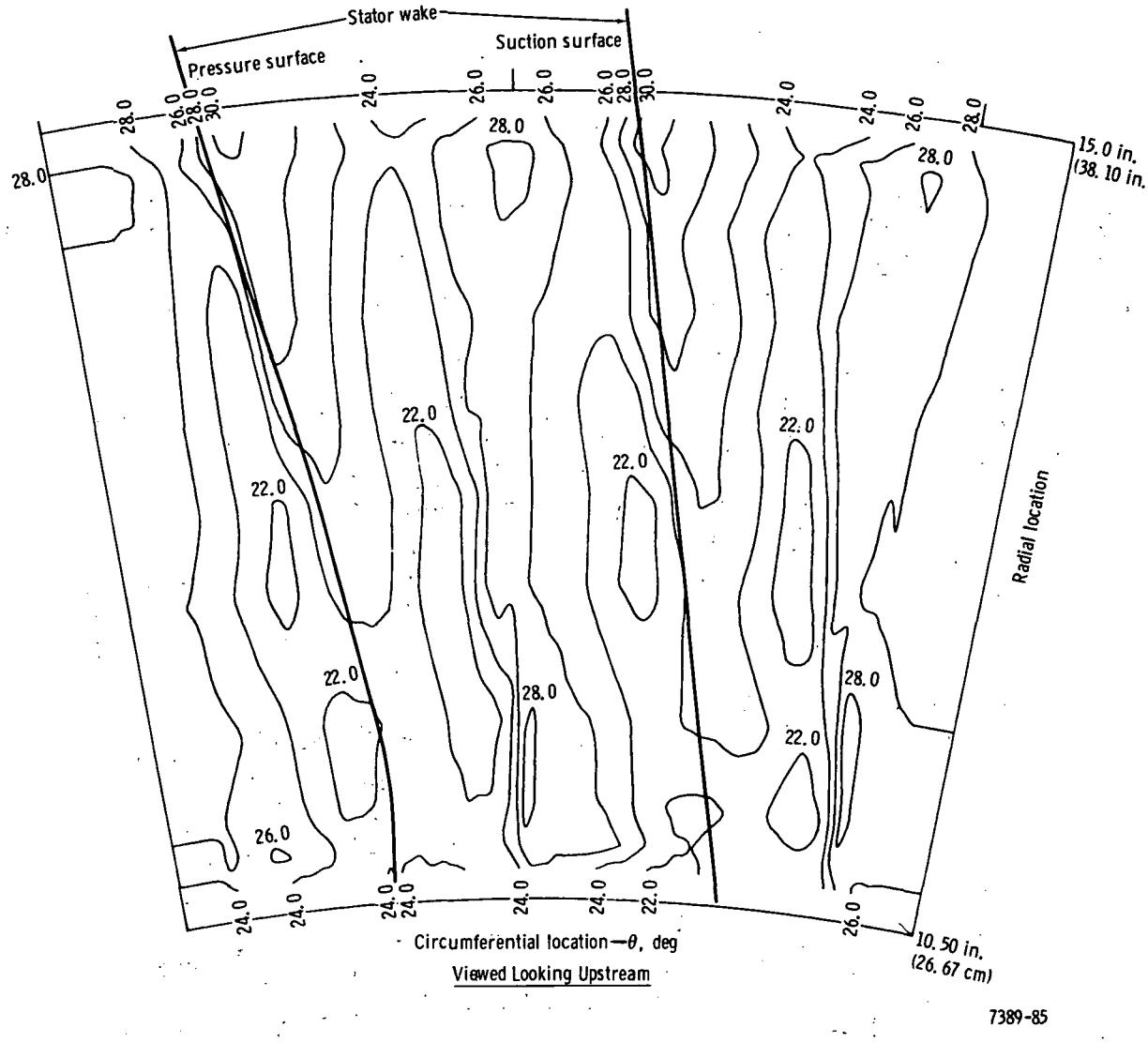

Figure 87. Stator exit absolute angle (from tangential) contour map for jet on ($P_{T_{IS}}/P_{T_0}$ = 1.0) and stator expansion $R_{e_{T\text{-}S_{0\text{-}1}}}$ = 2.4.

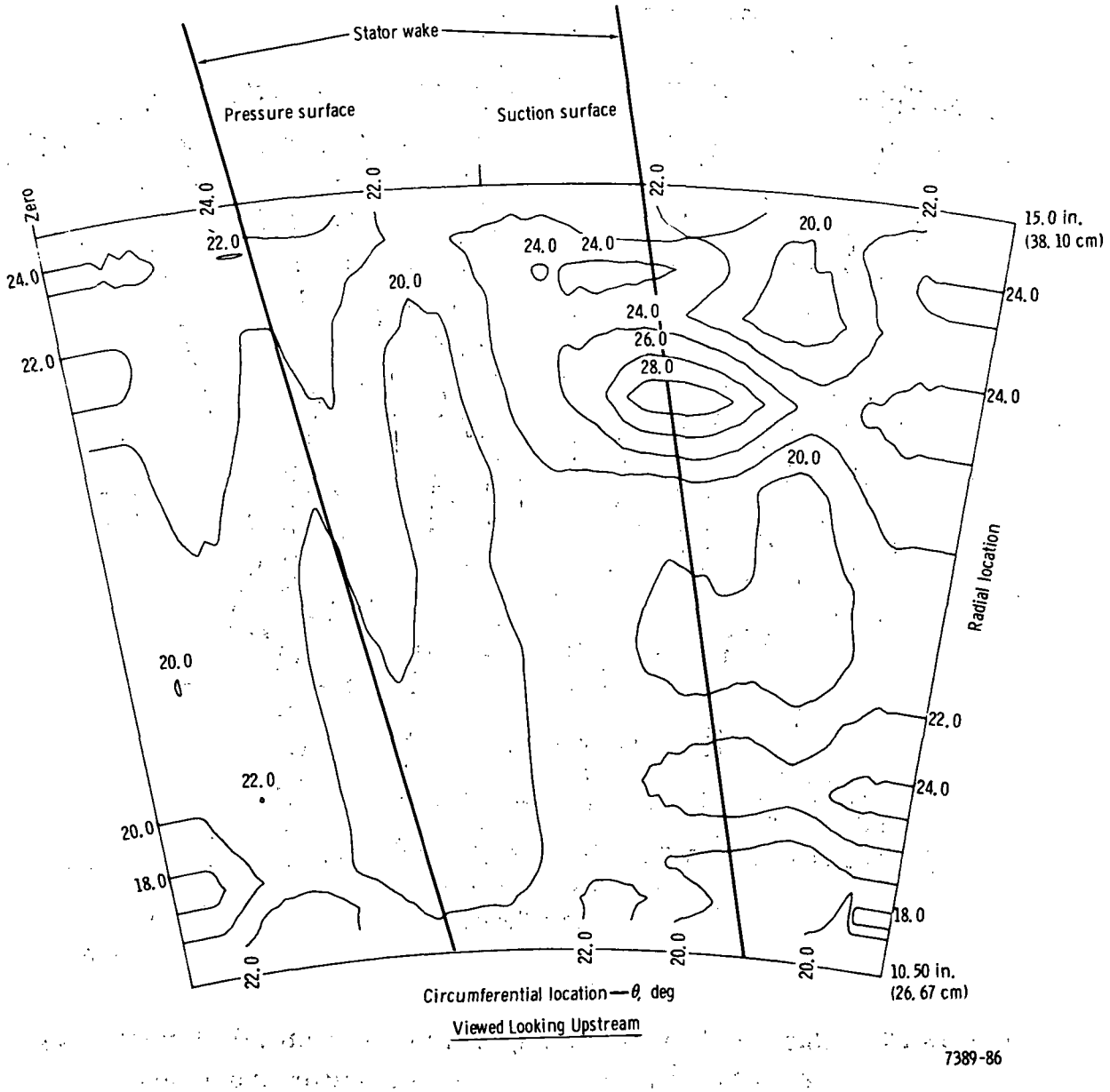

Figure 88. Stator exit absolute angle, α, (from tangential) contour map for jet on ($P_{T_{IS}}/P_{T_0}$ = 1.8) and stator expansion $R_{e_{T-S_{0-1}}}$ = 1.5.

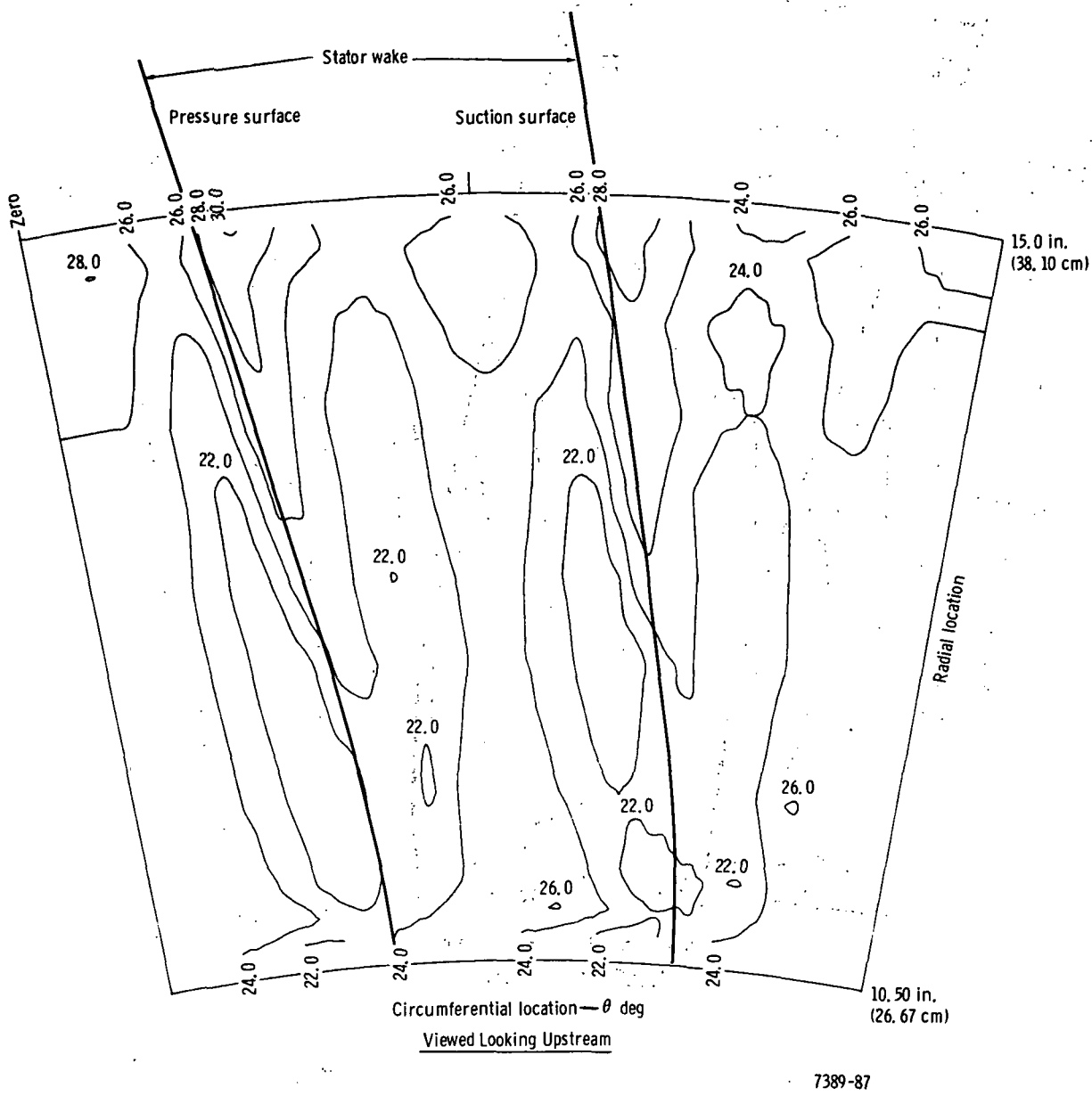

Figure 89. Stator exit absolute angle, α, (from tangential) contour map for jet on ($P_{T_{IS}}/P_{T_0}$ = 1.0) and stator expansion $R_{e_{T\text{-}S_{0\text{-}1}}}$ = 2.0.

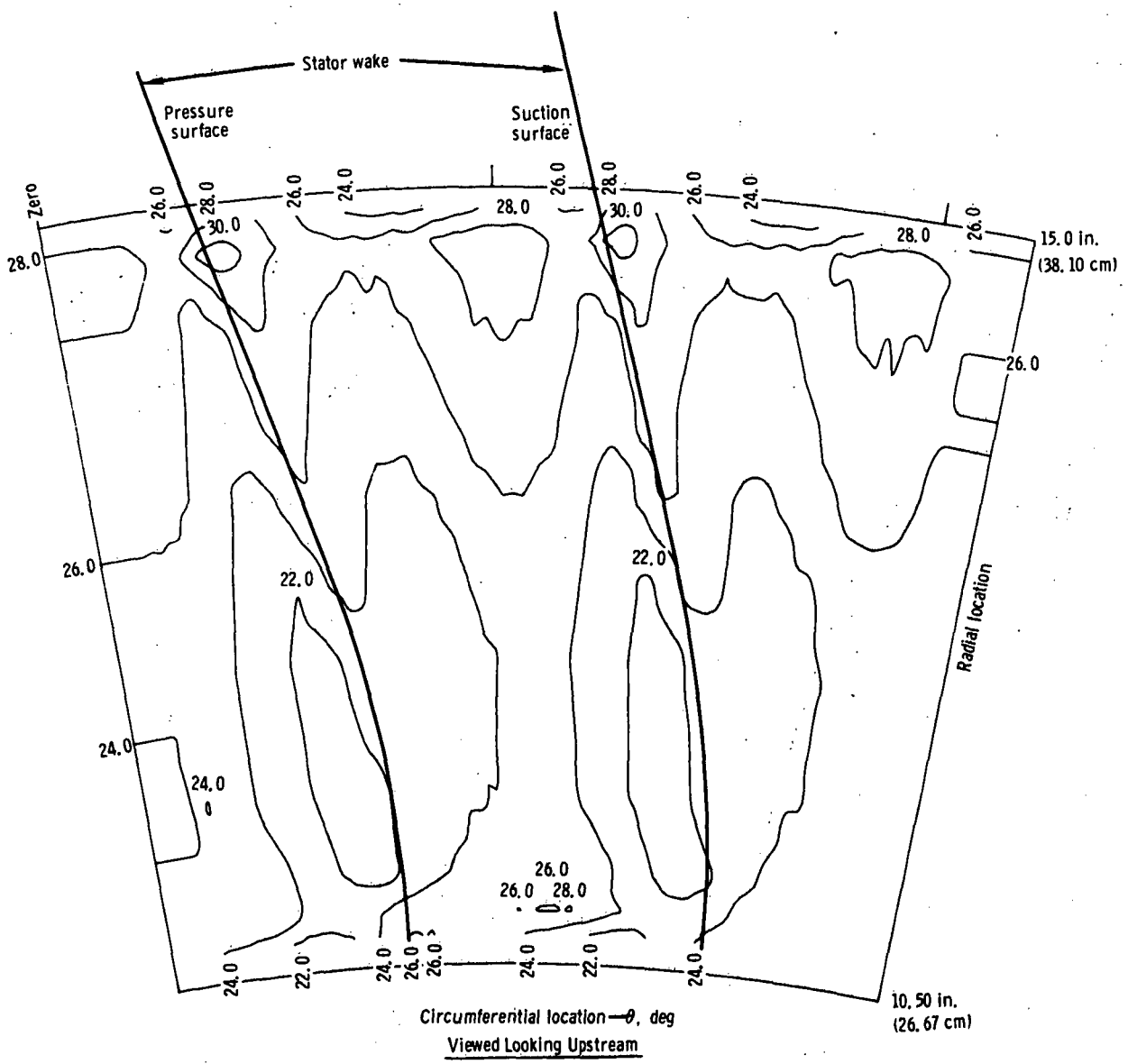

Figure 90. Stator exit absolute angle, α, from tangential contour map for jet-off condition and stator expansion ratio $R_{e_{T-S_{0-1}}} = 2.0$.

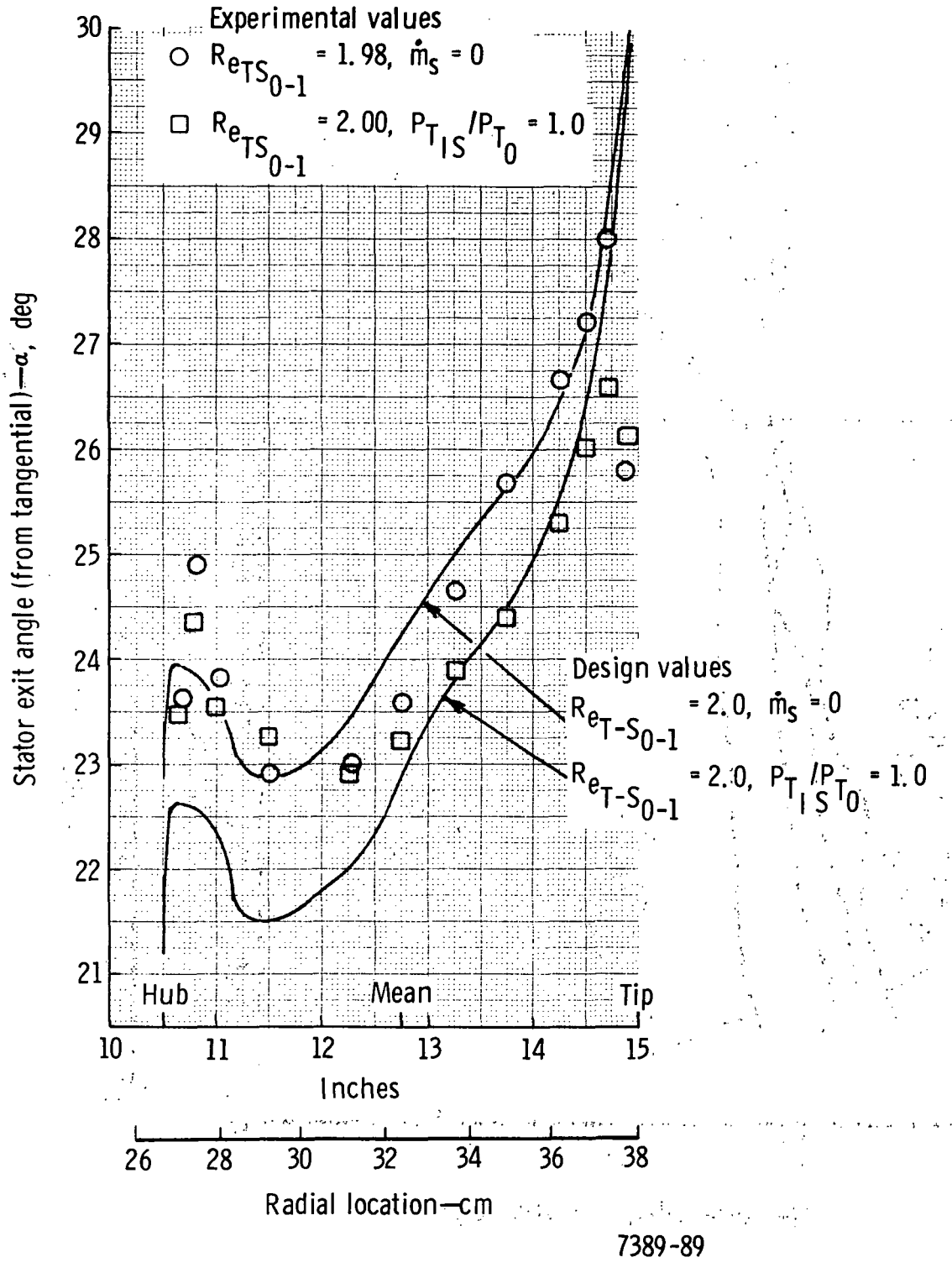

Figure 91. Radial variation of measured and design stator exit angle with jet off and with $P_{T_{IS}}/P_{T_0}$ = 1.0 at design expansion ratio.

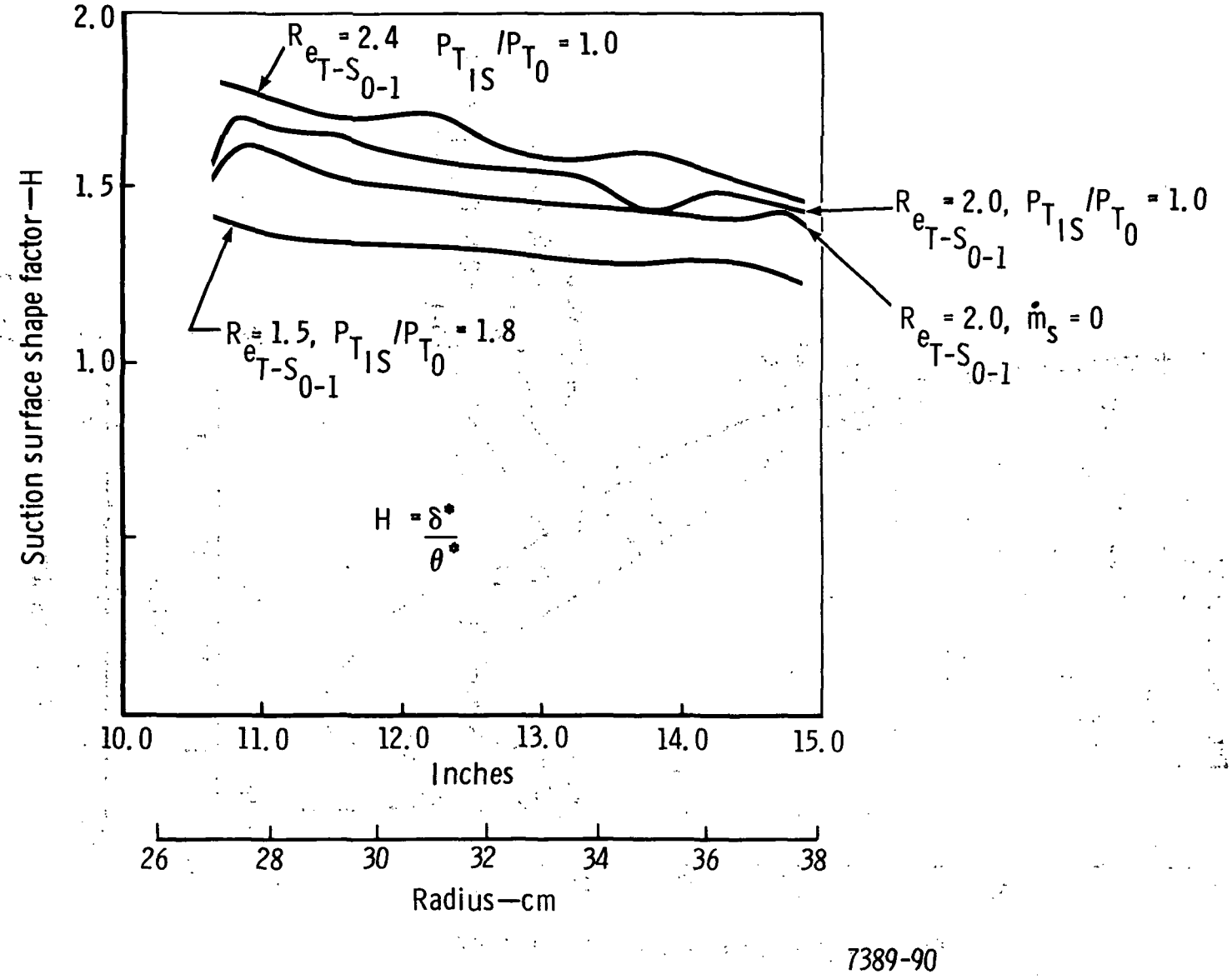

Figure 92. Variation in suction surface shape factor with radius for four survey operating points.

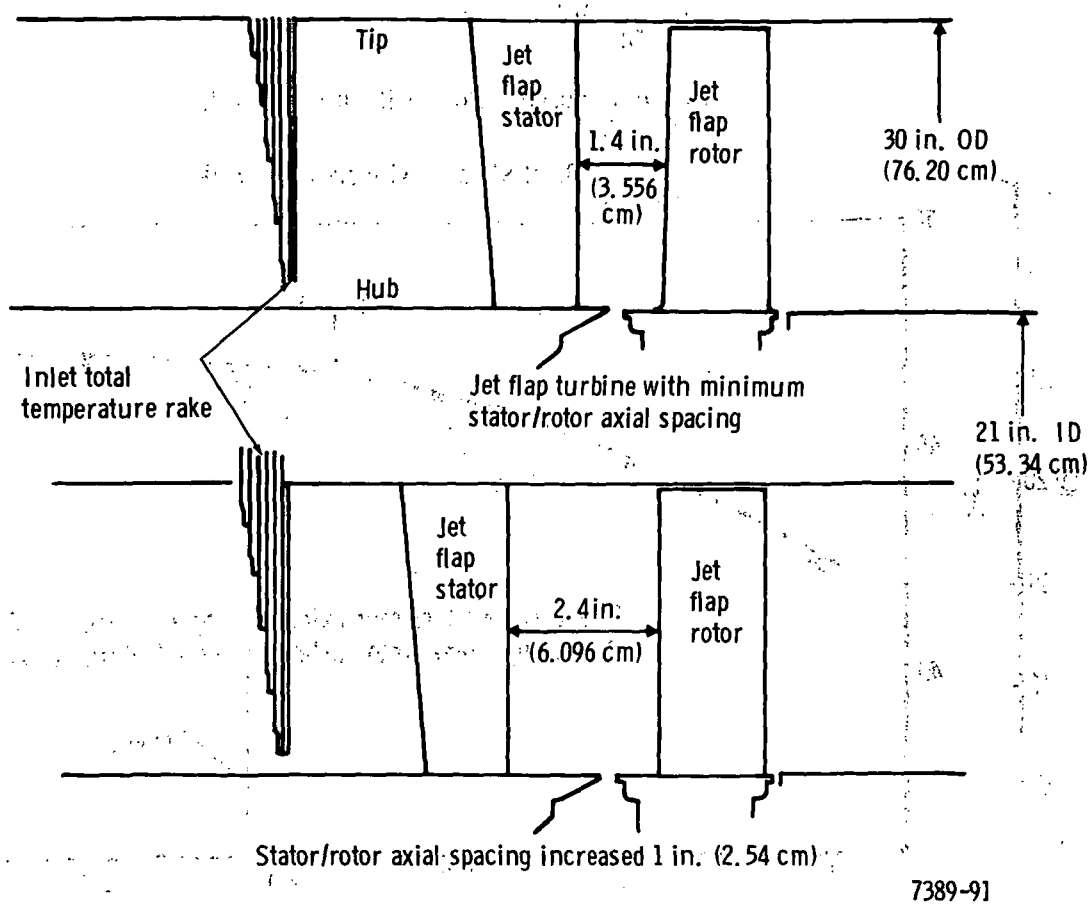

Figure 93. Jet flap turbine flowpath schematic showing stator/rotor axial spacing variations.

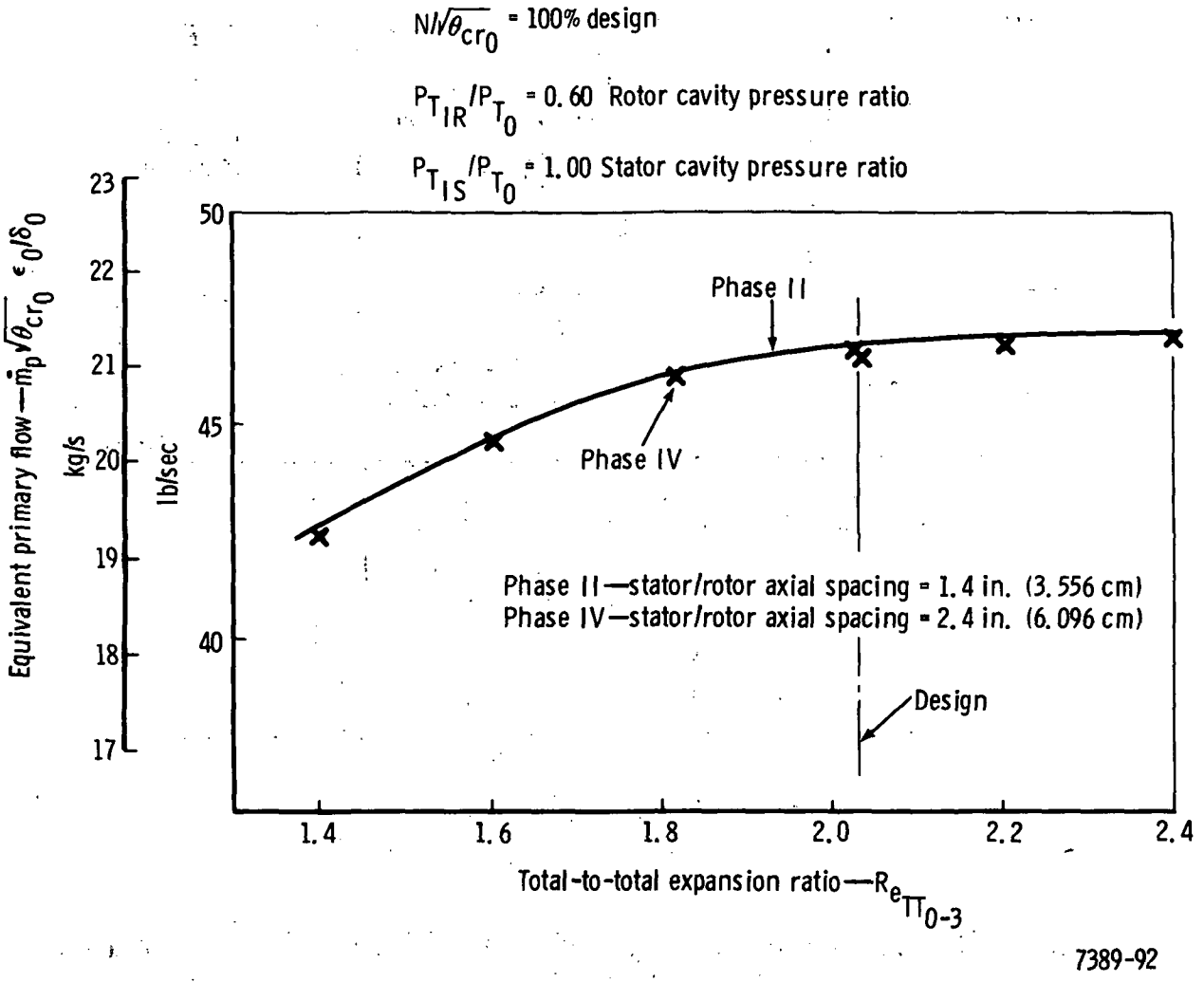

Figure 94. Effect of stator/rotor axial spacing on stator inlet equivalent flow rate.

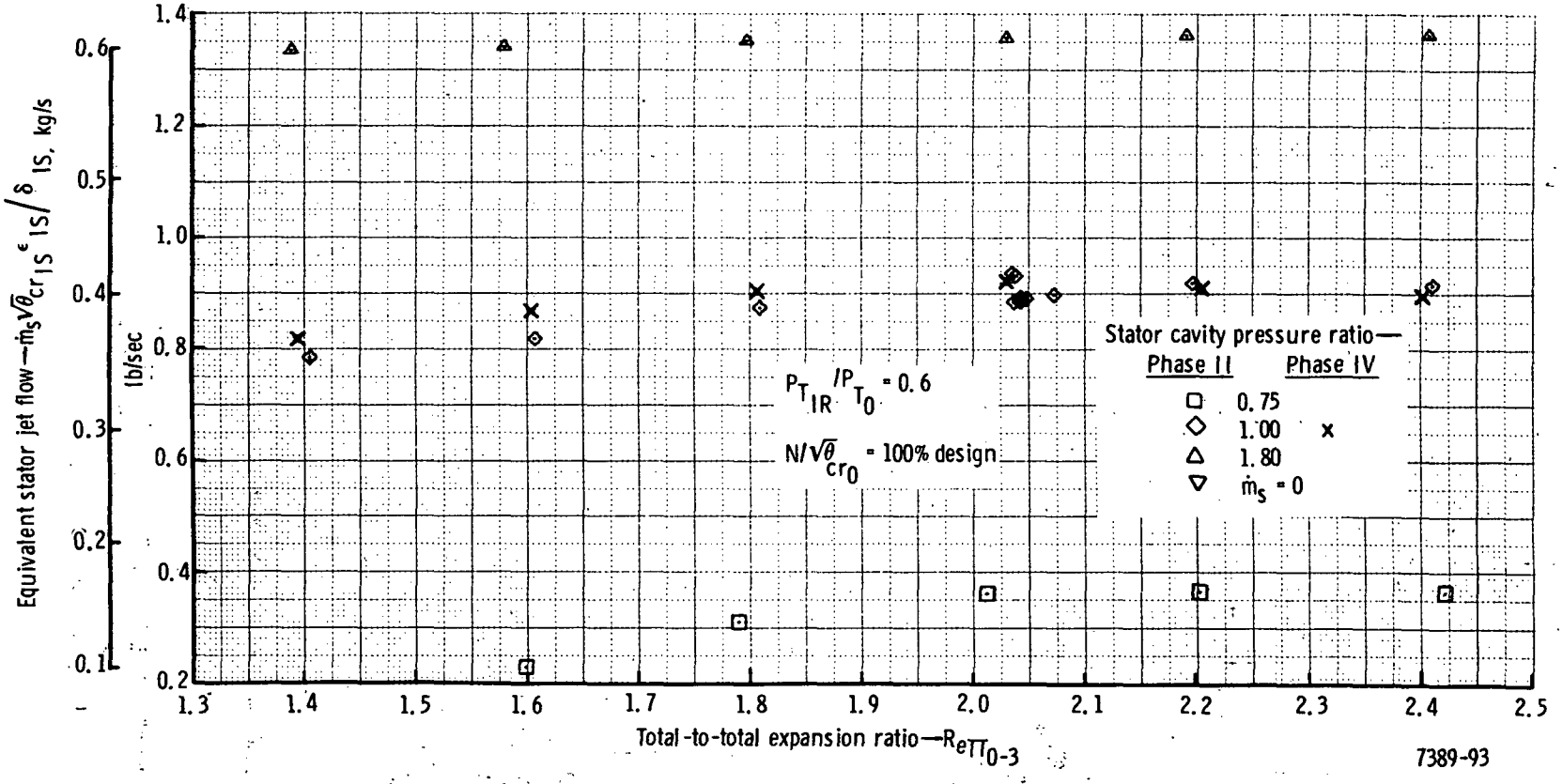

Figure 95. Equivalent stator jet flow variation with stage expansion for Phase II and IV.

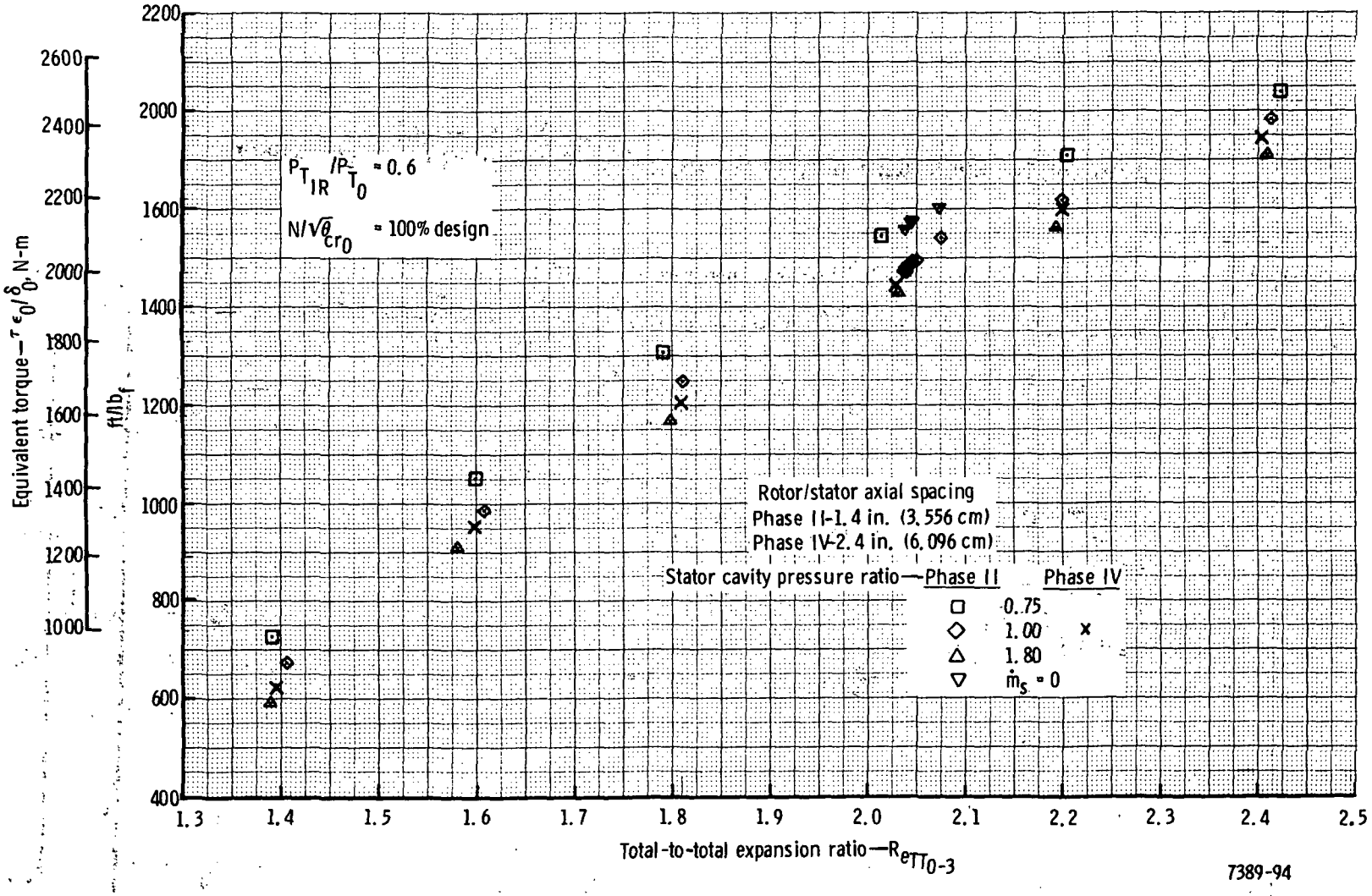

Figure 96. Equivalent torque variation with stage expansion for Phase II and IV.

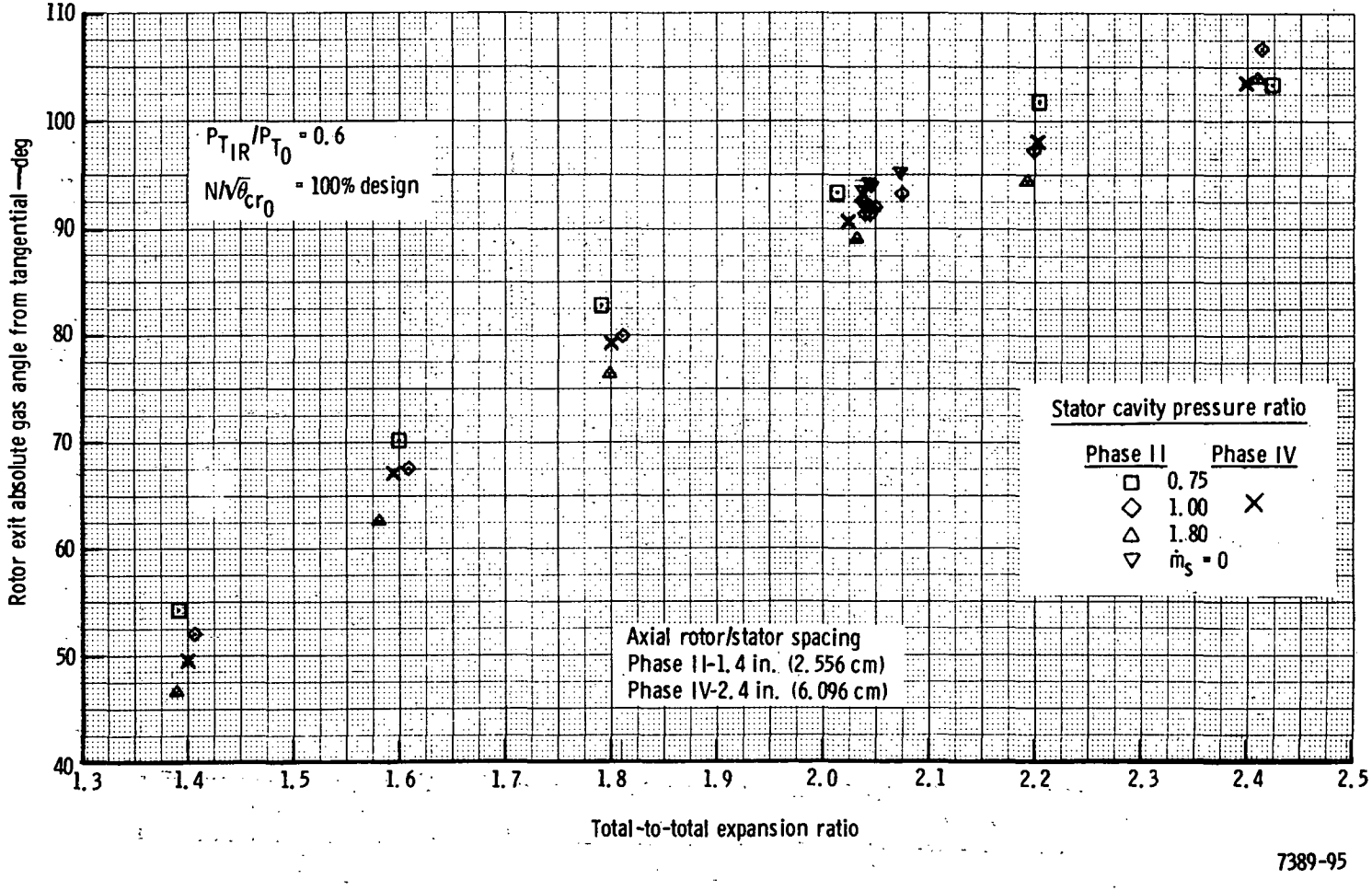

Figure 97. Absolute exit angle variation with stage expansion for Phase II and IV.

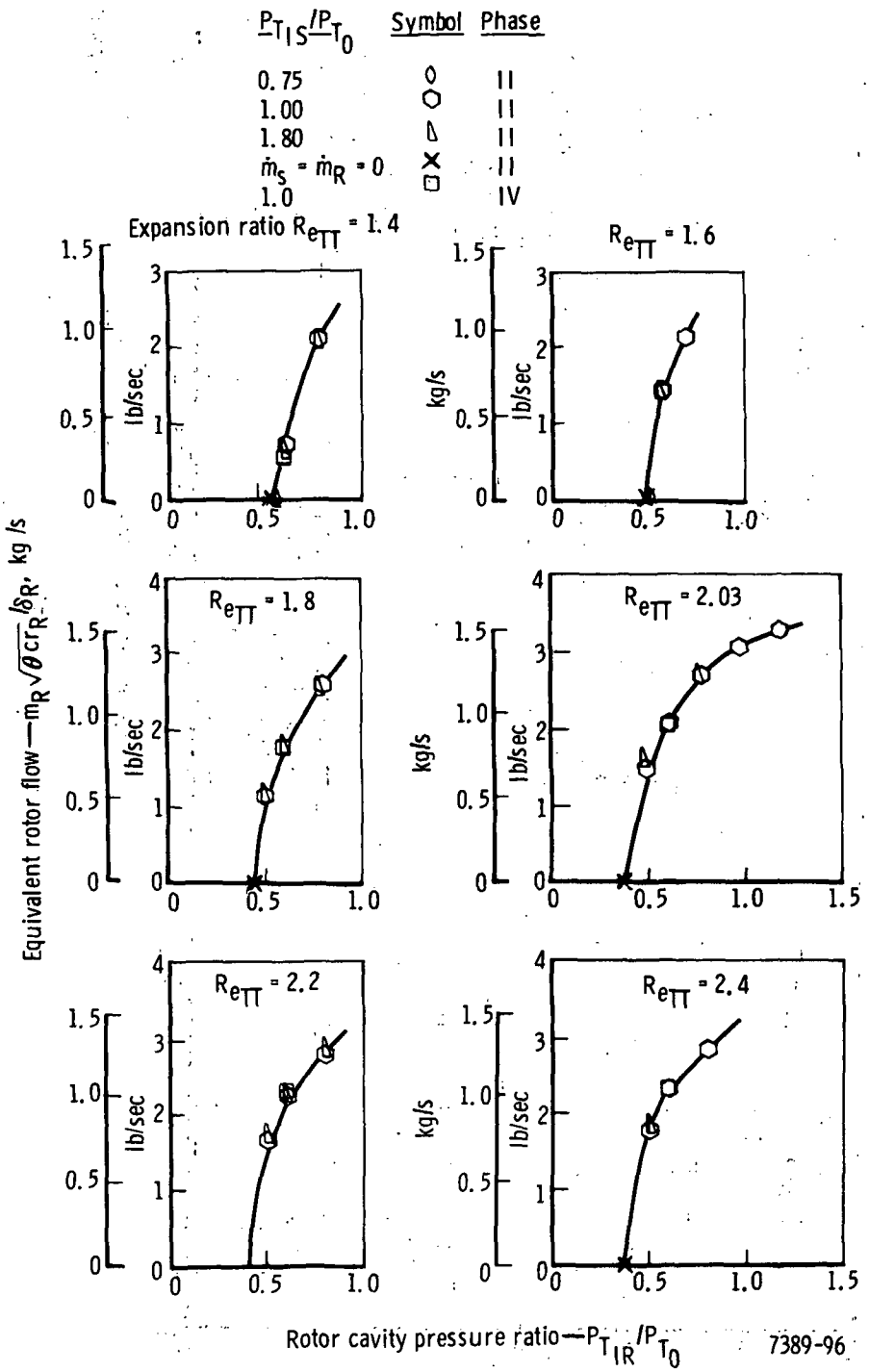

Figure 98. Variation of rotor jet flow with both stator and rotor cavity pressure ratios over a range of turbine expansion ratios $N/\sqrt{\theta}cr_0$ = 100% design.

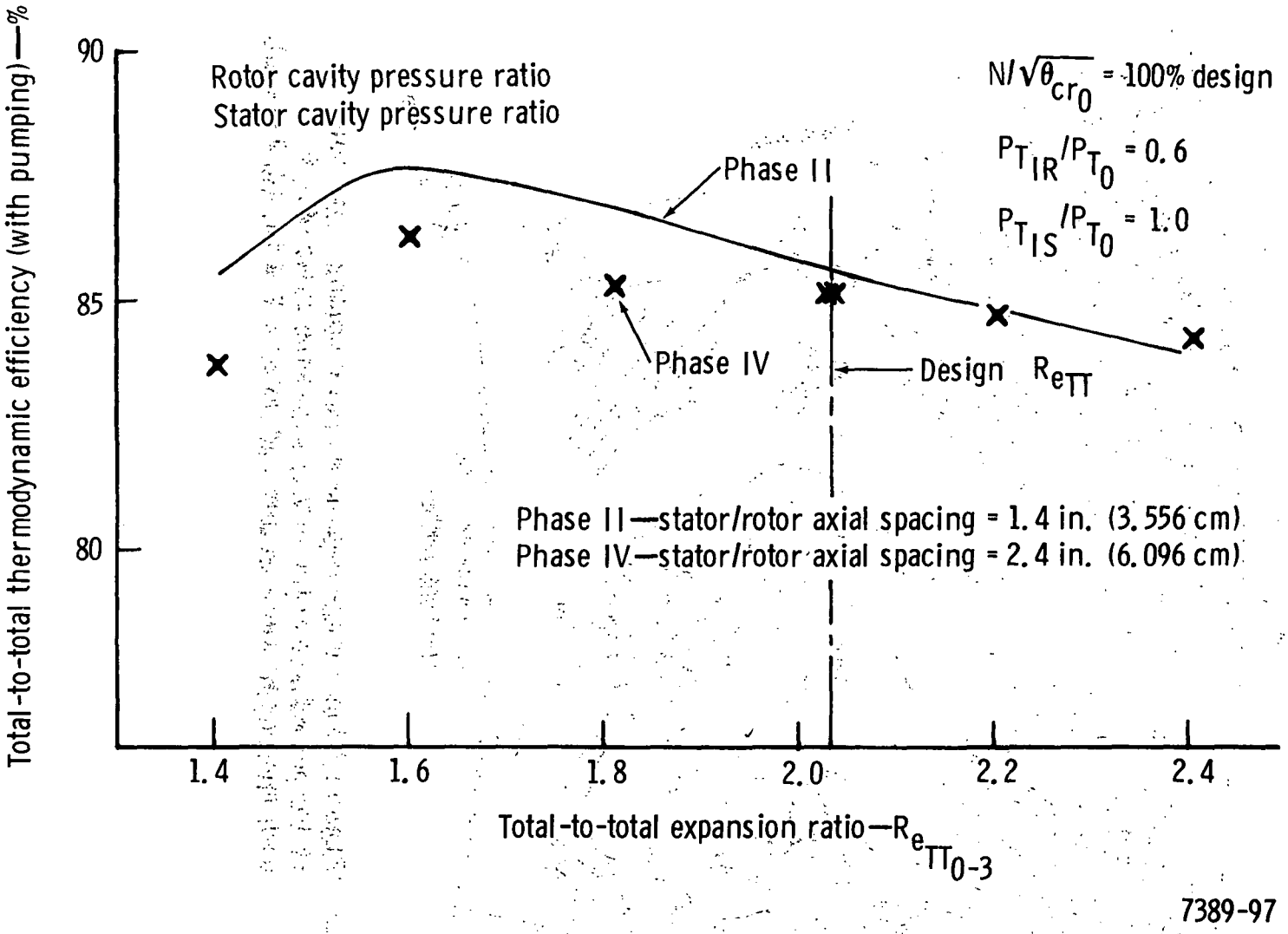

Figure 99. Effect of stator/rotor axial spacing on turbine efficiency.

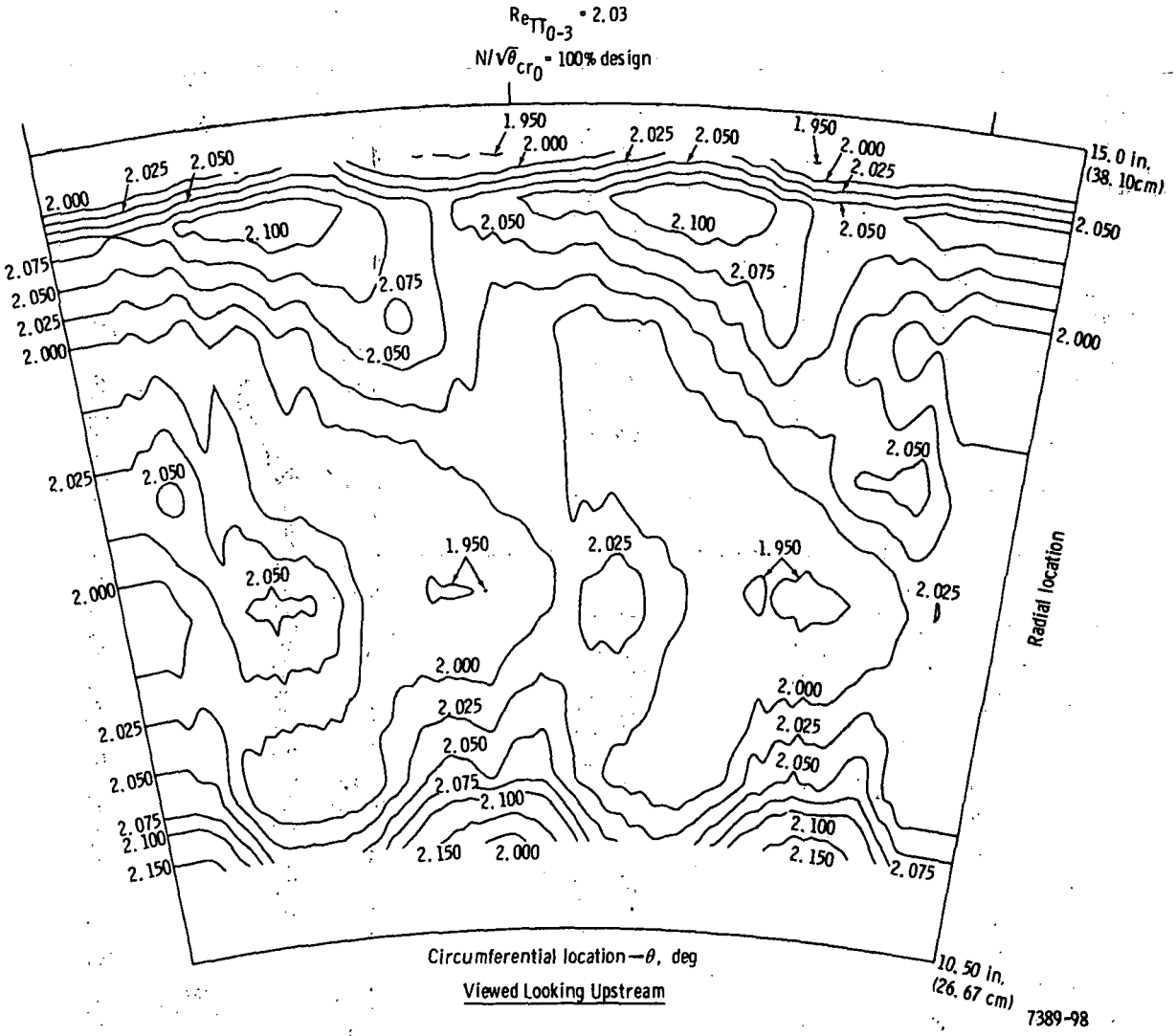

Figure 100. Phase IV local stage expansion ratio contour map for stator jet off and rotor cavity pressure ratio of 0.6 with spacing between stator and rotor = 2.4 in. (6.096 cm).

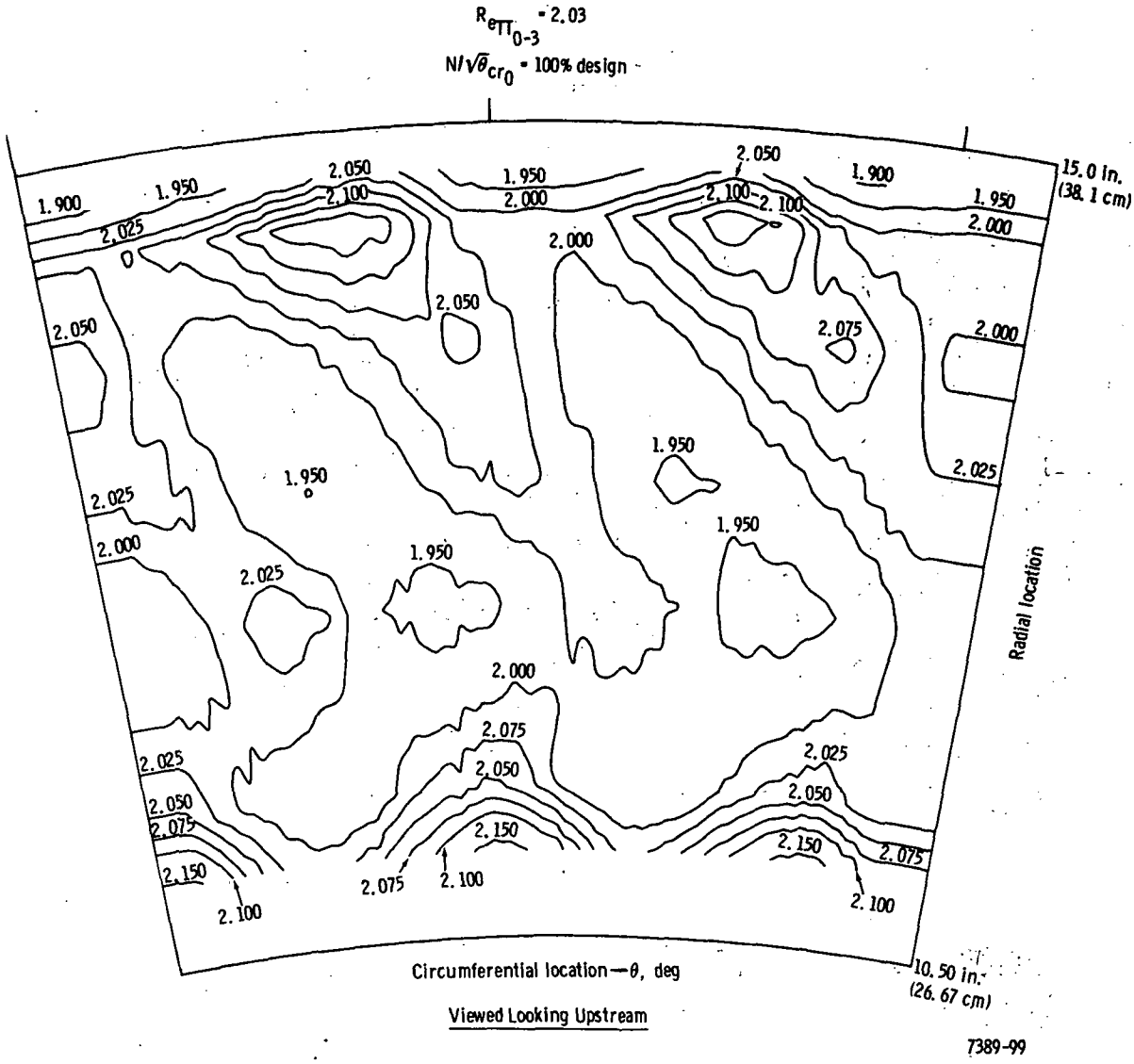

Figure 101. Phase IV local stage expansion ratio contour map for jet-on condition ($P_{T_{IS}}/P_{T_0}$ = 1.0 and $P_{T_{IR}}/P_{T_0}$ = 0.6) with axial distance between stator and rotor = 2.4 in. (6.096 cm).

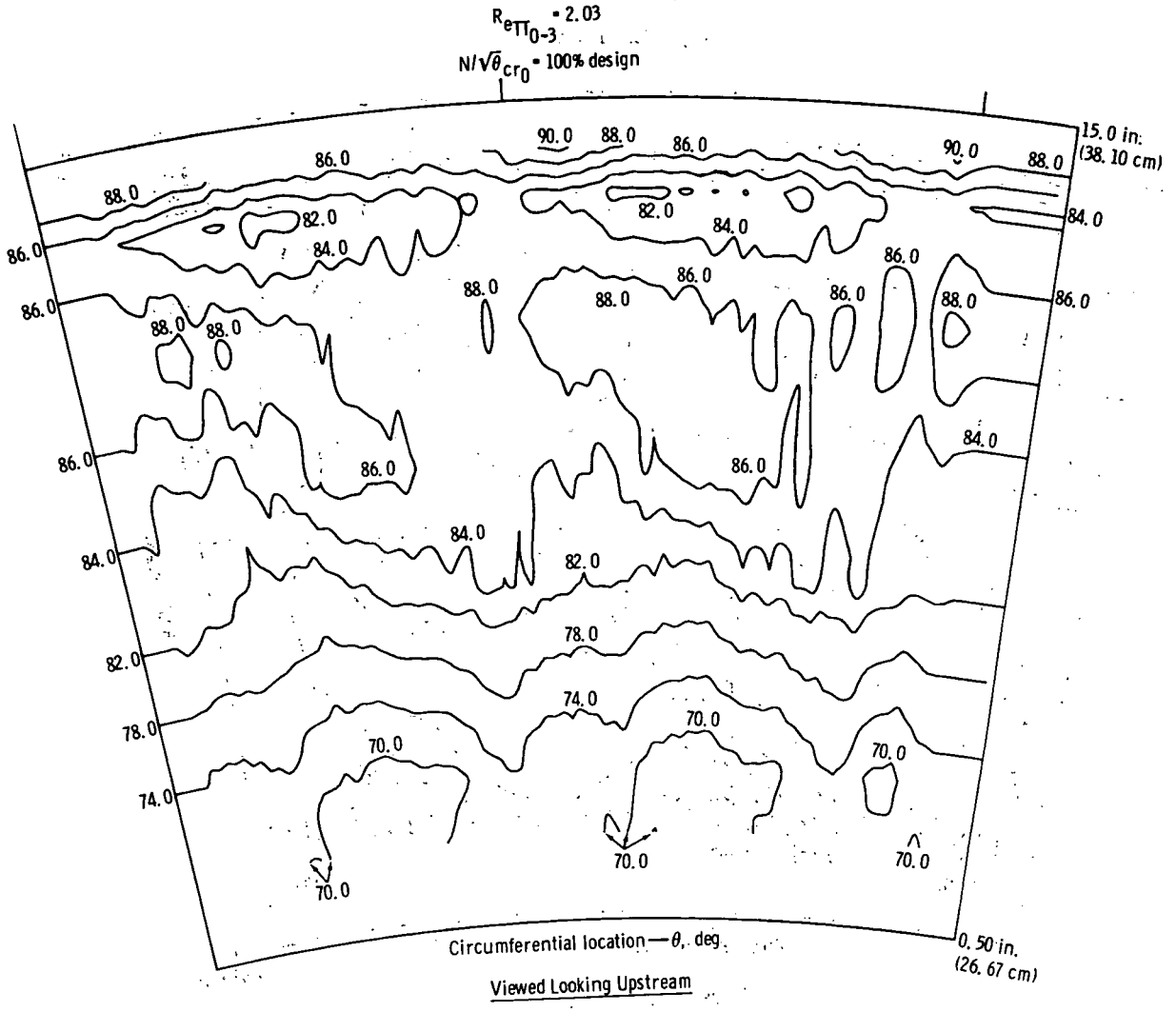

Figure 102. Phase IV efficiency contours at rotor exit for stator jet off and rotor cavity pressure ratio of 0.6 with spacing between stator and rotor = 2.4 in. (6.096 cm).

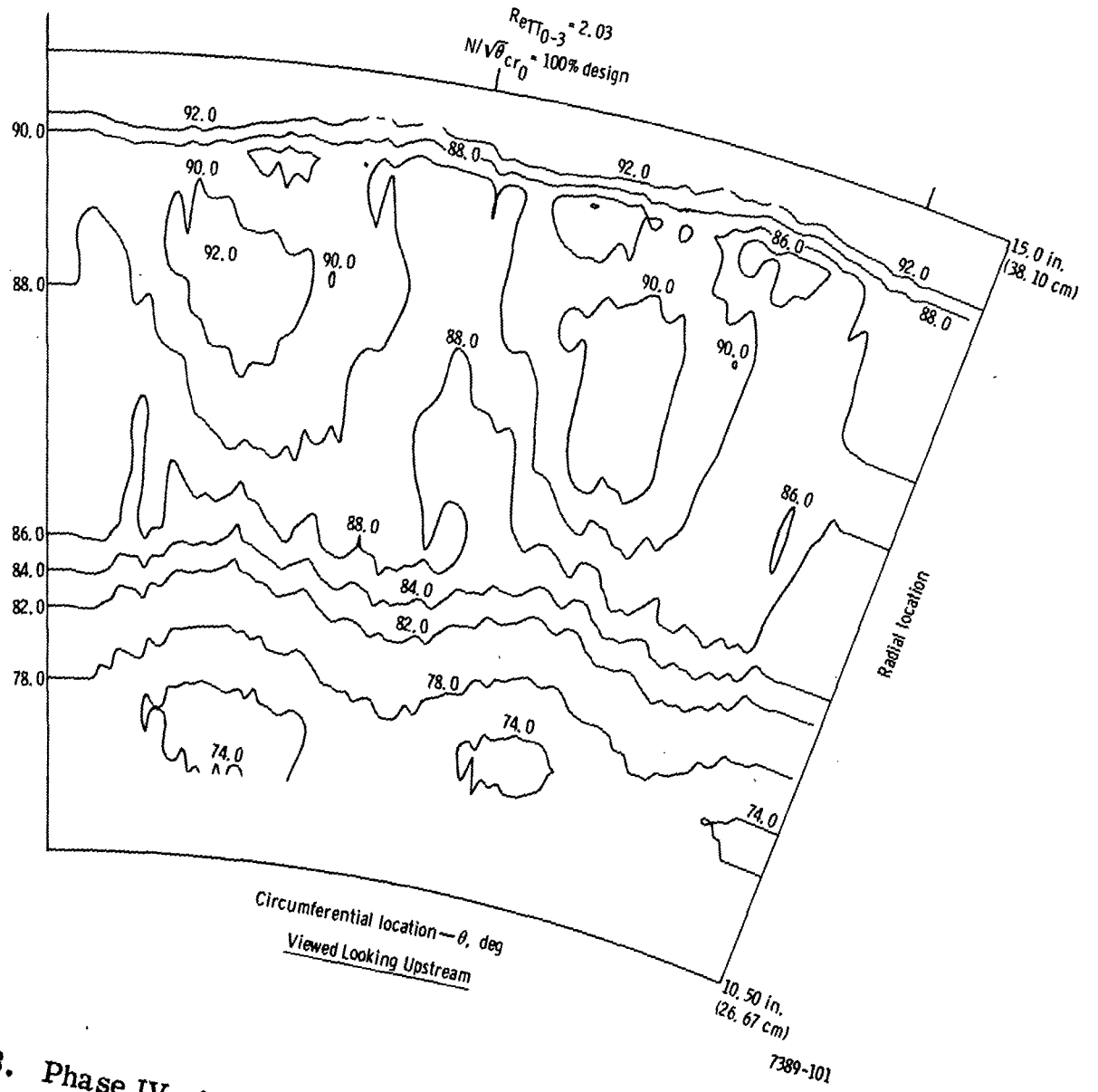

Figure 103. Phase IV efficiency contours at the rotor exit for jet-on condition ($P_{T_{IS}}/P_{T_0}$ = 1.0 and $P_{T_{IR}}/P_{T_0}$ = 0.6) with axial clearance between stator and rotor = 2.4 in. (6.096 cm).

GOVERNMENT PRINTING OFFICE: 1973-739-026/18

NATIONAL AERONAUTICS AND SPACE ADMINISTRATION
WASHINGTON, D.C. 20546

OFFICIAL BUSINESS
PENALTY FOR PRIVATE USE $300

SPECIAL FOURTH-CLASS RATE
BOOK

POSTAGE AND FEES PAID
NATIONAL AERONAUTICS AND
SPACE ADMINISTRATION
451

U.S.MAIL

POSTMASTER: If Undeliverable (Section 158 Postal Manual) Do Not Return

"The aeronautical and space activities of the United States shall be conducted so as to contribute . . . to the expansion of human knowledge of phenomena in the atmosphere and space. The Administration shall provide for the widest practicable and appropriate dissemination of information concerning its activities and the results thereof."

—NATIONAL AERONAUTICS AND SPACE ACT OF 1958

NASA SCIENTIFIC AND TECHNICAL PUBLICATIONS

TECHNICAL REPORTS: Scientific and technical information considered important, complete, and a lasting contribution to existing knowledge.

TECHNICAL NOTES: Information less broad in scope but nevertheless of importance as a contribution to existing knowledge.

TECHNICAL MEMORANDUMS: Information receiving limited distribution because of preliminary data, security classification, or other reasons. Also includes conference proceedings with either limited or unlimited distribution.

CONTRACTOR REPORTS: Scientific and technical information generated under a NASA contract or grant and considered an important contribution to existing knowledge.

TECHNICAL TRANSLATIONS: Information published in a foreign language considered to merit NASA distribution in English.

SPECIAL PUBLICATIONS: Information derived from or of value to NASA activities. Publications include final reports of major projects, monographs, data compilations, handbooks, sourcebooks, and special bibliographies.

TECHNOLOGY UTILIZATION PUBLICATIONS: Information on technology used by NASA that may be of particular interest in commercial and other non-aerospace applications. Publications include Tech Briefs, Technology Utilization Reports and Technology Surveys.

Details on the availability of these publications may be obtained from:

SCIENTIFIC AND TECHNICAL INFORMATION OFFICE

NATIONAL AERONAUTICS AND SPACE ADMINISTRATION

Washington, D.C. 20546